UNIVERSIDAD DE CHILE
FACULTAD DE CIENCIAS FÍSICAS Y MATEMÁTICAS
DEPARTAMENTO DE ASTRONOMÍA

THE NATURE OF FILAMENTARY STRUCTURES OF DENSE MOLECULAR GAS IN THE GALACTIC PLANE

TESIS PARA OPTAR AL GRADO DE DOCTORADO EN CIENCIAS, MENCIÓN ASTRONOMÍA

AUTOR:
YANETT CONTRERAS MORALES

PROFESOR GUÍA:
GUIDO GARAY BRIGNARDELLO
PROFESOR CO-GUÍA:
JILL MAREE RATHBORNE

MIEMBROS DE LA COMISIÓN:
DIEGO MARDONES PEREZ
RAINER MAUERSBERGER
PATRICIO ROJO RUBKE

SANTIAGO DE CHILE
JUNIO 2012

Resumen

Estudios recientes en longitudes de onda submilimétrica han mostrado que las estructuras filamentarias se ubican por todo el Plano Galáctico, estando en muchos casos asociadas a zonas de formación estelar. El estudio de las propiedades de los filamentos y su posible relación con con la formación estelar es clave para el entendimiento global de este fenómeno. En este trabajo llevamos a cabo un estudio cuidadoso de nubes moleculares filamentarias para determinar el link entre estas estructuras y el proceso de formación de estrellas de alta masa. Usamos datos en múltiples longitudes de onda para derivar las propiedades físicas de estas estructuras y compararlas con los modelos teóricos que describen la estabilidad y fragmentación de las nubes moleculares filamentarias.

Hemos encontrado que no todos las estructuras filamentarias detectadas en la emisión submilimétrica del polvo en el continuo representan una estructura única coherente. Las observaciones de las lineas moleculares fueron cruciales para evaluar esta coherencia física. La densidad de columna de los filamentos es similar a la de los valores observados en otras nubes moleculares típicas. La densidad de columna, masa virial y presión interna y externa encontrada para los filamentos es similar a la de los valores predecidos por modelos que explican la estabilidad de las nubes moleculares filamentarias debido a la presencia de un campo magnético toroidal dominante.

El espaciamiento observado entre los cúmulos inmersos en los filamentos ($\sim$ 2 pc) es consistente con la teoría de fluido-inestabilidad (o *"sausage"*) que podría explicar la fragmentación de filamentos isotérmicos dominados por turbulencias. Algunos de los cúmulos detectados dentro de los filamentos tienen altas masas (>200 $M_{\odot}$), altas densidades ($> 10^5$ cm^{-3}) y bajas temperaturas (< 20K), sugiriendo que estos cúmulos pueden ser los precursores de las estrellas de gran masa.

Abstract

Recent surveys at sub-millimeter wavelengths have shown that filamentary structures are ubiquitous along the Galactic Plane and many of them seems to be associated with star forming regions. The study of the properties of filaments and their possible link to star formation is key to the global understanding of this phenomena. In this work we carry out a careful study of filamentary molecular clouds to determine the link between these structures and the process of high mass star formation. We used multi wavelength data to derive the physical properties of these filamentary structures and compare them with theoretical models that describe the stability and fragmentation of filamentary molecular clouds.

We have found that not all the filamentary structures detected in sub-millimeter dust continuum emission represent single coherent structures. Molecular line observations were crucial to asses their physical coherence. The column density of filaments are similar to the values observed toward other typical molecular clouds. The column density, virial mass, internal and external pressure found for the filaments are similar to the values predicted by models that explain the stability of filamentary molecular clouds by the presence of a toroidal dominated magnetic field.

The spacing observed between the clumps embedded in the filaments ($\sim$ 2 pc) is consistent with the theory that a fluid, or *"sausage"* instability can explain the fragmentation of isothermal, turbulent dominated filaments. Some of the clumps detected within the filaments have high masses (>200 $M_{\odot}$), high densities ($> 10^5$ cm^{-3}) and cold temperatures ($<$ 20 K), suggesting that these clumps may be the precursors to high mass stars.

Contents

List of Figures

List of Tables

1

Introduction

This thesis investigates the physical and kinematical properties of filamentary molecular clouds. Dust continuum surveys have shown that filaments are ubiquitous along the Galactic Plane and that most of them harbor regions of low and high mass star formation. Knowing how filaments are formed, their physical properties, how are they stable and which are the processes that lead to the formation of stars within them will help us to understand the environment where high mass stars are born, which is key to the global understanding of the processes of high mass star formation.

Stars are the building blocks of our universe. The processes and energy involved in the formation of a stars determines on large scales the structure and evolution of Galaxies, while on smaller scales it is strongly linked to the formation of other stars and planetary systems. Moreover, all the chemical elements in our universe are formed within stars, thus, they are responsible for everything we know. Therefore, understanding how stars are formed is key to the understanding other processes in Galaxies and in our universe.

While for low mass stars great advances have been made understanding how they are formed, for high mass stars this is still far from being understood. High mass stars interact with their environment injecting great amount of energy which changes dramatically their surrounding for the next generation of stars and are responsible to trigger other processes in their parental molecular cloud, such as star formation. The study of the earliest stages of high mass star formation and their

environmental conditions is key to understand how high mass stars are formed.

In the following sections we overview the general properties of molecular clouds and discuss the current knowledge of the formation of low and high mass stars. We outline the current knowledge on filamentary molecular clouds and review the theories that describe the processes that lead to the fragmentation of filaments and the formation of stars clusters within them. We also summarizes the techniques and definitions used to derived the physical and kinematical properties for the filaments and clumps studied as part of this work.

1.1 Molecular clouds

Many years after the discovery of the first ”optically dark” cloud by Herschel (1785) these obscured regions in the sky were treated as curiosities. It was debated whether if they were holes in the interstellar medium left by stars or whether they represented obscured matter. Barnard (1919) was the first to suggest that these objects were obscuring bodies located in front of more distant stars. It was not until 1946 when Bok discovered that in fact stars could form within these dark objects.

Observations with radio telescopes at sub-millimeter and millimeter wavelength have shown that stars and planets are formed within these dark clouds, being able to detect the embedded proto starts within them. Moreover, the discovery of molecules in space showed that most of the mass in these dark clouds is in the form of molecules, hence they are referred to as molecular clouds.

1.1.1 Formation

To form stars from condensations in the interstellar matter, first it is needed to have molecular clouds massive and dense enough to be gravitationally bound. The exact mechanism related to how a molecular cloud is formed from the interstellar medium (ISM) remains unclear. If the interstellar mediums is partially supported by magnetic fields, then it is susceptible to instabilities that can concentrate the gas into large condensations or clumps (Parker 1966). If the ISM is heated (by cosmic rays of X-rays) it also becomes unstable separating into a dense cool phase (clouds) and a hot tenuous medium (Field 1970).

To form molecular clouds which are massive and dense to go under further collapse and form stars, three main mechanism are proposed: collisional aglomerations (Kwan 1979; Scoville and Hersh 1979; Stark 1979; Cowie 1980; Kwan and Valdes 1983), on which small clouds collide forming a high mass gravitationally bound cloud; gravithermal instability (Parker 1966; Mouschovias et al. 1974; Shu 1974; Elmegreen 1982); pressurized accumulation by shocks of supernovae (Opik 1953;

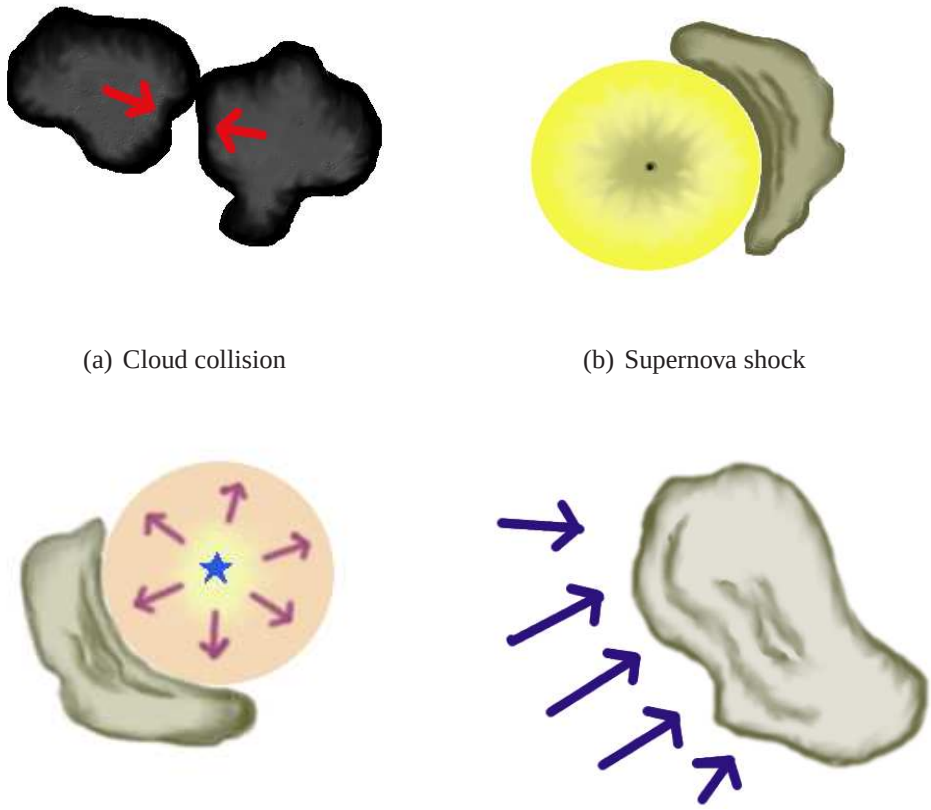

(a) Cloud collision

(b) Supernova shock

(c) Young star winds

(d) Galactic shock

Figure 1.1: Scheme of the formation of a molecular cloud. In this figure are shown some of the mechanisms that could explain how molecular clouds are formed.

Herbst and Assousa 1977), Galactic shocks (Woodward 1976) or winds from newly formed stars, on which the material is compressed by shocks (Figure 1.1). Some of these mechanisms also can form filamentary molecular clouds as the ones seen in the Galactic Plane.

1.1.2 Composition of molecular clouds

The majority of the mass of a cloud is molecular, however, the majority of their volume is atomic. The most abundant molecule in molecular clouds is, but other molecules have been also detected, such as CO, CS , NH_3, H_2O, HCN, N_2H^+, CH_3CN, etc. Also, about one percent of the mass of molecular clouds is in the form of dust, typically composed of silicates and graphites.

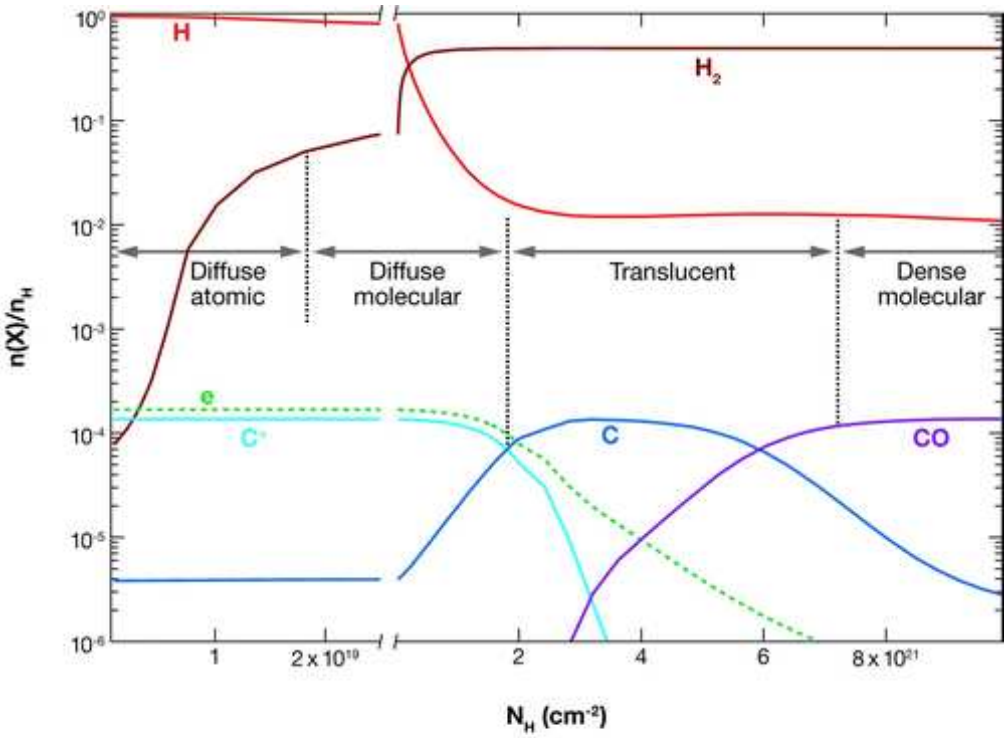

FIGURE 1.2: Scheme with the relation between the density and molecular and atomic abundance in molecular clouds. At higher density the composition is mostly in the form of molecular hydrogen and CO, while at the external part the gas is in atomic form. (Snow and McCall 2006)

Observations toward molecular clouds have shown that their shapes and sizes cover a wide range, however in general it is observed that most clouds have irregular borders and often present filamentary structures. Giant molecular clouds have sizes that ranges from 2 to 15 pc, masses between 10^3 to 10^5 $M_\odot$ and densities from 50 to 500 cm^{-3}.

Extended cloud complex have in their interior dense regions where most of their content will be molecular hydrogen, created by catalysis in the dust grains surface. These dense regions are surrounded by a layer of atomic gas with typical column densities of $N_H \sim 2 \times 10^{20} cm^{-2}$ and $A_v = 0.1$ mag (Bohlin et al. 1978). This layer is able to shield the interior of the molecular cloud from the interstellar UV radiation. Since CO needs a higher density to form, there is a layer of H_2 and atomic carbon ("dark gas"), however, this layer is very difficult to observe (Grenier et al. 2005). Figure 1.2 shows an scheme of the composition of a molecular cloud.

Because of the dust grains that they contain some molecular clouds appear dark, at optical wavelength, against the bright extended background. The light from the background stars is scattered and absorbed by the dust and this absorption will depends on the material that the dust is made off.

To derive the physical properties of molecular clouds we observe their emission arising from the excitation of the molecules within them. Although H_2 is the main component of molecular clouds, due to its symmetry has no dipole momentum, thus, its emission due to a rotating dipole is forbidden. This, added to the low temperatures at molecular clouds, makes H_2 emission very difficult to detect toward them. Thus, to derive the physical properties of molecular clouds, other less abundant molecules but easier to detect (e.g. CO, CS etc.) are used as tracers of H_2. Although these molecules are less abundant, they have several lines in the far infrared to millimeter range making them easy to detect toward molecular clouds.

Another method to study molecular clouds is via the thermal emission from the dust within them. Dust is heated by cosmic rays and stellar radiation and cools by emitting blackbody radiation. Temperatures derived from this blackbody radiation reveal that dust can be very cold ($\sim$ 10 K) because this blackbody peak from far infrared to millimeter wavelengths. Observations at these wavelengths can reveal the structure and properties of molecular clouds.

Identifying the regions where high mass stars are formed have been improved since recent infrared Galactic plane surveys (i.e. IRAS, ISO, MSX and Spitzer), both in molecular lines and dust thermal emission, carried out to search and study molecular clouds. A major finding of these surveys have been the identification of IRDCs, first by the *Infrared Space Observatory* (ISO) (Perault et al. 1996; Hennebelle et al. 2001) and then by the *Midcourse Space Experiment* (MSX) (Egan et al. 1998). It has been found that most of the sites of high mass star formation and cluster formation corresponds to dark clouds at infrared wavelength (Rathborne et al. 2006) and that most of these IRDC correspond to filamentary structures. These filaments have been observed in many sites of high mass star formation (e.g. Orion (Johnstone and Bally 1999)).

Moreover, recent dust continuum surveys such as ATLASGAL (Schuller et al. 2009) aims to have a complete census of the sites of high mass star formation. Since the regions where stars are formed have typical temperatures of 10 - 20 K their emission will peak at millimeter wavelength, therefore, mapping the continuum at this wavelength range is an excellent way to perform an unbiased survey of the dust content in the Galactic plane, identifying the places were star formation is taken place.

1.1.3 Structure

Molecular clouds are very inhomogeneous having regions within them with higher densities. These dense regions can be divided into two groups: clumps and cores. Clumps have typical masses ranging from 50 to 500 $M_\odot$, sizes of 0.3 - 3 pc and densities of 10^3 - 10^4 cm$^-$3. Clumps are defined as the sites where star clusters will be formed (Blitz and Williams 1999). On small scales clumps

TABLE 1.1: Typical properties of GMC, molecular clouds, clumps and cores (Blitz 1993; Garay and Lizano 1999; Bergin and Tafalla 2007; Beuther et al. 2007)

	GMC	Clouds	Clumps	Low mass cores	High mass cores
Mass ($M_\odot$)	$1-2\times10^5$	10^3-10^4	50-500	0.5-5	$\sim10^2$
Size (pc)	40	2-15	0.3-3	0.03-0.2	<0.1
Mean density (cm^{-3})	~50	50-500	10^3-10^4	10^4-10^5	10^5-10^8
Velocity extent (km s^{-1})	2-5	2-5	0.3-3	0.1-0.3	~0.3
Gas temperature (K)	≈ 10	≈ 10	10-20	8-12	10-50

also fragment into smaller denser objects defined as "cores". Cores are the sites were single stars or complex systems, such as binaries, will be formed. Cores that will give rise to a low-mass star have typical masses of 0.5 - 5 $M_\odot$, sizes of 0.03 - 0.2 pc and densities of 10^4 - 10^5 cm^{-3}. Cores that will give rise to high-mass cores have masses of $\sim 10^2$ $M_\odot$, typical sizes of < 0.1 pc and densities of 10^5 to 10^8 cm^{-3}. Table 1.1 summarizes the properties of molecular clouds, clumps and cores.

The temperatures of cores, clumps and molecular clouds ranges from 8 to 20 K. The dust and gas inside the molecular cloud have a kinetic temperature that is regulated by the equilibrium between the heating and cooling. The heating of the gas is mainly due to cosmic ray while the cooling is mainly due to the CO emission. The dust is in general heated by the absorption of UV and visible radiation and cools by thermal emission. At densities greater than 10^3 cm^{-3} the gas and the dust will be coupled thermally by collisions.

1.2 Star formation

The formation of stars can be divided in two categories: low mass star formation and high-mass star formation, with the division at 8 $M_\odot$. While low mass star formation has been widely studied and nowadays we have a clear picture of how low mass star are formed, the processes involved in high-mass star formation are far from being understood. This is mainly because high-mass are rare and evolve very rapidly making the processes that lead to their formation very difficult to observe.

Both, low and high-mass stars, are formed from clumps within molecular cloud. The theories that explain how clumps are formed inside molecular clouds are overviewed in Section 1.3.3. In this section we begin our review with the processes that happens once the clump has already been formed. Section 1.2.0.1 reviews the current knowledge on how low mass stars are formed. Section

1.2.0.2 describe the current theories involving high-mass star formation (For further detail please refer to McKee and Ostriker (2007) and Shu et al. (1987)). In Section 1.3.4 we discuss which is the role between filamentary structure and star formation.

1.2.0.1 Low-mass star formation

Low-mass star are formed from gravitationally bound cores. The processes from the fragmentation of clumps forming cores to the appearance of a newly formed star can be summarized by four stages (Shu et al. 1987). The first stage corresponds to the formation of the core from the fragmentation of a clump inside a molecular cloud (Figure 1.3 (a)).

Once the cores are formed within the clumps, cores which are magnetically supercritical will collapse from "inside-out", becoming very centrally condensed with a density profile that falls of as $\rho \sim r^{-2}$ (Bodenheimer and Sweigart 1968; Larson 1969). This will lead to the formation of a central protostar and a disk (Figure 1.3 (b)). This protostar-disk system will be embedded in an envelope of dust and gas from which it will accrete material, only if the turbulence in the envelope is low.

The collapse of a rotating core will lead to the formation of a protostar with a rotating disk. The accretion, eventually, will increase the mass of the protostar enough to start the deuterium ignition at its center. If the mass of the stars is $< 2M_{\odot}$ the star will be completely convective. Eventually the accreting material will fall mostly onto the disk, giving way to the stellar wind to escape from the weakest part of the system which corresponds to the axis of rotation. The escape of wind, through the rotation axis, will produce collimated jets and bipolar outflow. This corresponds to the third stage (Figure 1.3 (c)). As times goes on, the opening angle of the outflow increases sweeping out the envelope of the protostar completely. At this stage we can see a newly formed star (Figure 1.3 (d)).

1.2.0.2 High-mass star formation

Unlike the low mass scenario, the processes involved in the formation of high mass stars are still not well understood. This is mainly because high-mass stars are rare compared with low-mass stars. Moreover, most sites of high-mass star formation are further away from Earth, for example, one of the closest region of high-mass star formation is Orion located 400 pc from Earth. High mass stars are usually formed in clusters, needing high spatial resolution to avoid confusion to study how individual high-mass are formed, which makes difficult to study in detail the processes inside their parental molecular clouds. Only now we begin to be able to do this with next-generation telescopes such as ALMA. Moreover, the radiation from newly formed high-mass stars destroy their parental

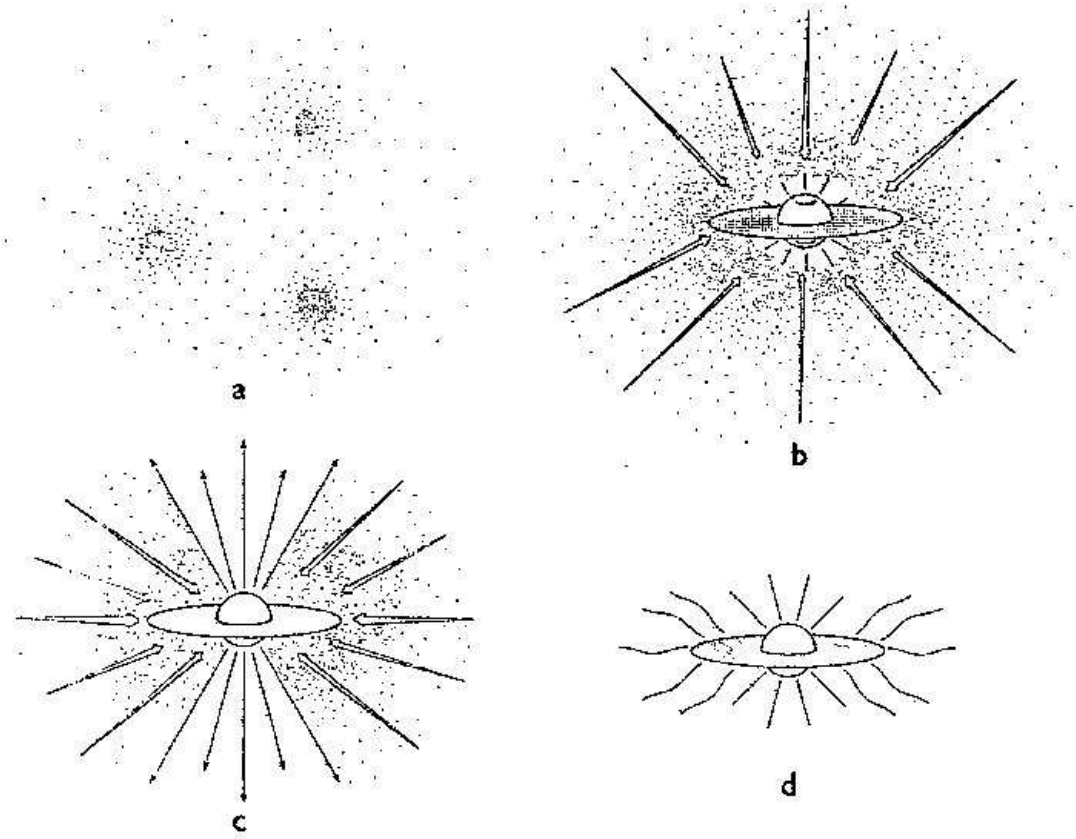

FIGURE 1.3: Four stages of low mass star formation. (a) When the magnetic and turbulent support is lost, cores can form within molecular clouds. (b) The core collapse from inside-out forming a protostar with a surrounding disk. (c) Bipolar flow is formed from the stellar wind along the rotational axis of the system. (d) The star is formed. (Shu et al. 1987)

environment very rapidly. Thus, we only can study the formation of high-mass star while they still are deeply embedded in its parental molecular cloud, which makes even difficult to observe them.

The main difference between the formation of a high-mass star and a low-mass stars, is that high-mass stars form first than their Kelvin-Helmholtz time, t_{KH}, which correspond to the timescale where the gravitational potential energy from the contraction of a mass of gas under gravity is converted to heat. Therefore they reach the main sequence while still accreting material from their surroundings. To try to describe how high-mass stars are formed three main theories have been proposed: competitive accretion, monolithic collapse and stellar mergers.

In the competitive accretion model (Bonnell et al. 2004), gravitational collapse form small stars ($\sim$ 0.1 $M_{\odot}$) within molecular clumps. These small stars grow from gravitational accretion of gas,

initially unbound to the them, until they reach a high-mass. This results in the segregation of high-mass stars to be formed at the center of a cluster, as observed. A drawback of this model is that for stars with masses higher than 10 $M_\odot$ the radiation pressure will disrupt the accretion (Edgar and Clarke 2004), thus the competitive accretion model could not be applicable for stars with masses above 10 $M_\odot$.

The second theory is that high-mass stars are formed from the gravitational collapse of individual cores (McKee and Tan 2003), as an scaled-up version of the low-mass star formation. In this scenario the mass from which the star will be formed is gathered before the star formation process begins. The proto-stellar core is formed by gravitational collapse and accretion of material is via a disc. To overcome the effects of the radiation pressure a massive outflow is developed early during the accretion phase. Observationally this theory implies that we should be able to find high-mass pre-stellar cores that live for a long time (Zinnecker and Yorke 2007).

Stellar mergers represent the most radical scenario. In this theory high-mass stars are formed via stellar collisions, which is only possible during a brief moment when the density of stars is $\sim 10^8$ stars pc^{-3} (Bonnell et al. 1998; Bonnell 2002). While this theory predicts an Initial Mass Function in agreement with observations, its main drawback is that such densities have not been observed in any Galactic star cluster. A plausible scenario is that the competitive accretion of forming stars, inside a Galactic cluster, increases the stellar density in the cluster creating a density where the collisions are possible.

A proposed evolution from a high mass core into a high mass star is shown in figure 1.4. The earliest evolutionary stage is a high-mass starless core (HMSC). This stage is the least observationally studied due to the difficulties of detecting them, so far none have been detected. They are cold (∼10 K), with masses ranging from 100 $M_\odot$ to few 1000 $M_\odot$, sizes of 0.25-0.5 pc and densities of 10^5 cm^{-3} (Beuther et al. 2007). Observationally, they are characterized by strong cold dust emission, molecular lines at sub-millimeter to millimeter wavelength (e.g ^{13}CO, N_2H^+ and HNC) and non detection in the mid-infrared.

Once the high mass star is turned on, the central star UV radiation heats its surrounding gas and dust. This phase is usually denominated as *"hot molecular core"* phase. Hot cores are internally heated (50-250 K), have masses of 100 to 300 $M_\odot$, sizes < 0.1 pc and densities of $10^5 - 10^8$ cm^{-3}. It is expected to exhibit considerable flux in the infrared: green fuzzies (enhancement at 4.5 μm), 24 μmpoint source emission. The emission at sub-millimeter to millimeter continuum is from thermal radiation of the hot dust. Hot cores are usually associated with molecular outflows and H_2O and Class II CH_3OH maser emission (Walsh et al. 1998; Kylafis and Pavlakis 1999; Beuther et al. 2002; Ellingsen 2006), both signature of an accretion disk (Garay and Lizano 1999; Kurtz et al. 2000). They also exhibit a rich chemistry, showing emission from complex molecules such as large organic carbon chains (e. g. CH_3CN, HC_3CN, $HC^{13}CCN$ and HNCO) (Blake et al. 1987;

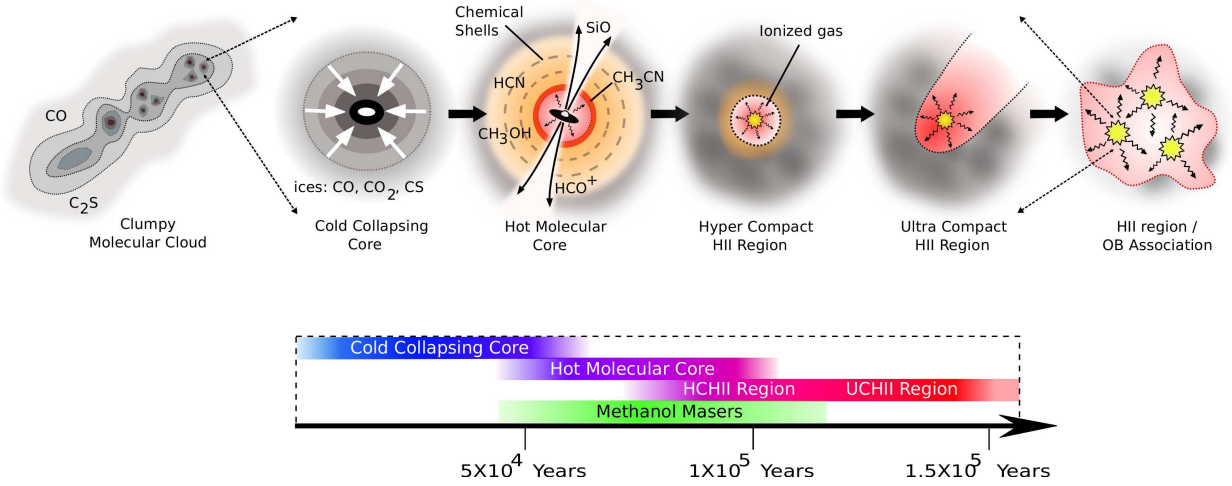

FIGURE 1.4: Proposed evolutionary sequence for a high-mass proto star. Image courtesy of Cormac Purcell.

Schilke et al. 2001) and shock tracers, such as SiO.

Once the high-mass star is formed, its radiation will ionize their surrounding forming an expanding bubble of ionized gas, a ultra-compact HII region (UCHII). The temperature in the ionized gas is $\sim 10^4$ with typical sizes of < 0.1 pc. Hyper compact HII regions (HCHII, sizes < 0.01 pc) may be an intermediate stage between an a hot core and a UCHII. Finally the we see OB associations at the center of a HII region.

1.3 Filamentary Molecular clouds

Recent surveys of dust thermal continuum emission (i.e. ATLASGAL (Schuller et al. 2009), BOLOCAM (Nordhaus et al. 2008), HiGAL (Molinari et al. 2010a)) have shown that filamentary structures are ubiquitous along the Galactic Plane and with lifetimes similar to that of molecular clouds (Myers 2009). Since most of these regions harbor sites of high mass star the study of such structures may help us to a better characterization of the initial condition of star formation and to understand how high mass stars are formed.

Because these filaments have been identified from recent surveys, their study has gained momentum recently. Much work is under way to attempt to study these clouds and their connection to star formation.

While several observational individual studies on individual filamentary regions have been done, such as Orion (Johnstone and Bally 1999), Taurus (Goldsmith et al. 2008), Lupus (Gahm et al. 1993), Ophiucus (de Geus et al. 1990), only few studies over a large sample of filaments have been performed (Schneider and Elmegreen 1979; Myers 2009). Results from simulations of high mass star forming regions also show that filaments are a natural evolution of molecular clouds. These results have helped to understand the physics of filaments, but observational constrains are needed to corroborate these theories.

In the following section we describe the current knowledge of filamentary molecular clouds, about their origin, stability, fragmentation and star formation within them.

1.3.1 Formation

The origin of filamentary structures is still unclear. Several theoretical models have been suggested to explain the formation of filamentary structures from the molecular cloud material. These models can be categorized in three classes: global turbulence, magneto hydrodynamics and global gravitation.

Models invoking global turbulence suggest that filaments arise from compression associated with flows. Simulations show that filaments can be formed only by turbulence, and once the inhomogeneities are formed if turbulence is shut down gravity will dominate and inhomogeneities will collapse giving birth to stars within them. Klessen et al. (2004) and Jappsen et al. (2005) suggest that filaments are formed as the result of compression of initially uniform gas through the collision of randomly convergent turbulent parsec-scale flows. In this, *flow-driven* scenario, turbulence will generate interacting shocks which will converge creating regions of higher densities. These turbulent flows will be responsible for forming the filamentary structures and the inhomogeneities

within them. If turbulence is shut down the inhomogeneities are gravitational dominated and, once the shock that formed them have passed, they will collapse to form clumps that will produce stars. These simulations show that irregular filaments can be formed, as seen for example in the Taurus region. Although the global turbulence theory can form filaments with a characteristic width as those observed by Hershel in the Galactic plane (André et al. 2010), they do not predict a regular spacing and direction observed in filaments (Myers 2009).

Models including magnetic fields, shows that once turbulence is dissipated, magnetized clouds collapse along the magnetic field lines creating dense layers. Ambipolar diffusion then allows gravitational instabilities to create filamentary structures presenting hubs and filaments, as seen toward filamentary molecular clouds (Li and Nakamura 2006).

Filaments can also arise from the compression of parsec-scale flow winds from expanding HII regions or supernova remnants. Observational evidence of star forming regions near OB association supports the idea that filaments can be form from stellar winds (Myers 2009). Winds sweep up low density medium creating self gravitating sheet like structures. These layers can go under further fragmentation due to periodic perturbations (symmetric Bessel function or sinusoid) (Spitzer 1942). If the self gravitating layer posses magnetic field, fluid instability models predicts its fragmentation into filaments that are parallel or perpendicular to the magnetic field depending if the external pressure of the layer is high or low respectively (Nagasawa 1987; Inutsuka and Miyama 1992; Nakamura et al. 1993; Tomisaka 1995).

Since observations show that most of filaments present a hub-tail structure (Myers 2009), corresponding to an elongated clump associated with one or more filamentary tails, such as the one observed in Serpens south cluster (Gutermuth et al. 2008) (Figure 1.5). To account for the hub-tail structure Myers (2009) suggest a scenario where a layer formed by stellar wind bubbles is vertically self-gravitating and density modulated in one horizontal direction and uniform in the perpendicular direction. This modulated layer can develop and maintain filamentary structures with hub tail morphology as observed.

1.3.2 Stability

Filaments can be approximated as self gravitating cylinder. Thus, we can apply the knowledge of these structures to filaments. The stability of self gravitating cylinder have been widely studied. Ostriker (1964) studied the stability of isothermal self gravitating cylinders, finding an analytical expression for the distribution of pressure, density and gravitational energy of an isothermal cylinder in equilibrium. They found that the density distribution, ρ, of an isothermal cylinder in

Figure 1.5: Example of a hub-tail configuration in the Serpens south cluster (Gutermuth et al. 2008). Two color image of IRAC 3.6 μm and 4.5 μm bands north to the right of the image and east to the top. Here we see the hub-tail configuration with two thin filaments to the south and south-east of the hub and a broad structure to the north-west (Myers 2009).

equilibrium is given by:

$$\rho = \rho_0 \frac{1}{(1 + r^2/8)^2}, \tag{1.1}$$

where ρ_0 is the central density and r is the radius of the filament. The mass per unit length is given by:

$$M(r) = \frac{2kT}{\mu m_0 G}\left(\frac{1}{1 + 8/r^2}\right), \tag{1.2}$$

where k is the Boltzmann constant, T is the temperature of the filament, μ is the mean molecular weight, m_0 is the hydrogen mass and G is the gravitational constant. As r tends to infinity the mass per unit length can be approximated as:

$$M = \frac{2kT}{\mu m_0 G}. \tag{1.3}$$

This is the simple case without magnetic field, however, because observations showed the presence of large scale magnetic fields towards giant molecular clouds, it was necessary to develop

more complicated theories that explain the stability of filamentary molecular clouds in the presence of large scale ordered magnetic fields (Fiege and Pudritz 2000; Fiege et al. 2004; Tilley and Pudritz 2003).

Observationally, there is ample evidence of magnetic fields associated with in filamentary molecular clouds. Alves et al. (2008) undertook optical polarimetry toward the diffuse gas in the Pipe nebula and found a large scale magnetic field perpendicular to the main axis of the cloud. Chapman et al. (2011) also found a magnetic field perpendicular to the long axis of the filamentary region B213 in Taurus. These results are interpret as evidence that the gas and dust collapsed along the field lines forming this filamentary structure. In Orion, Poidevin et al. (2010) measured the polarimetry of stars which led to a representation of the morphology of the magnetic field which is found to be a two-component or helical magnetic field wrapping the filament.

Fiege and Pudritz (2000) developed a new model of filamentary molecular clouds, truncated by external pressure and presenting a rather general helical magnetic field. To do this they used a version of the tensor equation of virial equilibrium to include the presence of magnetic field and external pressure in long filamentary clouds. The virial equilibrium is given by the following equation (see Appendix D.1 for full derivation of this equation):

$$\frac{P_S}{\langle P \rangle} = 1 - \frac{m}{m_{vir}}\left(1 - \frac{\mathcal{M}}{|\mathcal{W}|}\right), \tag{1.4}$$

where m is the mass per unit length; P_s is the surface pressure; $\langle P \rangle$ is the average internal pressure given by:

$$\langle P \rangle = \frac{\int P d\mathcal{V}}{\mathcal{V}}, \tag{1.5}$$

where $\mathcal{V}$ is the volume per unit length. m_{vir} is the virial mass per unit length given by:

$$m_{vir} = \frac{2\langle \sigma^2 \rangle}{G}, \tag{1.6}$$

where σ is the velocity dispersion and G is the gravitational constant. $|\mathcal{W}|$ and $\mathcal{M}$ are the gravitational and total magnetic energies respectively given by:

$$\mathcal{W} = -m^2 G, \tag{1.7}$$

$$\mathcal{M} = \frac{1}{4\pi}\int B_z^2 d\mathcal{V} - \left(\frac{B_{zS}^2 + B_{\phi S}^2}{4\pi}\right)\mathcal{V}, \tag{1.8}$$

where B_z is the magnetic field component along the axis of the filament and $B_{zS}, B_{\phi S}$ are the component z and ϕ of the magnetic field at the surface of the filament.

The value determined for $\mathcal{M}$ can be positive or negative, depending on whether or not the poloidal or toroidal component of the magnetic field is dominant. If $\mathcal{M} > 0$ then the magnetic field is poloidal dominates, if $\mathcal{M} < 0$ is toroidal dominated and if $\mathcal{M} = 0$ then the magnetic field could not exist and the non-magnetic form of the virial equation is recovered. The value of $\mathcal{M}/|\mathcal{W}|$ can be constrained by measuring the values of m/m_{vir} and $\langle P\rangle/P_s$ from observations. Fiege and Pudritz (2000) derived the values of $\mathcal{M}/|\mathcal{W}|$ for seven filamentary molecular clouds, using values of mass and pressure known from the literature, finding that almost all of the sample have values of $\mathcal{M}/|\mathcal{W}|< 0$, which corresponds to a dominant toroidal magnetic field.

Fiege and Pudritz (2000) constructed theoretical models of filaments, finding that the density profile falls off as $r^{-1.8}$ to r^{-2}. These results are shallower than the profile found in previous models, however, they agree with observations of filamentary molecular clouds (e.g. L977 Alves et al. (1998) and IC5146 (Lada 1998)). This density profile is in agreement with the presence of a toroidal magnetic field wrapping the filament in its outer region. This toroidal magnetic field would prevent the filament from expansion. This model also suggest that, if the dominant part of the magnetic field had a poloidal shape, then the density profile observed would be much stepper which is not the case for most of the filamentary molecular clouds observed in the Galaxy.

The stability of filamentary molecular clouds can be classified in two categories: non-magnetic, hereafter Ostriker case, and magnetic. In the former non-magnetic case the radial density profile will fall off as r^{-4} and $\mathcal{M}/|\mathcal{W}|= 0$ in the extended form of the virial equation. In the magnetic case, the radial density profile has a shallower shape falling off as $\sim r^{-1.8} - r^{-2}$. The magnetic field can be either poloidal or toroidal depending on whether $\mathcal{M}/|\mathcal{W}|$is positive or negative respectively. The presence or absence of a magnetic field can be inferred from observations. Summarizing, the presence of a magnetic field as a support for a filamentary molecular cloud can be inferred from:

- The column density profile. Perpendicular to the length of the filament the density profile, have a distinct shape if the filament is supported only by gravitation or by a magnetic field, which is described by (see Section 1.4.2.2):

$$\Sigma_\rho(r) = A_p \frac{\rho_c R_{flat}}{[1 + (r/R_{flat})^2]^{\frac{p-1}{2}}}. \tag{1.9}$$

  The shape of the density profile can be characterized by the exponent p. If $p = 4$, then the non-magnetic solution of a pure gravitational supported filament is valid, values $p \sim 2 - 3$ correspond to the presence of a magnetic field.

- The lineal mass, virial mass and pressure. With these quantities we can determine, using an extended version of the virial theorem to include magnetic fields, if the filament needs a magnetic support. With these values, it is also possible to determine whether the magnetic field is poloidal or toroidal.

$$\frac{P_S}{< P >} = 1 - \frac{m}{m_{vir}}\left(1 - \frac{\mathcal{M}}{|\mathcal{W}|}\right). \tag{1.10}$$

1.3.3 Fragmentation of filaments

Filaments aren't smooth but contain fragments typically observed along their length. These regions of high densities (clumps) are where the stars are formed. The spacing between the clumps formed within filaments are the result of a fragmentation process. Recent work suggest that this fragmentation might occur due to the "sausage" instability (Jackson et al. 2010)

In the "sausage" instability (Chandrasekhar and Fermi 1953; Nagasawa 1987; Inutsuka and Miyama 1992; Nakamura et al. 1993; Tomisaka 1995) perturbations with certain wavenumber grow faster than others, unlike the case of three-dimensional Jeans collapse where all the perturbations grow at the same rate. The clumps (over-densities) will be produced at a wavenumber that grows faster, corresponding to the most unstable wavenumber. Therefore, we should expect several clumps to be formed within a filament with a regular spacing given by the wavelength of the fastest growing unstable mode.

In the case of an incompressible fluid the spacing between clumps is given by $\lambda_{max} = 11R$ (Chandrasekhar and Fermi 1953), with R is the radius of the filament. For a infinite isothermal cylinder the spacing would be $\lambda_{max} = 22H$ (Nagasawa 1987; Inutsuka and Miyama 1992), where the isothermal scale height, H, is given by:

$$H = c_s(4\pi G\rho_c)^{-1/2}, \tag{1.11}$$

where c_s is the sound speed; G is the gravitational constant; ρ_c is the central gas mass density at the center of the filament. This equation is only valid in the case that the dominant pressure is the thermal pressure, however, in most molecular clouds the linewidth exceed the thermal linewidth, implying the presence of a turbulent component. To account for this turbulent pressure (Fiege and Pudritz 2000) the sound speed, c_s, should be changed by the velocity dispersion, σ, resulting in an effective scale height given by:

$$H_{eff} = \sigma(4\pi G\rho_c)^{-1/2}. \tag{1.12}$$

If we treat the filament as an isothermal cylinder with finite radius, then the spacing will be given by the ratio between R and H. In the case where $R \gg H$ the spacing will be given by $\lambda_{max} = 22H$ and if $R \ll H$ then the spacing will be similar to $\lambda_{max} = 11R$. This theory also predicts a maximum critical lineal mass density for a self gravitating cylinder in equilibrium, given by:

$$\left(\frac{M}{l}\right)_{max} = \frac{2v^2}{G}, \tag{1.13}$$

where v corresponds to the sound speed, c_s, in the case of thermal support (Ostriker 1964) or to the velocity dispersion, σ, if we considerer the turbulent support (Fiege and Pudritz 2000).

1.3.4 Star formation within filaments

Filamentary molecular clouds appears to be associated to star formation, they may enhance the accretion rates into cores, thus making possible the formation of high mass stars (Banerjee and Pudritz 2008; Myers 2009). Moreover, high mass star forming region often have filamentary shapes such as Orion.

IRDC, are examples of filamentary molecular clouds that appears as dark at infrared. Some of the IRDC shows star formation activity, and they high column densities (10^{22} - 10^{23} cm^{-2}) suggest that within them cluster of stars and high mass stars may be formed (Rathborne et al. 2006). Jackson et al. (2010) studied the fragmentation of Nessie, an extreme case of a filamentary molecular cloud, into clumps. This work shows that instabilities can be the responsible of the fragmentation of filaments into clumps and within these clump clusters of stars may be formed.

The formation of star forming clumps within IRDCs and the resemblance of high mass star forming complexes to filament lead Jackson et al. (2010) to propose an evolutionary sequence (Figure 1.6) where filamentary IRDCs fragment into clumps. These clumps eventually will collapse giving birth to stars clusters and high mass stars within them. The radiation from the newly formed stars create bubbles disrupting the filament. The HII regions will grow and overlap, and the filament will contain one or more bright cluster.

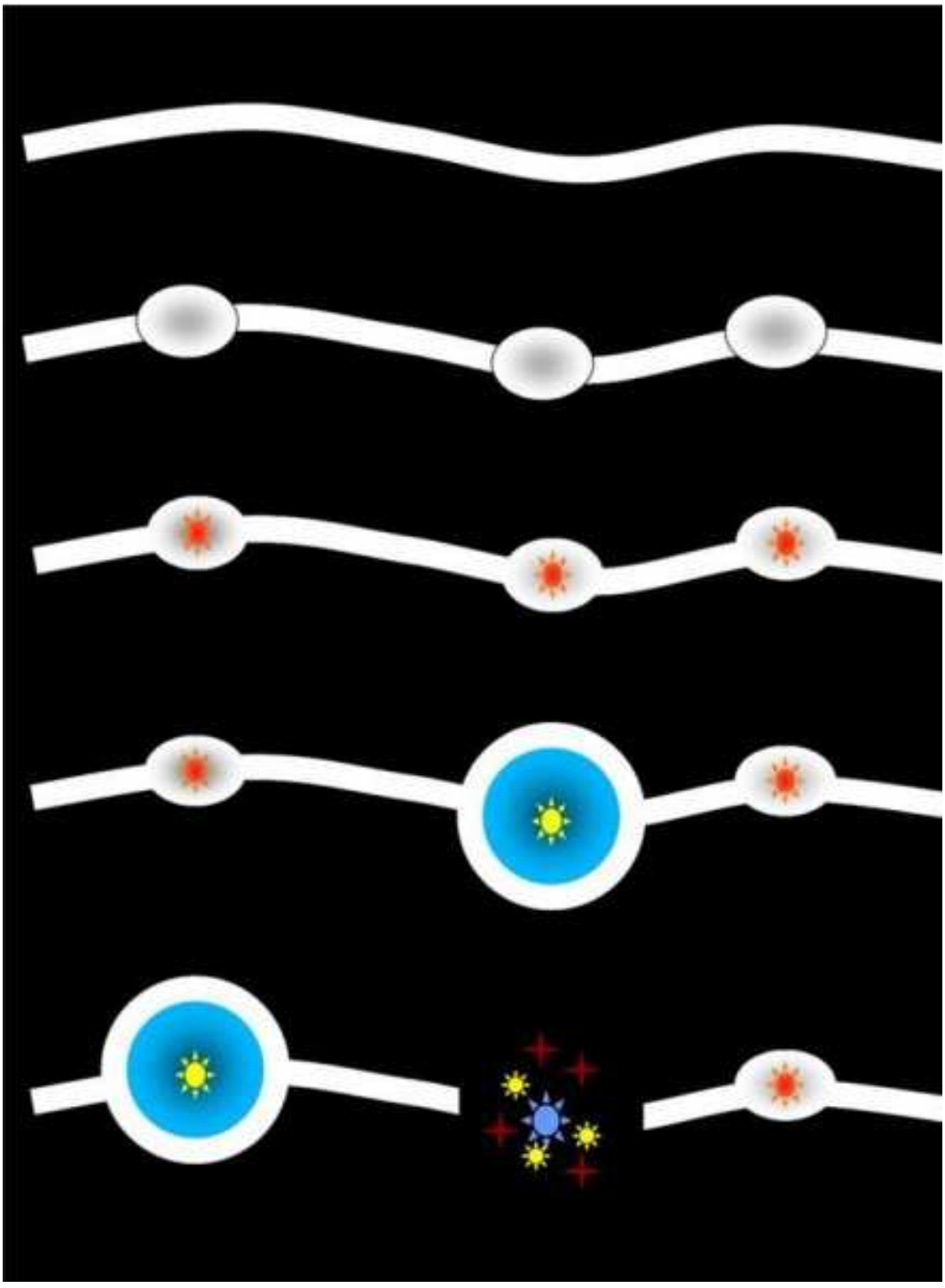

FIGURE 1.6: Evolution of filamentary molecular clouds. Time increases downward in this figure. Filamentary molecular clouds are formed; this filaments go under collapse forming clumps. These clumps will collapse forming massive stars and HII regions and finally stars clusters emerge from the filament (Jackson et al. 2010).

1.4 Identification and characterization of filaments

To better understand the initial conditions of high mass star formation it is necessary to study the places were high mass stars are born. Star formation occurs within dense regions of giant molecular clouds that are often filamentary in shape. Some molecular clouds are so cold and dense that they appear as dark patches in the sky at visible and even infrared wavelength (e.g. IRDCs).

Giant molecular clouds have cold temperatures (10-30 K) and their emission arises mainly from molecular lines and thermal dust continuum. At the temperatures and densities inside giant molecular clouds molecules will emit in rotational transitions that occur in the millimeter to sub-millimeter regime. Continuum emission from molecular clouds arise from the dust grains that are heated and re-emitted as a black body of equivalent temperature. A black body with a temperature between 10-30 K will have its peak emission at (sub)millimeter wavelengths. Therefore, to study the emission coming from either the dust or molecules it is best to observe at these wavelengths.

To identify regions of star formation in our Galaxy, several surveys have recently been carried out to trace dust thermal emission at (sub)millimeter wavelengths (e.g. Bolocam Galactic Plane Survey (BGPS; Nordhaus et al. 2008), ATLASGAL (Schuller et al. 2009), The Herschel Infrared Galactic Plane Survey (Hi-GAL; Molinari et al. 2010b)). These surveys have shown that filamentary molecular clouds are ubiquitous along the Galactic Plane.

To study filaments we follow the same approach as in the study of molecular clouds. We analyze both their molecular line and dust continuum emission. Because dust emission is the sum of everything emitting along the line of sight a filamentary structure determined visually from the dust thermal emission does not necessary corresponds to a single, physically distinct molecular cloud. It is possible that what we observe from the dust thermal emission is the superposition of several molecular clouds along the line of sight. To determine if it is a physically coherent structure we need to have information on its velocity which can only be obtained from molecular line observations.

In this section we describe the types of emission from molecular clouds and the information we can gather from its analysis. §1.4.1 overview the definitions and techniques used in filaments. §1.4.2 describe the mechanism of emission and parameters derived from the dust thermal continuum emission. §1.4.3 describe the mechanism of emission and parameters derived from molecular line emission.

1.4.1 Defining the filament

In this sub-section we describe the method used to identify the potential filamentary structure from the dust thermal emission, describe the importance of molecular line observations in the study of filamentary molecular clouds and Section 1.4.1.3 describes the terminology used to characterize the filaments.

1.4.1.1 Following the dust emission

ATLASGAL images, tracing the dust thermal emission at 870 μm, were used to identify possible filaments. We selected by eye the structures that appeared connected at 870 μm. Each of these *"filaments"* contained both extended emission and smaller peaks that appeared connected.

To enhance the filamentary structures we performed a median filter on the images. This filter smears out the isolated single peak of emission in regions that are not part of connected structures. Then, we used a Python algorithm to follows the peaks at 870 μm in these filtered sub-regions. The algorithm select the peaks in emission over a 3σ threshold and interpolate these peaks using a polynomial of high order (between 7 to 10). The path was inspected visually making sure that the path followed each peak observed at 870 μm.

The path defines the center of the filament and the width of the region containing the filament was chosen individually for each filament in order to contain the whole emission observed at 870 μm. This width usually correspond to 15-20 pixels to each side of the defined path and represent the region where we detect significant emission at 870 μm.

1.4.1.2 Physical coherence

While images from ATLASGAL show filamentary structures apparently connected at 870 μm, the observed emission arises from all emitting objects along the line of sight. Therefore, what appears connected may simply be the superposition of two or more molecular clouds along the line of sight.

To differentiate between a single coherent structure or several clouds superposed we need additional information about the distance to each point of the potential filament. The determination of distances to astronomical objects is usually a complicated task. For molecular clouds their kinematic distance is estimated using the observed velocity determined from molecular line observations and a model of the Galaxy rotation (see Section 1.4.3.2 for further details).

In this work we use ^{13}CO(3-2) molecular line observations to determine the velocity toward

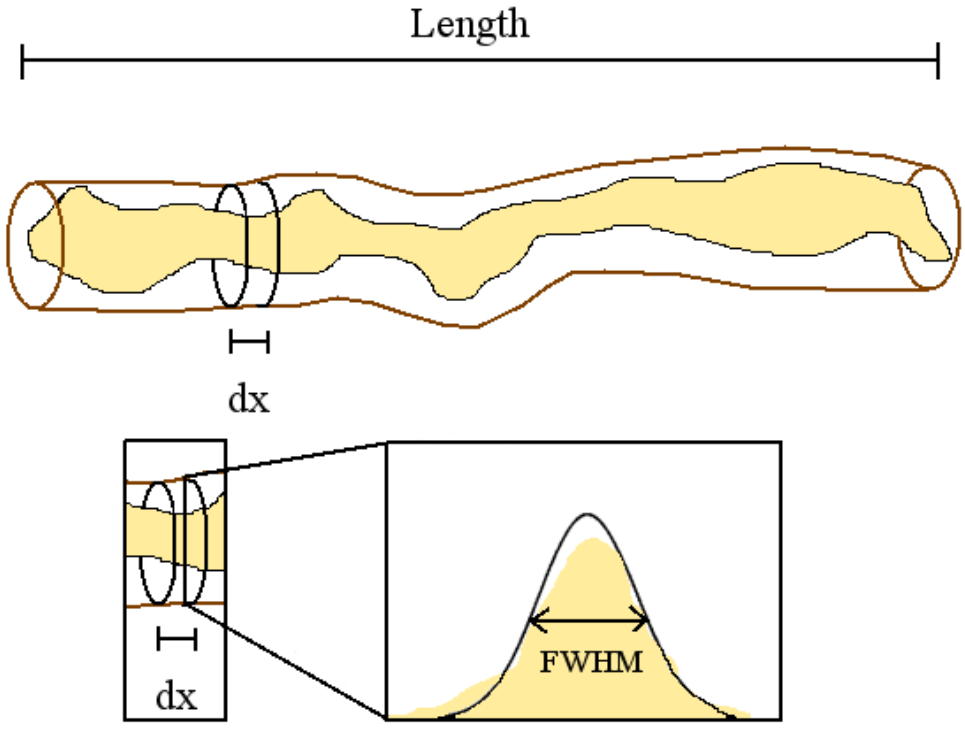

FIGURE 1.7: Scheme of a filament. This figure shows how the length, dx and radius are defined. dx correspond to the unit on which all the *lineal* properties (density, mass etc) of the filament were calculated.

each point in the filament. From the measured v_{LSR} at the emission line we determine the kinetic distance toward each point of the filament (see section 1.4.3.2 for further details).

If the velocity toward each point within the filament is similar, then the filament is considered as a single coherent structure. However, if we detect different velocities along the filament or if we detect more than one line at different velocities, we consider the regions with different velocities physically distinct clouds. In this way we distinguish between single structures and the superposition of clouds along the line of sight. To visualize this, we created position-velocity maps of the molecular line emission toward each filament. These maps shows the velocity of the emission along the galactic longitude and latitude, if we see a connected structure in the position-velocity maps this suggest that the molecular cloud is single coherent structure and if we detect more than one structure in these maps, this will indicate the presence of several molecular clouds

1.4.1.3 Filament terminology

In this section we describe the specific terminology used in this work to describe the filament parameters. We assume, for simplicity, that filamentary structures are cylinders. To avoid oversampling, we divided the filament in subsections of length dx (Figure 1.7), which corresponds to the ATLASGAL beam (18" at 870 μm).

The *"length"* of the filament is given by the extent of the longest section of the filamentary structure. To calculate the *"radius"* a Gaussian was fitted to the profile of the dust emission across the filament. The FWHM resulting from this fit was set as the diameter. Figure 1.7 illustrates the length (upper figure) and radius (lower-right figure) in a filament. The radius of the filament was calculated at each of the subsections of length dx along the filament. Thus, along the filament the measured radius is not constant. The average value of the radius was used to describe the radius of the filament as a global property.

The *"lineal mass"* of the filament (from the dust or virial), was defined as the mass derived from the emission of each subsection dx along the filament. Where the mass per unit length, $M_{\odot}$/pc, is obtained by integrating the density of the filament over it diameter.

Linewidth along the filament

In this work we made molecular lines observations toward each point of the filament. To study how the linewidth changes along the length of the filament we compute the average spectra across the radius of the filament at each point along the filament. This is illustrated in Figure 1.8.

1.4.2 Dust thermal emission

Emission from small grains of dust in molecular clouds give us important information about their physical properties such as: density and temperature. The dust temperature is physically determined by the balance between the heating and cooling. Dust grains absorb the UV radiation from its surrounding and re-emit them as thermal radiation. Cold molecular clouds, which appear as dark patches in the sky at infrared wavelengths, have typical temperatures of 10 to 30 K. With these temperatures their black body emission peaks at sub-millimeter to millimeter wavelengths.

The intensity of the radiation of a black body with temperature T at frequency, ν, is given by:

$$B_{\nu}(T) = \frac{2h\nu^3/c^2}{exp(h\nu/kT) - 1}, \tag{1.14}$$

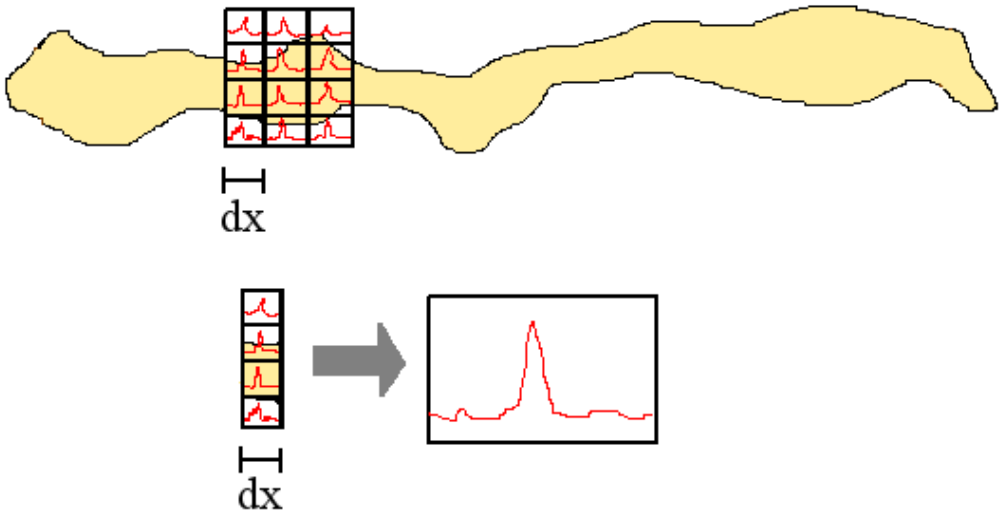

Figure 1.8: Scheme of the linewidth along a filament. This figure shows how the linewidth is calculated. The molecular line observations at each section defined by the beam size at 870 μm are averaged obtaining a single spectrum at each point.

where h is the plank constant, k is the Boltzmann constant and c is the speed of light. If $h\nu \ll kT$, we can approximate the exponential term as $\exp^{k\nu/kT} \cong 1 + h\nu/kT$ obtaining the following expression, called the Rayleigh-Jeans law:

$$B_\nu^{RJ} = \frac{2\nu^2}{c^2} kT. \tag{1.15}$$

In a idealized model, the flux density from a cool cloud can be expressed as the product of the black body intensity, B_ν, and a emissivity $\propto \nu^\beta$ by the following expression (Hildebrand 1983):

$$F_\nu = \frac{N\sigma}{D} B_\nu(T)\nu^\beta. \tag{1.16}$$

where, N is the column density, σ is the velocity dispersion, D is the distance to the object, ν is the frequency, β is the spectral index and $B_\nu(T)$ is the black body intensity at frequency ν and temperature T.

1.4.2.1 Observations : flux density

When we observe a radio source, we receive the electromagnetic radiation that is intercepted by the antenna. Assuming, for simplicity, that the radiation from the source travels through empty space, the infinitesimal power, dP, defined as the energy per unit time received by an antenna in the frequency range ν, $\nu + \delta\nu$ is given by:

$$dP = I_\nu \cos\theta d\Omega d\sigma d\nu, \tag{1.17}$$

where σ is the area collecting the emission; ν is the frequency; θ is the angle between the normal to the surface σ and the direction to Ω, which is the source solid angle; I_ν is the brightness or specific intensity defined as $I_\nu \equiv dP/\cos\theta d\Omega d\sigma d\nu$. For discrete sources with an angular size $\ll 1$ radian, the flux density, S, of an astronomical source is defined as the monochromatic intensity integrated over a solid angle subtended by the source and is given by:

$$S = \int I(\nu) d\Omega. \tag{1.18}$$

I_ν is independent of the distance and will only change if the radiation is absorbed or emitted. The change in I_ν is described by the equation of radiative transfer:

$$\frac{dI_\nu}{ds} = -\kappa_\nu I_\nu + \varepsilon_\nu. \tag{1.19}$$

In this equation the term $\kappa_\nu I_\nu$ will account for the absorption of the radiation, where κ_ν is the absorption coefficient and ε_ν represents the emissivity. If there is only emission $\kappa_\nu = 0$; if there is only absorption $\varepsilon_\nu = 0$. In the case of thermodynamic equilibrium (TE), where matter and radiation are in equilibrium at the same temperature, $\frac{dI_\nu}{ds} = 0$ and the brightness distribution, I_ν is equal to the Planck function, $I_\nu = B_\nu(T)$. Since, $\frac{dI_\nu}{ds} = 0$ we can write Equation 1.19 as:

$$\frac{dI_\nu}{ds} = 0 = -\kappa_\nu B_\nu(T) + \varepsilon_\nu, \tag{1.20}$$

obtaining,

$$I_\nu = B_\nu(T) = \varepsilon_\nu/\kappa_\nu. \tag{1.21}$$

This equation is called the *kirchoff* law. This law also applies even if the emitting/absorbing material is in local thermal equilibrium (LTE), i.e. it is not in equilibrium with the radiation field. Defining the optical depth as:

$$d\tau_\nu = -\kappa_\nu ds, \tag{1.22}$$

and assuming local thermodynamical equilibrium, LTE, equation 1.19 can be expressed as:

$$-\frac{1}{\kappa_\nu}\frac{dI_\nu}{ds} = \frac{dI_\nu}{d\tau_\nu} = I_\nu - B_\nu(T), \tag{1.23}$$

integrating this equation we have:

$$I_\nu(s) = I_\nu(0)\exp^{-\tau_n u(s)} + \int_0^{-\tau_\nu(s)} B_\nu(T)\exp^{-\tau}\, d\tau. \tag{1.24}$$

For large optical depth, i.e. $\tau_\nu \rightarrow \infty$ and no background source, then $I_\nu = B_\nu(T)$. In the Rayleigh-Jeans limit $B_\nu(T) = \frac{2\nu^2}{c^2}kT$, in this regime the brightness temperature, T_B, is defined as the temperature of the blackbody that would give the same intensity as the celestial source. This temperature can be measured when observing at millimeter and sub-millimeter wavelengths.

$$I_{RJ}(\nu, T) = \frac{2\nu^2}{c^2}kT_B. \tag{1.25}$$

In this regime, the flux density is given by the brightness temperature, T_B, integrated over the source solid angle:

$$S = \int I_{RJ}(\nu, T)d\Omega = \int \frac{2kT_B\nu^2}{c^2}d\Omega = \frac{2k\nu^2}{c^2}\int T_B d\Omega, \tag{1.26}$$

in the case of a Gaussian source, the above expression becomes:

$$\left[\frac{S_\nu}{Jy}\right] = 2.65T_b\left[\frac{\theta}{'}\right]^2\left[\frac{\lambda}{cm}\right]^2 \tag{1.27}$$

Therefore by measuring the flux of an astronomical source we can determine its brightness temperature by either measuring or assuming a solid angle.

1.4.2.2 Physical parameters derived from observations

In this section we overview the different physical parameters derived from observations of the thermal dust emission. We describe how the dust temperature is determined and the different mass measurement and their uncertainties. The mass is particularly a key parameter to characterize molecular clouds. We need accurate measurement of the mass of a molecular cloud to determine the stability and the amount of material available for the formation of stars within them.

Temperature

Through observations of the thermal emission from dust grains it is possible to estimate the temperature of molecular clouds. If observations at two wavelengths are available a color temperature can be computed using the ratio of the emissions (Schnee and Goodman 2005). The flux density from the dust at an optically thin frequency it is given by (Mitchell et al. 2001):

$$S_\nu = \Omega B_\nu(T_d)\kappa_\nu \mu m_H N_H, \tag{1.28}$$

where, $B_\nu(T)$ is the black body emission of the dust at temperature T (Equation 1.14); S_ν is the flux per beam; Ω is the solid angle of the beam; m_H is the mass of the hydrogen atom; $\mu = 2.33$ is the mean molecular weight of interstellar material in molecular clouds; N_H is the column density of hydrogen and κ_ν is the emissivity of the dust, given by:

$$\kappa_\nu = k_{230}\left(\frac{\nu}{230\ GHz}\right)^\beta, \tag{1.29}$$

with $\kappa_{230} = 0.005$ cm^2 g^{-1} (Andre et al. 1996; Preibisch et al. 1993), ν is the frequency and β is the emission spectral index. The dust color temperature is obtained from the ratio of the dust thermal emission at two different frequencies, via:

$$\frac{S_{\nu_1}}{S_{\nu_2}} = \left(\frac{\nu_1}{\nu_2}\right)^{3+\beta} \frac{\exp(hc/\nu_2 kT_{dust}) - 1}{\exp(hc/\nu_1 kT_{dust}) - 1}, \tag{1.30}$$

where ν_1 and ν_2 are the two frequencies at which the dust thermal emission is measured; β is the emissivity spectral index; and T_{dust} is the dust temperature.

Two assumptions are required for this method to be valid. The first is that the temperature of the molecular cloud is low. At low temperatures (10 K) using flux derived from sub-millimeter wavelengths (e.g. 350 μm and 870 μm), deviations from the Rayleigh Jeans law are considerable, implying that the ratio, $S_{870\mu m}/S_{350\mu m}$, is a strong function of both the dust temperature and the spectral index β (Kramer et al. 2003). Therefore, the second assumption, is to choose an appropriate value for β, which can range from 0.5 to 2 (Schnee and Goodman 2005), depending on the material of which the dust grains are made of (carbonaceous, silicate and/or metallic (Draine 2003)). Observations toward molecular clouds have shown that assuming β is 1.5 is valid for observation in the millimeter regime (Paradis et al. 2009), but so far a robust value of the spectral index still remains elusive.

Column density and mass

The column density and mass of a molecular cloud can be obtained from its dust thermal emission. One needs to assume that the ratio between dust and gas is relatively constant in the ISM. Not directly measured, but a value of 100 is commonly used. Thus, the column density of gas, which in molecular cloud is mostly in the form of molecular hydrogen, can be estimated through the measurement of the dust column density.

Dust is assumed to emit as a modified blackbody, and its flux density at an optically thin frequency is given by Equation 1.28 (Mitchell et al. 2001). The emissivity index β can have different values according to the nature of the dust grains: $\beta = 0$ correspond to a true blackbody, $\beta \sim 1$ corresponds to amorphous layer-lattice materials and for metal and crystalline dielectrics a value of $\beta \sim 2$ is commonly used (Henning et al. 1995). If we assume that the dust thermal emission at sub-millimeter wavelengths is optically thin, then the column density and the mass of the molecular cloud are given by:

$$N(H_2) = \frac{S_\lambda}{\Omega \kappa_\lambda \mu m_H B_\lambda(T)}, \tag{1.31}$$

$$M_{dust} = \frac{S_\lambda D^2}{\kappa_\lambda B_\lambda(T_d)}, \tag{1.32}$$

where, S_λ is the flux per beam; Ω is the solid angle of the beam; κ_λ is the emissivity of the dust and D is the distance to the source. The main uncertainties in this calculation are the distance to the molecular cloud, the flux error, which is $\sim$ 15% due to calibrations, the dust temperature and the assumed value if the dust to gas ratio which is included in the expression for the dust emissivity κ_λ (Equation 1.29).

Radial density profile and lineal mass of filaments:

When characterizing filaments it is useful to calculate the lineal mass, which is the mass per unit length ($M_\odot$/pc) at each point along the filament's length. The dust lineal mass is obtained by integrating over the width of the filament the radial column density, obtained from the observation of dust thermal emission.

To analyze the shape of the dust thermal emission in filaments, the observed radial profile is compared to an idealized model of a cylindrical filament with the following radial density and

column density profiles (Arzoumanian et al. 2011):

$$\rho_p(r) = \frac{\rho_c}{[1 + (r/R_{flat})^2]^{p/2}}, \tag{1.33}$$

$$\Sigma_\rho(r) = A_p \frac{\rho_c R_{flat}}{[1 + (r/R_{flat})^2]^{\frac{p-1}{2}}}, \tag{1.34}$$

where, $\Sigma_\rho(r) = \mu m_H N_{H_2}(r)$, μ is the mean molecular mass; A_p is given by $A_p = \frac{1}{\cos i} \int_{-\infty}^{\infty} du/(1+u^2)^{p/2}$, where i in the inclination angle, A_p is a finite constant for values of $p > 1$; ρ_c is the density at the center of the filament and R_{flat} is the radius corresponding to the inner flat part of the density profile; $\mu = 2.33$ is the mean molecular weight; m_H is the hydrogen mass and N_{H_2} is the column density. As shown by Arzoumanian et al. (2011) the effect of choosing $i \neq 0$ does not affect the shape of the radial density profile, thus in this work we will assume a value of $i = 0$.

This column density profile, $\Sigma_\rho(r)$, is compared to the observed column density, Σ_{obs}, which is obtained directly from the dust thermal emission using Equation 1.31 at each point along the filament. By fitting Σ to Σ_{obs} we obtain p which reveal the level of stability of the filaments (see Section 1.3.2)

The lineal mass of the filament is obtained by integrating the **observed** radial density profile across the width of the filament at each point (dx) along the filament.

$$M_{lineal} = \int \Sigma_{obs}(r) dr. \tag{1.35}$$

Lineal Density

The lineal density of the filament is defined as the ratio between the lineal mass and the *"lineal volume"*, as shown in Equation 1.36. The "lineal volume" is defined as the cross sectional area of the filament, for simplicity we assume the filament as a cylinder of radius R_s with cross sectional area πR_s^2. Thus, the lineal density can be written as,

$$\rho = \frac{m}{\mathcal{V}} = \frac{m}{\pi R_s^2}. \tag{1.36}$$

1.4.3 Molecular line emission

Emission from molecules can arise due to three different processes: rotational transitions, caused by rotation of the nuclei around an orthogonal axis; vibrational transitions, produced by oscillations of the relative positions of the nuclei to its equilibrium position and electronic transitions.

The main source of molecular emission in the millimeter regime arises due to rotational transitions. To produce this kind of emission, molecules need a non zero dipole momentum. Since quantum mechanics allows molecules to have discrete values of their angular momentum, the energy associated with the rotation is specific for each transition and each molecule. The amount of rotational energy of a molecule is given by:

$$E_{rot} = \frac{J(J+1)h^2}{8\pi^2 I}, \tag{1.37}$$

where I is the molecule's moment of inertia and J is the angular momentum quantum number. A molecule going from the rotational state J to $J-1$, will release an amount of energy given by:

$$\Delta E_{rot} = [J(J+1) - (J-1)J]\frac{\hbar^2}{2I}, \tag{1.38}$$

The frequency of the photon emitted by this transition will be:

$$\nu = \frac{\Delta E_{rot}}{h} = \frac{\hbar J}{2\pi I} \tag{1.39}$$

Although molecular hydrogen is the most abundant molecule in the interstellar medium it does not posses an electric moment dipole, therefore it produces no observable emission in the millimeter regime. For this reason, other less abundant molecules are used as a tracer of H_2 to study the properties of molecular clouds. The second most abundant molecule is CO and it is the most commonly used to study molecular clouds. CO produces several rotational transitions in the millimeter regime making it easy to observe at these wavelengths.

In order to be able to detect a molecular line transition, the molecule must be excited into $E_{rot} > 0$, which can happen through ambient radiation or collisions between molecules. Thus, molecules located deep inside molecular clouds will be excited by collisions while molecules at the edges of the cloud will typically be excited by the ambient radiation.

Each molecular transition is sensitive to the density and kinetic temperature of the gas. Molecules won't emit until they reach a certain temperature and the density reaches a critical value, which is

called *"critical density"*. This value corresponds to the density of the cloud at which the transition is thermalized, and is given by (Snell et al. 1984),

$$n_{crit} = \frac{A}{C(1 - e^{-h\nu/kT_{kin}})}, \tag{1.40}$$

where A is the inverse radiative lifetime, C is the collisional de-excitation coefficient, and T_{kin} is the temperature of the radiation field. If the kinetic temperature increases more levels higher energies will be populated. The population in each level is given by:

$$\frac{N_j}{g_j} = \frac{N_{tot}}{U(T_{ex})} e^{-E\,j/k_B T_{ex}}, \tag{1.41}$$

where, N_j is the number of molecules in the level J, g_j is the degeneracy, N_{tot} is the total number of molecules, k_B is the Boltzmann constant, $U(T_{ex})$ is the partition function and T_{ex} is the excitation temperature. In the case of local thermodynamic equilibrium, LTE, $T_{ex} = T_{kin}$.

Therefore, since each molecule will need a specific density and temperature to be excited and emit radiation, observations of CO, and other molecules less abundant such as CS, SiO, N_2H^+, HCO^+, etc. allow us to determine the distribution and the physical parameters of the molecular gas. Hence, by studying the strength, shape, velocity and, for some molecules, their hyperfine structure (due to the interaction of the magnetic dipole or electric quadrupole with electrons or other nuclei) we can reveal the conditions within molecular clouds.

1.4.3.1 Observations: Peak intensity, line width and velocity

From the molecular line emission of an astronomical source we can derive the properties of the emitting source through the analysis of the spectra observed. The three principal characteristics of a spectral line are: central velocity, the linewidth and intensity. The linewidth and velocity give information about the kinematics of the molecular cloud, and the intensity gives information about the density and temperature of the cloud.

The quantity measured with a radio telescope is called the *antenna temperature*. The antenna temperature is the temperature of a black body that would emit the equivalent power received by the radio telescope and can be related to the brightness temperature, T_B. If the source is small compared to the telescope beam, the antenna temperature is given by:

$$T_A = \frac{\Omega_s}{\Omega_b} \eta T_B, \tag{1.42}$$

where, Ω_s is the source solid angle, Ω_b is the antenna beam solid angle and η is the main beam efficiency. This temperature corresponds to the intensity of the spectral line detected by the radio telescope. When we detect a spectral line the antenna temperature is related to the excitation temperature, at which the line is produced, by the following expression:

$$T_A = \eta\phi(T_{ex} - T_{BG})(1 - \exp^{-\tau}), \tag{1.43}$$

where T_{ex} is the excitation temperature; T_{BG} is the background temperature; ϕ is the main beam filling factor; τ is the opacity of the molecular cloud and η is the efficiency factor of the antenna. Usually the antenna temperature is expressed as the main beam temperature, T_{MB}, that is equivalent to the antenna temperature multiplied by the antenna efficiency factor, η.

$$T_{MB} = T_A/\eta. \tag{1.44}$$

The width of a spectral line is the result of three different mechanisms of broadening:

- **Natural line width**, produced because the energy levels are not infinitely sharp, so the emitted photons have a range of frequencies given by:

  $$\Delta\nu \approx \frac{1}{2\pi\Delta t}$$

  , where, Δt is the lifetime of the excited state.

- **Thermal Dopper width**, due to the random motions of the individual atoms and molecules in the gas and is defined as:

  $$v_{th} = \sqrt{\frac{2kT_k}{m}} \tag{1.45}$$

  where m is the mass of the atom or molecule and T_k is the kinetic temperature of the gas.

- **Turbulent width**, due to bulk motions of the gas or turbulent motions or to the presence of outflows or inflows.

Typically, the mechanism that dominates the width of the line is turbulence due to motions of small clumps inside the molecular cloud. Therefore, the analysis of the width of a detected molecular line gives information about the global kinematics inside the cloud.

The Doppler shift in velocity, V_{LSR}, at what the line is observed tell us the radial velocity of the cloud in the Galaxy. Comparing this radial velocity and the position on the sky (Galactic longitude and latitude) to a model for Galactic rotation, we can obtain the distance toward the molecular cloud (see Section 1.4.3.2 for further details).

Moment maps

A useful tool to help analyze molecular line data is to create moments maps of the emission. Moment maps give us an easy way to visualize and interpret the observations. The three principal moment maps used are the Oth, 1st and 2nd. The Zeroth moment map, or the *integrated intensity* map, is defined as:

$$M_0 = \int I(v) dv. \tag{1.46}$$

This integrated intensity map reveals where the molecular line emission arises within the observed source. The first moment map, or the *intensity-weighted velocity map*, defined as:

$$M_1 = \frac{1}{M_0} \int I(v) v dv, \tag{1.47}$$

reveals the mean velocity within the source and provides valuable information about the overall kinematics. Generating these maps are especially crucial for the study filamentary molecular cloud, because they show whether the structure is a single coherent cloud or the superposition of two or more clouds along the line of sight.

The second moment map, or the intensity-weighted line width, it is defined as:

$$M_2 = \sqrt{\frac{1}{M_0} \int I(v)(v - M_1)^2 dv}, \tag{1.48}$$

and reveals the variation of the linewidth within the source. It is useful to identify regions where the line width is high and, therefore, where turbulence is high.

1.4.3.2 Kinematic distances to molecular clouds

Knowing the distance to a molecular cloud allows us to determine their physical properties, such as the mass and density. These quantities are important to determine reliably as these quantities are used to define and characterize molecular clouds. To calculate the distance to a molecular cloud we use the observed velocity of its molecular line emission, v_{LSR}, its position in the sky, and use a model of the rotation of the Galaxy. Galactic rotational models predict the Doppler velocity of molecular clouds in the Galaxy as a function of the galactic longitude. In this work we use the

model described in Brand et al. (1985), where the rotational curve of the Milky Way is given by:

$$V(r) = \begin{cases} (210.969 - 150)\frac{r}{2} + 150 & \text{for} \quad r \leq 2kpc \\ V_0\left(\left(\frac{1.00767|r|}{R_0}\right)^{0.0394} + 0.00712\right) & \text{for} \quad 2 < r \leq 17kpc \\ 229 & \text{for} \quad r > 17kpc, \end{cases} \tag{1.49}$$

where r is the Galactocentric distance; R_0 is the Galactocentric distance of the Sun, estimated to be 8.5 kpc and V_0 is the circular rotation velocity at the position of the Sun, assumed to be 220 km s^{-1}. The radial velocity of a molecular cloud in the Galactic plane is given by:

$$V_{rad}(l) = R_0\left(\frac{V(r)}{r} - \frac{V_0}{R_0}\right)\sin(l), \tag{1.50}$$

where, $V(r)$ is the velocity given by the rotational curve model (Equation 1.49); r is the Galactocentric distance and l is the Galactic longitude of the cloud. To obtain the V_{rad}, it is necessary to observe a molecular line transition toward the molecular cloud and obtain its v_{LSR}, which correspond to $V_{rad}(l)$ in Equation 1.50. With this value and replacing $V(r)$ in Equation 1.50 with the corresponding value of Equation 1.49 we can obtain the Galactocentric distance to the object. The distance to the molecular cloud will be given by the quadratic equation:

$$R = (d^2 \cos b^2 + R_0^2 - 2R_0 d \cos b \cos l)^{1/2}, \tag{1.51}$$

where R is the Galactocentric distance to the object, d is the distance to the object, b in the galactic latitude and l is the galactic longitude. Since this equation is quadratic there are two distances as possible solution for object located within the solar circle: near and far distance. It is impossible to distinguish between them based only on this calculation. To resolve this ambiguity we need additional information. A simple way to resolve this ambiguity is with information for molecular clouds that appear dark (like IRDCs) is to assume that they lie at the near kinematic distance because they are obscuring the extended background presumably coming from the Galaxy.

However, if the molecular cloud does not appear dark we cannot use this argument. To disentangle the kinematic distance several approach have been used. Combining measurement of H110α recombination line and H_2CO absorption lines Downes et al. (1980) and Araya et al. (2001) developed a method to distinguish between near and far kinematic distance. In this method, if the H_2CO absorption occurs at higher velocity than the H110α recombination line then the far kinematic distance is chosen, otherwise the near distance is selected.

Paladini et al. (2004) used the luminosity-physical diameter correlation of HII regions to distinguish between near and far kinematic distance. This method is based on the fact that the luminosity is proportional to the product of the lineal diameter (obtained from the emission measurement) and the square of the angular size.

Burton et al. (1978) and Liszt et al. (1981) used HI self-absorption to disentangle the kinematic distance. If a molecular cloud shows HI self-absorption, it implies that cold HI in the molecular cloud is absorbing warmer HI emission from the Galactic background. If this is the case, it is likely that the molecular cloud is at the near kinematic distance. However, in order for this to be observable the molecular cloud must contain sufficient cold atomic hydrogen.

1.4.3.3 Derivation of physical parameters

Mass from virial equilibrium analysis

The mass of a molecular cloud can be estimated from the virial theorem, assuming that the cloud is in virial equilibrium, i.e. that there is equilibrium between the potential energy and the kinetic energy inside the molecular cloud. The mass obtained from this method is called *virial mass*.

If the motions of small clumps inside the cloud are balanced only by gravity, since the broadening of the spectral lines is due mainly to the bulk motions inside the cloud, then it is possible to relate the width observed in a molecular line transition (in this work we use ^{13}CO(3-2)) with its underlying mass. If we consider a filamentary molecular cloud instead of the classical spherical model and we take into account the effects of the internal and external pressure over the cloud, the virial equation is given by Equation 1.4 (Fiege and Pudritz 1999) and the *lineal virial mass* is given by:

$$m_{vir} = \frac{2\langle\sigma^2\rangle}{G} \tag{1.52}$$

The *lineal virial mass* can be obtained directly from the molecular line observations and is independent of the width of the filament. In this equation σ is the velocity dispersion given by:

$$\sigma = \langle\sigma^2\rangle^{1/2} = \frac{\Delta v_{tot}}{\sqrt{8\ln(2)}}, \tag{1.53}$$

where, Δv_{tot} is related to the observed line-width, Δv_{obs}, by the Fuller and Myers (1992) formula:

$$\Delta v_{tot}^2 = \Delta v_{obs}^2 + 8\ln(2)kT\left(\frac{1}{\overline{m}} - \frac{1}{m}\right). \tag{1.54}$$

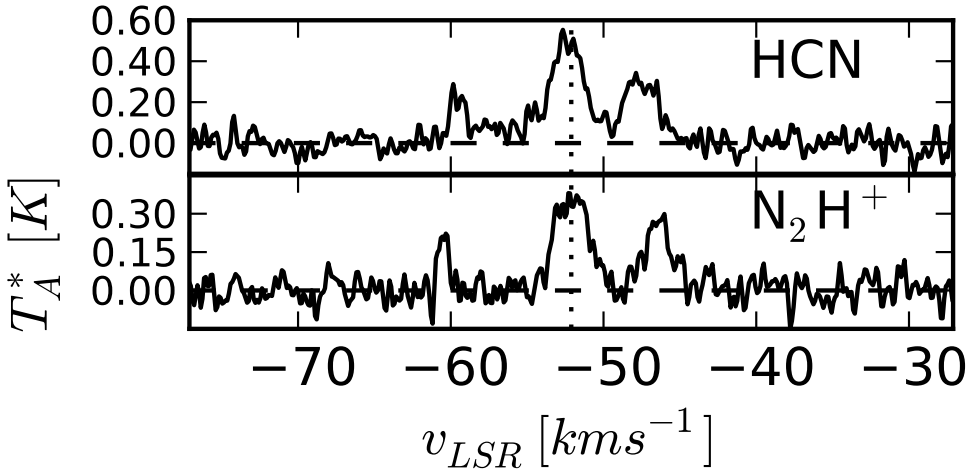

Figure 1.9: N_2H^+ and HCN hyperfine structure

This equation accounts for the fact that the emitting molecule, in our case ^{13}CO(3-2), is much more massive than the average molecule within the cloud. In this equation $\overline{m} = 2.33 m_H$ is the mean molecular mass of the gas. We use $m_{13CO} = 28 m_H$ as the mass of the ^{13}CO(3-2) molecule.

Column density and mass from hyperfine structure

By measuring the relative intensities of the hyperfine components of molecules with hyperfine structure we can derive the column density and mass of molecular clouds. Several molecules observed toward molecular clouds posses hyperfine structure, such as N_2H^+, HCN, HNC and C_2H. Figure 1.9, shows an example of the hyperfine structure of N_2H^+ and HNC observed toward one of the clumps studied in this work. In this figure we can distinguish clearly the three main components of the hyperfine structure.

The opacity of the line can be obtained by fitting the hyperfine components simultaneously, assuming that: all the components have the same excitation temperature; the lines have a Gaussian profile; and all the lines are distinct and have the same width. Under these assumptions, the opacity for each hyperfine component is computed via the expression:

$$\tau_i(v) = \tau_i \exp\left(-4 \ln 2 \left(\frac{v - v_{0,i}}{\Delta v}\right)^2\right), \tag{1.55}$$

where, Δv is the common FWHM of all components, $v_{0,i} = v_i + v_{LSR}$ is the central velocity of the *i*th component, v_{LSR} is the velocity of the reference line. The total opacity of the multiplet will be the sum of the opacity of each component (Equation 1.55).

Knowing the opacity, it is possible to compute the column density. This is calculated using the following expression:

$$N_{tot} = \frac{8k\pi\nu^2 \int T_b dv}{A_{ul} hc^3} \frac{Q(T_{ex})}{g_u} e^{(E_u/kT)} \left(\frac{\tau_\nu}{1 - e^{-\tau_\nu}} \right) \tag{1.56}$$

where, Δv is the line width; λ and ν are the wavelength and frequency of the observed transitions;T_b is the main beam temperature; $A_{u,l}$ is the Einstein coefficient; g_u is the statistical weight of the upper level; τ is the total optical depth; h is the Planck constant; T_{ex} is the excitation temperature; Q is the partition function; E_l is the energy of the lower level and k is Boltzmann constant.

For linear molecules, the partition function is given by:

$$Q(T_{ex}) = \sum_{J=0}^{\infty} (2J + 1) \exp(-E_J / kT_{ex}), \tag{1.57}$$

where,

$$E_J = J(J + 1)hB, \tag{1.58}$$

where, J is the rotational quantum number and B is the rotational constant. If the line is optically thin, then the expression for the column density is:

$$N_{tot} = \frac{8k\pi\nu^2 \int T_b dv}{A_{ul} hc^3} \frac{Q(T_{ex})}{g_u} e^{(E_u/kT)} \tag{1.59}$$

In this work we use the N_2H^+(1-0) molecular line to derive the column density. The values of A_{ul} and B for N_2H^+(1-0)used to determine N_{tot} are given in B.2, in the optically thin case a T_{ex} = 5 K it is assumed. Using the appropriate values for N_2H^+(1-0), the column density in the optically thick case is (Benson et al. 1998):

$$N(cm^{-2}) = 3.3 \times 10^{11} \frac{\tau \Delta v T_{ex}}{1 - e^{-4.47/T_{ex}}}, \tag{1.60}$$

and in the optically thin case:

$$N(cm^{-2}) = 8 \times 10^{11} \Delta v T_B \tag{1.61}$$

where T_B is the brightness temperature of the N_2H^+(1-0) line in K. Once the N_2H^+column density has been obtained, the total mass of the cloud can be calculated via the expression:

$$M_{N2H+} = N(N_2H^+)_{peak} \times m_{N2H+} \times D^2 \times \Omega_{FWHM}, \tag{1.62}$$

where, D is the distance and Ω_{FWHM} is the area of the clump. To obtain the total mass of the cloud it is assumed a typical N_2H^+/H_2 abundance ratio of 3×10^{-10} (Caselli et al. 2002). Section B.1 list the frequencies and relatives intensities of the hyperfine components for all the molecules observed in this thesis.

Pressure

In this section we describe the method utilized to estimate the internal and external pressure of filamentary molecular cloud from the observations.

Internal pressure The average internal pressure inside filamentary molecular clouds is given by the expression:

$$\langle P \rangle = \frac{\int_{\mathcal{V}} P d\mathcal{V}}{\mathcal{V}}, \tag{1.63}$$

where, $\mathcal{V}$ is the volume per unit length, which in the case of filamentary structures corresponds to the cross sectional area πR_f^2 where R_f is the radius of the filament and P is the effective pressure inside the cloud. The effective pressure can be expressed as $P = \sigma^2 \rho$, where the velocity dispersion, σ, takes into account the thermal and non-thermal components of the line width. The average square velocity dispersion can be expressed as:

$$\langle \sigma^2 \rangle = \frac{\langle P \rangle}{\langle \rho \rangle} = \frac{\int_{\mathcal{V}} \sigma^2 \rho d\mathcal{V}}{\int_{\mathcal{V}} \rho, d\mathcal{V}} \tag{1.64}$$

where, $\langle \rho \rangle$ is the lineal density. Thus, the average internal pressure in terms of observables becomes:

$$\langle P \rangle = \langle \sigma^2 \rangle \langle \rho \rangle = \left(\frac{\Delta v_{tot}}{\sqrt{8 \ln(2)}} \right)^2 \frac{m}{\pi R_f^2}, \tag{1.65}$$

where, Δv_{tot} is the corrected line width (given by Equation 1.54); m and R_f are the lineal mass and radius of the filament.

External pressure Molecular clouds and filaments are surrounded by atomic gas that confines the molecular cloud. This gas, like the gas inside molecular cloud, will be dominated by non-thermal motions. To determine the pressure exerted by the external gas over the filament we assume

that the pressure at the surface of the filament, *surface pressure*, will be equal to the pressure of the gas at the outer boundary of the filamentary structure.

To calculate this surface pressure, we compute the average density of the gas outside the filament. We use both the molecular line observation and the dust thermal observations, obtaining an average value for the density of the gas through two different methods. The velocity dispersion is obtained from the average in line width of the molecular line emission outside the filament, via $\langle\sigma^2\rangle = (\Delta v_{tot}/\sqrt{8\ln(2)})^2$. The external pressure is given by Equation 1.5.

1.5 Identification and characterization of star-forming clumps within filaments

Filament like molecular clouds have structure. The smaller, higher density regions within them, referred as *"clumps"*, are the sites where star formation is occurring or may occur. Thus, it is important to identify and characterize these sites.

1.5.1 Properties of the clumps

The properties of each clump were derived from both their continuum and molecular line emission. The color temperature was obtained in the same way as described for the filaments, using the emission at 350 μmand 870 μmon the clumps presenting low emission at infrared suggesting low temperatures. For those clumps exhibit considerable emission at infrared we assumed a dust temperature similar to temperatures observed toward clumps exhibit similar properties (see section 1.4.2.2).

The sizes of the clumps were defined as the diameter of the equivalent circle with an area enclosing the 50% of the peak emission. The column density and mass derived from the dust continuum emission were calculate directly from the dust emission is a similar manner to the overall filament. The only exception was made in the derivation of the virial mass for each clump, since the geometry of clumps is different to the filament.

Mass of the clumps from virial equilibrium analysis

For clumps, unlike for filaments, we can assume that their geometry is spherical. For this reason we use a different expression for the *virial mass*. The *virial mass* of the clumps is estimated from

the virial theorem, assuming that the clump is in virial equilibrium (there is equilibrium between the potential energy and the kinetic energy inside clump). Assuming that the clump has uniform density, we use the following relationship to estimate the virial mass of a clump of radius R and linewidth Δv:

$$\frac{M}{M_{\odot}} = 250\left(\frac{\Delta v}{kms^{-1}}\right)^{2}\left(\frac{R}{pc}\right) \tag{1.66}$$

The above expression is *only* valid for molecular clouds with spherical geometries. For other types of geometries it is necessary to change the value of the constant.

Relative spacing

Theories that explain the mechanism of fragmentation of filamentary molecular clouds predict a characteristic spacing between the clumps formed within the filaments. Thus, determining the spacing between the clumps is important to test these theories.

The spacing between the clumps was obtained from their positions obtained from the ATLASGAL catalog (see Section 3). The spacing was defined as the angular separation between two consecutive clumps, starting with the clump with more negative value in galactic longitude. The angular separation was expressed in unit of pc, derived from the distance determined for each filament.

1.5.2 Evolutionary sequence

To asses a connection between star formation and filamentary molecular clouds, we need to characterize the emission of clumps to asses they evolutionary stage. The clumps are divided in four categories depending on their emission at infrared and molecular lines: *quiescent* clumps, *proto stellar*, HII or photo dissociation region (PDR). We classify the clumps based on the following star formation indicators at their infrared and millimeter emission:

- Green fuzzies or extended green objects (EGOs): This corresponds to enhancement at 4.5 μm that may be due to shock excited lines such as H_2 0-0 S(9) and CO v=1-0.
- 8 μmemission: This emission arises from polycyclic aromatic hydrocarbons (PAHs), usually interpreted as signatures of star formation.

- 24 μm point source: The presence of point like emission at this wavelength suggest that star formation has already started. This emission traces warm dust that is heated as material accrete into a central proto star.
- Complex chemistry lines: The detection of complex molecular transitions toward the clumps suggest that this is a hot core.

Clumps that do not contain an accreting protostar will have temperatures to low to emit a detectable 24 μm emission (Rathborne et al. 2010) will be treated as *quiescent*. The detection of a green fuzzy and a 24 μm point source will be indicative of star formation, thus, we will classify the clumps as *proto stellar*. If significant emission is observed at 8 μm and 24 μm, presenting a bubble-like shape, we will classify the clump as HII region. If the emission at GLIMPSE and MIPSGAL is significant and the morphology is extended then the clump will be classified as PDR.

The presence and absence of certain molecular species can also be used to help define an evolutionary sequence (e.g. (Suzuki et al. 1992)). Sakai et al. (2010) propose an evolutionary sequence based on observations of SiO, CH_3OH, $HN^{13}C$ and $H^{13}CO^+$. These studies are possible because molecules are tracers specific conditions of density and temperature. For instance, N_2H^+, HNC, HCO^+ and HCN are good tracers of dense gas. HNC is usually found toward cold gas. HCO^+ is good as a tracer of infall or outflow signatures. Therefore we will expect to detect these molecules toward cold dense molecular clouds.

Complex organic molecules such as CH_3CN, HC_3CN, $HC^{13}CCN$, HNCOtraces hot molecular cores. These molecules are typically found around high mass proto stars where they have been liberated by radiation or shock. CH_3CN is commonly observed toward masers regions. C_2H is produced in photodissociation regions (Lo et al. 2009). SiO traces shocked regions, such as outflows. It is known to be absent in cold quiescent clouds, because Si is almost always depleted onto dust grains. SiO is released into the gas phase with a disruption like a grain-grain collision.

1.6 Thesis aims

How high mass stars are formed is still an open question is astrophysics. To understand the processes involved in high mass star formation we need to study the very earliest stages of star formation, thus characterizing the places where high mass stars are formed. Recent observations have shown that high mass stars may form within IRDCs (Rathborne et al. 2006). IRDCs are typically filamentary and show clumps in all stages of evolution.

This thesis aims to better understand the connection between filamentary molecular clouds and the formation of a high-mass star. Specifically we will address the following questions:

- Are the extended structures that are seen along the galactic plane really coherent filamentary molecular clouds?
- What are the characteristics of the filaments and their clumps?
- Are the filaments stable against gravitational collapse?
- How are filaments related to high-mass star formation? Are their clumps forming high-mass stars and clusters?

To provide answers to these questions we have embarked on a systematic characterization of these structures. Using multi wavelength data we aim to characterize filaments and their embedded clumps, to determine the connection between filaments and high-mass star formation.

2

The data

To study filamentary structures, we utilized combination of multi-wavelength datasets. The sections below outline the various datasets used, the telescopes, instruments and observing parameters. Section 2.1 describes the data from various Galactic Plane surveys while section 2.2 and 2.3 describe the continuum and molecular line observations obtained across the filaments and toward the clumps.

2.1 Galactic Plane Surveys

2.1.1 ATLASGAL: 870 μm continuum survey

The APEX Telescope Large Area Survey of the Galaxy (ATLASGAL) (Schuller et al. 2009) mapped dust thermal emission at 870 μm at high sensitivity (50 mJy/beam) with the aim of having a complete census of the regions of high mass star formation in the Galactic Plane.

The survey was carried out from 2007 to 2010 using the LABOCA bolometer receiver (Siringo et al. 2009) mounted at the 12 m sub-millimeter APEX (Atacama Pathfinder EXperiment) antenna (Güsten et al. 2006), located in Llano de Chajnantor, Chile. During 2007, the survey covered from -30° to +21°

in galactic longitude and from -1° to +1° in galactic latitude. From 2008 to 2010, the survey was extended to covering ±60° in galactic longitude, and ±1.5° in galactic latitude. In 2010 the Carina arm was included, extending this survey to cover galactic longitude -80°to -60°and galactic latitude -2°to +1°.

LABOCA is a 295 element bolometer array centered at 345 GHz with a bandwidth of 60 GHz, at this frequency the beam size is 19″.2. The survey was conducted by observing 1×2 degrees slices along the Galactic Plane, using on the fly (OTF) scanning velocity of $3'/s$. To avoid artifacts inherent to the observing technique, each position in the sky was covered twice, the two maps were observed with different scanning angles. Flux calibrations were made using planets as primary calibrators (Mars, Neptune and Uranus), and bright Galactic sources with known fluxes from the commissioning of LABOCA as secondary calibrators. The errors in flux are estimated to be lower than 15% (Schuller et al. 2009) and pointing *RMS* error is $\sim 4''$.

The data reduction was conducted using the BOlometer array data Analysis package (BoA; Shuller et al. in prep.). The steps involved in the data reduction are explained in detail in Schuller et al. (2009), and can be summarized as: flagging bad pixels, removing the correlated noise, flagging noisy pixels, despiking, low frequency filtering, and subtracting a first order baseline. The maps are then built by co-adding the signals from all bolometers, using a weighted mean with natural weighting. A weight map is also constructed, containing the sum of all the weights that contribute to each pixel. An *rms* map can then be computed as 1/sqrt(weight).

A problem inherent to the reduction of ground-based bolometer data is the loss of the extended emission, which is filtered out when the correlated noise is subtracted. As a result, uniform emission at angular scales larger than 2′.5 cannot be recovered. For this survey, the steps involved in the reduction of the data were optimized to recover compact sources. The final maps are generated with a pixel size of 6 arc sec, corresponding to a 1/3 of the telescope beam. The *RMS* of the maps is typically 50 mJy/beam.

The full survey data will be made available to the community[1] once the data quality checks are completed.

2.1.2 GLIMPSE: 3.6 μm - 8 μm continuum survey

Galactic Legacy Infrared Mid-Plane Survey Extraordinaire (GLIMPSE) (Benjamin et al. 2003) was carried out with the *Spitzer* space telescope and observed the inner part of the Galaxy at four different wavelengths: 3.6, 4.5, 5.8 and 8 μm, using the *Spitzer* Infrared Array Camera (IRAC). The aim of this survey was to study the structure of the inner Galaxy, the physics and statistics of

[1] http://www.mpifr-bonn.mpg.de/div/atlasgal/data.html

star formation regions and the interstellar medium.

Observations were carried out from March to November 2004. The survey covered 240 square degrees ranging from 10 to 70 degrees on both sides of the Galactic Center and spanning from -1°to 1°in Galactic Latitude. This survey includes some of the bulge population, the central bar, the molecular ring, the Sagittarius spiral arm tangent, and the Norma spiral arm tangent.

The Galactic Plane was observed in segments, each region of the plane was covered at least twice by stepping array by 1/2 of a detector width. All reduction was done by the *Spitzer* Science Center (SSC) pipeline. The GLIMPSE team also contributed to the processing of the data. The final data released to the public are fully reduced. The FITS headers contain relevant information from both the SSC pipeline and the GLIMPSE processing. The final products of this survey, including flux calibrated fits files of each of the 4 channels observations and the point source catalog are public available through NED[2] website. Survey coverage, beam size and pixel size of the images are summarized in Table 2.1.

We used available GLIMPSE images to make mosaics with a Python algorithm. A three color image (Fig. A.1) was generated using 8 μm (red), 4.5 μm (blue) and 3.6 μm (green). GLIMPSE 8 μm (red) wavelengths shows emission from Polycyclic Aromatic Hydrocarbons (PAHs), green ionized and shocked gas are visible at 4.5 μm (green) while at 3.6 μm (blue) the emission is dominated by stars.

2.1.3 MIPSGAL: 24 μm continuum survey

MIPS Inner Galactic Plane Survey (MIPSGAL) (Carey et al. 2005) observed the inner Galactic plane with the Multiband Imaging Photometer (MIPS) on board *Spitzer*. It obtained both images and photometry at 24, 70 and 160 μm. The 24 μm camera has a field of view of 5'. The main goal of this survey was to find regions of star formation and investigate the distribution and energetics of the dust and interstellar material in our Galaxy.

The data obtained with this survey is complementary to the GLIMPSE legacy project. MIPSGAL covered the same region as GLIMPSE and obtained a full sampling from $-68° < l < 69°$ in Galactic longitude and $|b| \leq 3°$.

The observations were reduced and calibrated by the SSC and the MIPSGAL team and mosaics of 1.1 by 1.1 degrees were created as FITS files with standard WCS and units of surface brightness (MJy/sr). Table 2.1 summarizes the details of the data. The mosaics are publicly available from NED.

[2]http://irsa.ipac.caltech.edu/data/NED/

TABLE 2.1: Details of the Galactic Plane surveys.

	Coverage	Wavelength [μm]	Beam size [']	Pixel size [']
ATLASGAL	$\|l\| = 10^\circ - 65^\circ, \|b\| \leq 1.5^\circ$	870	19.2	6
GLIMPSE	$\|l\| \leq 60^\circ, \|b\| \leq 1^\circ$	3.6 - 8	1.4 - 1.7	1.2
MIPSGAL	$-68^\circ < l < 69^\circ, \|b\| \leq 1^\circ$	24	6	1.2

2.2 Mapping the filamentary structures

This section describes the follow up observations toward the five filamentary structures selected to perform detailed studies. The filamentary structures, selected from the ATLASGAL survey, were mapped in both continuum and molecular line emission. Section 2.2.1 describe the continuum observation performed at 350 μm and in section 2.2.2 we describe the details of the molecular line observations.

2.2.1 350 μm continuum emission

In this section we describe the acquisition of the continuum data at 350 μm and the steps involved in the data reduction of these observations.

2.2.1.1 Data acquisition

The 350 μm continuum observations were made using the Submillimeter APEX Bolometer Camera (SABOCA) (Siringo et al. 2010), which consists of a bolometer array of 39 detectors, mounted on the APEX telescope, located in Chajnantor, Chile. The beam size of APEX at this wavelength is 7″ and the field of view is ∼90″. The observations were made using the on-the-fly mode. To avoid artifacts due to the scan mode each map was observed twice at orthogonal scanning angles.

The observations were carried out during June 2010, August 2010 and October 2011. Data toward each filamentary structure was obtained by the combination of small maps that covered the entire filament, with average sizes of 3' by 3'. Details of the smaller individual maps that covered each filamentary structure: center position of the maps; the size of the region covered by these observations; and the time were the observations were made are summarized in A.1.

Pointing and focus checks were made using planets (Mars and Neptune where available). The calibration was made using planets and secondary calibrators with known fluxes, the sources utilized in this observations were, B13134, IRAS 16293, G5.89 (details of these source are summarized in A.5). Each calibration source was observed every hour, skydips were also performed every hour to estimate the atmospheric opacity.

2.2.1.2 Data reduction

The data were reduced using BoA (BOlometer Array Analysis Software) software designed to read, handle, and analyze bolometer array data.

Each small orthogonal map observed towards each position was reduced and calibrated independently. Each map was initially flat field subtracted, opacity corrected, the base line was fitted, and any point sources extracted. Then, the noise in the map was reduced with a median correlated noise filter and any spikes removed. After this step the point source were re added back and the fluxes were corrected. The individual maps were then combined.

Once both orthogonal maps were added together, we construct a signal to noise map and a mask with the emission over a threshold of 5 σ, with σ the *r.m.s* of the map. Once we obtained this mask, each map was re-reduced following the steps mentioned above, using the mask as input for the emission.

All the small maps that covered the filamentary structure, once individually reduced, were added together in BoA to produce the larger map that covered the entire filament. Since the individual maps overlapped, the large map had a higher sensitivity than each individual map. Thus, we created a new mask for each filament and all the individual maps were re-reduced using this larger, more sensitive mask to remove the extended emission in the reduction process.

This reduction process was needed to extract the complex extended filamentary structure observed toward these filaments. However, the removal of the correlated noise in the maps make it impossible to recover all the extended diffuse emission. Nevertheless, the densest parts of the filaments are recovered well.q

2.2.2 ^{13}CO molecular line emission

In this section we describe the data acquisition and the reduction procedure for the ^{13}CO(3-2) molecular line observations.

2.2.2.1 Data acquisition

^{13}CO(3-2) maps across the filaments were obtained using the APEX-2, superconductor-insulator-superconductor (SIS) heterodyne receiver at APEX during June 2010, August 2010, October 2010 and October 2011. The beam size is of 18.2" at this frequency. The backend used during the 2010 observations was the Fast Fourier Transform Spectrometer (FFTS) and the eXtended Fast Fourier Transform Spectrometer (XFFTS) was used during the observation on October 2011. The velocity resolution of the spectra is 0.07 km s^{-1}.

Observations were obtained by mapping small regions (3' × 3') across the filament using the OTF mode. Since ^{13}CO is commonly found in the Galactic Plane, for the off position we used an absolute position below the Galactic plane to avoid contamination in the spectra. Table A.2 gives the center coordinates, the size of the mapped regions, the total integration time and date of the observations.

The system temperature was calibrated prior to each observation using the chopper mode. Pointing and focus were made on IRAS15194 every hour, the pointing accuracy was 2"-3". The average value of the water vapor column density ranged from 0.6 mm to 1.4 mm and the system temperatures were typically 300 K. T_A were converted to T_{MB} using a mean beam efficiency, $\eta_{MB} = 0.73$.

2.2.2.2 Data reduction

We used Continuum and Line Analysis Single-dish Software (CLASS) to reduce each of the individual maps. The steps involved are the following: First we selected the source, line, backend and offsets to get a list of observations for the OTF map. For each spectrum baseline were subtracted using the BASE command, using a 3 degree polynomial. Each spectra were written to a new output file and the spectra were then gridded using the algorithm GRID command, which produces two files, a .gtf and a .lmv file. The .gtf (Gildas Data Format) files contain the spectra as binary tables. The .lmv files contain the gridded cube in Gildas Data Format. These cubes have position dimensions on two axis (l,b) and spectral information on its third axis (v).

Finally the .lmv files were converted to fits cubes, using the task GILDAS_FITS. Using MIRIAD we created the larger maps that covered the filaments by combining the reduced individual maps. The maps were combined by using the standard deviation of the signal free channels (using the MIRIAD *imstat* task) to weight the final maps.

2.3 Observing the clumps

This section describes the data obtained towards the clumps identified within the filamentary structures. Section section 2.3.1 describes the MALT90 observations towards selected clumps and2.3.2 describes the N_2H^+(3-2) point observations.

2.3.1 MALT90

Toward each clump, within the selected filaments, maps of dense gas tracers were obtained as part of the recent MALT90 survey (Foster et al. 2011). MALT90, The Millimeter Astronomy Legacy Team 90 GHz survey, aims to characterize the physical and chemical evolution of high mass dense clumps by obtaining small maps towards a large sample of clumps in a range of evolutionary stages.

The survey was conducted using the Mopra 22-m radio telescope and the 8 GHz wide Mopra Spectrometer (MOPS), taking advantage of the fast mapping capability of Mopra. The selected lines at 90GHz offer a unique combination of optically thin and thick tracers and cover a broad range in critical excitation densities and temperatures (Table 2.2). The combination of data from the different molecules and transitions allow us to determine physical properties of the filaments and their clumps.

The observations used in this work were obtained during the winter of 2010. The coordinates of the regions observed are listed in Table A.4, these observations were made using OTF mapping mode of Mopra with a scan rate was 3.92" per seconds, covering a spatial region of 3' × 3'. Signal free reference positions were chosen at ± 1 degree in Galactic latitude away from the plane. All maps are combination of scanning strips in both galactic longitude and galactic latitude.

Pointing was checked using nearby SiO masers. The data has a pointing accuracy of ≤ 10". System temperatures were measured by paddle scans every 15 minutes finding typical values of 150 K - 250 K. The angular resolution of Mopra at 90 GHz is 36 arc seconds. The full 8 GHz bandwidth of MOPS was split into 16 zoom bands that were centered on the lines of interest giving a spectral resolution of 0.11 km s^{-1} . The typical 1σ *rms* in the spectra is 0.2 K per channel.

The maps were fully reduced by the MALT90 team using an automated reduction pipeline. The reduced and calibrated data products are available to the community via ATOA[3].

For each clump observed we produced moments maps (0th, 1th and 2th moments) from the MALT90 data. We also fitted a Gaussian profile to the spectrum at the peak position at each data

[3]http://atoa.atnf.csiro.au/malt90

cube and a 2D Gaussian to the integrated intensity maps, to determine the size of the clumps emission at each transition. For the N_2H^+(1-0) data we also fit their hyperfine component to measure the opacity, τ.

2.3.2 Deep N_2H^+ spectra

This section describes the data acquisition and reduction of the deep pointed observations carried out towards selected clumps embedded in the filamentary structures.

2.3.2.1 Data acquisition

The N_2H^+(3-2) observations were made using the APEX-2 heterodyne receiver on the APEX telescope during June and August of 2010.

We obtained deep single position switched observations toward the brightest clumps embedded within the filaments. These positions were selected based on their high 870 μm emission from the ATLASGAL compact source catalog. Table A.3 list the ATLASGAL name, coordinates, integration time per position and date for the observations.

For the point observations we selected a signal free reference position below the Galactic plane to avoid contamination with emission from other molecular clouds. System temperatures was calibrate prior to each observations using the chopper mode. Available planets and sources with knows flux were used for flux calibrators. Pointing and focus were made on IRAS15194 every hour, the pointing accuracy was of 2-3 arc seconds. The water vapor column density was in average 2.5 mm and 0.8 mm and the system temperatures were typically 200 K and 150 K during June and August respectively.

2.3.2.2 Data reduction

We utilized CLASS to reduce the data. A one degree polynomial was fit using signal free channels to remove the baseline for each spectra. All spectra from the same position were then averaged to obtain the final spectrum for each clump.

While N_2H^+ has hyperfine structure, for the majority of the cases our spectra did not resolve the individuals component due to large width in velocity of each component. When it was possible, we fit the hyperfine component with the CLASS tasks HFS and MINIMIZE. The input file given to this

Table 2.2: List of the molecular lines observed with Mopra (MALT90) and with APEX. Column 1 indicate the molecule, column 2 the transition, column 3 the rest frequency, column 4 shows the critical density and in column 5 is indicated which kind of object traces the corresponding molecule

Line	Transition	Frequency MHz	n_{crit} cm^{-3}	Tracer
^{13}CO(3-2)	J=3-2	330587.97	2.199×10^{4}	Column density
N_2H^+	J=3-2	279511.701	1.352×10^{7}	Density
N_2H^+	J=1-0	93173.480	9.432×10^{4}	Density, chemically robust
^{13}CS	J=2-1	92494.303	1.417×10^{5}	Column density
H	41α	92034.475		Ionized gas
CH_3CN	$J_K=5_1$-4_1	91985.316	5.780×10^{5}	Hot core
HC_3N	J= 10-9	91199.796	5.779×10^{5}	Hot core
$^{13}C^{34}S$	J=2-1	90926.036	1.189×10^{5}	Column density
HNC	J=1-0	90663.572	2.689×10^{5}	Density; cold chemistry
HC^{13}CCN	J=10-9, F=9-8	90593.059	1.891×10^{5}	Hot core
HCO^+	J=1-0	89188.526	4.186×10^{5}	Density
HCN	J=1-0	88631.847	8.024×10^{4}	Density
HNCO	$J_{K_a,K_b}=4_{1,3}$-$3_{1,2}$	88239.027	3.566×10^{5}	Hot core
HNCO	$J_{K_a,K_b}=4_{0,4}$-$3_{0,3}$	87925.238	6.187×10^{5}	Hot core
C2H	N=1-0,J=3/2-1/2, F=2-1	87316.925	2.207×10^{4}	Photodissociation tracer
HN^{13}C	J=1-0	87090.735	4.834×10^{4}	Column density
SiO	J=2-1	86847.010	2.908×10^{5}	Shock/outflow tracer
$H^{13}CO^+$	J=1-0	86754.330	7.152×10^{4}	Column density

task had only the three main component of the hyperfine structure, with their respectively frequencies and relative strengths. The outputs of this task are the main opacity, the excitation temperature and the line width. When it was not possible to fit the hyperfine structure, we computed a multiple Gaussian to fit the hyperfine components. From these fits we obtained the peak temperatures, line widths, integrated intensity and line velocities. In the majority of the cases the values obtained for the line width are not representatives of the true values of the spectral lines due to the blending of their hyperfine structure.

3

Galactic plane continuum survey: ATLASGAL

The formation of a high-mass star is very difficult to observe due to their short time scales compared with their lower masses analogs. Recently, many surveys have been carried out to study the environments of high-mass star-forming regions. The drawback of many of these surveys is that they target samples which fulfill certain criteria (e.g. maser emission , or peculiar far-infrared colors). As such, they are biased towards particular evolutionary stages (see Wyrowski 2008). For example, methanol masers have been found to be exclusively associated with the very early stages of high-mass star formation and were the subject of the recent methanol multi-beam (MMB; Green et al. 2009) survey. The Red MSX Source survey (RMS; Urquhart et al. 2008) targets the slightly later high-mass young stellar objects (MYSOs) that are known to be mid-infrared bright, while the **C**o-**O**rdinated **R**adio a**n**d **I**nfrared **S**ource for **H**igh-Mass Star Formation (CORNISH; Hoare et al. (*in prep.*), Purcell et al. (*in prep.*)) targets ultra-compact HII region stage at which point the young embedded star has already begun to ionize its surroundings.

All of these surveys provide useful statistics on the particular stage they targeted and are an evolutionary snapshot, but do not provide a complete overview of the evolution of a high-mass core into a high-mass star. What is needed is a Galaxy wide survey using an unbiased tracer that will identify all the stages in the formation and evolution of a high-mass star. The ideal tracer to do probe all stages is the sub-millimeter emission from dust as it is optically thin, traces the material across the galaxy, and is associated with all stages of high-mass star formation. However, up until

now limitations in mapping speeds have resulted in limited coverage of the Galactic plane. For example, during SCUBAs 9-year lifetime it only surveyed a total of 29.3 deg^2 at 850 μm.

The need for unbiased surveys to get a complete census of the high-mass star forming regions has recently led to several projects to map the Galactic plane at (sub-)millimeter wavelengths, including the APEX[1] Telescope Large Area Survey of the Galaxy (ATLASGAL; Schuller et al. 2009), the Bolocam Galactic Plane Survey (BGPS; Nordhaus et al. 2008) and The Herschel Infrared Galactic Plane Survey (Hi-GAL; Molinari et al. 2010b). Sub-mm surveys, as opposed to other surveys at shorter wavelengths such as GLIMPSE (Benjamin et al. 2003) or MIPSGAL (Carey et al. 2009), are sensitive to dust in a broad range of temperatures, including the coldest dust. Therefore, such surveys have the potential to trace the earliest stages in the formation of high-mass star.

This chapter focuses on ATLASGAL and describes the source extraction method, the catalogue and how the filaments were selected. ATLASGAL is an unbiased survey of the Galactic plane performed at 870 μm with LABOCA (Large APEX Bolometer Camera). The catalogue presented here is extracted from the data collected from 2007 to 2010, which covered 153 deg^2. These data will provide details of the different stages in the formation of high-mass stars and will be complementary to the other Galactic plane surveys at sub-millimeter such as UKIDSS (Lawrence et al. 2007) and **V**ISTA **V**ariables in the **V**ia Lactea (VVV; Saito et al. 2012) at the near-infrared, GLIMPSE and MIPSGAL at the mid- to far-infrared (Benjamin et al. 2003 and Carey et al. 2009 respectively), HiGAL which spans the far-infrared and sub-millimeter wavelengths (70-500 μm; Molinari et al. 2010b) between MIPSGAL and ATLASGAL, and finally the 5GHz CORNISH Survey. Combined these surveys provide complete wavelength coverage of the from the near-infrared to the radio, and will also form a unique database for follow-up observations.

ATLASGAL data has already been used in a variety of studies: Tackenberg et al. (2012) performed a identification of starless cores, using indicators of star formation in GLIMPSE and MIPSGAL images; Wienen et al. (*submitted*) performed a follow up study of ammonia toward ~1000 clumps identified from the ATLASGAL images and currently underway is the MALT90 project (Foster et al. 2011), which aims is to observe simultaneously 16 molecular transitions with Mopra toward selected clumps from the ATLASGAL catalogue.

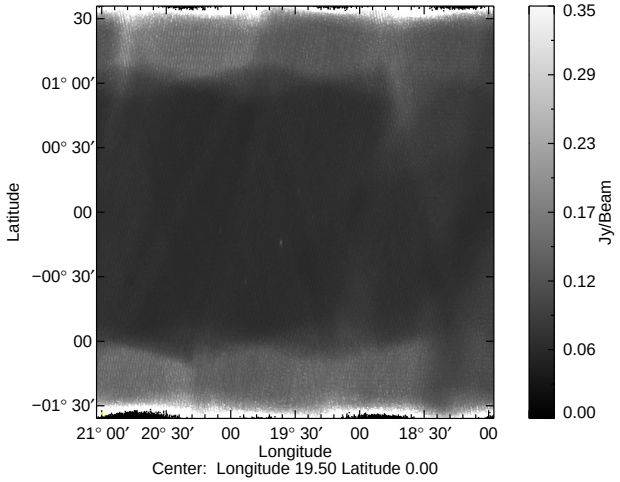

FIGURE 3.1: Noise map of a 3°×3° field centered on $\ell = 19.5°$ and $b = 0$ showing how the noise varies as a function of Galactic longitude and latitude.

3.0.3 Source extraction

We used the extraction algorithm SExtractor (Bertin and Arnouts 1996) to extract compact sources. Although SExtractor was originally created as a method of source extraction for visible and infrared images, it has been used with good results for the extraction of sub-mm sources as well with SCUBA (Thompson et al. 2006) and more recently by the *Planck* team to produce the higher frequency components of their compact source catalogue (217-857 GHz; Planck Collaboration et al. 2011).

Most source extraction algorithms assume that the noise level is constant across the emission map supplied. However, in most surveys this is unlikely to be the cases as variations in survey coverage, weather, elevation and instrumental effects result in the real noise level varying: this is indeed the case for the ATLASGAL survey. In Figure 3.1 we present the noise map for a $3° \times 3°$ field centered on $\ell = 19.5°$ and $b = 0$. The fact that most source extraction algorithms assume a constant noise can lead to real sources being missed because they lie in the region of higher noise, and conversely there is a danger that spurious noise spikes will be mistakenly interpreted as real sources.

In order to reduce the number of spurious sources and avoid missing genuine sources we have

[1]This publication is based on data acquired with the Atacama Pathfinder Experiment (APEX). APEX is a collaboration between the Max-Planck-Institüt für Radioastronomie, the European Southern Observatory, and the Onsala Space Observatory.

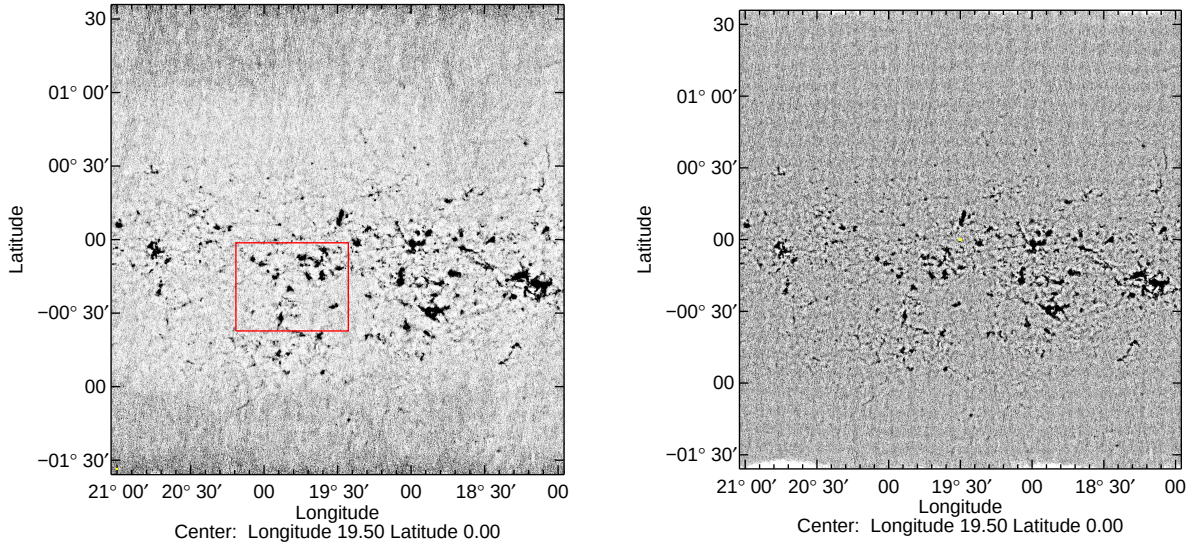

FIGURE 3.2: Example of an ATLASGAL emission map (left panel) and the corresponding filtered signal-to-noise ratio map right panel (see text for details). The region outlined in red indicates the field presented in Fig. 3.3.

created signal-to-noise ratio map by dividing the emission map by the noise map. These signal-to-noise maps also contain a large fraction of low surface brightness diffuse and filamentary emission, particularly towards the Galactic center, the tangent with the Norma spiral arm, and other prominent star forming regions. This not only complicates the identification of compact source but can also lead to the identification of a large number of spurious sources. To limit these issues we have used the program `FINDBACK`, which is part of the `CUPID`[2] clump identification and analysis package, to remove the large scale diffuse emission. Removal of the large scale background is beneficial because it produces maps with a higher contrast between compact sources and their local background. In Fig. 3.2 we present an emission map to show the effect of the varying noise level in the left panel, while in the right panel we show the same map after smoothing the variations by dividing through by the noise map and then spatially filtering to remove the diffuse background. These two images nicely illustrate the advantages of using this method.

`SExtractor` can work on two images simultaneously, one for the source detection and one for measuring the physical parameters of each source. We have therefore use the filtered signal-to-noise map for source detection, however, we use the original emission maps to extract the corresponding source parameters. In this way, the flux and size of the sources are not affected by the filtering process performed for the source detection. These steps should ensure that only genuine sources

[2] `CUPID` is part of the `STARLINK` software suite.

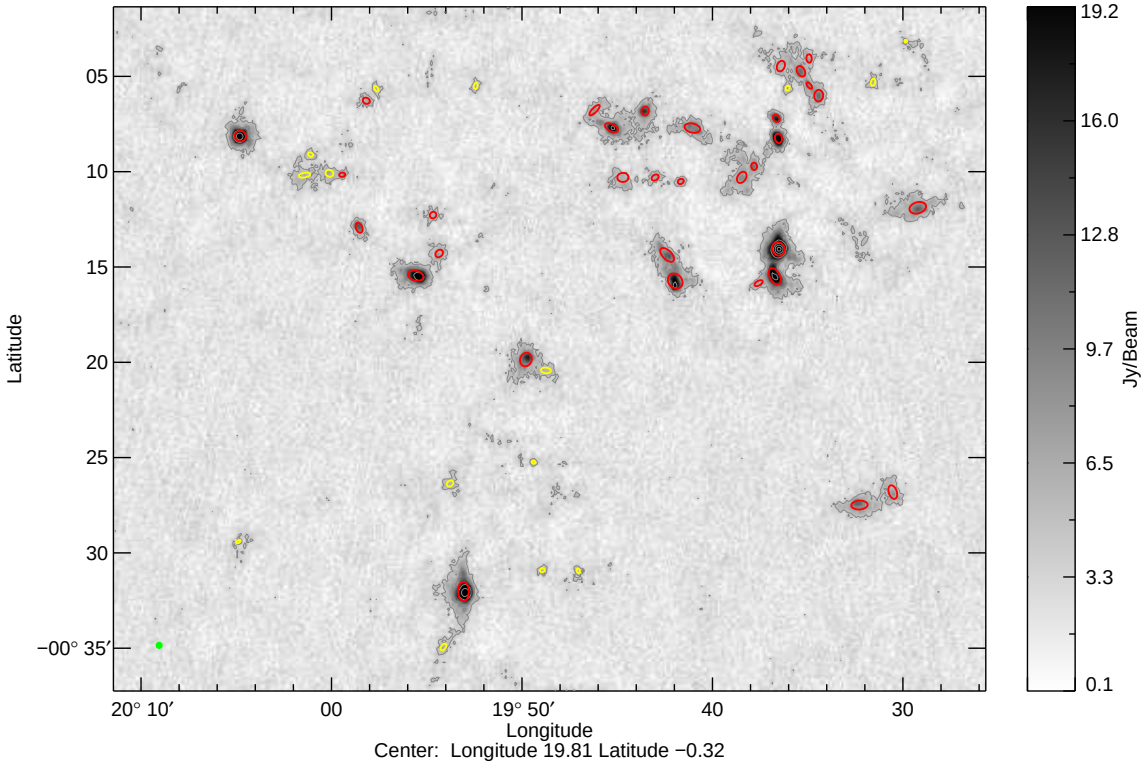

FIGURE 3.3: Example of the sources identified from the ATLASGAL image. The field shown in grey scale is the region outlined in red in the left panel of Fig. 3.2. The positions and sizes of sources identified by SExtractor are shown as red and yellow ellipses (see discussion in Sect. 3.0.5 for details). The ATLASGAL beam size is shown in green in the lower left corner of the map.

make it into the final catalogue. In Fig. 3.3 we present a subregion, taken from the emission map presented in the left panel of Fig. 3.2, showing the positions and sizes of typical sources identified by SExtractor.

The ATLASGAL maps were searched for emission above a threshold of $3.2\sigma_{\rm rms}$, where $\sigma_{\rm rms}$ is the local noise level determined from a user defined box by SExtractoraround each source. The value of the threshold used was determined empirically by varying its value for a number of test regions so as to optimize the number of genuine sources detected while avoiding the inclusion of the more dubious sources. In addition to the threshold we also reject any sources with fewer pixels than the FWHM beam (9 pixels).

To separate possible blended sources, SExtractor divided the emission into 40 sub-levels of flux. In each of these 40 levels, the ratio of the integrated intensities of adjacent pixels is computed.

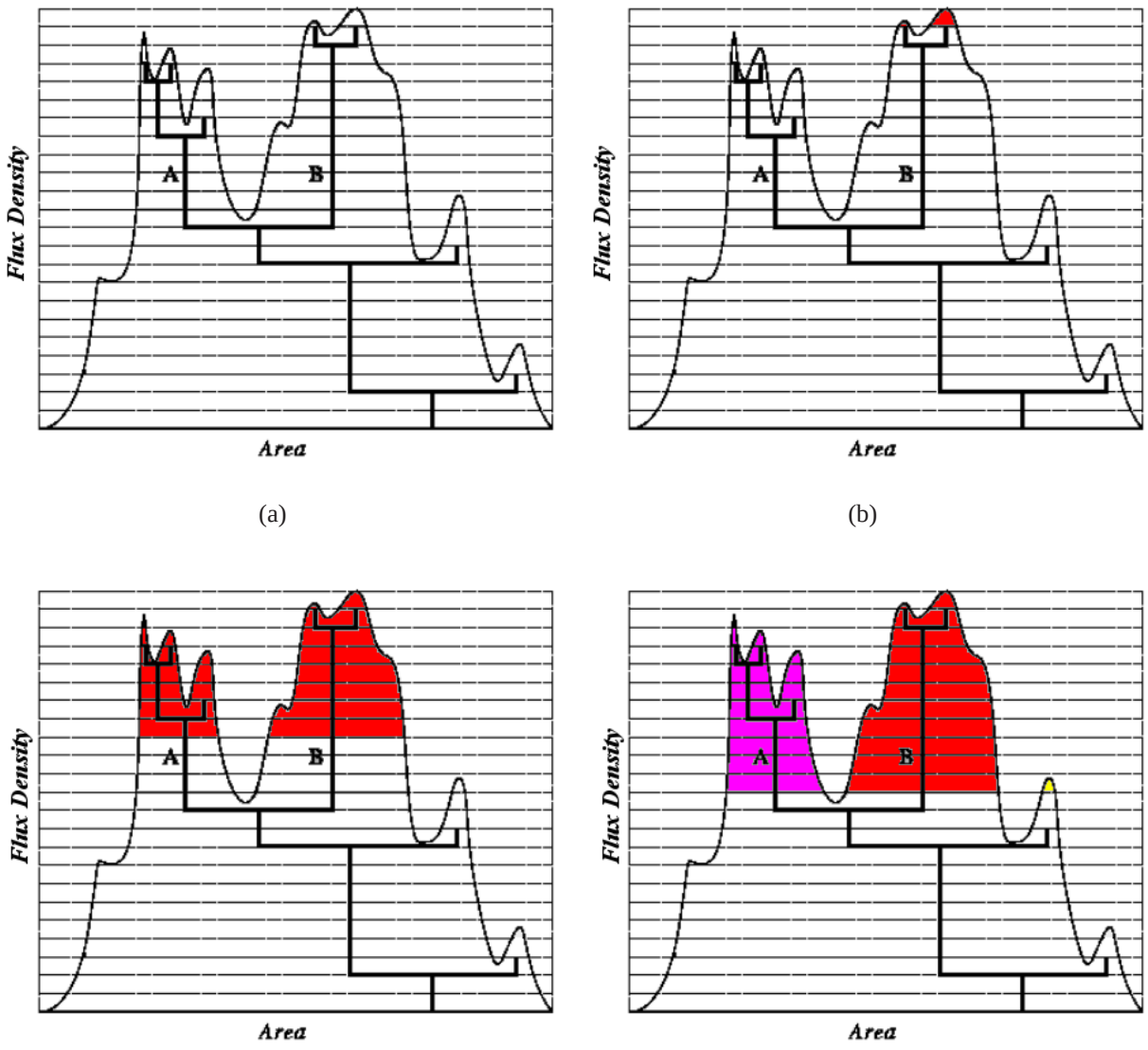

FIGURE 3.4: Separation of blended sources. (a) initial separation in branches; (b) the branches corresponding to the first level are analyzed, since neither of them has a flux greater than 30 percent of the total flux, they are considered as ONE source; (c) the same analysis is carried out until this level where each branch has a flux greater that 30 percent of the total flux and therefore are considered TWO separate sources; (d) the following branches founded (yellow) are assigned to the nearest main branch, in this case B

If this ratio is greater than 0.001 those pixel are considered part of a different source, if not they are considered to be part of the same source. This comparison is done for each pixel in each level. To illustrate this process we present a schematic diagram in Fig. 3.4. For each level the branch is considered to be an individual source if the two following conditions are satisfied:

- The integrated flux in the branch is greater that a certain fraction of the total flux of the blended sources (without any subdivision). For example, the branch B in Figure 3.4
- There is at least one other branch whose integrated flux is also greater this fraction. For example, the branch A in Figure 3.4

3.0.4 Compact source catalogue

3.0.5 Catalogue description

SExtractor was run separately on each of the seventeen $3^\circ \times 3^\circ$ fields that make up the inner most portion of the ATLASGAL survey (i.e., $-30^\circ < \ell < 21^\circ, 153$ degree^2). The results obtained for each field were subsequently combined in order to compile a complete catalogue of sources, taking care to eliminate duplicated sources located in the overlap regions between adjoining fields. In total we have identified 6814 in the 153 deg^2. Only 30% of these are associated with *MSX* point sources and 10% with IRAS sources, which would suggest the majority of sources are devoid of any star formation (see Sect. 3.0.6 for a detailed discussion of these associations).

In Table C.1 we present a sample of the catalogue (for the region presented in Fig. 3.3) as an example of its form and content. The full and up-to-date catalogue and ATLASGAL emission maps will be hosted by the ATLASGAL project page[3], the ESO[4]. The table we present the source name, the peak flux and source barycentric position, the size of the semi-major and minor axis and their position angle, the deconvolved radius, the peak and integrated fluxes and their associated errors and any warning flags generated by the algorithm.

The source names are based on the Galactic coordinates of the peak flux position, which are given in columns 2 and 3. The barycentric coordinates are determined from the first order moments of the longitude and latitude profiles. The barycentric position generally defines the center position of a source, however, if the emission profile of a source is strongly skewed or is associated with substructure, the peak position can be a more accurate measure of a source's position. The source sizes describe the detected source as an elliptical shape, the semi-major and semi-minor axis lengths

[3] www.mpifr-bonn.mpg.de/div/atlasgal/
[4] TBA

represent the maximum and minimum spatial r.m.s. dispersion in *l* and *b* of the source profile along any direction. The position angle is given as clockwise from north. The angular radius ($\theta_{\rm R}$) is calculated from the geometric mean of the deconvolved major and minor axes and multiplied by a factor η which relates the r.m.s. size of the emission distribution of the source to its angular radius (Eqn. 6 of Rosolowsky et al. 2010):

$$\theta_{\rm R} = \eta \left[(\sigma^2_{\rm maj} - \sigma^2_{\rm bm})(\sigma^2_{\rm min} - \sigma^2_{\rm bm}) \right]^{1/4}, \tag{3.1}$$

where σ_{bm} is the size of the beam (i.e., $\sigma_{bm} = \theta_{\rm FWHM}/\sqrt{8\ln 2} \simeq 8''$). The value of η depends of the size of the source with respect to the beam and the emission distribution. Rosolowsky et al. (2010) adopted a value of 2.4, which is the median of the values derived from a range of models, however, they note that the value of η can vary by a factor of 2 in their simulations. For consistency and to facilitate comparisons between the BGPS and ATLASGAL catalogues we also adopt this value.

The peak flux is directly obtained from `SExtractor`. However, since the algorithm treats each pixel in the given emission map in a statistically independent manner and the ATLASGAL maps are gridded with ∼3 pixels per beam, it is necessary to account for the beam area to determine the final measured fluxes and their associated uncertainties. This was simply done by dividing the flux values given by `SExtractor` in the `FLUX_AUTO` and `FLUX_AUTO_ERR` keywords by the beam integral. The errors given for the peak and integrated fluxes include the absolute calibration uncertainty of 15% (see Schuller et al. (2009) for details) combined in quadrature with the intrinsic measurement error. In the case of the integrated flux the error is provided by `SExtractor`, however, the error in the peak flux is derived from the local r.m.s. noise in the image.

In the final column of the table we present the quality flag given by SExtractor which gathers all the information about possible problems or artifacts affecting the source (Bertin and Arnouts 1996). For each source, this flag is either zero (no particular problem), or is equal to the sum of one or more number(s) with the following meanings: (1) the object has neighbors, bright and close enough to significantly bias the photometry, or bad pixels (more than 10% of the integrated area affected); (2) the object was originally blended with another one; (4) at least one pixel of the object is saturated (or very close to); (8) the object is truncated (too close to an image boundary); (16) object's aperture data are incomplete or corrupted; (32) object's isophotal data are incomplete or corrupted; (64) a memory overflow occurred during deblending; (128) a memory overflow occurred during extraction. For example, a flag value of 10 means that the object was originally blended with another source *and* that it is truncated because too close to the edge of the map.

In Figure 3.3 we overplot the positions of sources detected by `SExtractor` towards an small region to demonstrate its performance. To check the reliability of sources with high flag values we plot sources with flag values less than 4 (which are the most reliable) in red while those with higher

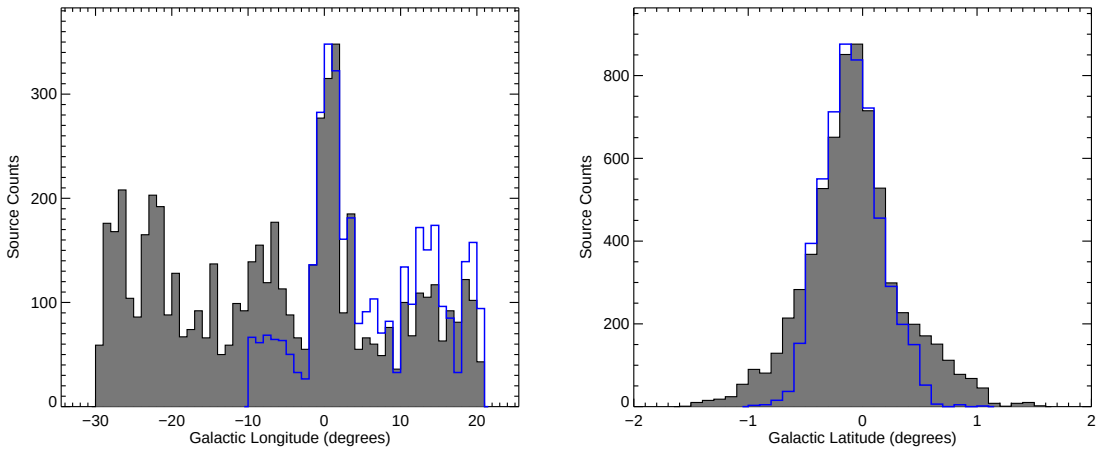

FIGURE 3.5: Histograms of the Galactic longitude (left) and latitude (rigth) distribution for ATLASGAL sources (grey filled histogram) and the BGPS (blue histogram). In both plots the peak of the BGPS distribution has been normalized to the peak of the ATLASGAL distribution. The bin sizes used for the longitude (left panel) and latitude (right panel) distributions is 1° and 0.1° respectively. The peaks in galactic longitude shows clearly the location of the galactic center and the spiral arms.

flag values shown in yellow. In this example it is clear that the sources with the higher flag values are associated with genuine emission. However, the emission is weaker, more diffuse, than those with lower flag values. A similar situation is seen in other region examined and so we conclude that these high flag detections do identify genuine sources of emission, but with the caveat that their associated parameters are somewhat less reliable.

3.0.5.1 Global source properties

In this section we will look at the Galactic distribution of sources detected and the overall distribution of their derived parameters. As a check on the reliability of the ATLASGAL catalogue we will compare our results to those obtained from the Bolocam Galactic Pane Survey (BGPS; Aguirre et al. 2011) that were recently presented by Rosolowsky et al. 2010.

The BGPS covers 150 $\deg^2$ of the Galactic plane, including the majority of the first quadrant with a latitude range of $|b| < 0.5°$. Although the overlap between the BGPS and ATLASGAL region presented here is relatively modest ($\sim$30 $\deg^2$) when compared to the total area covered by the two surveys, the overlapping region does contain some of the highest density regions in the plane, and thus, provides a large number of source in common to both surveys. Another thing to bear in mind when comparing the two catalogues is that the two surveys were preformed at different wavelengths and have different resolutions and sensitivities and so we do not expect a

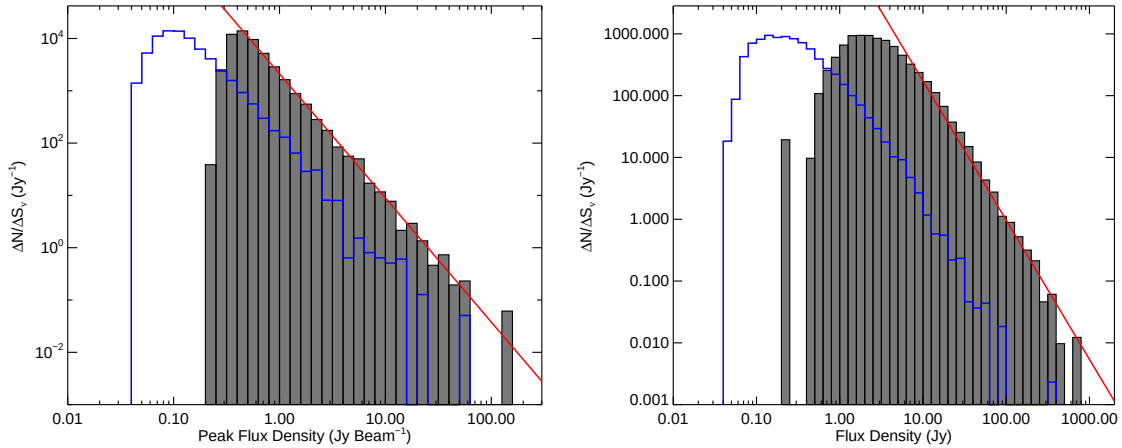

FIGURE 3.6: Flux density number distribution for ATLASGAL sources (grey filled histogram) and the BGPS (blue histogram) of the peak (left) and integrated flux density (right). In both plots the peak of the BGPS distribution has been normalized to the peak of the ATLASGAL distribution. The red line on each plot shows the result of a linear least-squares fit to flux densities larger than the peak of each distribution.

one to one correlation between individual sources or their parameters. However, we do expect the overall distribution of source parameters to be correlated. To facilitate the comparisons between the two catalogues we have followed the structure and present the same parameters in Table C.1 as are given in the BGPS catalogue (cf. Table 1; Rosolowsky et al. 2010).

Galactic distribution

In Fig. 3.5 we present histograms showing the Galactic longitude and latitude distribution of the ATLASGAL catalogue (left and right panels respectively). Inspection of longitude distribution reveals a number of peaks in the source counts; these are located at approximately $-27°$, $-22°$, $-8°$, $0°$ with a weaker peak at $14°$. The positions of the peaks in source counts coincide with the positions of the tangent of the Norma arm, the farside of the Near 3-kpc arm, the NGC6334/NGC6357 star forming regions, the Galactic center region, and finally M16 and M17 regions, respectively.

Comparing the longitude distribution of ATLASGAL sources with the BGPS distribution we see they are broadly similar, both showing the same peaks, however, we note that the ratio of the Galactic center peak to the other peaks is quite different. This is likely to be a result of the different resolution of the two surveys. In the case of the ATLASGAL data the higher resolution has allowed the complex emission seen towards the Galactic center to be more easily deblended resulting in a higher number of sources being detected in this region. Conversely, the lower resolution of the BGPS observations results in a higher sensitivity to lower surface brightness structures resulting in

a higher proportion of sources being found away from the Galactic center.

The latitude distribution shown in the right panel of Fig. 3.5 peaks significantly below 0° as also notes by Schuller et al. (2009) and more recently by Beuther et al. (2012). Comparing the latitude distribution to that of the BGPS we find them to again be similar. Both ATLASGAL and BGPS distributions have the same FWHM. We note than the tails of the distributions appear to be significantly different, however, the BGPS latitude range is $|b| < 0.5°$ with only a few excursions to larger value of $|b|$ and so the distributions are not really comparable for latitudes $|b| > 0.5$.

Flux distribution

In Fig. 3.6 we present plots of the peak and integrated flux distributions for ATLASGAL sources (grey filled histogram) and BGPS sources located in the overlap region (blue histogram). These distributions show the differential flux density spectrum (i.e., $dN/dS\nu \simeq \Delta N/\Delta S\nu \propto S^{-\alpha}$; Rosolowsky et al. 2010). Comparing the distributions of the peak and integrated fluxes for the two catalogues they can be seen to be very similar, however, with the higher frequency (ATLASGAL) measurements being shifted to higher values.

The flux distributions above the turnover can be approximated by a power-law that extends over three orders of magnitude. Fitting these parts of the distributions with a linear least-squares fit we find the peak and integrated distributions can be represented by the values of $\alpha = 2.4$ and 2.1 respectively. The results of these fits are indicated by the red lines overplotted on the left and right panels of Fig. 3.6. Both of these values are in excellent agreement with the values obtained from the same fit to the BGPS peak and integrated flux distributions, which are 2.4 and 1.9 respectively.

The difference in the slope between the peak and integrated flux densities results from the fact that point sources dominate the peak distribution towards the completeness limit, whereas brighter sources tend to be larger and thus have larger total flux densities than for the smaller sources. As pointed out by Rosolowsky et al. (2010), this make the integrated flux density top-heavy and effectively lowers the magnitude of the exponent.

Another interesting feature of the peak distribution is that the main shape of the distribution drops off completely at $\sim$70 Jy beam^{-1}, however, there are several sources with fluxes of $\sim$150 Jy beam^{-1}. The bright sources that contribute to this flux density bin are the brightest 870 μm sources in the catalogue and form part of a dust ridge associated with the Sgr B2 high-mass star forming region.

Angular size distribution

In Fig. 3.7 we present plots showing the size distributions of the catalogued sources. In the upper left panel of this figure we show histograms of the semi-major ($\sigma_{\rm maj}$) and semi-minor ($\sigma_{\rm min}$) distributions and the ATLASGAL beam size (red dotted line, $\sigma_{\rm bm} \simeq 8''$). We note that there is a significant number of sources with sizes smaller than the beam, particularly with regards to the semi-minor axis. This anomaly is due to the fact that the sizes are derived from moment measurements of the emission distribution above the threshold value ($\sim 3\sigma$) and therefore do not take account of all of the emission associated with each source down to the zero-intensity level. As previously noted by Rosolowsky et al. (2010) this has a disproportionate effect on weaker sources and often results in their sizes being underestimated.

In the upper right panel of Fig. 3.7 we present a histogram showing the elongation distribution, that is the ratio of semi-major to semi-minor axes. The distribution has a peak and median value of 1.3 and 1.6 respectively, which indicates that the sources in the catalogue are significantly elongated. The elongation distribution closely matches that found for the BGPS sources with the only noticeable difference being that the ATLASGAL catalogue tends to have a slightly higher degree of elongation, possibly a result of the higher resolution of ATLASGAL survey. However, both catalogues appear to contain a significant number of very elongated sources.

In the lower panel of Fig 3.7 we present the effective radii of the ATLASGAL and BGPS detections. The two distributions again appear to be broadly similar, however, the whole BGPS source distribution appears to have been shifted 10-15 arcsec to the right of the ATLASGAL distribution, which is clearly a result of the different survey resolutions.

3.0.6 Cross correlation with existing catalogues

We performed a cross correlation of our catalogue with the far-infrared *IRAS* Point Source Catalogue (Joint Iras Science 1994), and with the mid-infrared *MSX* Point Source Catalogue (Egan et al. 2003). In addition, we looked for detection of the CS(2-1) line by Bronfman et al. (1996) towards sources associated with *IRAS* point sources. We used a search radius of 30 arcsec ($\sim$ 2 telescope beams) around the peak flux position from our catalogue for all the catalogues mentioned above. We want to stress that MSX and LABOCA have the same spatial resolution, which makes the correlation between both wavelengths relatively straightforward. Further associations with other catalogues (e.g. those extracted from the *Spitzer* GLIMPSE and MIPSGAL surveys) will be addressed elsewhere.

Infrared emission detected by the *IRAS* and *MSX* surveys generally implies that star formation

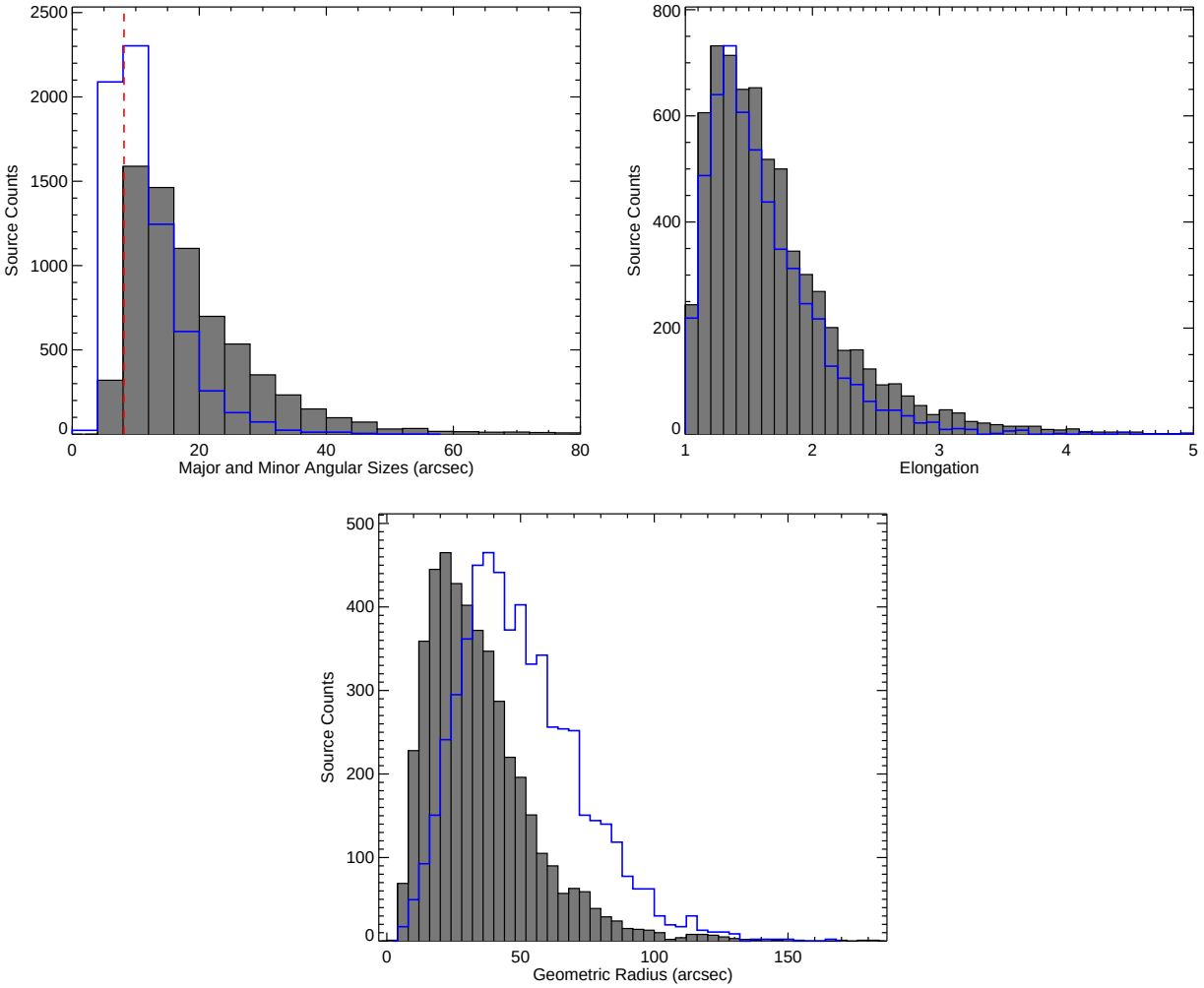

FIGURE 3.7: Histograms of the angular size distribution of detected ATLASGAL sources. In the upper panel we plots of the semi-major (filled grey histogram) and semi-minor (blue open histogram) size distributions of detected ATLASGAL sources. The bin size used for both parameters is 4 arcsec. In the middle and lower panels we present histograms of the elongation and geometric radii of ATLASGAL sources (grey filled histogram) and the BGPS (blue histogram). In both cases the peak of the BGPS distribution has been normalised to the peak of the ATLASGAL distribution. The bin sizes used for the elongation and radii distributions is 0.1 and 4 arcsec respectively.

has already started within the sources, therefore tracing a relatively evolved stage of star formation. From the 6814 compact sources in this Catalogue, we found that 789 are associated with *IRAS* sources, 2531 are associated with *MSX* emission, and only 190 *IRAS* sources have been observed and detected in the CS(2-1) transition (Bronfman et al. 1996). The number of sources with *IRAS*, *MSX* and CS association are 190 and a total number of 5371 sources have no association in any of the catalogues mentioned above. This implies that these sources could be cold, and they could be in a very early stage of star formation, prior to the birth of high-mass protostars. Follow up studies of the sources with no association in the *IRAS* and *MSX* catalogues will tell us valuable information about the nature of these sources, and could give a better understanding of the processes involved in the formation of a high-mass star.

3.1 Finding filaments

One of the major discoveries made by recent surveys at sub milliliter wavelengths is the ubiquitous presence of filamentary structures along the Galactic Plane; all of which contain multiple smaller, denser clumps. These kinds of structures are observed both in regions where current star formation is observable and in regions where there is no evidence of active star formation (Figure A.1).

The sensitivity of the ATLASGAL survey, allows us to identify filaments that may be related to high-mass star formation. To identify filaments for detailed study we selected a region of the Galactic Plane covered by the ATLASGAL survey that shows different amount of infrared emission. This is important because we wanted to select filaments that contained clumps in a range of evolutionary stages.

To enhance the filaments, we applied a Fourier tampering filter on the maps. This method consisted of applying a Fourier transform to the maps and in the Fourier space, masking all the emission longer than a given wavelength and then apply an inverse Fourier transform to the masked images. With this method compact sources will be deleted from the images, which will result in a map with an enhancement of the extended features such as filaments.

Over this filtered map, we then created a mask for all the emission above a threshold of 1.5σ. In this way, we can clearly identify the filamentary structures present in the maps (Figure 3.8 top panel). We then selected by eye the structures that appears to be connected; these regions possible contain filaments (Figure 3.8 lower panel). With this method we recovered Nessie (Jackson et al. 2010), a unique filamentary structure recently identified as an IRDC from *Spitzer* images.

3.2 Overview of the selected filamentary structures

We identify five filaments for further study (Fig 3.9). Since the aim of this thesis is to characterize filaments in different stages of evolution, to establish a connection between these structures and the formation of stars within them, the five filamentary structures selected show a broad range in their infrared emission.

Filaments A and C, were selected because they are associated with almost no infrared emission, suggesting that they have no current star formation occurring within them. These are likely examples of filaments in an early evolutionary stage where the star formation process has not begun or it is just starting.

Toward filament B we see both dark and bright infrared emission. This filamentary structure is an example of a filament with clumps potentially in different evolutionary stages. Filaments D and E show considerable more star formation activity. These filament will reveal the properties of filaments where the star formation has already begun and allow us to compare their properties to those that are more 'quiescent' (filament A and C).

In the following chapters, we describe the observed and derived properties from the multi-wavelength study carried out to better characterize and understand these filaments.

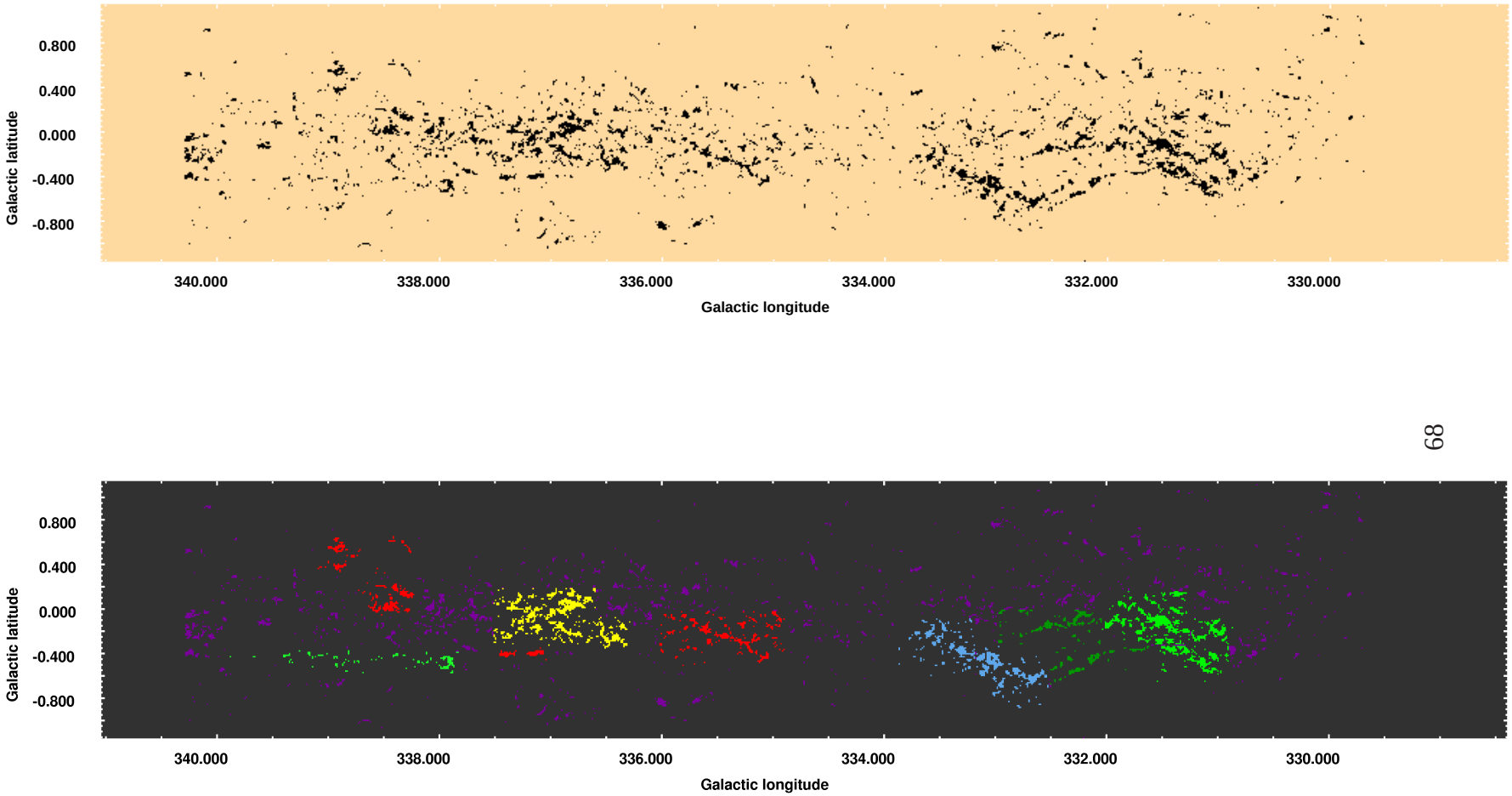

FIGURE 3.8: Extended structure detected in the ATLASGAL images. Top panel: mask created from the emission above 1.5σ on the filtered images. Lower panel: Regions containing possible filaments, each region is identified by a different color.

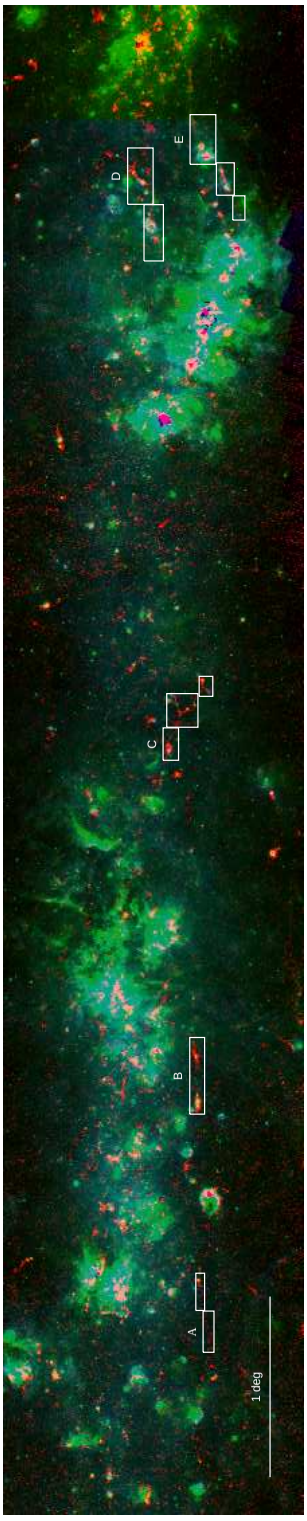

Figure 3.9: Color image of the 20 square region containing the five filamentary structures selected for this work. Red: ATLASGAL 850 μm, Green: MIPS 24 μm, Blue: IRAC 8 μm. Boxes correspond to the sub-regions containing the filaments selected to carry out a detailed study.

4

Filament A: Nessie

This filamentary structure, known as the ”Nessie” Nebula (Jackson et al. 2010), corresponds to an extreme case of a filament with an aspect ratio of 150:1. *Spitzer* GLIMPSE/MIPSGAL images at 3.6 μm, 4.5 μm, 5.8 μm, 8 μm and 24 μm show this filamentary structure as a very long IRDC. At these wavelengths there is also some evidence of star formation, given by the presence of green fuzzies (emission enhancement at 4.5 μm) and point sources at 24 μm. Panels (a) and (b) of Figure 4.1 show a three color image made from the 3.6 μm, 4.5 μm and 8 μm *Spitzer*/GLIMPSE data and an image of the emission at 24 μm respectively. Clearly seen is the filamentary structure as an IRDC against the diffuse bright background, with two very bright regions at 24 μm.

Dust thermal emission at 870 μm shows a similar morphology with a length of ~90 arc minutes and several clumps distributed along it (Figure 4.1, panel c). The small region covered by SABOCA at 350 μm shows that the emission at this wavelength is well correlated with the emission at 870 μm. Figure 4.2 shows a 350 μm image toward the small region covered of this filament.

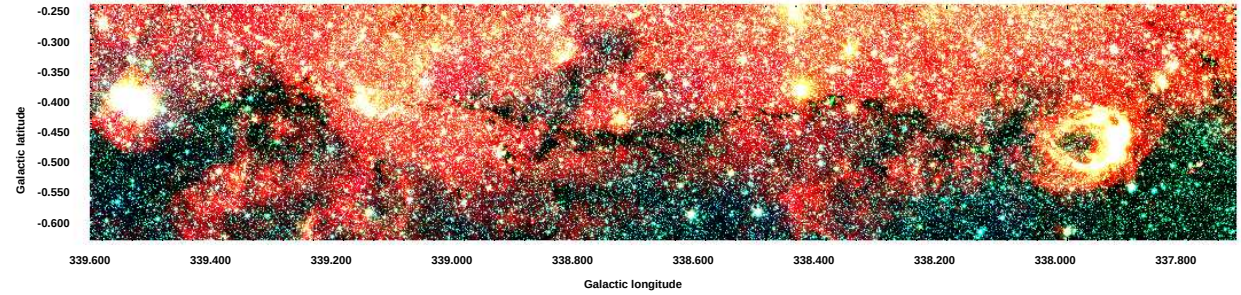

(a) *Spitzer*/GLIMPSE 3.5 μm - 8 μm

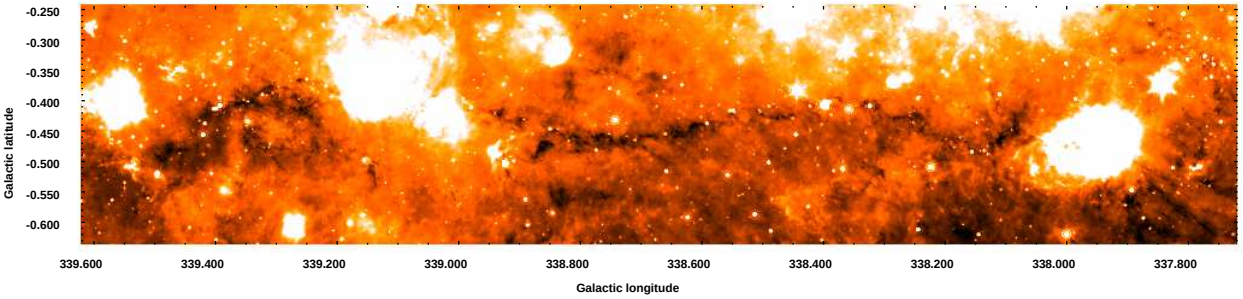

(b) *Spitzer*/MIPSGAL 24 μm

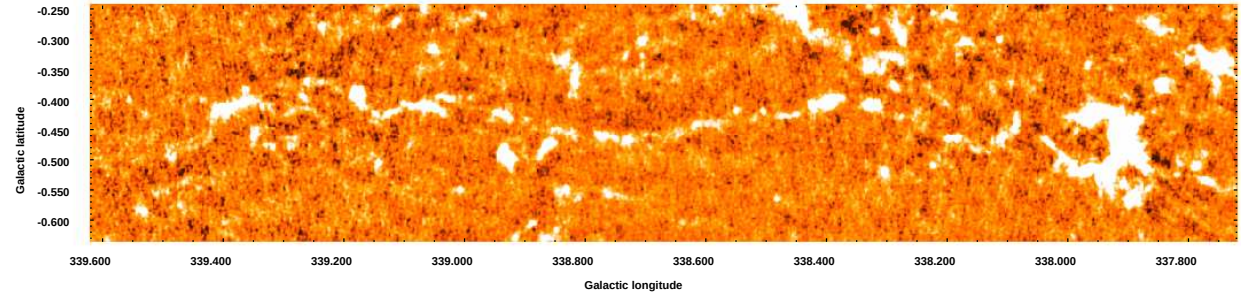

(c) APEX/LABOCA 870 μm

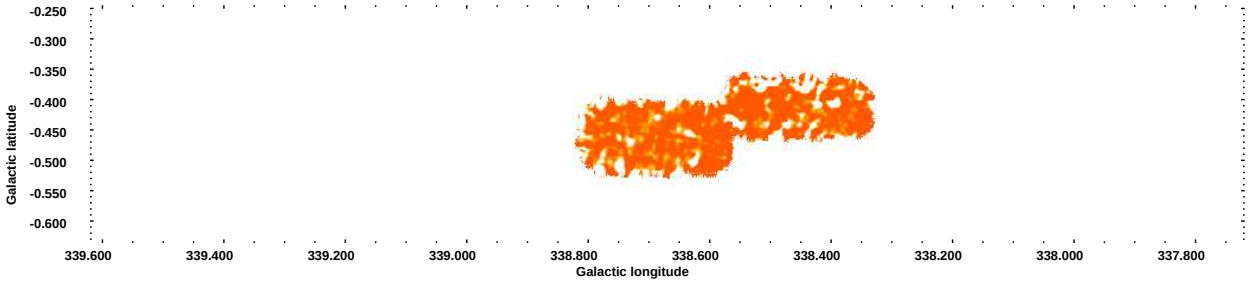

(d) APEX/SABOCA 350 μm

FIGURE 4.1: Multi-wavelength continuum images of Nessie. This Figure shows that at infrared wavelength this structure appears as an infrared dark cloud in the *Spitzer* images, while in the ATLASGAL and SABOCA images the dust continuum emission appears bright, showing clearly the filamentary structure.

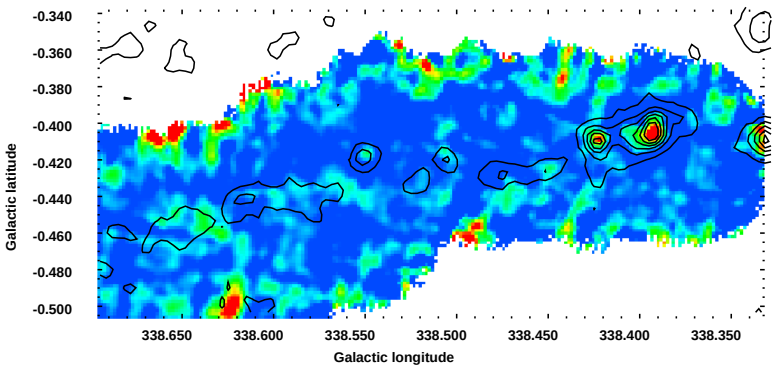

FIGURE 4.2: Color image of the region covered by the observation at 350 μm. Overlaid in black contours is the emission from ATLASGAL at 870 μm. At 350 μmonly the brightest clumps are noticeable.

4.1 Defining the filament

To identify the potential filament we defined a path that follows the peaks in the emission at 870 μm. The path was created with a Python algorithm that interpolates the emission between the peaks (for a more detailed explanation see Section 1.4.1). Once the path is defined, the width of the region containing the filamentary structure was set to 15 pixel to each side of the path in order to cover the full extend of the emission, giving a width of ~3 arc minutes (Figure 4.3).

Figure 4.4 shows a plot of the flux density at 870 μm and 350 μm along the defined filamentary path. Clearly distinguished are the position of the clumps embedded in this filament. The mean *rms* in the maps is ~ 4.7 mJy and 0.18 Jy at 870 μm and 350 μm respectively, thus the emission of the entire structure is significantly higher that the average noise at both wavelengths.

From the emission at 870 μm we estimated the projected diameter of the filamentary structure. This was obtained by measuring the radial dispersion of the emission across the filament at each point along the defined path and fitting a Gaussian to this radial dispersion (see section 1.4.1.3). The projected radius was defined as the FWHM/2, obtained from the Gaussian fit. For this filament the radius has a mean value of ~32 arc seconds.

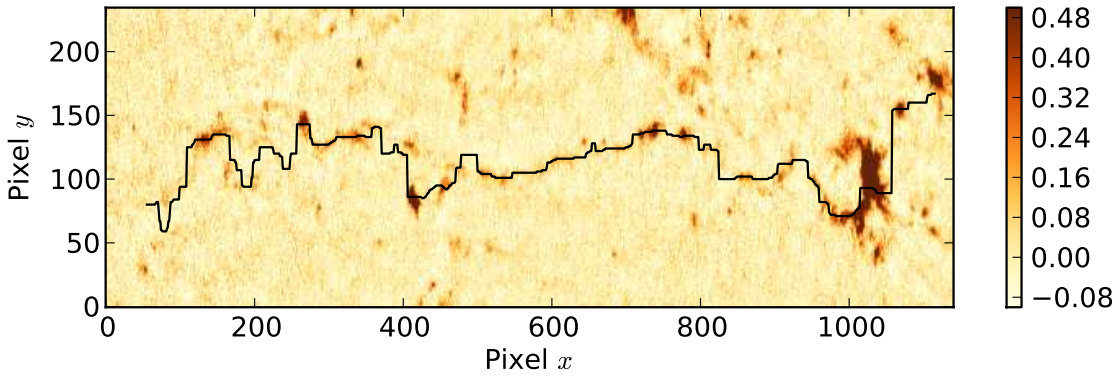

FIGURE 4.3: Path defined for Nessie. Color scale shows the 870 μm emission (in Jy/beam). The black line shows the path defined for the filament using the Python algorithm that follows the peaks in the emission. The region containing the filament is defined to be 15 pixels to each side of this path.

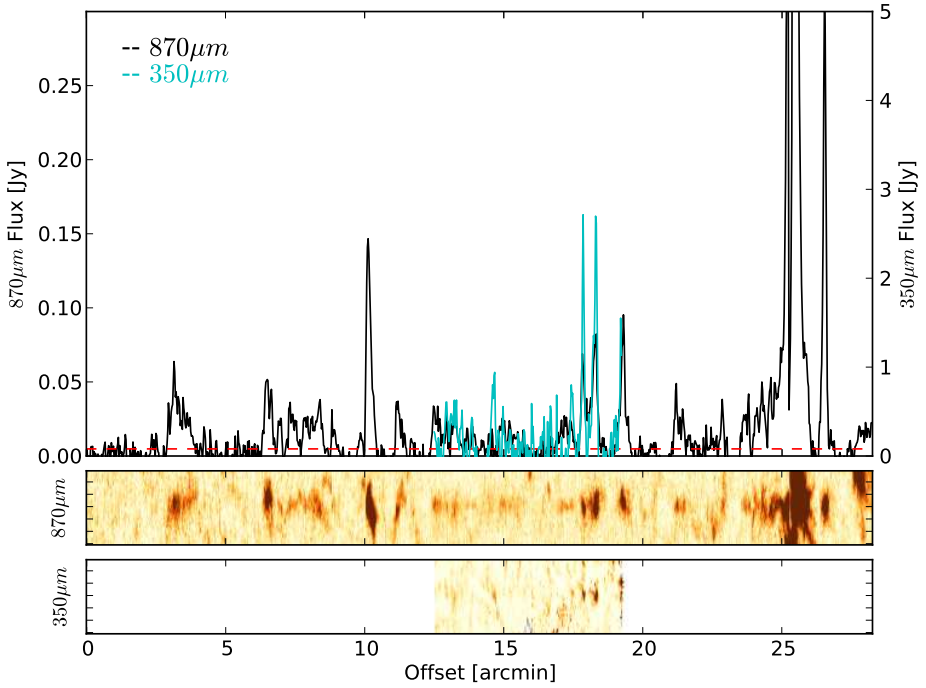

FIGURE 4.4: Distribution of dust continuum emission along the filament. Top panel: Flux along the path defined for this filament for both 870 μm (black line) and 350 μm (blue line) continuum emission, the red dotted line shows the mean noise in the maps (4.7 mJy at 870 μm and 0.18 Jy at 350 μm). Lower panels: Color image of the emission at 870 μm and 350 μm along the path defined for this filament using a width of 15 pixel to each side.

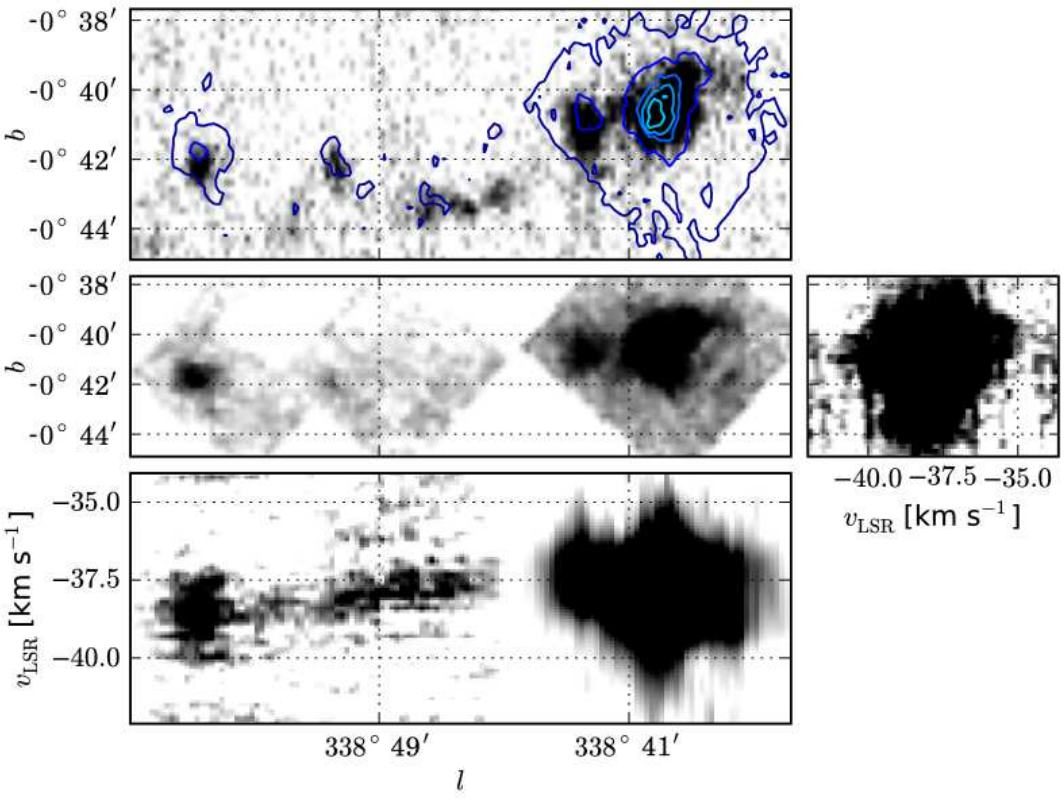

FIGURE 4.5: ^{13}CO(3-2) emission toward filament A. Top panel: Contours of the integrated intensity emission over the 870 μm observations from 3 to 30 σ, with σ = 8 K km s^{-1}. Middle panel shows the ^{13}CO(3-2) velocity integrated intensity map. This image shows that the morphology of the ^{13}CO(3-2) emission follows well the dust emission at 870 μm. Lower and right panels: Position velocity map, this plots show that the emission occurs at the same velocity, thus, indicating that the filament is a single coherent structure.

4.2 Physical coherence of the observed filamentary structure

Although the dust continuum emission appears to trace a filament, it is not possible to determine whether the observed structure is physically coherent since the observed emission arises from all objects along the line of sight. Therefore, to asses the physical coherence of this structure it is necessary to get information about its velocity. This was obtained through the measurement of

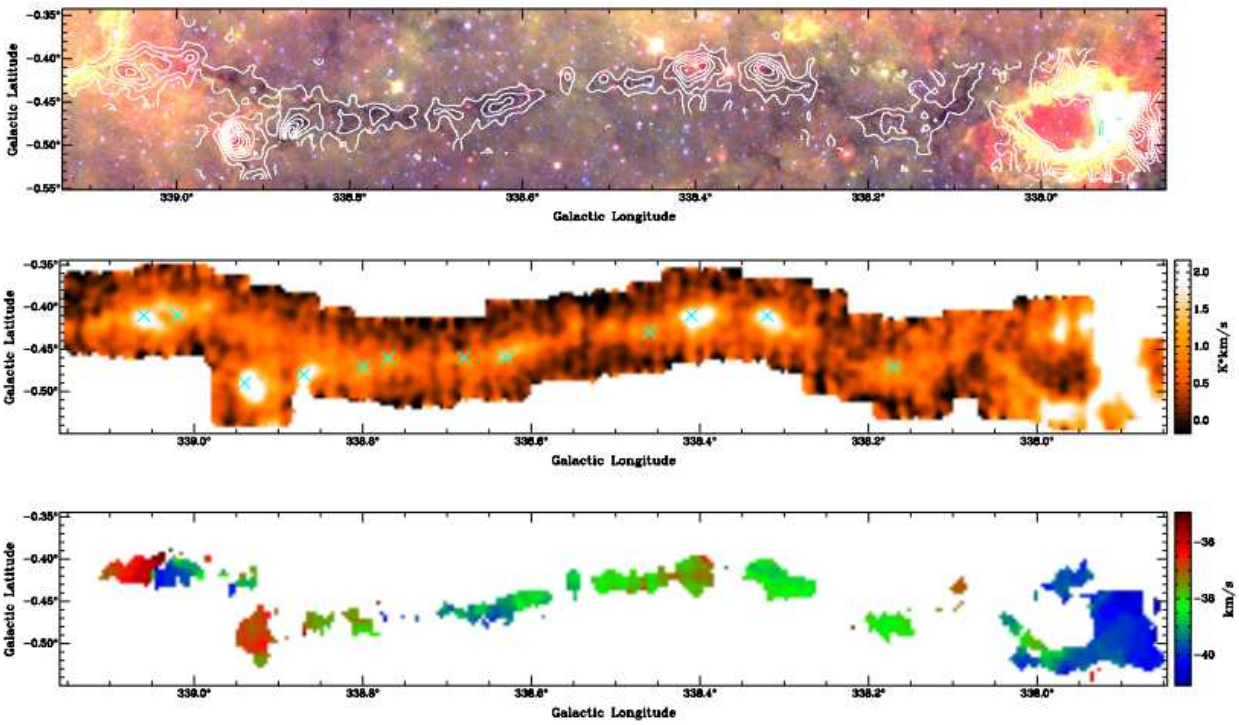

FIGURE 4.6: Observation of HCN(1-0) toward filament A. Top panel: Contours of the HCN(1-0) integrated intensity map overlaid on the *Spitzer* 3 color image (blue 3.6 μm, green 8 μm and red 24 μm). Middle panel: HCN(1-0) integrated intensity maps, crosses indicate the position of the clumps detected at this wavelength. Lower panel: velocity-field map of the HCN(1-0) observations. Image from Jackson et al. (2010)

the central velocity, v_{LSR}, of ^{13}CO(3-2) molecular line emission. The ^{13}CO(3-2) observations do not cover the whole filament, but only a small portion. The information about the velocity was complemented with observations of other molecular lines observed toward the clumps embedded in this structure.

Figure 4.5 (top panel) shows the emission at 870 μm overlaid with contours of the ^{13}CO(3-2) velocity integrated emission. Clearly seen is that the morphology of the ^{13}CO(3-2) emission traces well the morphology of its dust thermal emission. Bottom and right panels of this figure presents the position-velocity map of the ^{13}CO(3-2) emission showing that the emission along the filament is almost at the same velocity, ~-37 km s^{-1}, indicating that this part of the molecular cloud is physically coherent. Observations of the HCN(1-0) line made by Jackson et al. (2010) show that Nessie has the same range in velocity which indicates that this long filamentary structure is actually physically connected (Figure 4.6). Thus, it appears that the structure seen in the dust continuum is actually a physically coherent filamentary molecular cloud.

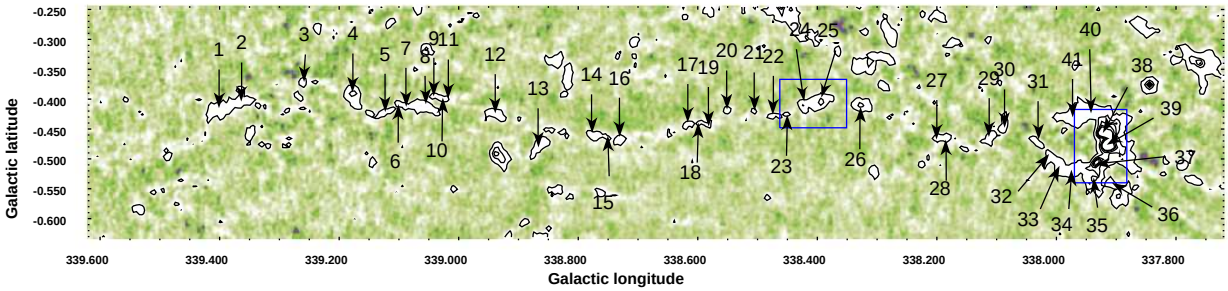

FIGURE 4.7: Color image of the 870 μm dust continuum emission toward filament A. Arrows indicated the positions of the clumps identified from the ATLASGAL catalog. We can see that the clumps are evenly distributed along the filament. Contours shows the emission > 3σ.

From the ^{13}CO(3-2) central velocity we calculate the distance to this filament assuming a model of the Galaxy's rotation (see section 1.4.3.2). The distance obtained for this filament is $\sim$ 3 kpc. We assumed the near kinematic distance since we observe this filament as dark against the bright extended background. This implies that the physical length of the filament is 80 pc and its radius is 0.44 pc.

4.3 Properties of the embedded clumps within the filament

Using the ATLASGAL point source catalog (Contreras et al. in prep.), we identify 41 clumps embedded in this filament. Figure 4.7 shows a 870 μm image and the position of the clumps along the filament. The ATLASGAL catalog names of these clumps are based on their peak position in Galactic coordinates, however, for simplicity we use the IDs A1, A2, A3 etc. for each clump ordered by Galactic longitude along the filament. ATLASGAL names are included in Table 4.1.

A comparison of the 870 μm image with GLIMPSE and MIPSGAL infrared images allows to investigate the star formation activity within each clump. The star formation activity can be traced via an excess emission at 4.5 μm (green fuzzies which traces shocked gas) or emission at 24 μm(suggesting the presence of a central protostar). Some clumps don't show any infrared emission suggesting that they might be in an early evolutionary stage. We found a wide range of evolutionary stages within the clumps embedded in this filament. Clumps A1, A2, A15, A16, A17, A27, A28, A29 and A30 show no emission at both GLIMPSE and MIPSGAL images, being possible starless clumps in an early evolutionary stage. Clumps A31 to A41 are all immersed in the IR bubble in the edge of this filament showing significant emission at both 8 μm and 24 μm. The remaining clumps show some indication of star formation activity either a green fuzzy, a 24 μm point

source or both. Table 4.1 summarizes the properties of the clumps from their emission at infrared and millimeter wavelengths and their association with IRAS sources.

From the 870 μm and 350 μm observations we measured the peak flux, size and integrated flux for each clumps. These values were computed from the emission above the 3σ noise level at both wavelengths, the values obtained are summarized in Table 4.2. The maximum emission in the filament, ~24 Jy/beam, is at the position that corresponds to the bright infrared bubble. Using the position of the clumps from the ATLASGAL point source catalog, we derived their relative spacing along the filament. The spacing was defined as the distance to the nearest clump found to the right of each clump, starting with the clump located at the far left end of the filament (A1).

The properties of clumps A20, A21, A22, A24 and A25 derived from the ^{13}CO(3-2) molecular line observations were also determined. This was done by averaging the ^{13}CO(3-2) emission > 3σ at each clump and fitting a Gaussian profile to the average spectrum. From this fit we derived the peak antenna temperature (T_{peak}), line central velocity (v_{LSR}), line width (Δv) and integrated intensity (II). The values obtained are summarized in Table 4.2.

Four clumps were also observed in the N_2H^+(3-2) line (A17, A20, A22 and A25). These clumps correspond to those with the strongest emission at 870 μm within the region covered by the 350 μm observations. N_2H^+(3-2) possess hyperfine structure, however, as seen on the spectra obtained (Figure 4.8) the components of the hyperfine structure are blended due to the large line width of each component. For clumps A17, A20 and A25 it was possible to fit the hyperfine components with CLASS, however, due to the large width of each component the fit was not good. For this reason we did not use the value of the opacity obtained from these fits to derive the mass of the clumps. For clump A22 we perform a three component Gaussian fit, with fixed position for each component. From this fit we derived: the peak antenna temperature, central velocity, line width and integrated intensity. The values obtained from the hyperfine component fit and Gaussian fit are listed in Table 4.2.

4.4 Chemistry, evolutionary stage and kinematics of the brightest clumps

The chemical state of these clumps was assessed by also considering data from the MALT90 survey, which observed 16 molecular lines near 90 GHz toward the clumps. The MALT90 observations were performed toward two regions in the filament that covered clumps A24, A25, A37, A38 and A39.

Figure 4.9 shows maps of the velocity integrated emission in the molecular lines detected toward

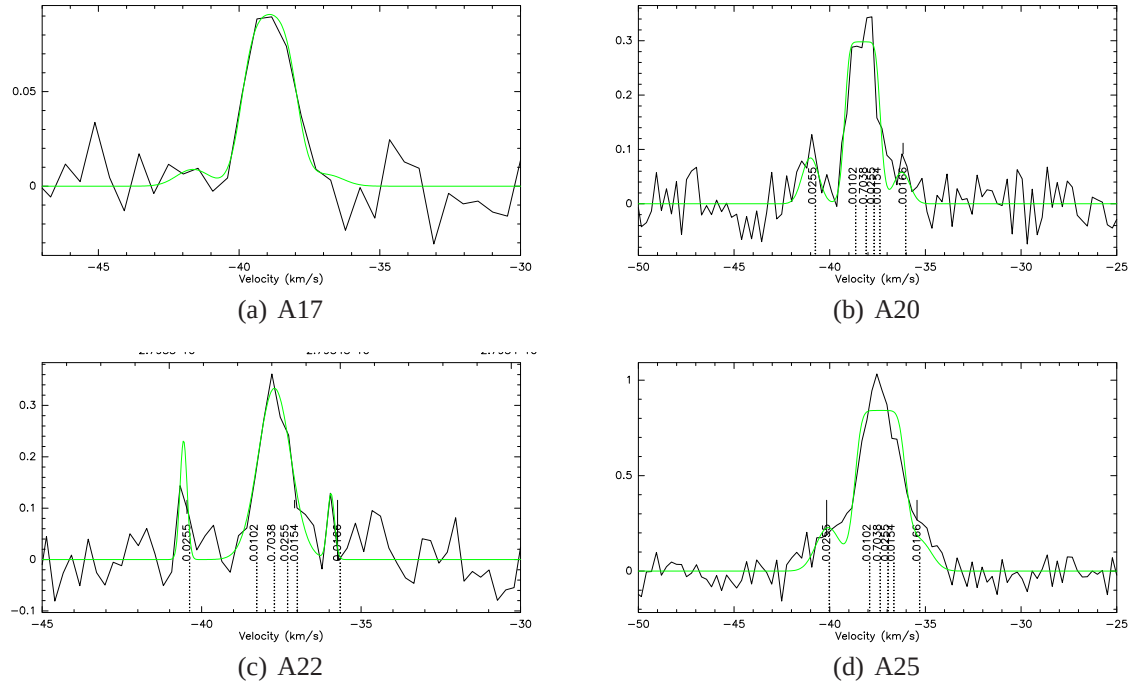

(a) A17 (b) A20

(c) A22 (d) A25

FIGURE 4.8: Spectra of the N_2H^+observations toward clumps A17, A20, A22, A25. Each plot shows the position of the individual hyperfine component. The numbers indicate the relative intensity of the lines. The green line is the fit tho the spectra.

clumps A24 and A25. These moment 0th maps were produced by integrating the emission over the velocity range from -39 km s^{-1} to -36 km s^{-1} for all the transitions, except HCO^+ where the velocity range used for the integration ranged from -42 km s^{-1} to -36 km s^{-1}. The morphology of the N_2H^+ emission traces well the dust continuum and ^{13}CO(3-2) molecular line emission. The emission at HCO^+ is concentrated only toward the clump A25 being barely detectable toward clump A24. Figure 4.10 shows maps of the integrated intensity in molecular lines detected toward clumps A37, A38 and A39. This figure we can see that the dense gas traces very well the bubble observed at 870 μm and at infrared wavelengths. Clump A37 shows emission in ten of the sixteen molecular lines.

Gaussian fits to the observed line profiles at the peak position of each core were made in all the detected molecular lines. From these fits we derived the peak antenna temperature (T_{peak}), the central velocity of the line (v_{LSR}), line width (Δv) and integrated intensity ($\int T_b dv$, II in the table). We also obtained the (l,b) position of the peak spectrum expressed as the offset with respect to the position of the peak spectrum of N_2H^+(1-0) (Δl and Δb) and the total integrated intensity (I_T). These values are summarized in Table 4.3. We also fitted the hyperfine structure observed in the N_2H^+(1-0) emission. From these fits we obtained the excitation temperature, line widths and

opacity toward each clump. These values are summarized in Table B.1.

Figure 4.11, 4.12, 4.13, 4.14 and 4.15 show the spectra of the molecular emission detected toward clumps A24, A25, A37, A38 and A39 respectively. Of the 16 lines observed toward A24, only two were detected with significant emission (integrated intensity emission > 3σ): N_2H^+(1-0) and HNC. Both of those molecular lines are tracers of dense gas. Their detection and the lack of emission of hot chemistry tracers such as HNCO, HC_3CN, CH_3CN suggest that this core is dense and cold. Observing the emission of this clump in the *Spitzer*/GLIMPSE images we detect emission at 24 μm and a green fuzzy towards it, thus, it appears to harbor a newly formed star within it that heats the dust.

Toward clump A25 we detected emission in four of the sixteen lines observed: N_2H^+(1-0), HNC, HCO^+ and HCN. The HCO^+ spectrum peaks at a significantly different velocity than that of the N_2H^+. The ^{13}CO(3-2) spectrum shows broad wings. From the N_2H^+ spectra we see that the relative intensities of the hyperfine components correspond to the optically thin case. Figure E.1 shows the channel maps of N_2H^+(1-0) for the region covering clumps A24 and A25.

Ten of the sixteen lines were detected toward clump A37: HCO^+, $H^{13}CO^+$, N_2H^+, HCN, HNC, HC_3CN, CH_3CN, C_2H, ^{13}CS and SiO. The spectra of HCO^+, HNC and HCN have their peak blue-shifted with respect to the central velocity of N_2H^+, there is also asymmetry in the HCO^+ and HC_3CN spectra, both showing a skewed red profile suggesting inward motions.

Toward A38 we also detected 10 of the sixteen molecular lines. The emission at HNC, HCO^+ and $H^{13}CO^+$shows a broad wings to the blue side of the spectra suggesting outflows. The SiO emission is very broad also possibly coming from the outflow emission. The C_2H emission is very bright corresponding to the PDR observed at infrared in GLIMPSE. Toward clump A39 we detected the same 10 molecular lines. The spectra are narrow presenting a skewed red profile at HCO^+, suggesting inward motions. The C_2H emission is bright corresponding to the PDR. However, the SiO emission is weak suggesting that there is no many shocked gas. Figure E.2 and E.3 shows the channel maps of ^{13}CO(3-2) and N_2H^+(1-0) for the region covering clumps A37, A38 and A39.

TABLE 4.1: Filament A, IR sub-millimeter classification of the observed clumps.

ID	ATLASGAL Name	GLIMPSE 3.6 - 8 μm	MIPSGAL 24 μm	ATLASGAL[b]	IRAS
A1	AGAL339.401-0.414	Green Fuzzy[a]	Point source	Weak	-
A2	AGAL339.364-0.406	Dark	Dark	Weak	-
A3	AGAL339.261-0.372	Dark	Dark	Weak	-
A4	AGAL339.176-0.391	Bright 3.6-8 μm	Bright	Bright	16419-4602
A5	AGAL339.124-0.422	Bright 3.6-8 μm	Bright	Weak	-
A6	AGAL339.101-0.407	Bright 8 μm	Bright	Weak	-
A7	AGAL339.089-0.412	Bright 8 μm	Bright	Weak	-
A8	AGAL339.054-0.412	Dark	Diffuse emission	Weak	-
A9	AGAL339.043-0.396	Dark	Diffuse emission	Weak	-
A10	AGAL339.027-0.401	Bright 8 μm	Bright	Weak	-
A11	AGAL339.026-0.401	Dark	Bright	Weak	-
A12	AGAL338.939-0.424	Green Fuzzy[a]	Point source	Weak	-
A13	AGAL338.867-0.479	Green Fuzzy[a]	Dark	Weak	-
A14	AGAL338.779-0.459	Green Fuzzy[a]	Dark	Weak	-
A15	AGAL338.751-0.466	Dark	Dark	Weak	-
A16	AGAL338.732-0.469	Dark	Dark	Weak	-
A17	AGAL338.616-0.441	Dark	Dark	Weak	-
A18	AGAL338.599-0.441	Green Fuzzy[a]	Point source	Weak	-
A19	AGAL338.582-0.442	Green Fuzzy[a]	Dark	Weak	-
A20	AGAL338.551-0.419	Green Fuzzy[a]	Point source	Weak	-
A21	AGAL338.506-0.419	Green Fuzzy[a]	Dark	Weak	-
A22	AGAL338.476-0.429	Green Fuzzy[a]	Dark	Weak	16396-4631
A23	AGAL338.452-0.426	Near bright 3.6-4.5 μm	Near emission	Weak	-
A24	AGAL338.422-0.409	Green Fuzzies[a]	Point source	Weak	-
A25	AGAL338.394-0.406	Green Fuzzies[a]	Point source	Bright	16390-4637
A26	AGAL338.327-0.409	Green Fuzzy[a]	Point source	Bright	-
A27	AGAL338.199-0.464	Dark	Dark	Weak	-
A28	AGAL338.182-0.464	Dark	Dark	Weak	-
A29	AGAL338.112-0.464	Dark	Dark	Weak	-
A30	AGAL338.089-0.447	Dark	Dark	Weak	-
A31	AGAL338.027-0.476	Bright 8 μm[c]	Bright	Weak	-
A32	AGAL338.011-0.494	Bright 8 μm[c]	Bright	Weak	-
A33	AGAL337.994-0.514	Bright 8 μm[c]	Bright	Weak	-
A34	AGAL337.974-0.519	Bright 8 μm[c]	Bright	Weak	-
A35	AGAL337.937-0.532	Bright 8 μm[c]	Bright	Bright	-
A36	AGAL337.909-0.541	Bright 8 μm[c]	Bright	Weak	-
A37	AGAL337.932-0.506	Bright 8 μm[c]	Bright	Bright	-
A38	AGAL337.916-0.477	Bright 8 μm[c]	Bright	Bright	-
A39	AGAL337.922-0.456	Bright 8 μm[c]	Bright	Bright	-
A40	AGAL337.934-0.419	Bright 8 μm[c]	Bright	Weak	-
A41	AGAL337.974-0.437	Bright 8 μm[c]	Bright	Weak	-

[a] Green fuzzy: Enhancement at 4.5 μm.

[b] Bright emission: Peak emission > 1 Jy/beam; weak emission: Peak < 1 Jy/beam

[c] This emission corresponds to the bubble observed to the right of the filament

TABLE 4.2: Parameters of the clumps in filament A, from their continuum and molecular emission.

ID	870 μm				350 μm				^{13}CO(3-2)					N_2H^+(3-2)			
	Peak Flux	Diameter		Int. Flux	Peak Flux	Diameter		Int. Flux	T_{peak}	v_{LSR}	Δv	II	Diameter	T_{peak}	v_{LSR}	Δv	τ
	Jy/Beam	’	pc	Jy	Jy/Beam	’	pc	Jy	km s^{-1}	km s^{-1}	K	K km s^{-1}	pc	km s^{-1}	km s^{-1}	K	
A1	0.68	0.5	0.4	7.79(0.15)													
A2	0.47	0.4	0.4	2.38(0.15)													
A3	0.33	0.2	0.2	0.52(0.15)													
A4	1.02	0.3	0.3	2.79(0.15)													
A5	0.41	0.3	0.3	1.66(0.15)													
A6	0.34	0.1	0.1	0.49(0.15)													
A7	0.30	0.2	0.2	0.54(0.15)													
A8	0.50	0.4	0.4	4.78(0.15)													
A9	0.32	0.2	0.2	0.49(0.15)													
A10	0.40	0.3	0.3	0.78(0.15)													
A11	0.37	0.2	0.2	0.87(0.15)													
A12	0.48	0.4	0.4	3.22(0.15)													
A13	0.66	0.4	0.4	3.95(0.15)													
A14	0.40	0.3	0.3	2.16(0.15)													
A15	0.27	0.1	0.1	0.35(0.15)													
A16	0.38	0.3	0.3	1.33(0.15)													
A17	0.31	0.7	0.6	0.83(0.36)	2.71	0.4	0.3	7.8 (4.3)						0.1	-38.99	1.35 (0.13)	3.79 (1.71)
A18	0.25	0.7	0.6	0.47(0.27)	2.88	0.5	0.4	11.7(4.3)									
A19	0.17	0.2	0.2	0.20(0.15)													
A20	0.38	0.8	0.7	0.99(0.37)	4.22	0.4	0.3	11.2(5.3)	4.96	-38.55	1.12(0.21)	5.95(1.11)	0.65	0.32	-38.51	0.97 (0.05)	13.1 (0.9)
A21	0.34	0.9	0.8	0.75(0.42)	5.06	0.5	0.4	14.8(5.0)	3.04	-38.15	1.25(0.51)	4.04(1.60)	0.43				
A22	0.31	0.8	0.7	0.68(0.33)	2.24	0.4	0.3	<1	3.79	-38.15	0.54(0.09)	2.17(0.34)	0.38	0.23	-40.56	0.26 (0.94)	-
														0.33	-37.71	1.21 (0.13)	-
														0.12	-35.94	0.26 (0.14)	-
A23	0.25	0.7	0.6	0.56(0.39)	5.22	0.5	0.4	17.7(6.1)-									
A24	0.82	1	0.9	2.85(0.51)	14.8	0.5	0.4	42.9(2.9)	2.91	-37.15	2.36(0.23)	7.32(0.71)	0.65				
A25	1.04	1	0.9	6.31(0.63)	14.9	0.6	0.5	64.9(8.1)	7.98	-37.15	1.25(0.16)	10.64(1.36)	1.22	0.95	-37.38	1.41 (0.08)	12.3(2.7)
A26	1.00	0.2	0.2	2.26(0.15)													
A27	0.52	0.2	0.2	1.37(0.15)													
A28	0.36	0.2	0.2	0.98(0.15)													
A29	0.42	0.3	0.3	2.24(0.15)													
A30	0.40	0.3	0.3	1.29(0.15)													
A31	0.44	0.2	0.2	0.67(0.15)													
A32	0.49	0.3	0.3	2.20(0.15)													
A33	0.53	0.4	0.4	4.00(0.15)													
A34	0.62	0.3	0.3	3.69(0.15)													
A35	1.07	0.2	0.2	3.61(0.15)													
A36	0.41	0.3	0.3	1.16(0.15)													
A37	3.74	0.6	0.5	21.7(0.15)													
A38	24.73	0.2	0.2	81.42(0.15)													
A39	7.40	0.5	0.4	77.12(0.15)													
A40	0.68	0.7	0.6	14.53(0.15)													
A41	0.54	0.4	0.4	3.06(0.15)													

Table 4.3: Filament A: Parameters derived from Gaussian fits to the MALT90 spectra

Source	Molecule	Δl[a]	Δb[a]	T_{peak}	V_{LSR}	Δv	II[b]	I_T[c]	*rms*
		"	"	K	km s^{-1}	km s^{-1}	K km s^{-1}	K km s^{-1}asec^2	K/channel
A24 AGAL338.422-0.409	N_2H^+	0	0	0.71	-37.42	2.23	2.64	1099	0.23
	HNC	0	7	0.72	-38.08	1.80	2.47	1377	0.23
A25 AGAL338.394-0.406	N_2H^+	0	0	0.95	-37.52	2.07	2.09	1680	0.23
	HCO^+	72	18	0.42	-40.44	2.07	0.92	22	0.23
	HNC	0	9	0.92	-37.16	1.83	1.79	295	0.23
A37 AGAL337.932-0.506	N_2H^+	0	0	2.13	-38.72	2.77	14.4	758	0.23
	HCO^+	14	4	0.36	-39.86	1.69	2.16	274	0.23
	HCN	14	14	0.59	-40.15	2.04	3.75	794	0.23
	HNC	14	4	1.01	-39.54	2.79	3.46	1957	0.23
	HC_3N	14	4	0.59	-38.74	1.62	2.42	753	0.23
	C2H	14	4	0.82	-38.8	2.18	2.86	1001	0.24
A38 AGAL337.916-0.477	N_2H^+	0	0	2.46	-39.21	2.23	12.32	1507	0.23
	HCO^+	18	6	1.81	-40.33	2.74	7.93	1256	0.23
	$H^{13}CO^+$	18	10	0.78	-39.60	1.64	3.44	1673	0.23
	^{13}CS	18	18	0.74	-38.58	2.15	4.01	200	0.23
	HCN	18	6	1.37	-40.17	2.77	11.9	1365	0.24
	HNC	7	7	2.83	-40.22	2.6	11.92	1197	0.23
	HC_3N	18	0	0.96	-40.36	1.22	5.41	1986	0.24
	C_2H	7	7	0.90	-39.26	2.73	4.53	1399	0.24
A39 AGAL337.922-0.456	N_2H^+	0	0	3.67	-40.10	2.46	22.34	428	0.23
	HCO^+	3	7	2.86	-40.86	1.65	9.16	412	0.23
	HCN	3	18	2.8	-39.92	1.76	13.2	550	0.24
	HNC	3	15	3.58	-39.88	1.90	1.83	647	0.23
	HC_3N	3	18	1.00	-41.04	1.22	4.07	690	0.24
	C_2H	14	7	1.06	-40.04	1.97	4.65	686	0.23

[a] Offset of the peak emission from the N_2H^+(1-0)peak.

[b] Integrated intensity

[c] Total integrated intensity

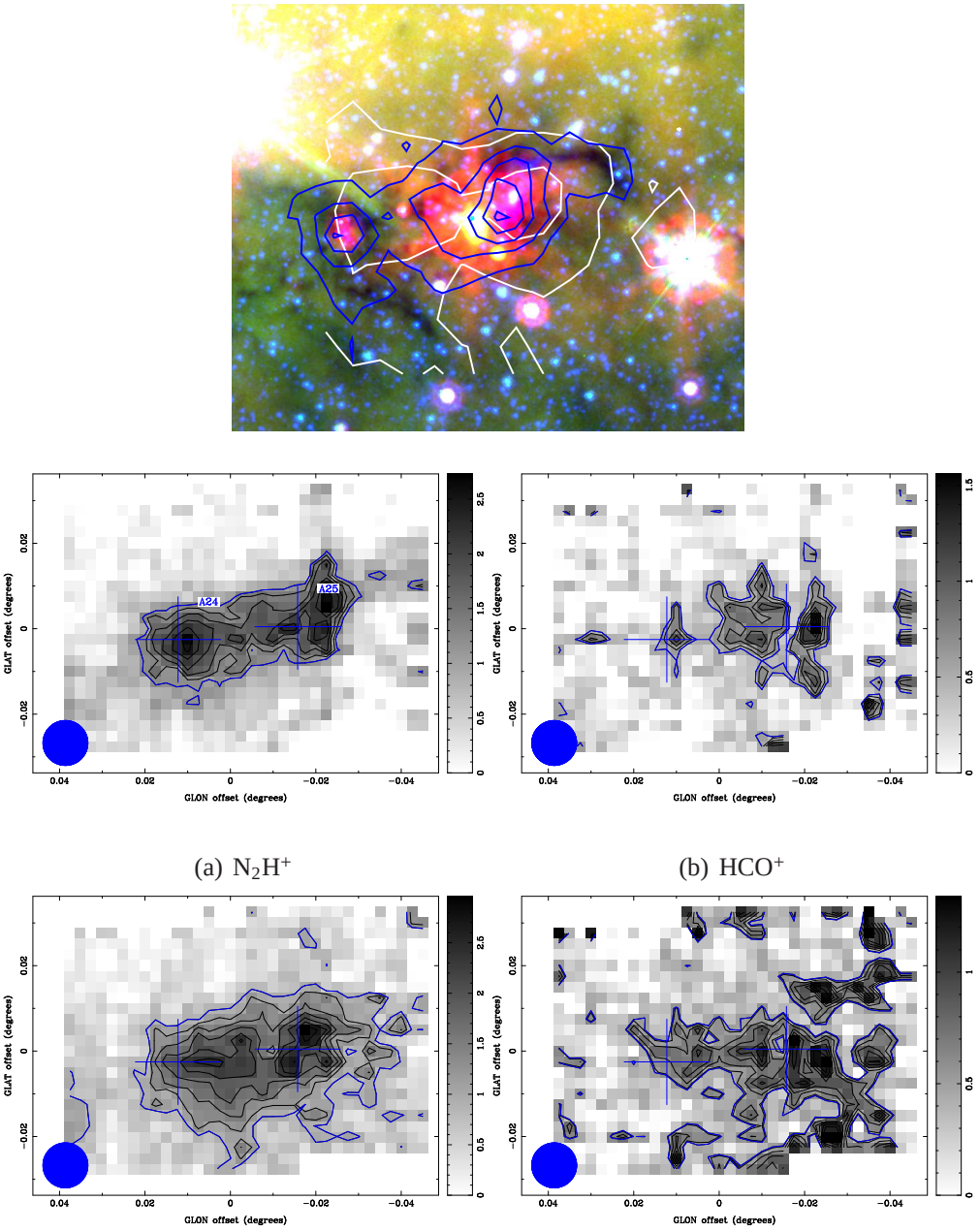

(a) N_2H^+ (b) HCO^+

(c) HNC (d) HCN

FIGURE 4.9: Integrated intensity maps toward clumps A24 and A25. Top panel: IRAC three color image of the region covered by the MALT90 data (Red: 24 μm, blue: 8 μm, green: 4.5 μm), blue contours show the emission at 870 μm, while the white contours N_2H^+(1-0) emission. Panels (a)- (d): Maps of integrated intensity of the detected molecular line transitions (II > 3σ). Contours represent the emission from 90% of the peak to 3σ noise emission (blue contour) in steps of 10%. The crosses indicate the positions of the clumps and the blue circle shows the beam size. The color bar shows the value of the peak in the integrated intensity for each molecular line.

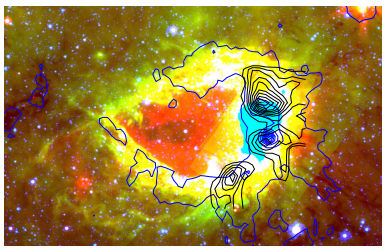

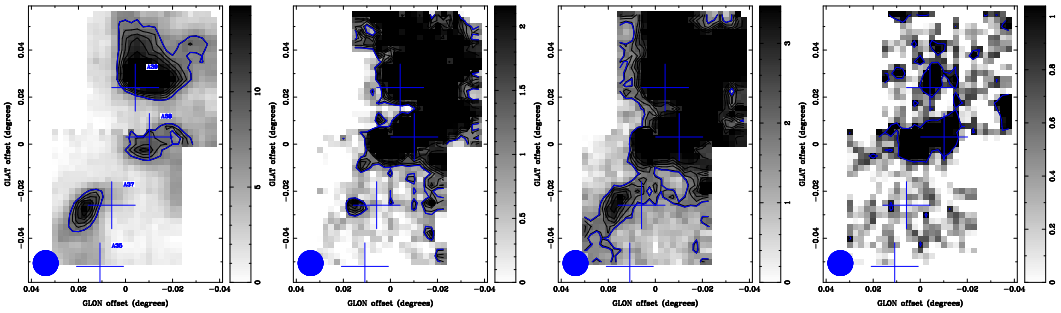

(a) N_2H^+ (b) HCO^+ (c) HNC (d) ^{13}CS

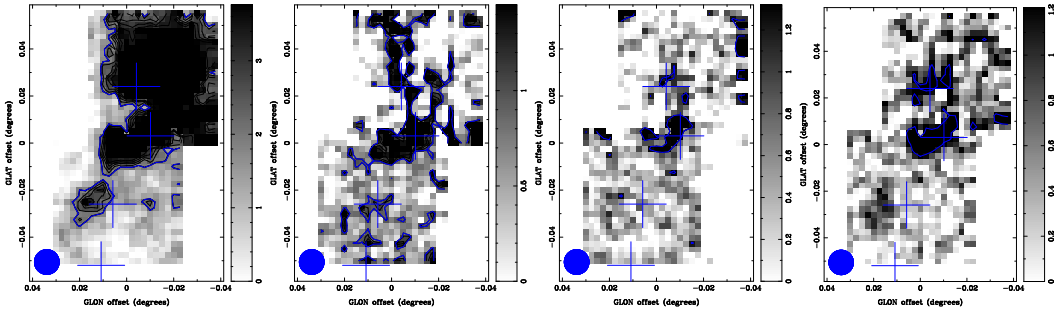

(e) HCN (f) $H^{13}CO^+$ (g) CH_3CN (h) SiO

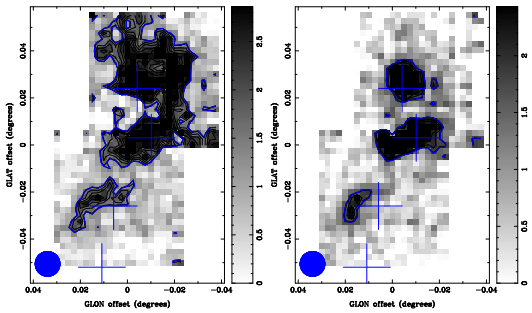

(i) C_2H (j) HC_3CN

FIGURE 4.10: Integrated intensity maps toward clumps A35, A37, A38 and A39. Upper panel: Color image of the region covered by the MALT90 observation toward clump A37 (Red: 24 μm, blue: 8 μm, green: 4.5 μm) blue contours emission at 870 μm, black contours N_2H^+(1-0)emission. Panels (a)-(k) : Maps of integrated intensity of the detected molecular line transitions. Contours represent the emission from 90% of the peak to 3σ noise emission (blue contour) in steps of 10%. The cross shows the position of the clumps and the blue circle shows the beam size. The color bar shows the value of the peak at each molecule.

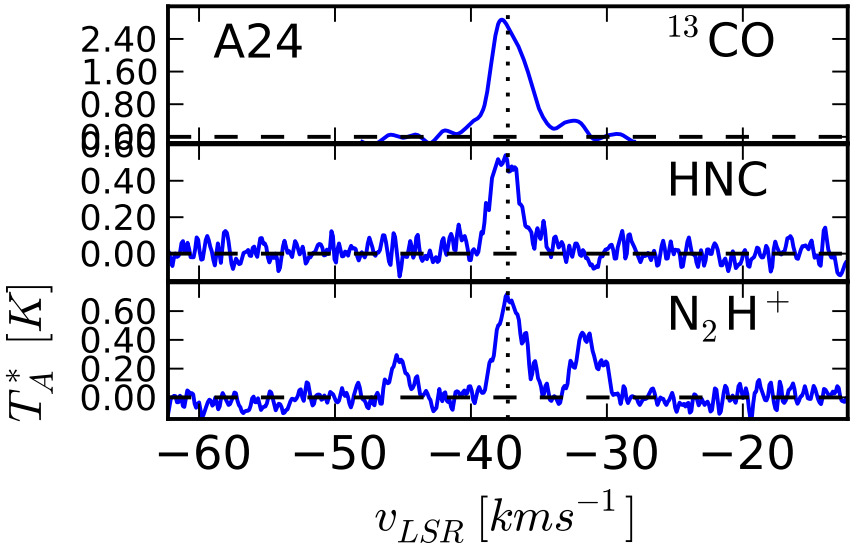

FIGURE 4.11: Spectra toward clump A24. Each spectrum are at the (l,v) position corresponding to the peak emission at N_2H^+. Dotted line shows the central velocity of the N_2H^+(1-0) emission.

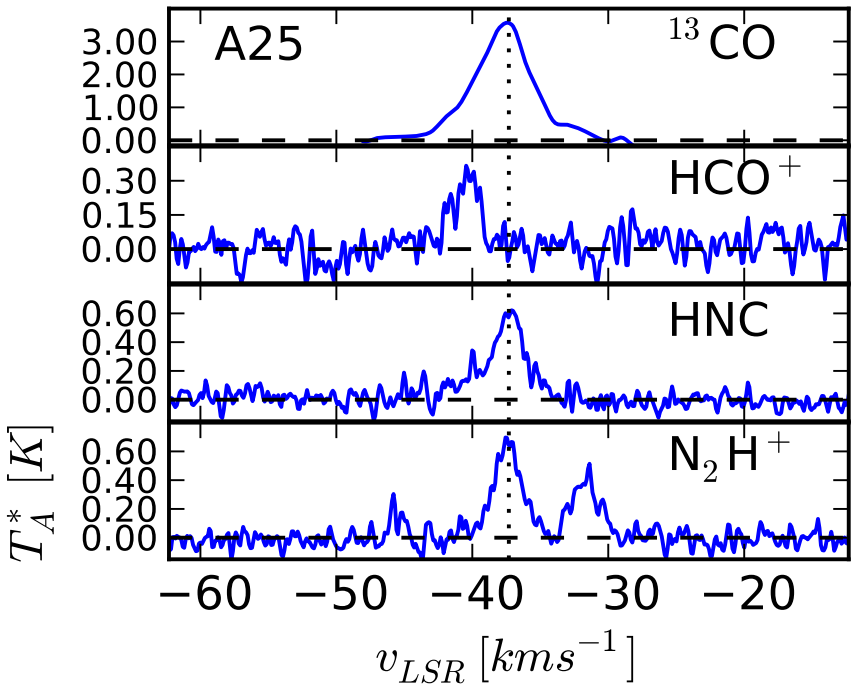

FIGURE 4.12: Spectra toward clump A25. Each spectrum are at the (l,v) position corresponding to the peak emission at N_2H^+. Dotted line shows the central velocity of the N_2H^+(1-0) emission. We can observe asymmetric profiles at ^{13}CO(3-2) and HCO^+.

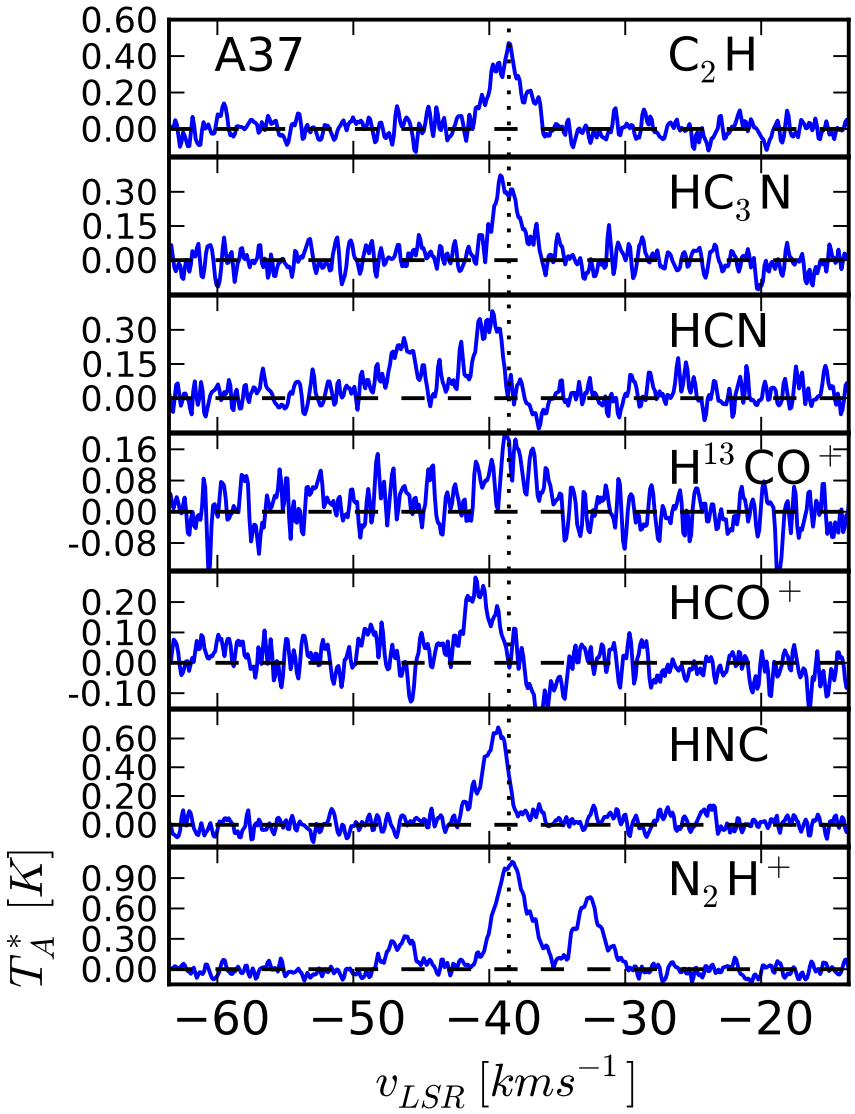

FIGURE 4.13: Spectra toward clump A37. Each spectrum are at the (l,v) position corresponding to the peak emission at N_2H^+. Dotted line shows the central velocity of the N_2H^+(1-0) emission. We see in this plot the asymmetry in the HCO^+, HCN, HC_3CN and HNCprofiles.

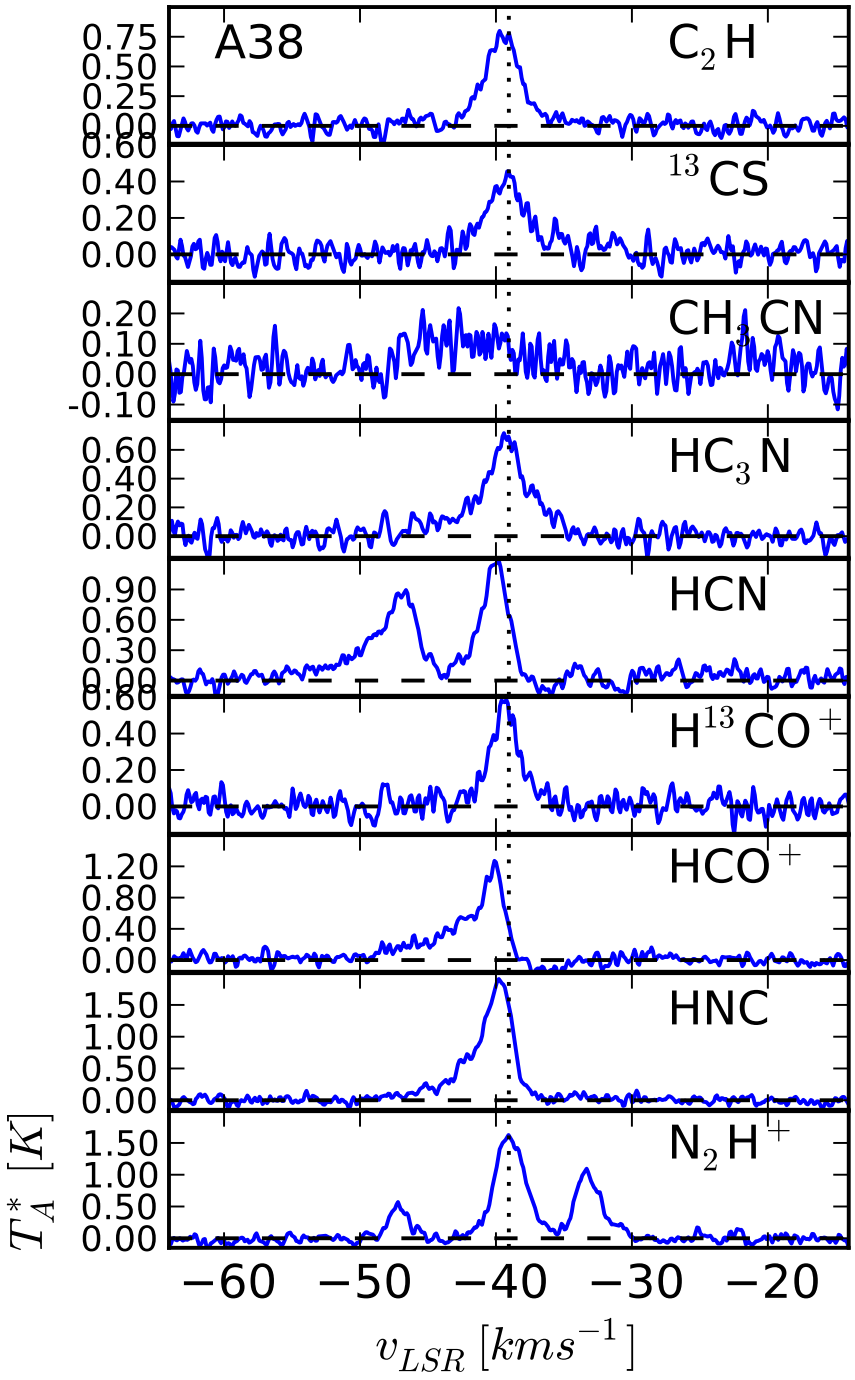

FIGURE 4.14: Spectra toward clump A38. Each spectrum are at the (l,v) position corresponding to the peak emission at N_2H^+. Dotted line shows the central velocity of the N_2H^+(1-0) emission.

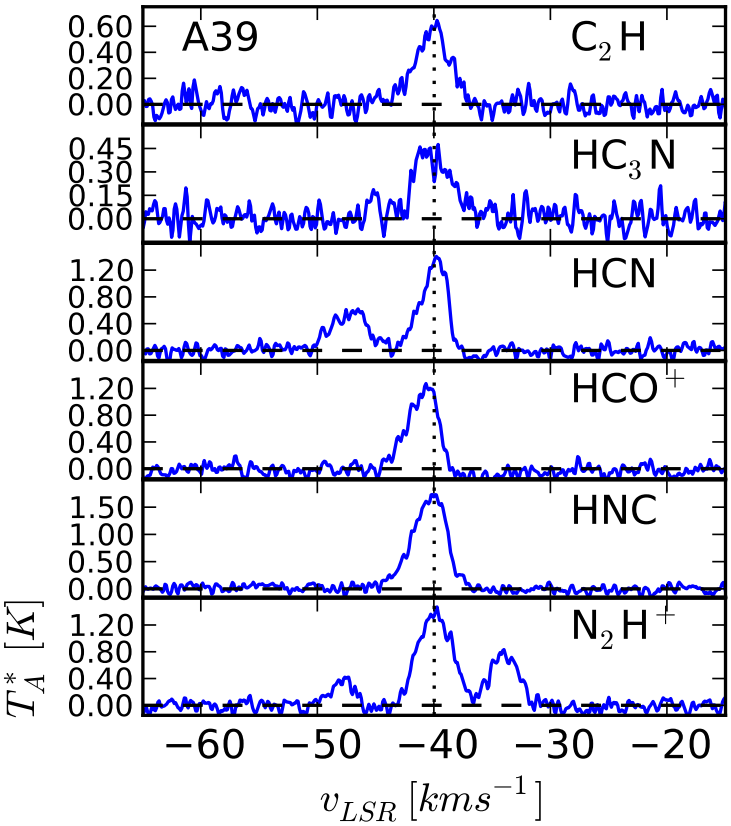

FIGURE 4.15: Spectra toward clump A39. Each spectrum are at the (l,v) position corresponding to the peak emission at N_2H^+. Dotted line shows the central velocity of the N_2H^+(1-0) emission.

4.5 Physical properties

In this section we combine the continuum and molecular line observations to derive the physical properties of filament A, such as temperature, density profile, mass and pressure, for both the filament and the embedded clumps.

4.5.1 Color temperature

We calculate the *color temperature* of this filament from the 870 μm and 350 μm continuum data using Equation 1.30. Since the beam size at 350 μm is smaller that the one at 870 μm we smoothed the 350 μm images to match the beam of the 870 μm data (18"). The color temperature, using these wavelengths, is only valid toward the regions of the filament that have cold temperatures (<20 K). Since the majority of this filament appears as an infrared dark cloud with little evidence of star formation, its dust temperature should probably be low. Thus, the temperature obtained with this method is probably a good approximation to the temperature within this filament.

The color temperature obtained via this method relies on the knowledge of the emission spectral index, β. Since β is not know we calculated the color temperature using four different values for β: 1, 1.5, 2 and 2.5. The maps of color temperatures using these four values for β are shown in Figure 4.16. We found that the derived color temperature for this filament has an average values that ranges from 18 K to 9 K, using a value of β between 1 and 2.5.

For the clumps we find, assuming a spectral index of $\beta = 1.5$, that the average value for the derived color temperature ranges between 18 K and 40 K. For clumps A18 and A22 the 350 μm continuum emission is noisy, therefore, the derived color temperature in these clumps might not be a good estimation to the actual temperature. For this reason we will assume a dust temperature based on other properties of these clumps. Clump A18 shows green fuzzies in the GLIMPSE images and a point source emission at 24 μm, indicating that the dust is presumably heated from an embedded protostar. This mid infrared emission is indicative of star formation activity, therefore, we will assume a dust temperature of ~35 K which is representative of temperatures observed toward clumps with similar star formation tracers (Rathborne et al. 2010). Based on the presence of green fuzzies and the absence of both emission at 24 μm and molecular lines representatives of hot clump chemistry, for clump A22 we assume a temperature of ~30 K, which corresponds to the temperature observed towards cores with similar characteristics at infrared wavelengths (Rathborne et al. 2010).

For the remaining clumps, located outside the region covered by the 350 μm emission, we

assumed a temperature based on their emission at infrared, dividing the clumps into three categories: Clumps with no emission at infrared wavelengths (Dark in GLIMPSE and MIPSGAL), for which we assume a temperature of 20 K; Clumps with either a green fuzzies or a 24 μm point source emission, for which we assume a temperature of 30 K; and clumps with both emission at GLIMPSE wavelengths and 24 μm emission, for which we assumed a temperature of 35 K. Table 4.5 summarize the derived and assumed color temperature for each clump.

4.5.2 Column density and mass

In this section we describe how we determined the column density and mass of filament A. From the continuum emission at 870 μm we obtained the column density, from which we calculated the total and lineal mass of the filament and the masses for each clump. From the ^{13}CO(3-2) molecular line emission we calculated the virial mass and lineal virial mass.

4.5.2.1 Column density and total mass of the filament

The radial column density was computed from the dust thermal continuum emission at 870 μm using equation 1.28. In this calculation we used the color temperatures profile obtained with a spectral index $\beta = 1.5$ (see Section 4.5.1) and a dust opacity coefficient $k_{870} = 0.012$ cm^{2}gr^{-1}. From the derived value of the radial column density along filament A we compute the total mass of this filament by integrating the radial column density over the diameter and length of the filament. The mean column density obtained is 2×10^{22} cm^{-2} reaching values of 10^{23} cm^{-2} toward the clumps while the total mass derived for filament A was found to be 3.4×10^4 M$_\odot$.

The virial mass is obtained from the ^{13}CO(3-2) molecular line emission. Unfortunately, because the coverage of the observation only covers the central part of filament A, we only have information of the virial mass in this part of the filament. Because of the filamentary shape of this molecular cloud, the virial mass was computed at each point of the filament using Equation 1.6. Then, to calculate the total virial mass we integrated the values for the virial mass along the filament obtaining a total virial mass of 4×10^3 M$_\odot$. The total dust mass along this part of the filament is 2×10^3 M$_\odot$.

4.5.2.2 Mass of the clumps

From the observations of the 870 μm continuum and ^{13}CO(3-2) molecular line emission toward the clumps embedded in this filament, we computed their total and virial masses. To compute the mass from the dust continuum emission we used the color temperature derived (or assumed) and a

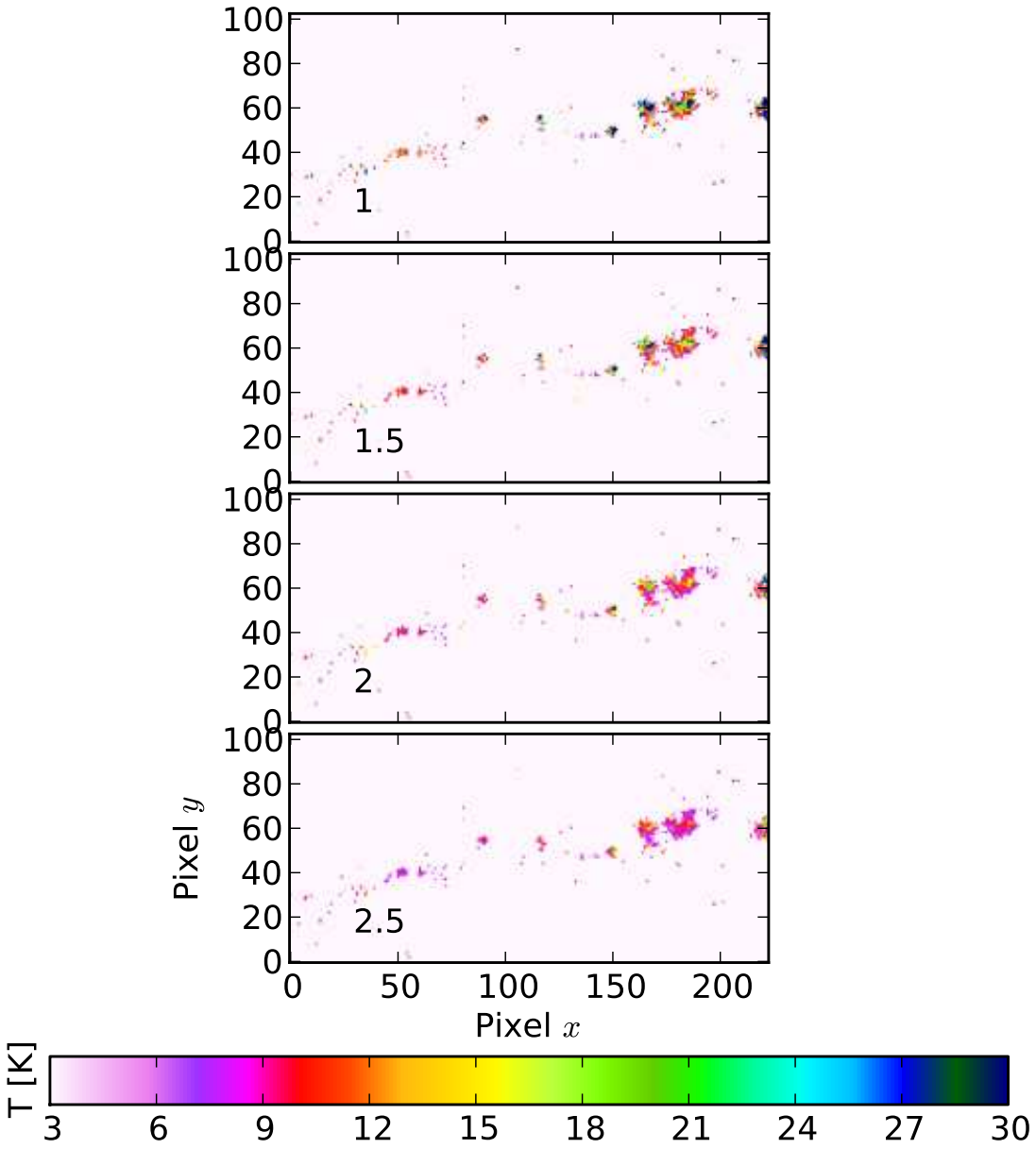

FIGURE 4.16: Derived color temperature for filament A. The panels show the color temperatures obtained by assuming different values of the emission spectral index, β. Note that overall the filament have a similar temperature, while in the clumps we observe localized regions with slightly higher temperatures.

dust opacity coefficient k_{870} = 0.012 cm^{2}gr^{-1}. The mass derived for the clumps range from ~40 to ~3000 $M_\odot$, with mean value of ~200 $M_\odot$.

For each clump with observations in the ^{13}CO(3-2) line, we calculated the virial mass from the average emission > 3σ enclosing the clumps. In all the clumps we assumed that they have a spherical shape and are in virial equilibrium. Clumps A20, A21, A22, A24 and A25 have a virial masses of 101 $M_\odot$, 83 $M_\odot$, 14 $M_\odot$, 452 $M_\odot$ and 238 $M_\odot$ respectively.

Using the opacity, excitation temperature and line widths derived from the fit to the hyperfine components observed in the N_2H^+(1-0) emission, we derived the mass of the clumps observed in MALT90. The masses were obtained using equation 1.4.3.3. The values of the mass obtained for these clumps are summarized in Table 4.5.

The ratio between the mass obtained from the dust emission, m, and virial mass, m_{vir}, ranges between 0.3 and 4 for the clumps observed in ^{13}CO(3-2). A ratio ~ 1 suggests that there is virial equilibrium for a clump and if their are gravitationally bound, which is observed toward clumps A20, A21 and A25. Clump A24 have a virial mass higher than it *dust mass* and clumps A22 have a virial mass much lower that its *dust mass* implying that these clumps are not in virial equilibrium. Table 4.5 summarizes the dust masses and virial masses obtained for the clumps.

4.5.2.3 Lineal mass along the filament

The lineal mass was computed by integrating the observed radial column density over the diameter of the filament, at each point along the filament. We used the temperatures previously computed, which have a varying temperature increasing locally toward the clumps. The lineal masses obtained from this method have a mean value of 142 $M_\odot$. The lineal mass distribution is shown in Figure 4.17.

To calculate the ”lineal virial mass” we averaged the molecular line emission over the diameter of the filament and perform an automatic Gaussian fit to the averaged spectra obtained. From this fit we obtained the central velocity, antenna temperature and linewidth at each point along the path of the filament. We then use Equation 1.6 to compute the lineal virial mass using the values found for the linewidth at each point. For this filament we found a mean value of 260 $M_\odot$, the lineal virial mass distribution along the filament is show in Figure 4.17. In this figure it is also shown the lineal mass distribution derived from the dust continuum emission, we see that the virial mass is higher than the dust mass on the region were the emission overlap.

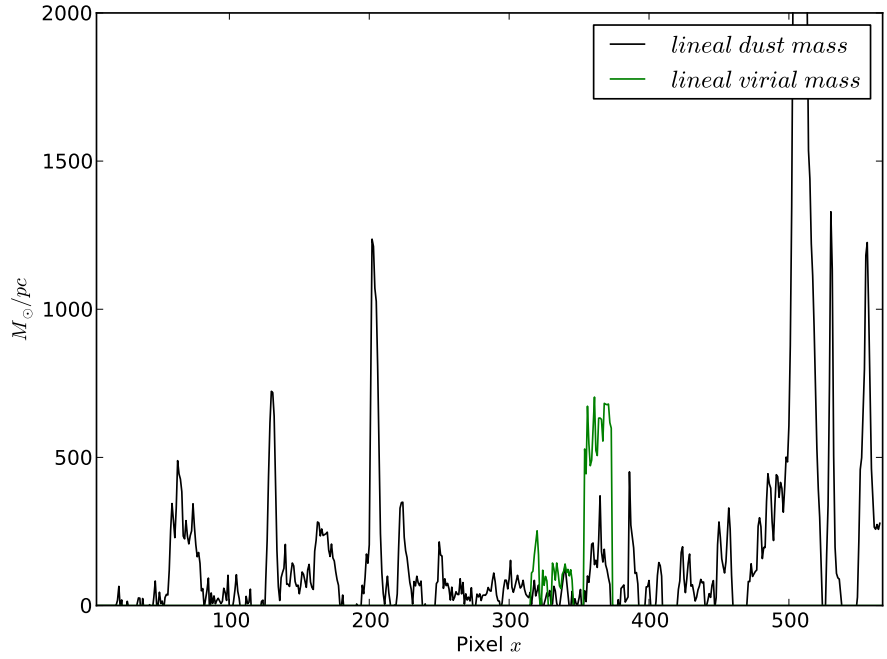

FIGURE 4.17: Lineal dust and virial mass distribution along the filament. Green, lineal virial mass; black, lineal dust mass from 870μmobservations. Maximum in 1.2×10^3 $M_\odot$, which is out of the scale of this plot

4.5.3 External and internal pressure

To calculate the internal and surface pressure we consider the region of the filament were we have ^{13}CO(3-2) molecular line observations. The external pressure (Fiege and Pudritz 2000):

$$\langle P \rangle = \langle \sigma^2 \rangle \langle \rho \rangle, \tag{4.1}$$

was computed from the mean density obtained from the dust continuum emission and the velocity dispersion obtained from the ^{13}CO(3-2) molecular line emission. The velocity dispersion was computed from the linewidth observed toward regions that were clearly outside the boundaries of the filament. The average value for the velocity dispersion is 1.12 km s^{-1}. The mean density was computed from the region outside the filament, obtaining a average value of $\langle \rho \rangle = 1 \times 10^{-21}$ gr cm^{-3}. From these values we estimate an external pressure on this filament of $P_s/k = 10^5$ K cm^{-3}.

The internal pressure was computed using the ^{13}CO(3-2) line width and the density obtained for each point along the filament, using Equation 4.1. The density at each point of the filament

was obtained by dividing the lineal mass over the volume per unit length (see Section 1.4.2.2), the mean lineal density was found to be 4.6×10^{-20} gr cm^{-3}. The average velocity dispersion is $\langle\sigma\rangle = 0.75$ km s^{-1}. Thus, the mean internal pressure in the filament is $\langle P\rangle/k = 4.5 \times 10^5$ K cm^{-3}, with k the Boltzmann constant. Along the filament's path the internal pressure ranges from $\langle P\rangle/k = 10^5$ to 10^7 K cm^{-3}.

4.6 Stability of the filament: magnetic field support

In this section we compare the properties derived for filament A with prediction from theories that describe the stability of filamentary molecular clouds, in particular whether the existence of a magnetic field contributes to their overall support. The presence of a magnetic field is analyzed by two methods: its influence over the radial column density profile and by a virial equilibrium analysis.

4.6.1 Radial density profile analysis

In this section we analyze how the presence of a magnetic field can be inferred by analyzing the profile of the radial intensity of the emission observed at 870 μm. The radial intensity emission was fitted assuming a column density profile given by:

$$\Sigma_\rho(r) = A_p \frac{\rho_c R_{flat}}{[1 + (r/R_{flat})^2]^{\frac{p-1}{2}}}. \tag{4.2}$$

The fit was done at each point along the filament. For the fit we use as free parameters: the central density, ρ_c, the inner flat region, R_{flat}, and the parameter p. The parameter p represents the shape of the column density profile, which gives an indirect measurement of the magnetic field support over the filament. For a pure gravitationally bounded filament, without a magnetic field, the radial column density is best fitted by a profile with $p = 4$ (Ostriker 1964). If the radial column density is best fit by a profile with $p < 3$ then, as shown by Fiege and Pudritz (2000), the filament likely has a magnetic field to support it.

To compare our observations to these models, we first divided the filament into two groups: a group containing the *clumps* and group containing the *inter-clump* material. Since the shape of the filament's radial intensity is only characterized by the value of p, we averaged and normalized the radial intensity for each group. Thus, we obtained for both the clumps and inter-clump material a mean value for the radial intensity from the 870 μm emission.

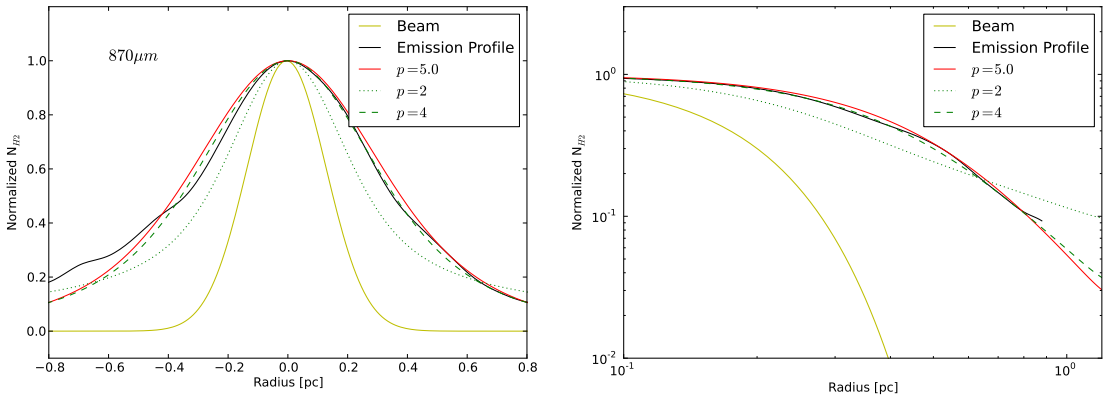

FIGURE 4.18: Density profile of the normalized mean density of the clumps in filament A obtained from the 870 μm emission. The left panel shows lineal plot of the profiles and the right panel the profiles in logarithmic scales. The red solid lines represents the best fit to the density profile, the beam profile is shown with the solid yellow line, the hydrostatic solution p=4 (green dashed line) and magnetized solution p=2 (green dotted line) are also shown. We can see that in general the shape of the radial density follows the shape of a profile with $p = 4$.

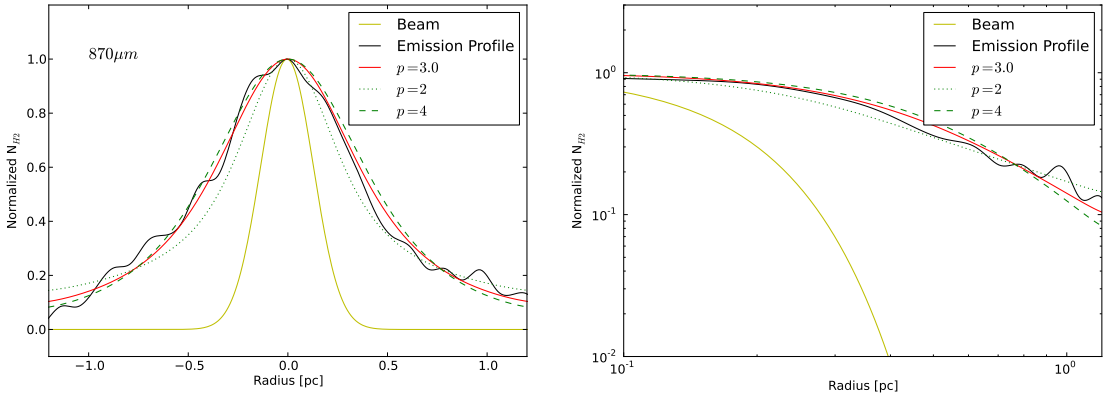

FIGURE 4.19: Density profile of the normalized mean radial density of the inter-clump region in filament A. The left panels show lineal plot of the profiles obtained from the 870 μm emission and right panels shown the profiles in logarithmic scales. The beam profile is shown with the solid yellow line, the hydrostatic solution (green dashed line) and magnetized solution (green dotted line) are also shown. We can see that the shape of the radial density differs from the observed at the clump looking more similar to a solution with $p \sim 2$.

For the clumps, we found that the radial intensity at 870 μm has a profile that is best fit by a column density profile with $p = 5$ (Figure 4.18). This implies that for the clumps their stability can be explained by hydrostatic equilibrium only, without the need for a magnetic field to support them. For the inter-clump material the 870 μm emission is very weak, thus, the mean normalized

radial intensity profile is not very well defined. The wings of the column density profile are more prominent and the best fit is given by a profile with $p = 3$ (Figure 4.19). This suggests that a magnetic field is needed to explain the stability of the inter-clump material.

To determine how the shape of the column density, and hence p, changes along the filament we performed a fit to the radial intensity at each point along the filament. This fit was performed using a χ^2 minimization between the observed column density and the model given by Equation 4.2. This fitting was only obtained for regions along the filament where the emission at 870 μm had a signal to noise higher than 3σ. The values of p obtained from a fit with $\chi^2 < 2$ are shown in Figure 4.20. In this plot the black dots correspond to the fits made to the inter-clump material and the red dots correspond to the fits made to the clumps, error bars shows the χ^2 value from these fits. We have found that for the inter-clump material the values of p range between 1 and 2.5. For the clumps (red dots) the fit gives values of p that typically range between 2.5 and 4.5. Most of the points have a value of $p < 4$ implying that, in general, the shape of the density profile is best fit by a model that includes magnetic field support.

These results show that for the filament, a non magnetized model cannot explain the shape observed in the column density profile and nor describe its stability. However, the mean values of the column density for the clumps and inter-clump material suggest that while the clumps stability can be described by hydrostatic equilibrium the inter-clump material cannot. Thus, it appears that the filament requires the presence of a magnetic field to further support it (against expansion or collapse).

4.6.2 Virial equilibrium analysis

We now analyze the stability of filament A by studying the relationship between their lineal mass, lineal virial mass, internal pressure, external pressure, gravitational energy and magnetic field. We followed the work of Fiege and Pudritz (2000) which uses an extended version of the virial equilibrium equation for filamentary molecular clouds that includes magnetic field support.

Equation 1.4 was used to describe the relationship between the masses of the filament (from dust and virial), its internal and external pressure and the presence of a magnetic field. A plot (Figure 4.21) was made using lines of constant values of the ratio between the total magnetic energy per unit length, $\mathcal{M}$, and lineal gravitational energy, $|\mathcal{W}|$. In the models the total magnetic energy can be positive or negative depending of the shape of the magnetic field that supports the filament. In the plot the region delimited by negative values of $\mathcal{M}/|\mathcal{W}|$ implies that a toroidal dominated magnetic field is needed to support the filament against expansion while positive values of $\mathcal{M}/|\mathcal{W}|$ implies the need of a poloidal dominated magnetic field to avoid the gravitational collapse of the filament.

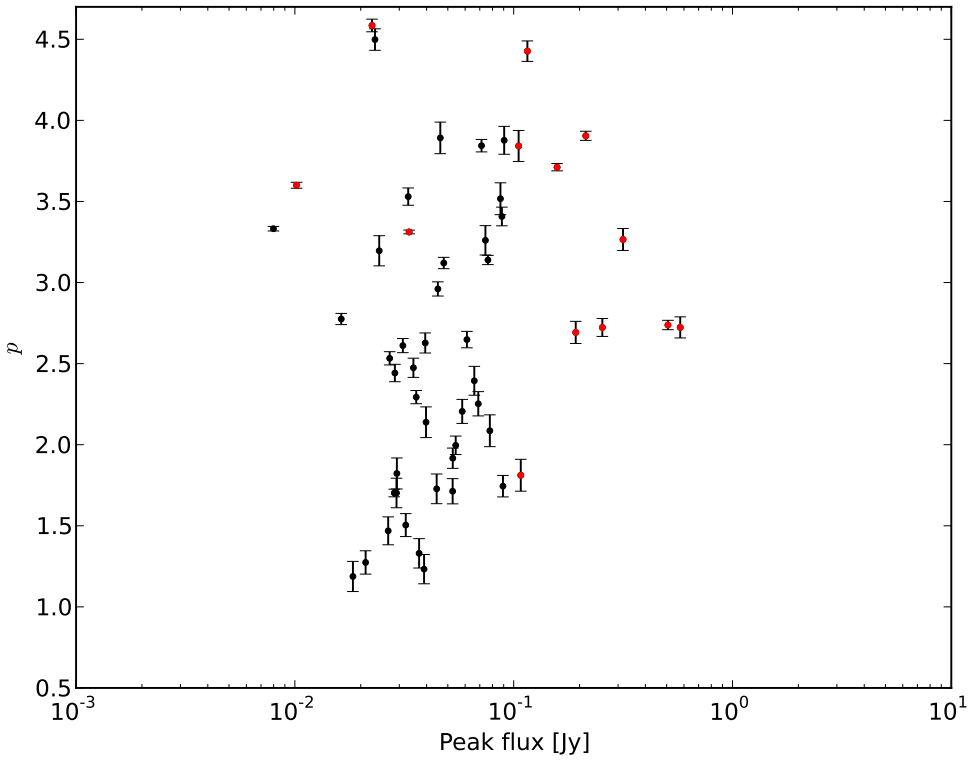

FIGURE 4.20: Plot of p, the parameter that defines the shape of the density profile, vs peak flux for the clump (red point) and inter-clump (black points) material. The error bars show the χ^2 between the fit and the observed radial density. We can see that, in general, the inter-clump material have values of p lower than the clumps, suggesting that they need a magnetic field as support.

A value of $\mathcal{M}/|\mathcal{W}| = 0$ represents the non magnetic solution for virial equilibrium.

In this plot the average value of the ratio between the lineal dust mass and lineal virial mass,m/m_{vir}, and the ratio between the mean internal pressure and surface pressure, $\langle P\rangle/P_s$, are 0.75 and 0.05 respectively, which gives $\mathcal{M}/|\mathcal{W}|$=-0.25. This suggests that the existence of a toroidal dominated magnetic field is needed to prevent the filament from expansion (Figure 4.21). The clumps have typical values of $\langle P\rangle/P_s$=0.004 and m/m_{vir}=0.24, implying $\mathcal{M}/|\mathcal{W}|$=-3.0. This corresponds to the region of this plot indicating that a toroidal dominated magnetic field is needed. For the inter-clump region $\langle P\rangle/P_s$=0.18 and m/m_{vir}=0.05 giving $\mathcal{M}/|\mathcal{W}|$=-13.4 also corresponding to the toroidal part.

The virial equilibrium analysis suggests that if we treat this filament as a whole coherent structure, its stability can be explained by the presence of a toroidal magnetic field that prevents the

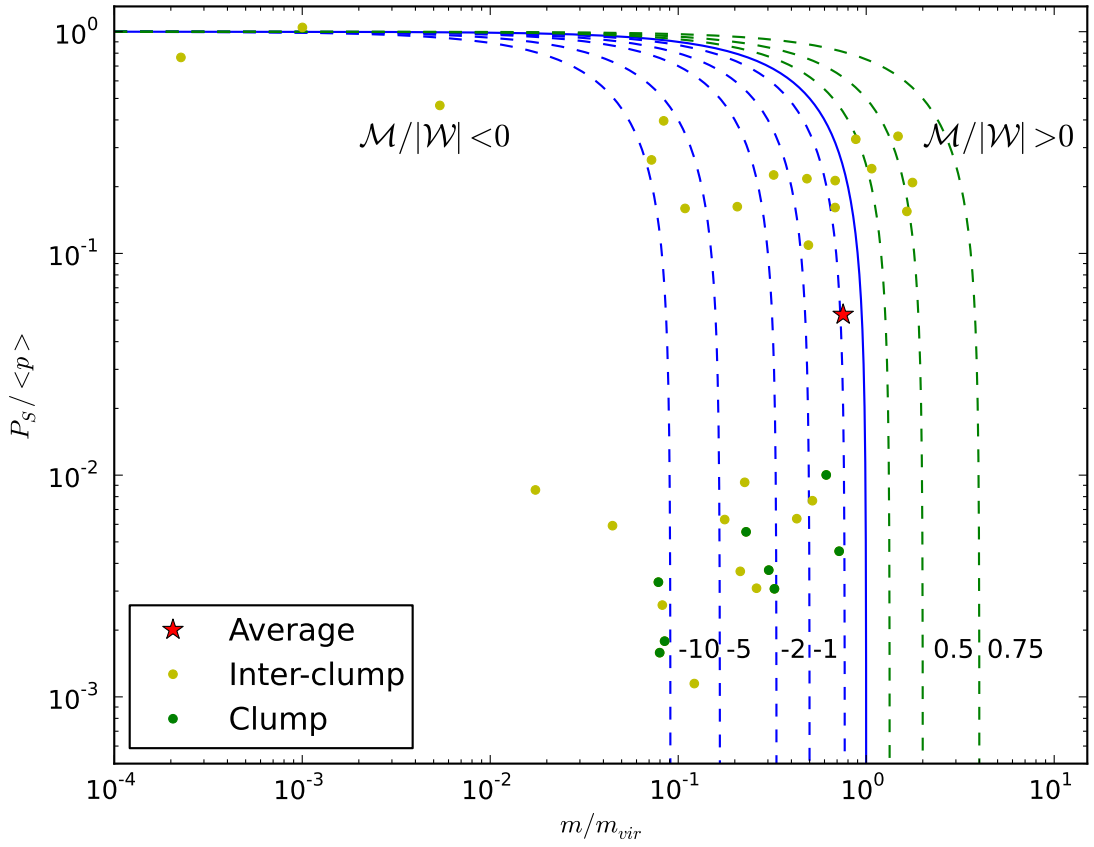

FIGURE 4.21: Plot of the $\langle P \rangle / P_s$ vs m/m_{vir} for the clumps and inter-clumps material for filament A. Blue dashed lines: toroidal magnetic fields, blue solid line: unmagnetized solution, green dashed lines: poloidal magnetic field. Yellow dots: values found for the inter-clump material; black dots: values found for the clumps and the red star: average value for the entire filament.

filament from expansion. However this analysis corresponds only to a small fraction of the filament, therefore, to obtain a more reliable result it would be necessary to extend this analysis to the full extent of the filament. Nevertheless this result is consistent with the analysis of the radial intensity emission, suggesting that the filament needs a magnetic support.

4.7 Fragmentation

In this section we discuss the fragmentation of the filament. To do this we assume that the filament is a cylinder and analyze the fragmentation due to fluid, or *"sausage"*, instabilities in a self-gravitating

cylinder. This instability produces several clumps (or over densities) with a spacing given by the wavelength of the fastest growing unstable mode of fluid instability (Jackson et al. 2010). The spacing between the clumps depends whether the filament is treated as an incompressible fluid (Chandrasekhar and Fermi 1953) or as an isothermal gas cylinder.

For Nessie, we find that the typical clump radius is 0.44 pc. Based on the location of the clumps we derived a mean separation between them of ∼2.3 pc. Treating Nessie as an incompressible fluid, the separation between the clumps is expected to be $\lambda_{max} = 11 * 0.44\ pc = 4.8\ pc$. This value is greater than the observed separation of the clumps within Nessie.

Treating Nessie as a isothermal cylinder, then the expected separation will depend on its scale of heigh. The average ^{13}CO(3-2) line width along the filament is ~ 1.3 km s^{-1}. Based on the observations at 870 μm, we derived a central density of 2.5×10^{-19} gr cm^{-3}, similar to the value assumed by Jackson et al. (2010). Using these values, we find a scale of heigh of $H \sim 0.09$. Since the radius $R \gg H$, the expected spacing between the clumps is given by: $\lambda_{max} = 22H$ =∼2 pc. This is similar to the average spacing of 2.3 pc found for the filament.

Jackson et al. (2010) using HNC(1-0) emission found that the spacing between the clumps in also similar to the expected spacing for an infinite isothermal cylinder, however the separation observed at this emission is larger matching the clumps with 24 μm point source emission. We found that the separation observed at ^{13}CO(3-2) matches well the separation between the cores observed at 870 μm . Since, the continuum emission not only takes into account the clumps with emission at 24 μm but all the clumps regarding their evolutionary stage, this makes ^{13}CO(3-2) a better molecular transition to study the fragmentation scale in filaments.

TABLE 4.4: Filament A: derived properties of the filament.

Distance	**Length**	**Radius**	**N cores**	**Δv**	**Temperature**	**Total mass**			**Lineal mass**			**P_s/k**	**$\langle P \rangle/k$**
				^{13}CO		**m**	**m_{vir}**	**m/m_{vir}**	**m**	**m_{vir}**	**m/m_{vir}**		
pc	pc	pc		km s^{-1}	K	$M_\odot$	$M_\odot$		$M_\odot$	$M_\odot$		10^4 K cm^{-3}	10^4 K cm^{-3}
3020	80	0.44	8	1.76	15	33600	4000	–	262	447	1.71	10	188

TABLE 4.5: Filament A, properties of the clumps

	Temperature		m_{dust}	m_{vir}	m_{N2H+}	m_{dust}/m_{vir}	Spacing
	Color	Assumed					
	K		$M_\odot$	$M_\odot$	$M_\odot$		pc
A1	-	35	110	-	-	-	2.09
A2	-	20	163	-	-	-	5.56
A3	-	20	114	-	-	-	4.43
A4	-	40	140	-	-	-	3.04
A5	-	40	56	-	-	-	1.26
A6	-	40	47	-	-	-	0.63
A7	-	40	41	-	-	-	1.57
A8	-	30	99	-	-	-	0.93
A9	-	30	63	-	-	-	0.87
A10	-	40	55	-	-	-	0.60
A11	-	30	73	-	-	-	4.24
A12	-	35	78	-	-	-	4.75
A13	-	30	130	-	-	-	4.66
A14	-	30	79	-	-	-	1.50
A15	-	20	93	-	-	-	1.06
A16	-	20	131	-	-	-	6.03
A17	18	-	126	-	-	-	1.02
A18	-	35	40	-	-	-	0.89
A19	-	30	33	-	-	-	2.01
A20	20	-	130	101	-	1.3	2.37
A21	20	-	118	83	-	1.4	1.84
A22	-	30	61	14	-	4.3	0.95
A23	25	-	63	-	-	-	1.54
A24	40	-	113	452	-	0.3	1.60
A25	28	-	225	238	352	0.9	3.44
A26	-	35	162	-	-	-	7.23
A27	-	20	180	-	-	-	0.72
A28	-	20	124	-	-	-	3.67
A29	-	20	145	-	-	-	1.64
A30	-	20	138	-	-	-	3.05
A31	-	40	60	-	-	-	1.51
A32	-	40	67	-	-	-	1.21
A33	-	40	73	-	-	-	0.98
A34	-	40	85	-	-	-	1.81
A35	-	40	147	-	-	-	1.67
A36	-	40	56	-	-	-	2.19
A37	-	40	516	-	-	-	1.84
A38	-	40	3400	-	1079	-	1.16
A39	-	40	1020	-	-	-	2.24
A40	-	40	93	-	-	-	1.64
A41	-	40	74	-	-	-	-

[a] Distance to the nearest core along the filament

[b] Lineal values

5

Filament B: AGAL337.406-0.402

Filament B, AGAL337.406-0.402, was identified from ATLASGAL images and extend more than 26' in the dust continuum images. Figure 5.1 panels (a) and (b) shows *Spitzer*/GLIMPSE and MIPSGAL images respectively. These images show that the majority of the filament is infrared dark, only presenting considerable infrared emission toward one side of it. There are clearly localized regions of star formation occurring along its length, identified via bright green fuzzies (enhancement at 4.5 μm), bright extended 8 μm emission and 24 μm point sources. Because these are tracers of star formation, these regions clearly already contains embedded protostars. Thus, this filament contains both cold pre-stellar clumps and those that are more evolved and associated with HII regions.

Figure 5.1 panels (c) and (d) show the dust continuum emission, observed with LABOCA at 870 μm and SABOCA at 350 μm respectively. We see that the continuum emission at both wavelengths, traces well both the infrared dark and the infrared bright regions along this filament. At 350 μm the emission is more concentrated and the clumps embedded are more evident.

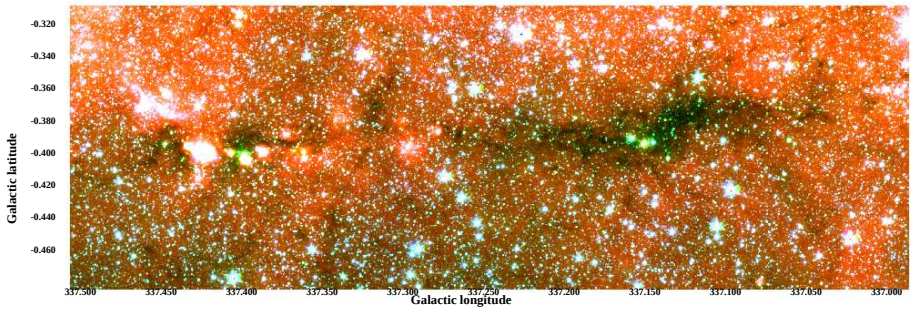

(a) *Spitzer*/GLIMPSE 3.5 μm - 8 μm

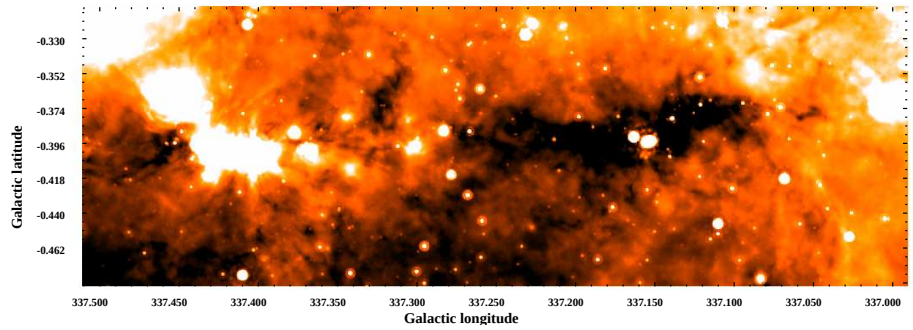

(b) *Spitzer*/MIPSGAL 24 μm

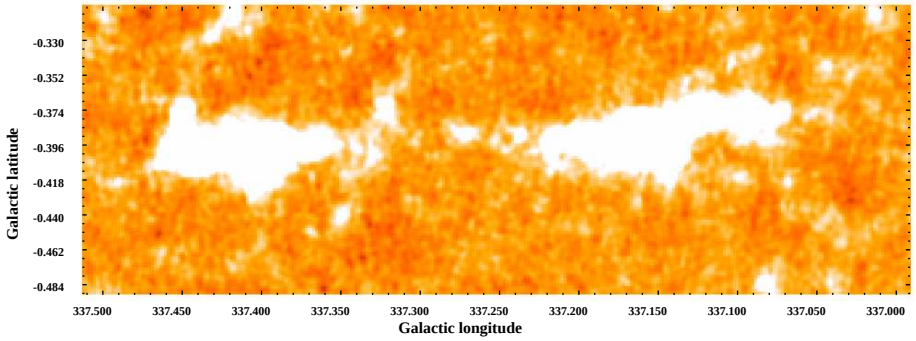

(c) APEX/LABOCA 870 μm

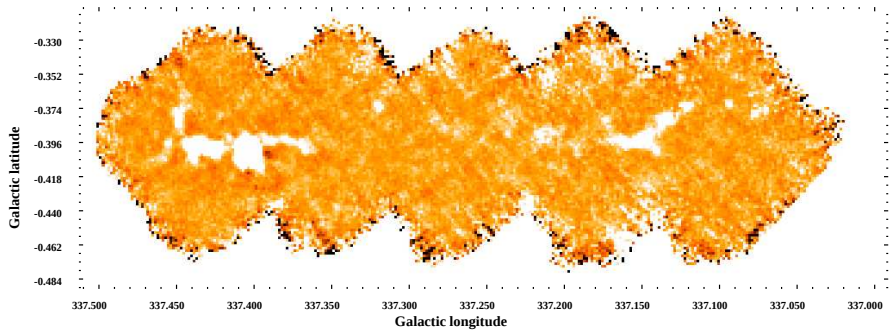

(d) APEX/SABOCA 350 μm

FIGURE 5.1: Multi wavelength continuum images of filament B. *Spitzer* images show that most of the filament can be seen as an infrared dark cloud. However, is clearly seen several regions with active star formation occurring (e.g. green fuzzies, bright 8 μm , 24 μm emission). The dust continuum emission at 870 μm matches well both the infrared dark and IR bright regions. At 350 μm we can identify several clumps embedded in this filament.

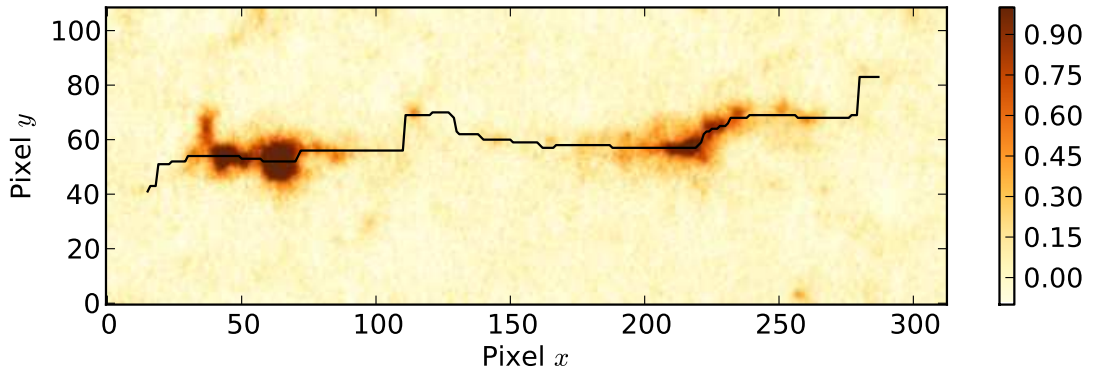

FIGURE 5.2: Path defined for filament B. Color scale showing the 870 μm emission (scale in Jy/beam) toward filament B. The black line shows the path defining the filament, based on the Python algorithm that follows the 870 μm peaks. The region containing the filament was set to 15 pixel to each side of this path.

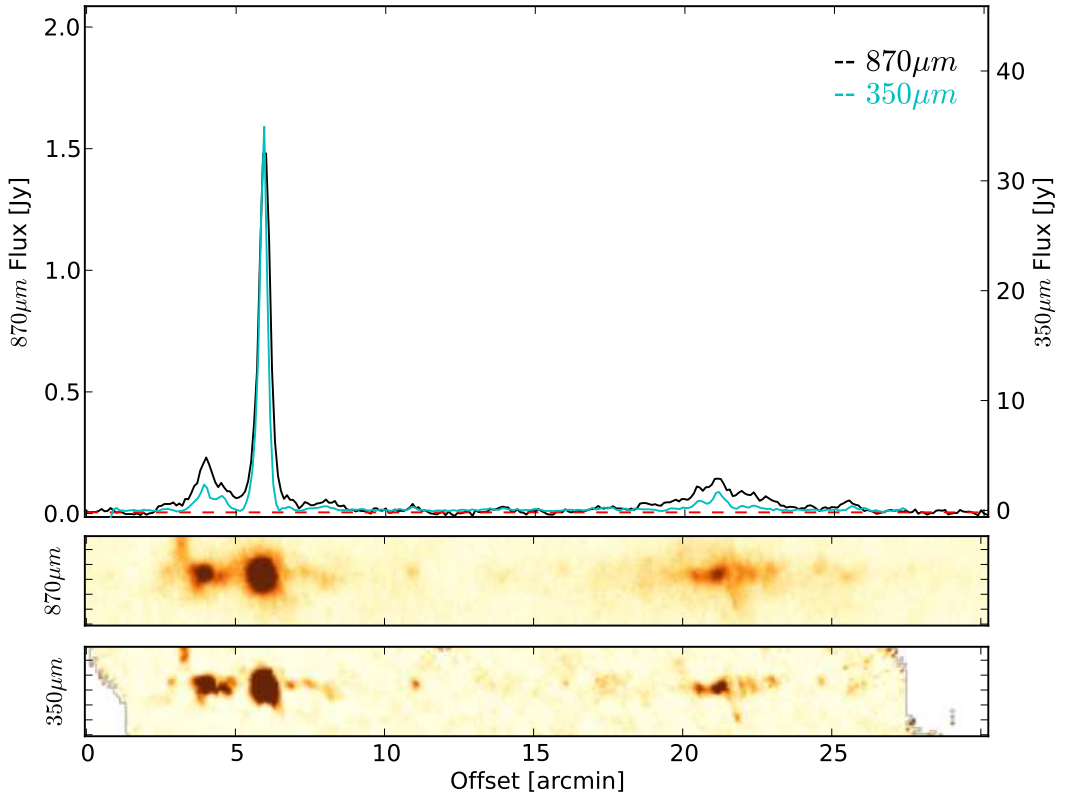

FIGURE 5.3: Distribution of dust continuum emission along the filament. Top panel: Flux along filament B, at the each point of the path defined for both 870 μm (black line) and 350 μm (blue line) continuum emission, the red dotted line shows the mean noise in the map (4.7 mJy at 870 μm and 0.75 Jy at 350 μm). Lower panels: Color images of the filament at 870 μm and 350 μm.

5.1 Defining the filament

The filament was named after the brightest clump within it, using the ATLASGAL catalog denomination. To define the potential filament we use a Python algorithm that follows the peaks in the emission at 870 μm (for a detailed explanation see section 1.4.1). Figure 5.2 shows the path defined for this filament, the black line marks this path as it follows the 870 μm peaks. Once the path was obtained, the width of the filament either side of this path was set to be 15 pixels (180"). This width was chosen to cover the full extent of the emission at 870 μm. The same region was used to define the filament from the 350 μm continuum emission.

Figure 5.3 shows the peak flux density at 870 μm and 350 μm along filament B. This plot clearly shows the well defined clumps within the filament. Moreover, the overall emission along the filamentary structure is higher than the average noise level found in the maps (red dashed line), which is ~4.7 mJy for the 870 μm image and 0.75 Jy for the 350 μm image.

Using the 870 μm dust continuum emission we also determined the radial dispersion of the emission along the filament to estimate its projected width (see section 1.4.1.3). This was done by fitting a Gaussian profile to the emission at 870 μm across the filament. From this fit we obtained the FWHM of the emission at each point along the filament. We find that the mean projected radius of this filament is ~30 arc seconds.

5.2 Physical coherence of the observed filamentary structure

To determine whether the observed filamentary structure is physically coherent we made observations of ^{13}CO(3-2) molecular line emission. Because the observed continuum emission arises from all the clouds along a line of sight, it alone cannot distinguish between a single molecular cloud or the superposition of two or more molecular clouds along the line of sight. By measuring the velocity of the ^{13}CO(3-2) molecular line emission toward it and morphologically matching the ^{13}CO(3-2) emission to the filaments, we can distinguish between these scenarios.

Figure 5.4 (top panel) shows the ^{13}CO(3-2) integrated intensity image overlaid on the 870 μm continuum emission. The ^{13}CO(3-2) emission traces closely the continuum emission seen at 870 μm towards this filament. However, the ^{13}CO(3-2) position-velocity maps, Figure 5.4 (bottom and right panels), show that the ^{13}CO(3-2) emission is actually a superposition of three discrete molecular clouds along the line of sight; one background cloud at -48 km s^{-1}; the main cloud at -41 km s^{-1} and a foreground cloud at -18 km s^{-1}. The main component has a central velocity of -41 km s^{-1} and extends along length of the observed filamentary structure indicating that the majority of

this structure is physically connected. Moreover, the morphology of this cloud matches the morphology of the filamentary structure observed at 870 μm. Because it has a single velocity, extend along the length of the filament and matches the filamentary morphology at 870 μm , we select the cloud at -41 km s^{-1} to be associated with the observed continuum filamentary structure.

The foreground cloud with a mean velocity of -18 km s^{-1} is located toward the right side of the filament. Because the 870 μm emission is the sum of the emission of both of these clouds, this molecular cloud will contaminate the emission at 870 μm. Therefore, the emission at 870 μm toward this part of the filament will be the result of the combined emission from the main filament and this secondary molecular cloud.

The background cloud, with mean velocity of -48 km s^{-1}, correspond to a distinct clump at 870 μm located slightly above the observed filament (l=337.323, b=-0.372). Thus, for further analysis we will mask out this clump from the emission at 870 μm and have redefined the path of the filament excluding this background clump.

With the measured velocity we estimated the distance to the filament using the model for the rotational curve outlined in Section 1.4.3.2. Since this structure appears as dark against the extended Galactic background emission we assumed that this cloud lies at the near kinematic distance. Under these assumptions we find its distance to be 3.2 kpc. Using this distance, the average radius of the filament is 0.45 pc and the length is 24 pc.

5.3 Properties of the embedded clumps within the filament

The ATLASGAL 870 μm continuum emission point source catalog (see section 3) contains seven clumps along this filament. The clumps are evenly distributed along the filament, their locations are shown in Figure 5.5. The ATLASGAL catalog names these clumps based on their peak position in Galactic coordinates (e.g AGAL337.437-0.399), however, for simplicity, we use the ID B1, B2, B3 etc. for each clump, ordered by decreasing Galactic longitude along the filament.

Clumps B1 and B2 are bright at both 8 μm and 24 μm suggesting that star formation has already begun within them. Clump B3, which is not part of this filament, is also dark in *Spitzer* images. *Spitzer*/GLIMPSE images reveal that clump B6 located at the right side of the filament, is associated with three green fuzzies (enhancement at 4.5 μm) and bright emission at 24 μm(suggesting heated dust from protostellar object), both indicators of star formation activity. The rest of the clumps (B4,B5 and B7) appear dark, even at 24 μm, which suggest that these clumps are at an early stage of evolution. Table 5.1 summarizes the observed sub-millimeter and infrared emission toward each clump, which reflects their star formation activity. We also show the association of the clumps with

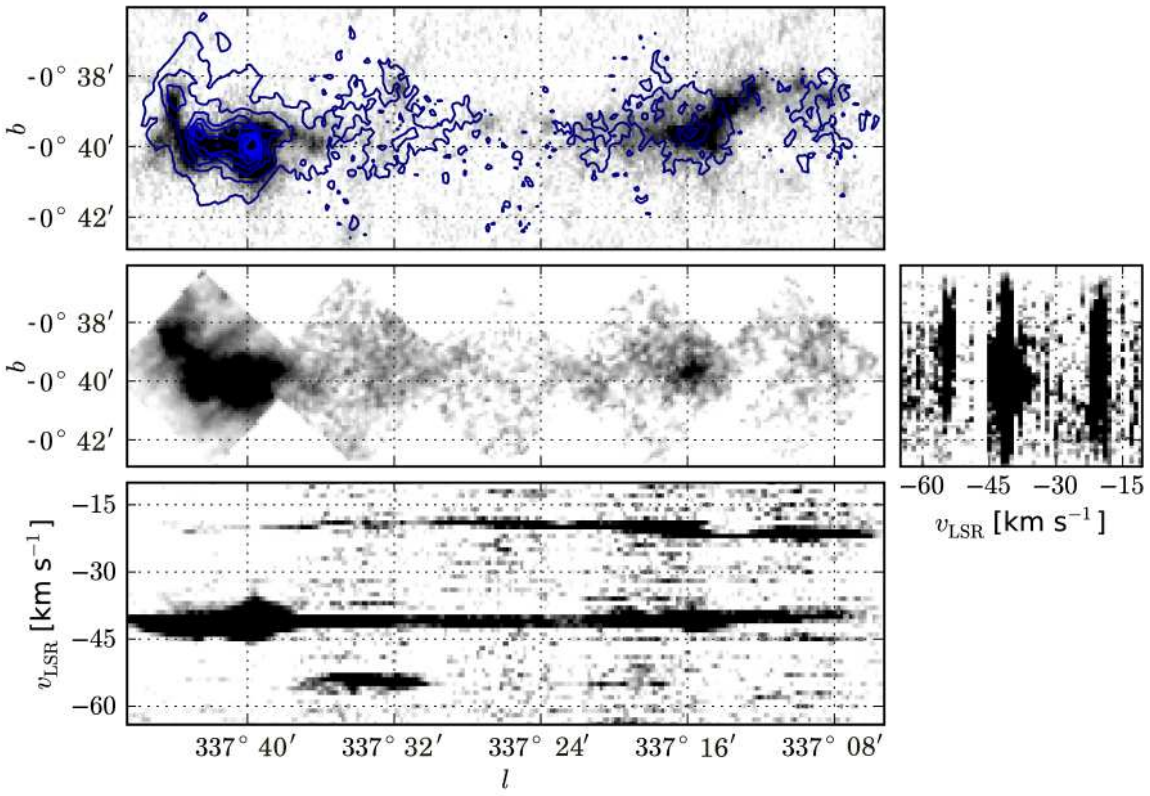

FIGURE 5.4: ^{13}CO(3-2)emission toward filament B. Top panel: dust emission at 870 μm overlaid with contours of the ^{13}CO(3-2) integrated intensity . Middle panel: ^{13}CO(3-2) integrated intensity. Lower and right panels: position velocity maps (l,v) and (b,v) integrated over both Galactic latitude and longitude respectively. These images reveal that the ^{13}CO(3-2) emission toward this filament reveals three discrete molecular clouds along the line of sight ((l,v) lower panel).

IRAS sources, which typically correspond to the clumps where we see bright emission in the mid infrared.

From the images at 870 μm and 350 μm we measured the peak flux, diameter and integrated flux toward the clumps. These values were computed from the emission above the 3σ noise of each clump. The size of the emission at half the peak gives the diameter of the clump. The values obtained for each clump, at 870 μm and 350 μm , are listed in Table 5.2. The spacing between the clumps were computed using the position (from the ATLASGAL catalog) and their angular separation. These was measured between two consecutive clumps, starting with the clump B1. The derived relative separations are listed in Table 5.5. The average separations observed between two consecutive clumps is ∼2 pc. In this average separation we did not considered B3, as this clump is

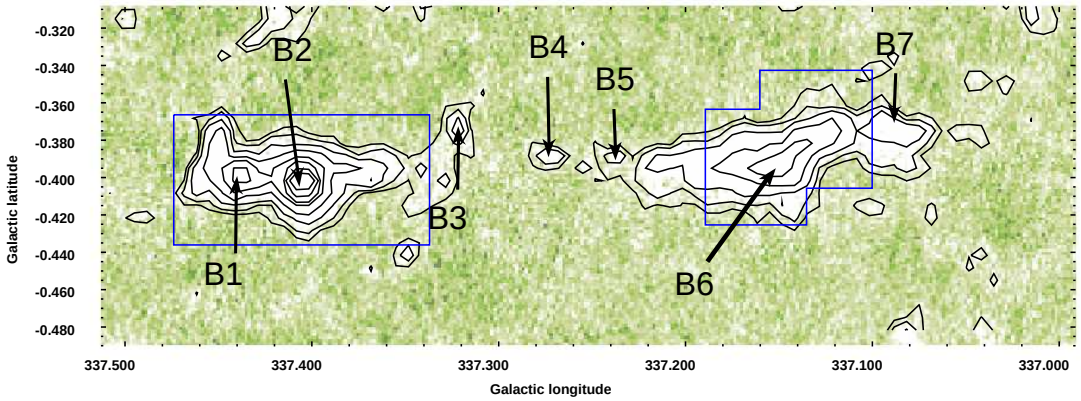

Figure 5.5: Color image of the 870μm continuum emission toward filament B, contours from 3σ to peak emission in logarithmic scale. Arrows indicate the position of the clumps embedded within the filament and blue boxes shows the area covered by the MALT90 observations. We can see that the clumps are evenly distributed along the filament.

Table 5.1: Filament B, IR and sub-millimeter classification of the observed clumps.

ID	ATLASGAL Name	GLIMPSE 3.6 - 8 μm	MIPSGAL 24 μm	ATLASGAL[b]	IRAS
B1	AGAL337.437-0.399	Bright 8 μm	Bright	Bright	-
B2	AGAL337.406-0.402	Green Fuzzies[a]	Point source	Bright	16340-4732
B3	AGAL337.323-0.372	Dark	Dark	Weak	-
B4	AGAL337.271-0.389	Dark	Dark	Weak	-
B5	AGAL337.238-0.391	Dark	Dark	Weak	-
B6	AGAL337.153-0.394	Green Fuzzies[a]	Point Source	Bright	16351-4722
B7	AGAL337.094-0.371	Green Fuzzies[a]	Dark	Weak	16352-4721

[a] Green fuzzies: Enhancement at 4.5 μm.

[b] Bright emission: Peak emission > 1 Jy/beam; weak emission: Peak < 1 Jy/beam

not part of the filament.

From the ^{13}CO(3-2) molecular line emission we obtained the velocity information for each clump. In order to improve the signal to noise of each spectrum, we average all the emission > 3σ around each clump. On this averaged spectrum we perform a Gaussian fit, obtaining the velocity (v_{LSR}), peak antenna temperature (T_{peak}), line width (Δv) and integrated intensity ($\int T_b dv$, II in the

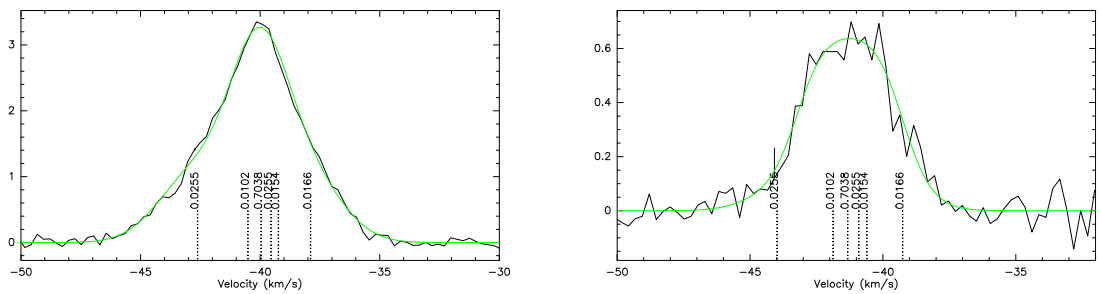

(a) B2 (b) B6

FIGURE 5.6: N_2H^+emission. Each plot show toward B2 (left) and B6 (right) the expected positions of the individual hyperfine component for each spectra. The numbers indicate the relative intensity of the lines. The green line is the fit tho the spectra. Clearly seen is that the hyperfine components is blended.

table). The values obtained from these fits are summarized in Table 5.2.

N_2H^+(3-2) observations were carried out toward two clumps: B2 and B6. These clumps correspond to those with strongest emission at 870 μm and bright IR emission. N_2H^+ has hyperfine components, but due to the large line widths of each component they appear blended in the spectra (Figure 5.6). Toward clumps B2, we perform a three component Gaussian fit to its spectrum to determine the peak antenna temperature (T_{peak}), line width (Δv), velocity (v_{LSR}) and integrated intensity (II). Because the fit was done to the blended components of N_2H^+(3-2), the line width obtained is likely to be overestimated, being dominated by the blend of the four central component of the hyperfine structure. Toward B6 we could fit the hyperfine component using CLASS, however the spectrum of this clump appears noisy making the opacity obtained from this fit not very accurate. The results of these fits are summarized in Table 5.2.

5.4 Chemistry, evolutionary stage and kinematics of the brightest clumps

To asses the chemical state of these clumps we also include data from the MALT90 survey. These observations mapped regions covering clumps B1, B2 and B6 (see Figure 5.5). Towards B1 we detect 8 of the sixteen observed molecular lines (Integrated intensity > 3σ noise). Emission was detected in dense gas tracers (HCN, HNC, N_2H^+ and HCO^+), and their optically thin isotopomers ($H^{13}CO^+$ and $HN^{13}C$), as well as in HC_3CN and C_2H which are usually found in hot cores and photo dissociation regions. The detected lines indicate that this clump is dense and the lack of significant emission from the other hot core chemistry molecules (i.e. CH_3CN, $HC^{13}CCN$, SiO)

suggest that this clumps is either cold or in an early evolutionary stage. This clump shows bright infrared emission in the GLIMPSE/MIPSGAL images, however the peak of the IR emission is not coincident with the peak emission of either the dust continuum or the N_2H^+(1-0). This implies that the IR emission may not arise from this clump but instead from a foreground or background region (Figure 5.7).

Towards clump B2, we detect 11 of the sixteen molecular lines observed (with integrated intensity $> 3\sigma$ noise). In addition to the dense gas tracers and their optically thin isotopomers (HCN, HNC, N_2H^+, HCO^+, $H^{13}CO^+$ and $HN^{13}C$), we also detected emission from several molecular transitions indicative of hot core chemistry such as CH_3CN. We also detected SiO, indicative of shocked gas and C_2H which is detected towards photodissociation regions. All the evidence indicate that clump B2 is associated with star formation, shocks, outflows, therefore is likely that this clump is hot and in a evolve stage.

Clump B6 shows emission (Integrated intensity $> 3\sigma$ noise) only from the following molecules: HNC, $HCO^+$and N_2H^+(1-0). The presence of these lines and the lack of emission from the other molecules are usually observed in dense molecular clouds with low temperatures.

Velocity integrated intensity maps were created for each of the detected molecular transitions towards the clumps (B1 and B2), using a velocity range of -48 km $s^{-1}$to -37 km s^{-1}(Figure 5.8). These maps shows that the integrated intensity for clump B2 is stronger than that for clump B1 in all molecular transitions except in N_2H^+(1-0) where is weaker at clump B2 compared with clump B1. Chemical models of star formation evolution suggest that the difference in N_2H^+abundance reveals different stages of evolution in clumps. These models shows that the abundance of N_2H^+ will decrease as cores evolve from the pre-stellar phase to the proto-stellar phase (Lee et al. 2004). Based on this chemistry we speculate that clump B2 is in a more evolved stage than B1, approaching a proto-stellar phase.

Figure 5.9 shows the integrated intensity maps of the molecular line detected toward clump B6, the range used to create these maps was -44 km $s^{-1}$to -38 km s^{-1}which contains the emission of the main filament at -41 km s^{-1}. The integrated intensity maps shows that the emission of N_2H^+ and HCN follow the morphology observed at the 870 μm dust continuum emission 5.9 (top panel), while the HCO^+ emission is weaker than the others two and is not as extended as the others molecules.

For all the molecular lines detected towards each clump, we performed a Gaussian fit to the peak spectrum obtaining: the velocity of the emission (v_{LSR}), peak antenna temperature (T_{peak}), line width (Δv) and integrated intensity (II). We also obtained the (l,b) position of the peak spectrum expressed as the offset with respect to the position of the peak spectrum of N_2H^+(1-0) (Δl and Δb) and the total integrated intensity (I_T). For all the clumps the detections were defined as the emission

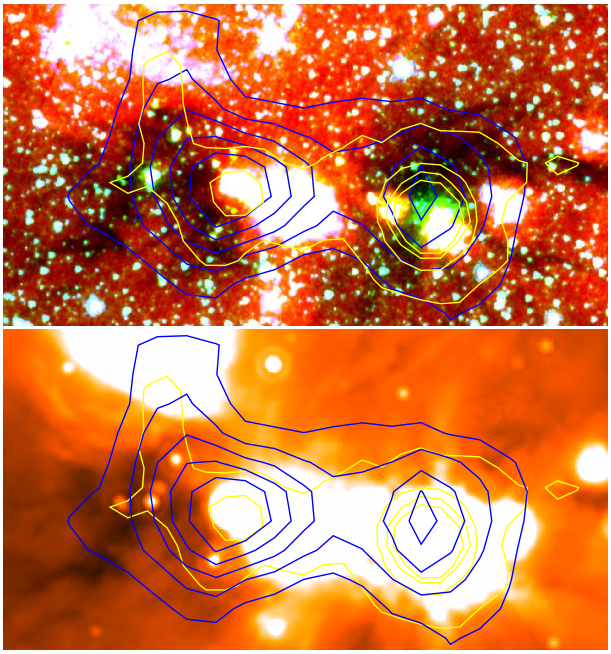

FIGURE 5.7: Zoom in around the clumps B1 and B2 (left, right). Top panel: Three color IRAC image: 3.6 μm (blue) 4.5 μm (green) and 8 μm (red), yellow contours shows the 870 μm continuum emission and blue contours showing the N_2H^+(1-0) integrated intensity. Lower panel: Color image of MIPS 24 μm with yellow contours of 870 μm continuum emission and blue contours of N_2H^+(1-0) integrated intensity.

of II > 3σ. The list of the parameters derived, for each of the detected molecules, are summarized in Table 5.3. To the peak N_2H^+(1-0) emission, we fit the hyperfine structure obtaining the excitation temperature, line width and opacity. The values obtained from these fits are summarized in Table B.1.

Figures 5.10, 5.11, 5.12 shows the spectra of the detected molecules toward B1, B2 and B6 respectively. The spectra correspond to the N_2H^+(1-0) peak position The spectra toward clump B1 do not show a "2 peak" auto absorption in any transition, although, the emission at HCO^+ present a red skewed profile suggesting inward motions. Toward clump B2 clearly is seen the self absorption in ^{13}CO and HCO^+. Clump B6 is the weaker of the three clumps observed. The ^{13}CO emission shows a blue asymmetry suggesting inward motions. These spectra also show the second molecular cloud detected toward this filament, clearly seen at HCO^+ and ^{13}CO.

Table 5.2: Parameters of the clumps in filament B from their continuum and molecular emission.

	870 μm				**350 μm**				**^{13}CO(3-2)**					**N_2H^+(3-2)**			
ID	Peak Flux	Diameter		Int. Flux	Peak Flux	Diameter		Int. Flux	T_{peak}	v_{LSR}	Δv	II	Diameter	T_{peak}	v_{LSR}	Δv	τ
	Jy/Beam	’	pc	Jy	Jy/Beam	’	pc	Jy	km s^{-1}	km s^{-1}	K	K km s^{-1}	pc	km s^{-1}	km s^{-1}	K	
B1	3.14	0.9	0.8	9.53(0.87)	23.15	0.6	0.6	79.27(1.78)	14.05	-41.9	2.84(0.13)	42.65(1.90)	0.5	-	-	-	
B2	18.34	1.3	1.2	49.31(0.87)	176.22	1.0	0.9	876.45(2.67)	14.07	-41.9	5.19(0.21)	78.09(3.08)	0.9	1.01	-42.74	3.54(0.12)	
														2.72	-40.07	2.83(0.06)	
														0.91	-37.99	3.42(0.13)	
B3	0.55	0.5	0.5	0.64(0.22)	3.24	0.4	0.4	7.20(0.83)	2.25	-54.7	2.73(0.77)	6.59(1.87)	0.3	-	-	-	
B4	0.37	0.5	0.5	0.54(0.22)	1.06	0.3	0.3	1.41(0.61)	2.16	-41.9	1.66(0.54)	3.82(1.24)	0.7	-	-	-	
B5	0.32	0.4	0.4	0.31(0.22)	1.79	0.3	0.3	2.30(0.50)	1.14	-40.5	1.66(0.54)	2.02(0.66)	0.3	-	-	-	
B6	1.70	0.7	0.6	4.68(0.76)	7.13	0.4	0.4	19.97(1.16)	4.02	-41.9	1.66(0.54)	7.12(2.32)	0.8	0.64	-41.36	2.84(0.29)	3.22 (1.8
B7	0.51	0.3	0.3	0.66(0.33)	1.95	0.3	0.3	3.22(0.66)	0.79	-39.6	2.15(0.21)	1.81(0.18)	0.3	-	-	-	

TABLE 5.3: Filament B: Parameters derived from Gaussian fits to the MALT90 spectra

Source	Molecule	Δl[a]	Δb[a]	T_{peak}	V_{LSR}	Δv	II[b]	I_T[c]	*rms*
		"	"	K	km s^{-1}	km s^{-1}	K km s^{-1}	K km s^{-1}asec^2	K/channel
B1 AGAL337.437-0.399	N_2H^+	0	0	2.25	-41.78	2.75	6.60	1180	0.24
	HCO^+	18	9	1.39	-41.13	2.21	3.27	17	0.24
	$H^{13}CO^+$	27	0	0.44	-41.40	2.26	1.06	186	0.25
	HCN	63	18	0.76	-40.57	2.23	1.80	892	0.24
	$H^{13}CN$	9	-9	0.37	-41.33	1.46	0.57	1100	0.24
	HNC	0	0	1.93	-41.78	2.66	5.47	1214	0.24
	HC_3N	18	0	0.40	-41.99	1.53	0.65	35	0.23
	C_2H	18	0	0.57	-42.04	1.81	1.10	89	0.24
B2 AGAL337.406-0.402	N_2H^+	0	0	1.35	-41.52	3.29	4.37	13	0.18
	HCO^+	0	0	1.28	-39.36	2.37	3.23	765	0.28
	$H^{13}CO^+$	18	0	0.62	-39.96	3.39	2.24	110	0.18
	^{13}CS	9	0	0.51	-40.97	2.82	1.53	93	0.17
	HCN	0	0	0.94	-48.99	3.72	3.73	1225	0.18
	$HN^{13}C$	0	7	0.43	-40.20	1.24	0.56	225	0.18
	HNC	18	9	1.75	-40.16	3.29	6.14	1707	0.18
	CH_3CN	9	0	0.33	-46.86	1.76	0.62	64	0.17
	HC_3N	9	9	0.90	-40.57	3.03	2.90	205	0.17
	C_2H	0	9	0.77	-40.72	2.82	2.31	227	0.18
	SiO	9	9	0.40	-39.54	2.89	1.23	103	0.18
B6 AGAL337.153-0.394	$N2H^+$	0	0	0.91	-39.01	1.98	1.92	72	0.38
	HCO^+	-89	63	0.68	-41.72	1.76	1.27	179	0.36
	HNC	-63	27	1.09	-41.61	1.55	1.80	131	0.38

[a] Offset of the peak emission from the N_2H^+(1-0) peak.

[b] Integrated intensity at the peak.

[c] Total integrated intensity, from the MALT90 catalog.

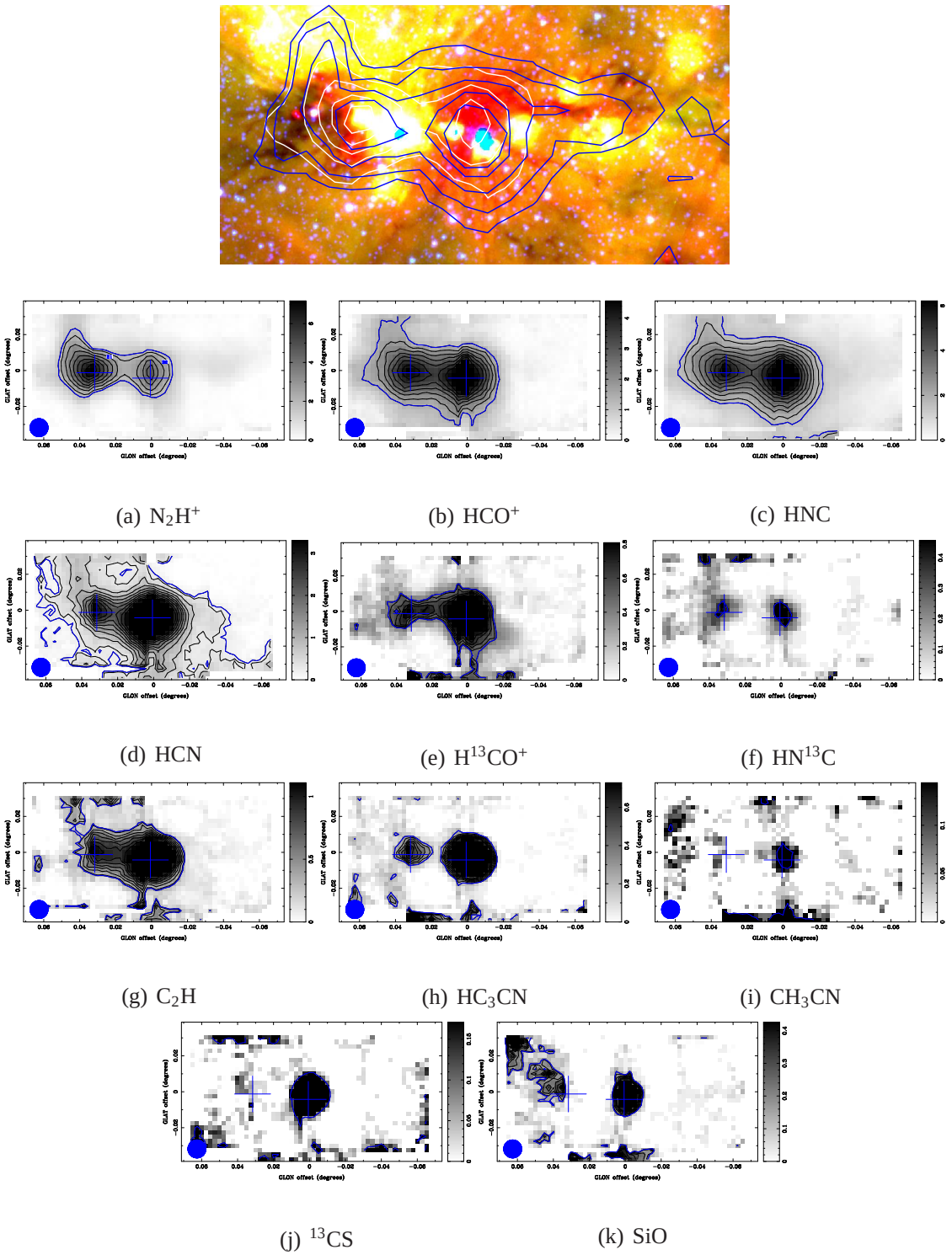

(a) N_2H^+ (b) HCO^+ (c) HNC

(d) HCN (e) $H^{13}CO^+$ (f) $HN^{13}C$

(g) C_2H (h) HC_3CN (i) CH_3CN

(j) ^{13}CS (k) SiO

FIGURE 5.8: Maps of the velocity integrated intensity in the molecular lines detected toward B1 and B2 from the MALT90 data. Top panel: Three color *Spitzer*/IRAC (Red: 24 μm, blue: 8 μm, green: 4.5 μm, blue contours: 870 μm, white contours: N_2H^+(1-0)). Panels (a)-(k): Maps of integrated intensity from each of the detected lines (II > 3σ). Contours represent the emission from 90% of the peak to 3σ noise emission (blue contour) in steps of 10%. Crosses shows the position of the clumps and the blue circle shows the beam size. The color bar shows the value of the peak at each molecule.

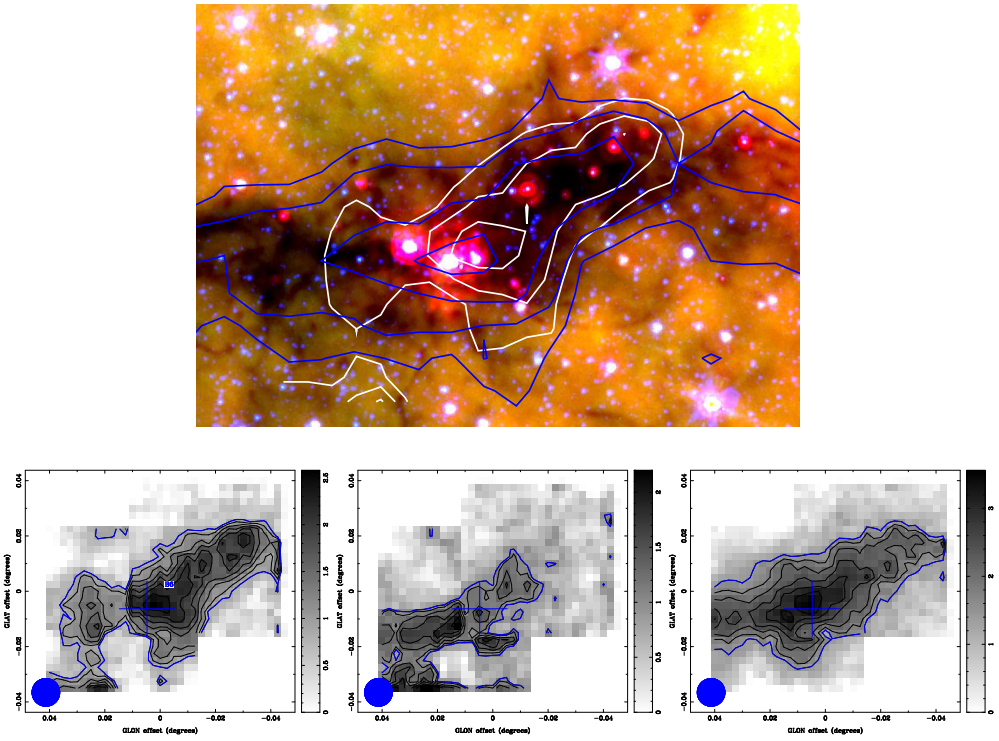

(a) N_2H^+ (b) HCO^+ (c) HNC

FIGURE 5.9: Maps of the velocity integrated intensity in the molecular lines detected toward B6 from the MALT90 data. Top panel: Three color *Spitzer*/IRAC image (Red: 24 μm, blue: 8 μm, green: 4.5 μm, blue contours: 870 μm, white contours: N_2H^+(1-0)). Panels (a)-(k): Maps of integrated intensity from each of the detected lines (II > 3σ). Contours represent the emission from 90% of the peak to 3σ noise emission (blue contour) in steps of 10%. Crosses shows the position of the clumps and the blue circle shows the beam size. The color bar shows the value of the peak at each molecule.

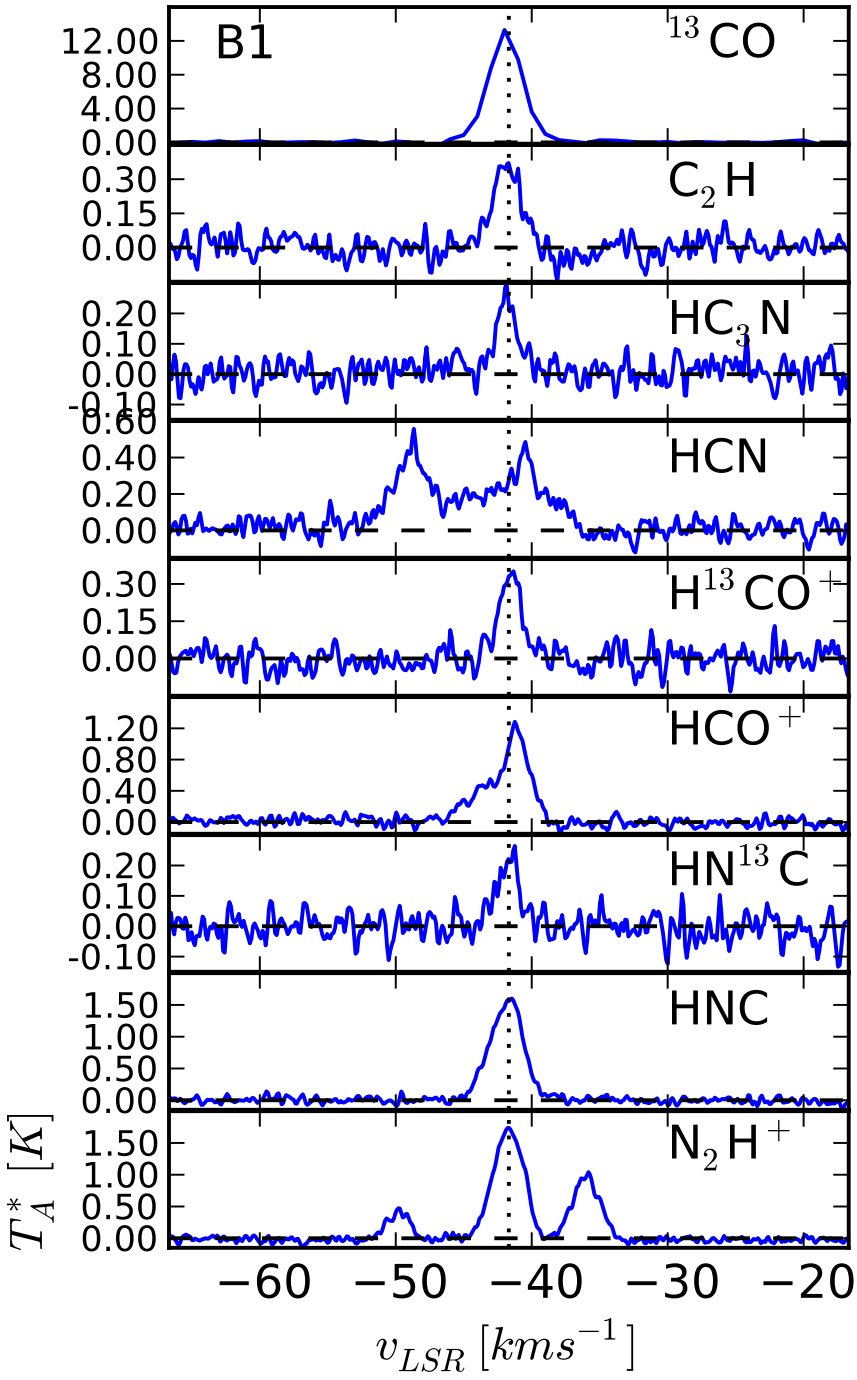

FIGURE 5.10: Spectra toward clump B1. Each spectrum are at the (l,v) position corresponding to the peak emission at N_2H^+. Dotted line shows the central velocity of the N_2H^+(1-0) emission. In this figure we can see that all the molecules except HCN have their peak at the same velocity. HCO^+ shows an asymmetric profile and we do not see self absorption in any of the lines.

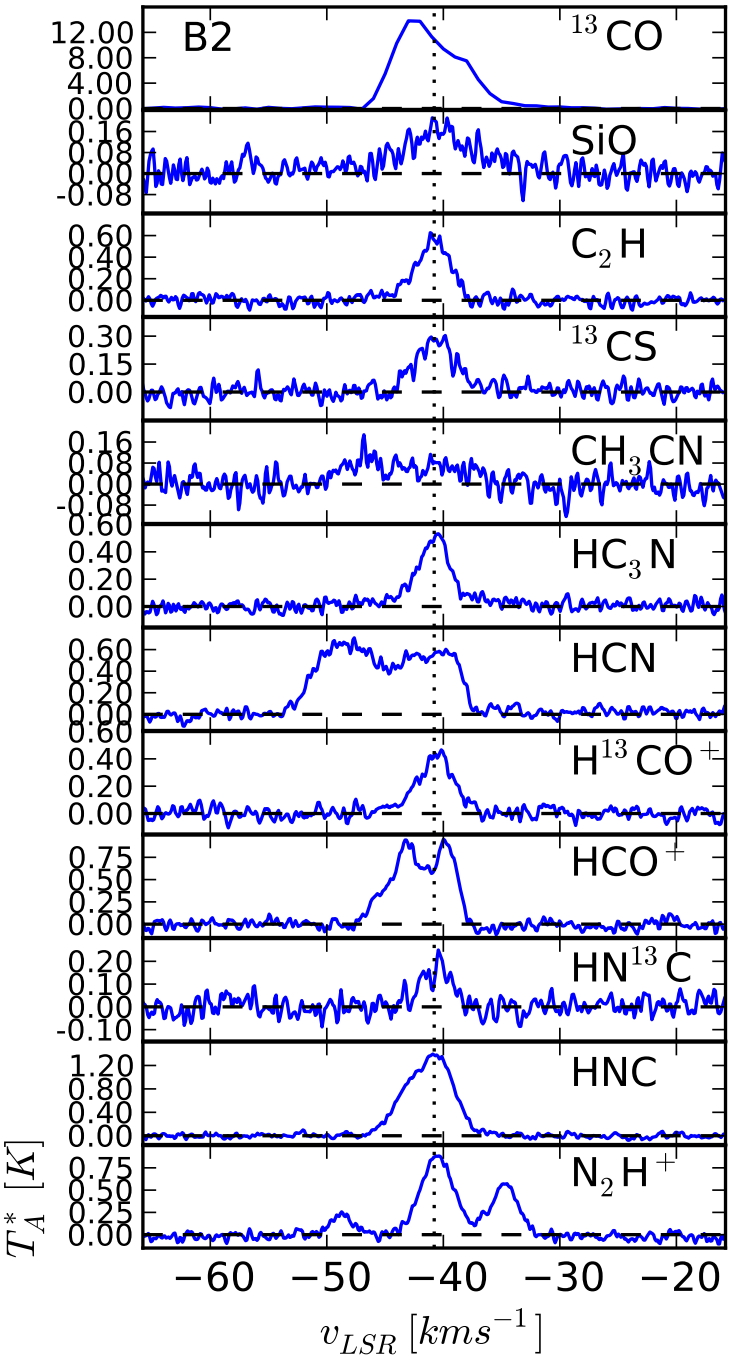

FIGURE 5.11: Spectra toward clump B2. Each spectrum are from the (l,v) position corresponding to the peak emission at N_2H^+. Dotted line shows the central velocity of the N_2H^+(1-0) emission. We see asymmetric profile in several molecular lines (HC_3CN, ^{13}CO(3-2), HNC) and self absorption at HCO^+ .

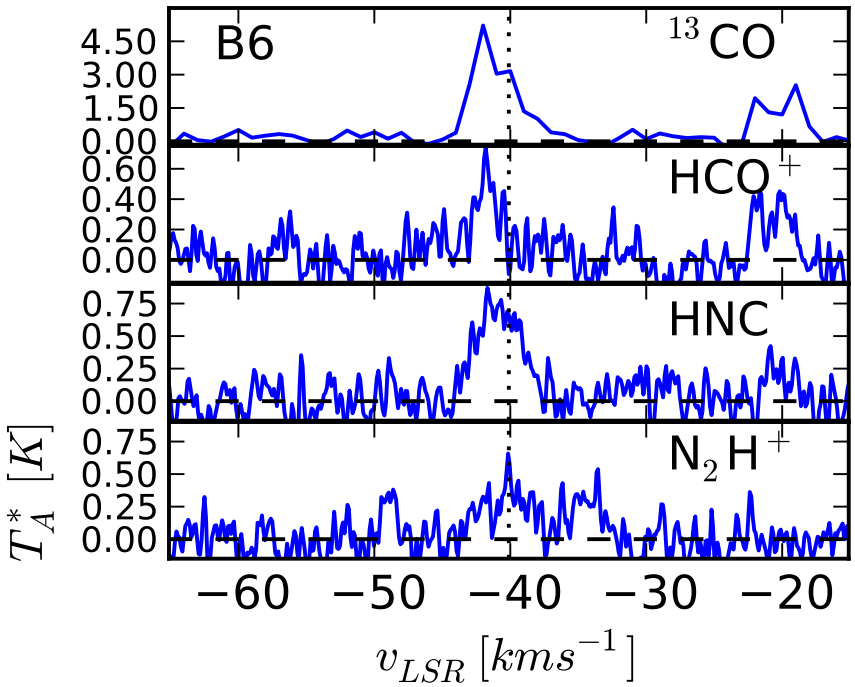

FIGURE 5.12: Spectra toward clump B6. Each spectrum are from the (l,v) position corresponding to the peak emission at N_2H^+. Dotted line shows the central velocity of the N_2H^+(1-0) emission. This clumps shows only emission in three of the 16 lines observed in MALT90. The emission is asymmetric in HCN and HCO^+having wings to the left and right respectively.

5.5 Physical properties of the filament and its clumps

In this section we discuss the derivation of the physical properties of the filament B and its clumps (temperature, masses and pressure) using the multi wavelength data described in the previous section.

5.5.1 Color temperature

The color temperature along this filament was determined using the dust continuum observations at 870 μm and 350 μm, following the method described in Section 1.4.2.2. The color temperature, using these wavelengths, is only valid toward the part of the filament that has low temperatures. Because most of the filament is seen as an IRDC, its temperature is likely to be low. Therefore, we feel that the assumptions made to calculate the color temperature in the IR-dark regions are adequate.

The average color temperature determined for this filament ranged from 13 K to 6 K assuming spectral indexes β of 1 to 2.5. Figure 5.13 shows the temperatures obtained with the different spectral indexes used. Clearly seen is that the mean temperature along the filament remains fairly constant at ~10 K, while the temperature increases locally towards the clumps, reaching ~100 K toward some clumps.

Observations of dust continuum emission towards cold dense molecular clouds, made with Hershel, indicate that these clouds have typical temperatures of ~10 K (Peretto et al. 2010). The temperatures obtained using an spectral index of 2 and 2.5 are lower (6 K - 8 K) than these typical temperatures, therefore, in the following analysis we will assume β = 1.5 which is typical for most star formation regions (Schnee et al. 2010).

The peak temperature derived for clump B2 is 100 K (assuming β = 1.5). Since we detect emission from the hot core molecules (i.e. CH_3CN, SiO, C_2H) toward B2 and observations of other hot clumps indicate that they have typical dust temperatures of ~100 K. The temperature derived for this clump may be a good estimation.

Towards the remaining clumps (B1, B2, B4, B5 and B6) the peak temperatures range between 14 K to 30 K. Because these clumps display a range in their star formation activity from cold dense clumps to warm clumps, these values are consistent with the dust temperature found for other typical cold and warm clumps respectively (Rathborne et al. 2010). For clump B7, due to its significant emission at infrared, we assume a temperature of 30 K which correspond to a typical temperature observed toward warm clumps. Table 5.5 summarizes the temperature obtained/assumed for each clump.

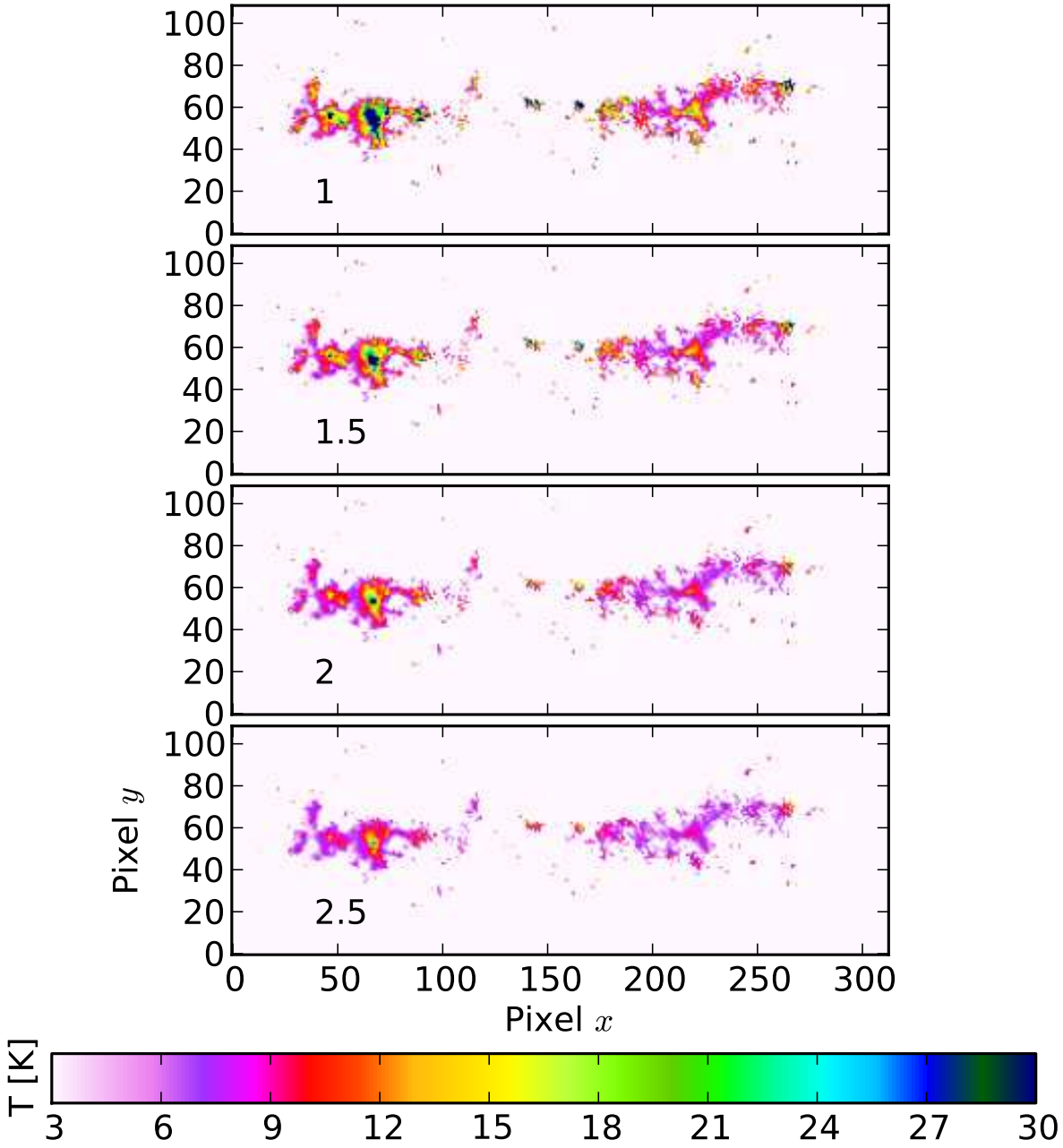

FIGURE 5.13: Derived color temperature for filament B. The panels show the derived color temperature using different values for the spectral index β. The temperature along the filament decreases with higher values of β, the average temperature is ~10 K and in all cases the temperature peaks locally toward the clumps.

5.5.2 Column density and mass

In this section we describe how we determined the column density and mass of filament B. The column density and masses were obtained from both the dust continuum and ^{13}CO(3-2) molecular line emission. We calculated the total mass of the filament, the clumps masses, and the filament's lineal mass.

5.5.2.1 Column density and total mass of the filament

The radial density was computed from the dust thermal continuum emission at 870 μm using Equation 1.34. In this calculation we used the color temperature, described in section 5.5.1, assuming a spectral index $\beta = 1.5$ and a dust opacity coefficient $k_{870} = 0.012$ cm^{2}gr^{-1}. The column density have an average value of 3×10^{22} cm^{-2}. The total dust mass of the filament was computed by integrating the radial column density over the diameter and lengths of the filament. The total dust mass derived for this filament is 1×10^4 M$_\odot$.

We use the ^{13}CO(3-2) line width along the filament to compute the lineal virial mass at each point along the filament. The total virial mass was determined by integrating these individual masses along the filament. Using this method we obtained a total virial mass of 1.2×10^4 M$_\odot$.

We found that there is a good agreement between the total dust mass and the total virial mass. The ratio between the dust mass (m) and the virial mass (m_{vir}), m/m_{vir}, is 0.81. This implies that the filament on global scales is close to virial equilibrium.

5.5.2.2 Mass of the clumps

To calculate the clump masses from the dust thermal emission, we use their total flux and the derived color temperature toward each individual clump. We assumed an spectral index $\beta = 1.5$ and a dust opacity of $k_{870} = 0.012$ cm^{2}gr^{-1}. Clumps B4, B5 and B7 have dust masses of 71 M$_\odot$, 20 M$_\odot$ and 32 M$_\odot$ respectively. Clump B1 has a dust mass of 462 M$_\odot$. Clump B2 has the highest mass, with a derived mass of 1960 M$_\odot$ and clump B6 has a mass of 698 M$_\odot$.

The virial mass, obtained from the ^{13}CO(3-2) line width, assumes that the clumps are in virial equilibrium and have spherical geometry. For each clump we determine the line width from the average ^{13}CO(3-2) spectra. We found that clump B1 has a virial mass of 500 M$_\odot$, B2 has a virial mass of 3000 M$_\odot$, B6 have a virial masses of 225 M$_\odot$ and the clumps B5 and B7 have the lowest virial masses of 100 and 125 M$_\odot$ respectively.

Using the opacity, excitation temperature and line widths derived from the fit to the hyperfine components observed in the N_2H^+(1-0) emission, we derived the mass of clumps B1, B2 and B6. The masses were obtained using equation 1.4.3.3. The values of the mass obtained for these clumps are summarized in Table 5.5.

The ratio between the dust mass and the virial mass (m/m_{vir}) for most clumps is < 1, suggesting that most of the clumps are not gravitationally bound. We find that clump B1 is close to virial equilibrium. For clump B6, the dust mass excess the virial mass suggesting that this clump is unstable against gravitational collapse.

5.5.2.3 Lineal mass along the filament

At each point along the filament we obtained a total flux per point, by integrating the 870 μm continuum emission across the radius of the filament. Lineal dust masses were obtained, at each point, using Equation 1.34. For this calculation we used the temperature profile obtained from the color temperature analysis and assume a dust opacity of $k_{870} = 0.012$ cm^{2}gr^{-1}. The lineal masses obtained with this method ranges from a few $M_\odot$ pc^{-1} in the inter-clump region to 6000 $M_\odot$ pc^{-1} toward the brightest clumps in the filament. The average value of the lineal mass for this filament is 410 $M_\odot$ pc^{-1}. The lineal mass distribution along the filament is shown in Figure 5.14.

The lineal virial mass was computed from the ^{13}CO(3-2) line width at each point along the filament. To determine the ^{13}CO(3-2) line width along the radius of filament, we computed by fitting a Gaussian profile to the mean spectrum across the filament at each point along the filament (see Section 1.4.1.3). We found that the mean linewidth is $\Delta v = 2.4$ km s^{-1}. Using this linewidth we find the lineal virial with a mean value of 552 $M_\odot$ pc^{-1}. Figure 5.14 also shows the distribution of the lineal virial mass for filament B. Overall, both the lineal dust mass and lineal virial mass have a similar distribution, but we see a great discrepancy between both masses at the position of one of the clumps. This difference can be associated to the under estimation of the temperature associated with this part of the filament.

From the ^{13}CO(3-2) observations we know that some portion of the filament is actually the superposition of two discrete molecular clouds, thus the lineal dust mass derived in these regions is the combination of both molecular clouds. Since we can estimate the fraction of the total virial mass (foreground cloud + filament) that corresponds to the foreground molecular cloud, we can attempt to correct for this. The foreground molecular cloud, at -18 km s^{-1}, has a mean linewidth of $\Delta v = 1.3$ km s^{-1}, this gives a mean lineal virial mass of the background molecular cloud of 258 $M_\odot$ pc^{-1}. Figure 5.15 shows the lineal virial mass along the filament from the ^{13}CO(3-2) emission toward both molecular clouds. The total virial mass of the foreground cloud corresponds to ∼25% of the total mass (foreground + filament). Thus, for further analysis, we take this contribution into

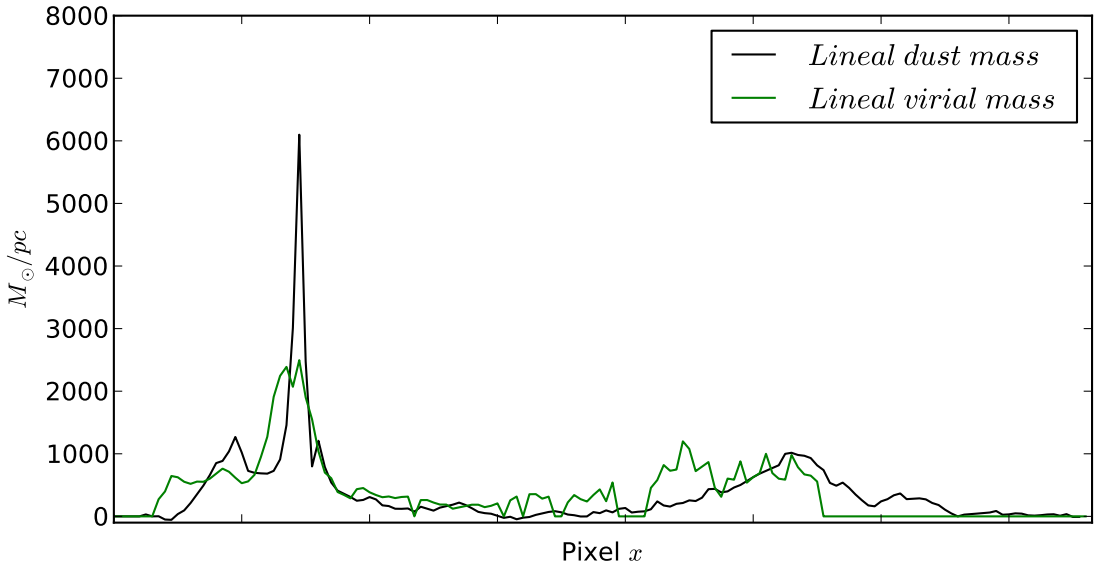

FIGURE 5.14: Lineal dust and virial mass distribution along the filament. Top panel: Black line, lineal mass from 870 μm dust continuum emission; green line, virial mass from ^{13}CO(3-2) emission. Overall both masses have a similar morphology.

consideration deriving a "corrected" mean lineal dust mass and total dust mass for the filament of 308 $M_\odot$ and 7.5×10^3 $M_\odot$ respectively.

5.5.3 External and internal pressure

The external pressure acting on the filament was estimated from the molecular emission detected outside the region delimiting the filament. We estimated the mean density of the gas surrounding the filament from the intensity of the dust thermal emission, obtaining a mean density of 3.5×10^{-21} gr cm^{-3}. From the ^{13}CO(3-2) emission, detected outside the boundaries of the filament, we found that the mean velocity dispersion is $\langle\sigma\rangle$=1.45 km s^{-1}. These values give an external pressure of $P_s = 5.3 \times 10^5$ K cm^{-3}. This value is comparable to the values obtained for the external pressure in other filamentary molecular clouds (e.g. Hernandez and Tan 2011)

The internal pressure was computed at each point along the filament from Equation 1.5 using the measured ^{13}CO(3-2) line width and lineal density obtained from the dust continuum emission (for a detailed explanation see Section 1.4.2.2). The values obtained for the internal pressure within the filament and clumps range from $\langle P\rangle \sim 10^6 - 10^8$ K cm^{-3}. The mean internal pressure of the entire

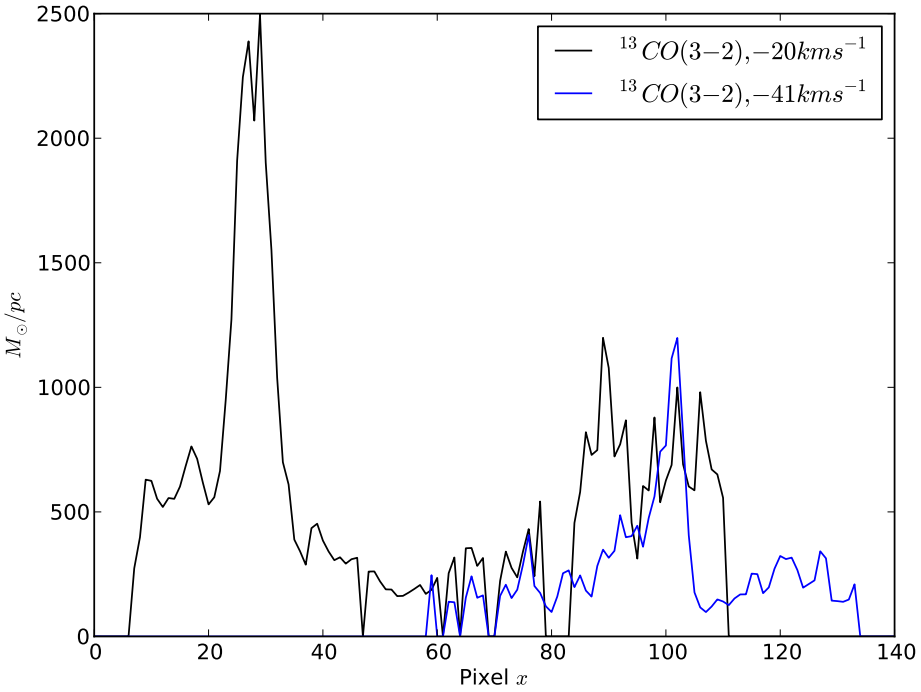

FIGURE 5.15: Lineal virial mass distribution along the filament from both emission detected at ^{13}CO(3-2). Black line, virial mass from ^{13}CO(3-2) molecular line emission at -41 km s^{-1}; Blue line, virial mass from ^{13}CO(3-2) emission at -18 km s^{-1}

filament, was calculated from the mean ^{13}CO(3-2) line width and the mean lineal mass, giving a value of $\langle P \rangle = 1.189 \times 10^7$ K cm^{-3}.

5.6 Stability of the filament: magnetic field support

In this section we compare the properties of filament B with theories that describe the stability of filamentary molecular clouds. We analyze the magnetic field support in this filament via two different methods. Firstly we analyze the shape of the radial density profile using the 870 μm and 350 μm dust emission data. Secondly, we use a virial equilibrium analysis.

5.6.1 Radial density profile analysis

In this section we characterize the observed radial intensity profile obtained from the dust thermal emission. The observed intensity is compared with a model that describe the radial column density in the presence of a magnetic field. The shape of the radial intensity is determined by the value of p in Equation 1.34. Th value of $p = 4$ for the non-magnetic hydrostatic solution (Ostriker 1964) and $p \sim 2$ for the magnetic case (Fiege and Pudritz 2000) (see section 1.3.2 for further details)

To do this we separate the filament into two groups: a group containing the clumps and a group containing inter-clump material. We calculated the normalized mean radial intensity at 870 μm and 350 μm, obtaining a mean radial intensity profile for the clumps and the inter-clump material. We found that the normalized radial mean intensity for the clumps, is best fitted with profiles with p index of ~ 4 for both the 870 μm and 350 μm dust continuum emission (Figure 5.16). This implies that the radial profile of the clumps at large radii goes like $\rho \sim r^{-4}$, which based on theoretical arguments suggest that clumps are isothermal and in hydrostatic equilibrium (Ostriker 1964). We find that there is no need for an external magnetic field to explain the clump stability.

Towards the inter-clump material of this filament, the mean radial intensity profile has a different shape than that observed towards the clumps, having in general broader wings (Figure 5.17). At 870 μm the emission is noisier toward one side of the filament making it difficult to perform a good fit to this emission. However, we see that, in general, the profile resembles more closely a column density profile with $\rho \sim r^{-2}$ (see Figure 5.17 top panels). At 350 μm the emission is fitted well by a profile with $p = 2$ (Figure 5.17 bottom panels). From the theory, a column density profile with $p = 2$ implies that the filament is most likely to be isothermal with magnetic support. This suggest that while the clumps appear to be in hydrostatic equilibrium, overall the filament needs a magnetic field to explain its stability.

To analyze how the column density profile changes along the filament, we performed the same fit using Equation 1.34 to the radial intensity at each point along the filament, obtaining a value of the inner radius, central density, peak position and p. We defined a "good fit", as the fit with a $\chi^2 < 2$ between the model and the observations. The derived values of p for the good fits are shown in Figure 5.18, where the error-bar correspond to the χ^2 value from the fit. In this plot we see that most of the points corresponding to the inter-clump material (black points) are best fitted with a value of $p < 4$, while the clumps (red points) have typically larger values of p (~ 3.5 in average). Since the shape of the radial density profile, and thus p, reflects the presence of magnetic field support in the filament, values of $p \sim 2$ imply that, in general, hydrostatic equilibrium is not enough to explain the stability of this filament it is therefore likely that a magnetic field is needed to explain the observed radial density profile.

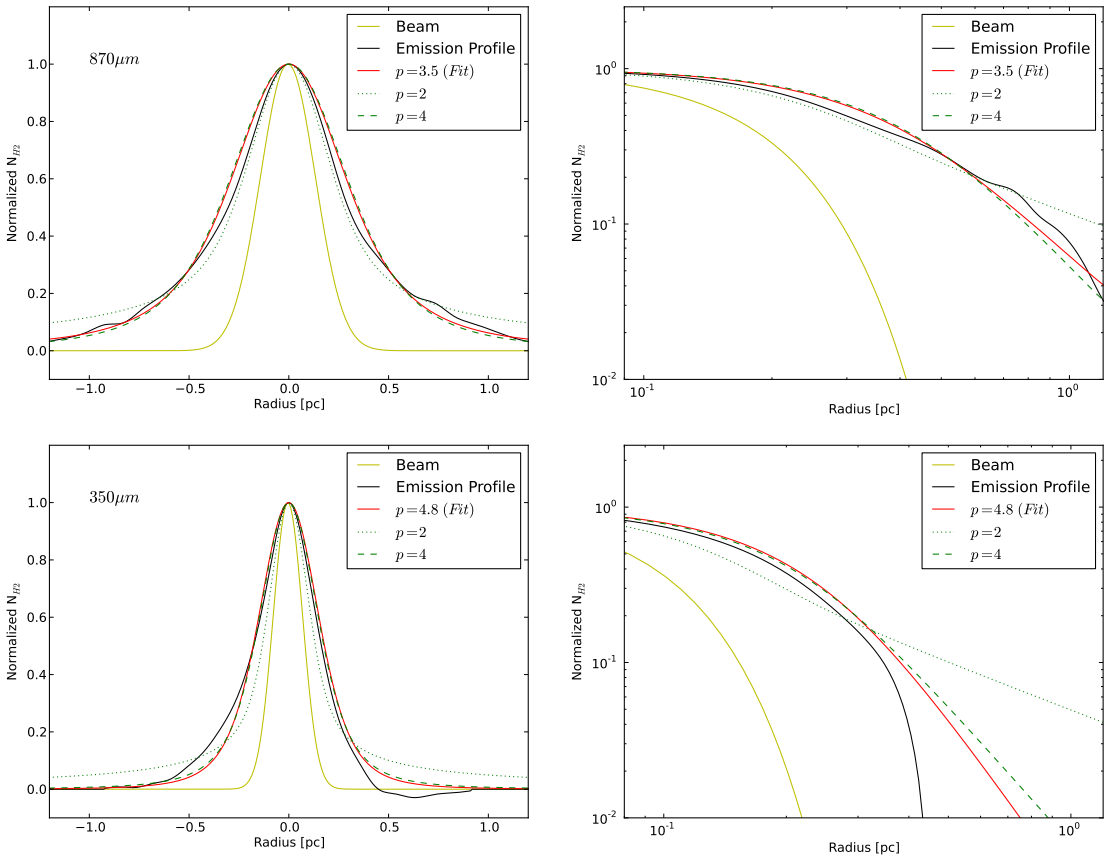

FIGURE 5.16: Density profile of the normalized mean density of the clumps in filament B. Top panels show the 870 μm emission, bottom panels show the 350 μm emission. The left panels show lineal plot of the profiles and right panels shown the profiles in logarithmic scales. The red solid lines represents the best fit to the density profile, the beam profile is shown with the solid yellow line, the hydrostatic solution p=4 (green dashed line) and magnetized solution p=2 (green dotted line) are also shown. We can see that in general the shape of the radial density follows the shape of a profile with p = 4.

5.6.2 Virial equilibrium analysis

To test whether magnetic fields are important in the stability of filaments, we use a virial analysis that includes pressure and magnetic field support, described by Fiege and Pudritz (2000). In this analysis we use the lineal dust mass (m, corrected for the contamination of the second molecular cloud observed toward this filament), lineal virial mass (m_{vir}), internal pressure ($\langle P \rangle$) and external pressure (P_s), calculated in the previous sections. Following the work of Fiege and Pudritz (2000) we plot the values of $\langle P \rangle / P_s$ against m/m_{vir} (Fig 5.19). Included on this plot are lines of constant values of $\mathcal{M}/|\mathcal{W}|$, the ratio between the total magnetic energy per unit length $\mathcal{M}$ and the lineal

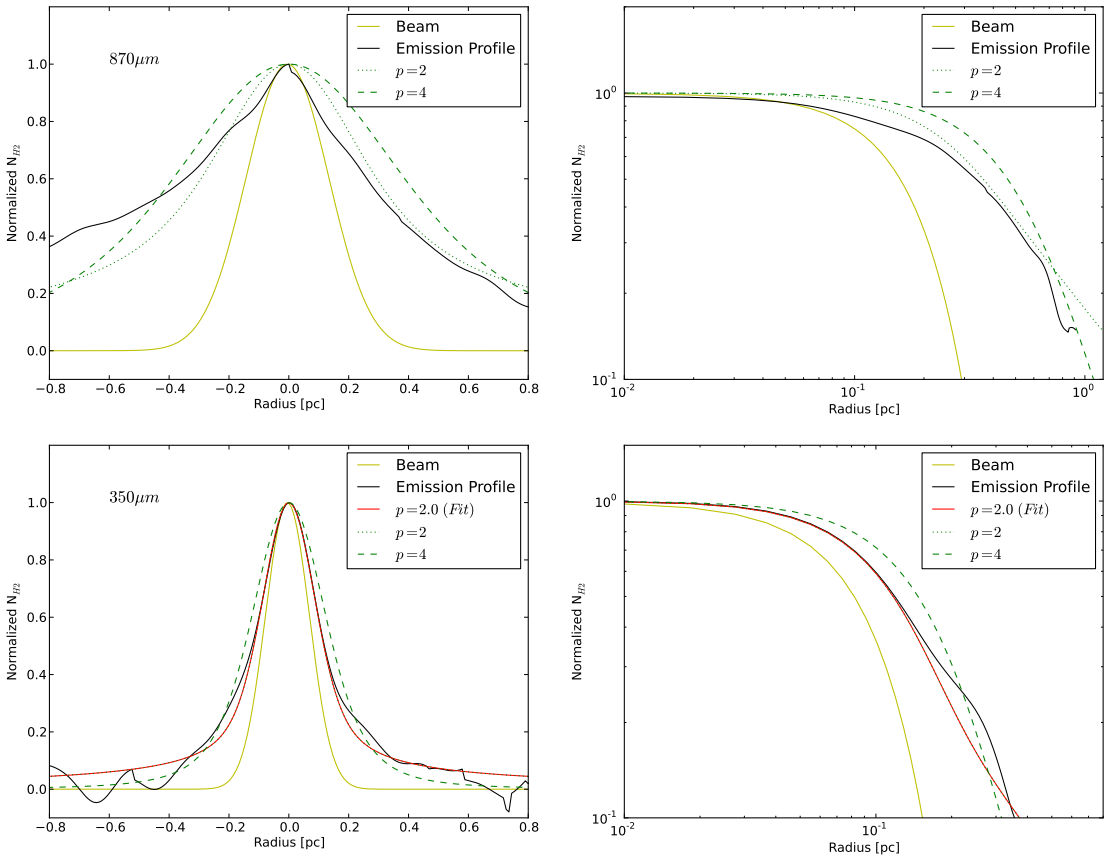

FIGURE 5.17: Density profile of the normalized mean radial density of the inter-clump region in filament B. Top panels show the 870 μm emission, bottom panels show the 350 μm emission. The left panels show lineal plot of the profiles and right panels shown the profiles in logarithmic scales. The beam profile is shown with the solid yellow line, the hydrostatic solution (green dashed line) and magnetized solution (green dotted line) are also shown. We can see that the shape of the radial density differs from the observed toward the clump looking more similar to a solution with $p \sim 2$ at both wavelengths.

gravitational energy $\mathcal{W}$. This plot allows one to visualize the magnitude and shape of the magnetic field needed to provide stability to this filament. Negative values of $\mathcal{M}/|\mathcal{W}|$ suggest that the support is given by a magnetic field dominated by a toroidal component while positive values of $\mathcal{M}/|\mathcal{W}|$ suggest that the support is due to a poloidal dominated magnetic field, i.e. along the length of the filament. A value of $\mathcal{M}/|\mathcal{W}|= 0$ suggest the absence of a magnetic field.

We find that the mean value of $\langle P \rangle / P_s$ for the entire filament is 0.044 and the mean ratio of the masses is m/m_{vir} = 0.74. The values calculated for $\langle P \rangle / P_s$ and m/m_{vir} for the entire filament imply $\mathcal{M}/|\mathcal{W}|$ =-0.28. This result suggests that a toroidal dominated magnetic field is needed to provide stability to this filament.

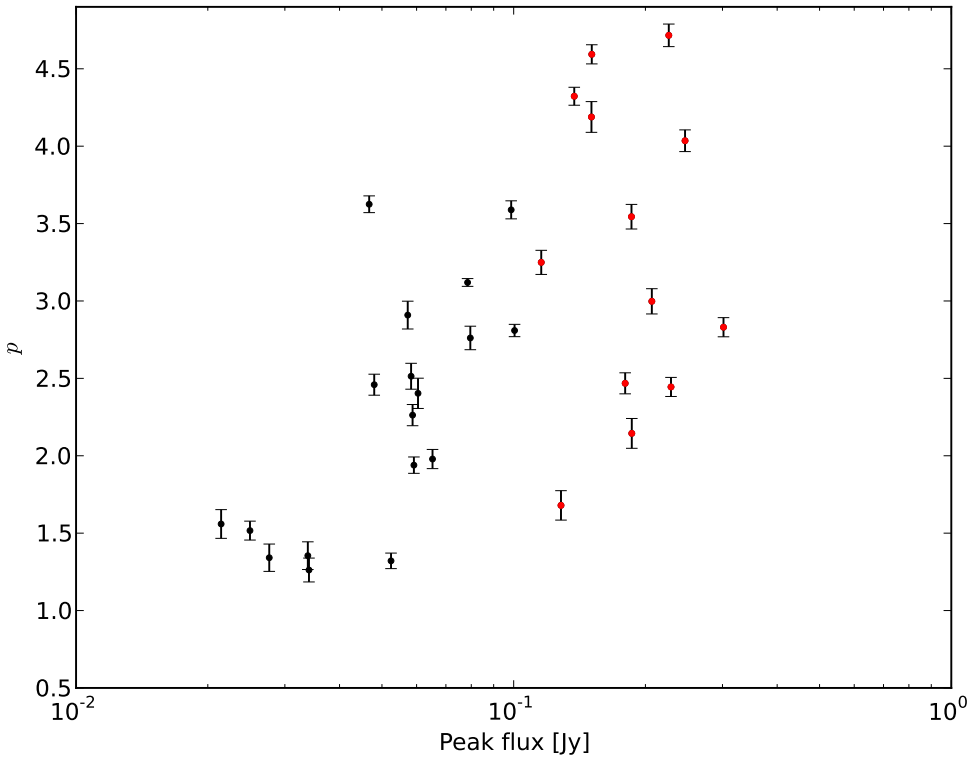

FIGURE 5.18: Plot of p, the parameter that define the shape of the density profile, vs peak flux for the clump (red points) and inter-clump (black points) region in filament B. The error bars show the χ^2 between the fit and the observed radial intensity. We can see that in general the inter-clump regions have values of p lower than the clumps.

For the inter-clump material we find an average value of $\mathcal{M}/|\mathcal{W}|$ =-2. This result implies that we need a toroidal magnetic field for the stability, this toroidal magnetic field would confine the filament preventing its expansion. For the clumps we find an averaged value $\mathcal{M}/|\mathcal{W}|$ of 0.04, closer to 0 which represent the unmagnetized solution.

This result is consistent with the analysis of the radial density profile which suggest that the filament needs a magnetic field to explain its stability. However, locally the clumps are closer to the solution with $\mathcal{M}/|\mathcal{W}|$= 0 which represent the non-magnetic solution of the virial equilibrium.

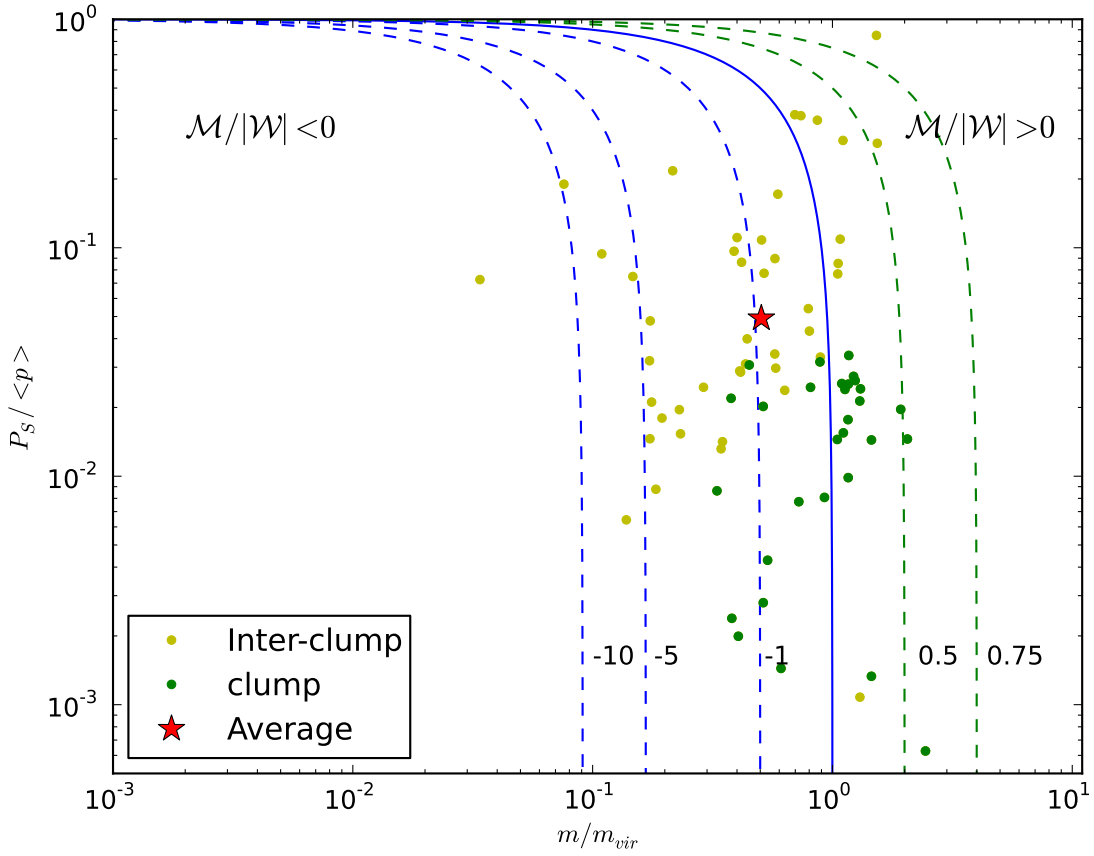

FIGURE 5.19: Plot of the $\langle P \rangle / P_s$ vs m/m_{vir} for the clumps and inter-clumps regions for filament B. Blue dashed lines: toroidal models for magnetic fields, blue solid line: unmagnetized solution, green dashed lines: poloidal magnetic field models. Yellow dots: values found for the inter-clump region of the filament; black dots: values found for the regions were clumps are located and the red star: mean value for the filament

5.7 Fragmentation

In this section we study the fragmentation of filament B. To do this we assumed that the filaments can be approximated to cylinders. We based our analysis on the fluid or *"sausage"* instability model that predict a typical separation between the clumps, given by the wavelength of the instability (see Section 1.3.3 for more details). This expected separation also depends on the nature of the filaments, whether if they can be treated as incompressible fluids or isothermal cylinders.

For filament B, we have found that the average observed separation between the clumps embedded in this filament is 2.9 pc. The average radius of the filament is 0.45 pc. If this filament is modeled as an incompressible fluid, then, the expected separation is $\lambda_{max} = 11 * 0.45\ pc = 4.95\ pc$

which is larger than the average separation observed between the clumps.

If we model this filament as an infinite isothermal cylinder, the central density derived from the 870 μm continuum observations is $\rho_c \sim 5 \times 10^{-19}$ gr cm^{-3} and the mean value of the line width observed at ^{13}CO(3-2) is 2.5 km s^{-1}, then, its scale height is $H \sim 0.12$. Comparing this scale heigh with the radius (R) of this filament, we find that the characteristic scale of fragmentation when $R \gg H$ is $\lambda_{max} = 22H = 2.6$ pc, similar to the observed separation between the clumps at 870 μm.

This suggest that if we treat filament B as an isothermal turbulent dominated filament, the separation observed between the clumps is in agreement with the theory of fluid instability that explain the fragmentation of filamentary molecular clouds into clumps.

TABLE 5.4: Filament B: derived properties of the filament.

Distance	**Length**	**Radius**	**N clumps**	**Δv**	**Temperature**	**Total mass**			**Lineal mass**			**P_s/k**	**$\langle P \rangle/k$**
				^{13}CO		**m**	**m_{vir}**	**m/m_{vir}**	**m**	**m_{vir}**	**m/m_{vir}**		
pc	pc	pc		km s^{-1}	K	$M_\odot$	$M_\odot$		$M_\odot$	$M_\odot$		10^4 K cm^{-3}	10^4 K cm^{-3}
3160	24	0.45	7	2.37	11	1×10^4	1.23×10^4	0.81	410	552	0.74	53	1189

TABLE 5.5: Filament B, properties of the clumps

	Temperature		$\mathbf{m_{dust}}$	$\mathbf{m_{vir}}$	$\mathbf{m_{N2H+}}$	$\mathbf{m_{dust}/m_{vir}}$	**Spacing**
	Color	Assumed					
	K		$M_\odot$	$M_\odot$	$M_\odot$		pc
B1	30	-	462	500	2149	0.92	1.9
B2	35	-	1960	3000	1215	0.64	5.3
B4	15	-	71	240	-	0.28	1.7
B5	24	-	20	100	-	0.20	4.5
B6	14	-	698	225	197	2.53	1.0
B7	-	30	32	125	-	0.18	-

6

Filament C: AGAL335.061-0.427

Filament C, AGAL335.061-0.427, is immersed in a region that exhibit little emission at infrared wavelengths. *Spitzer*/GLIMPSE image shows the filament as an Infrared Dark Cloud (IRDC), presenting a very irregular morphology, exhibiting some ramifications (or arms) that are perpendicular to the main axis of the filament (Figure 6.1, panel a). Some localized infrared emission suggesting star formation, such as green fuzzies, 8 μm emission, are observed but not many along the filament.

The 24 μm *Spitzer*/MIPSGAL image shows this filamentary structure as a dark cloud against the diffuse bright background, presenting a few 24 μm point sources within the filament, also indicative of star formation activity (panel b of Figure 6.1). The lack of considerable emission at infrared wavelengths suggests that this filamentary structure is in an early evolutionary stage making it an ideal object to study filaments at earliest stages of star formation.

The 870 μm the continuum emission correlates very well the IRDC seen at the GLIMPSE/MIPSGAL images, tracing the main branch and the arms observed in this filament. The dust continuum emission at 870 μm is rather smooth, having a length of $\sim$32 arc minutes along the main branch. The observed morphology is an example of a hub-tail filament (Myers 2009), with a big molecular cloud at one end, two other clumps along the main branch and ramifications to the side. At 350 μm the fragmentation of this filament is more evident, distinguishing clearly the clumps embedded in it. The emission at this frequency follows very well the emission observed at 870 μm (Figure 6.1

panels c and d).

6.1 Defining the Filament

The filament was named after the brightest clump within the region in the ATLASGAL catalog. We define the filamentary structure by following the peaks in the 870 μm emission, along the main branch. To follow these peaks we used a Python algorithm that interpolate the emission between them, obtaining the path shown in Figure 6.2. The width of this region was set to be 15 pixels (90") to each side of the path, which encloses all the emission from the main branch.

Figure 6.3 shows the flux density at 870 μm and 350 μm along the previously defined path. The shape distribution of the emission is very similar at both wavelengths and higher than the average noise of the images (4.7 mJy at 870 μm and 0.2 Jy at 350 μm). Clearly distinguished are the the sub structures within the filament, identifying the regions where the clumps are located, even the clumps embedded in the more extended emission. .

From the 870 μm emission, we derived the projected diameter of filament C. This was done by fitting a Gaussian to the radial dispersion of the detected at 870 μm at each point along the path of the filament. The FWHM obtained from this fit was used to estimate the projected radius of the filament, defined as FWHM/2. This filament has a mean radius of ~32 arc seconds.

6.2 Physical coherence of the observed filamentary structure

To establish whether the filament observed at 870 μm is a single coherent structure, we mapped the ^{13}CO(3-2) molecular line emission toward it. Figure 6.4 (top panel) shows the velocity integrated intensity maps of the ^{13}CO(3-2) emission, overlaid to the continuum emission. This figure shows a high correlation in the morphology of the main branch of this filament observed between the continuum and molecular line emission.

Figure 6.4 (right and lower panels) shows the position-velocity map (l,v) and (b,v) integrated over both Galactic latitude and longitude respectively, of the ^{13}CO(3-2) emission. This figure shows two different central velocities along this filament: the upper left side has a mean velocity of -43 km s^{-1} while the lower left part of this filament has a mean central velocity of -40 km s^{-1} . In the middle part of the filament we observe emission at both velocities. Since the ^{13}CO(3-2) line widths are relatively wide, ranging from 2 km s^{-1} to 4 km s^{-1}, the difference in velocities are

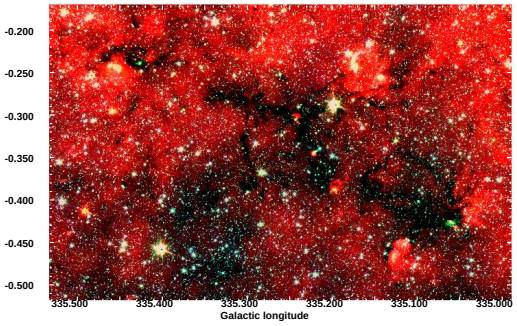

(a) *Spitzer*/GLIMPSE 3.5 μm- 8 μm

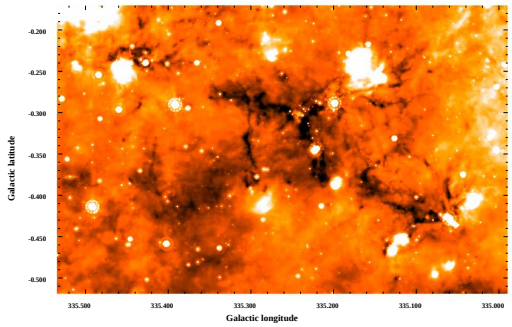

(b) *Spitzer*/MIPSGAL 24 μm

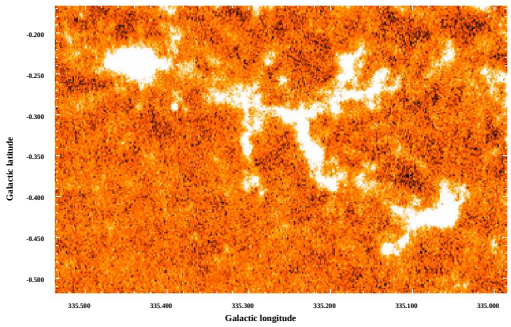

(c) APEX/LABOCA 870 μm

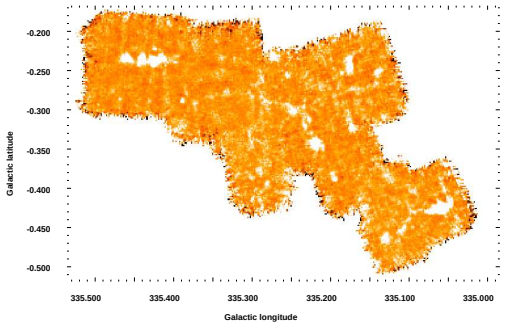

(d) APEX/SABOCA 350 μm

FIGURE 6.1: Multi wavelength continuum images of region C. We can see at *Spitzer* images that this filamentary structure appears as an infrared dark cloud even at 24 μm, indicating an early evolutionary stage. However, we can see localized regions with point sources at 24 μmand other star formation indicators (e.g. green fuzzies, bright 8 μm). The emission at millimeter wavelength from LABOCA and SABOCA traces very well the IRDC seen and the clumps embedded.

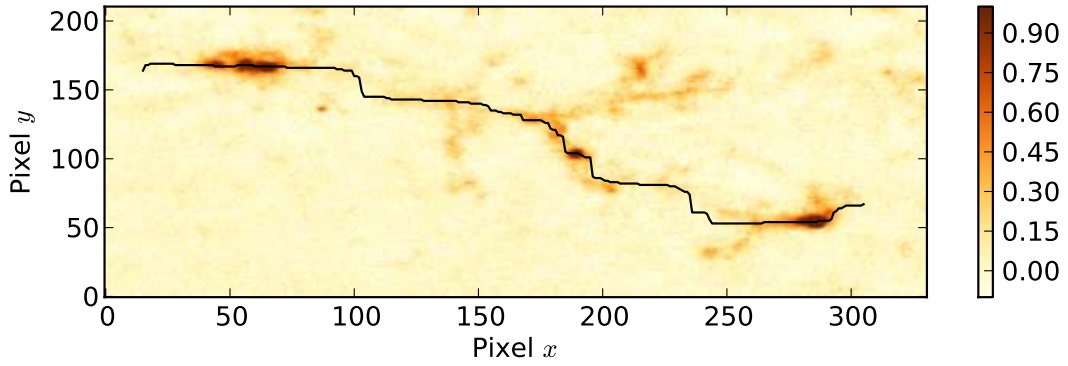

FIGURE 6.2: Path defined for filament C. Color scale show the 870 μm emission (scale in Jy/beam), in black is the path defined for this filament. The width of the region that contains the dust continuum emission was defined as 15 pixel along each side of this path.

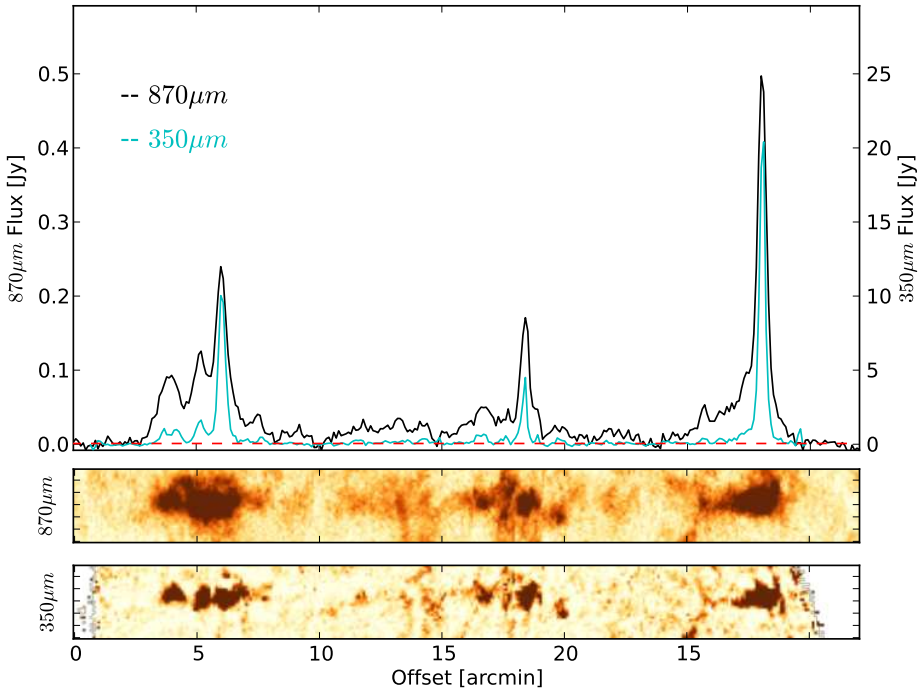

FIGURE 6.3: Distribution of dust continuum emission along the filament. Top panel: Flux detected both 870 μm (black line) and 350 μm (blue line) continuum emission along the path defined for filament C, red dotted line represents the mean noise in the map (4.7 mJy at 870 μm and 0.2 Jy at 350 μm). Lower panels: Color image of the emission at 870 μm and 350 μmobserved toward the filament.

Table 6.1: Filament C, star formation activity

ID	ATLASGAL Name	GLIMPSE 3.6 - 8 μm	MIPSGAL 24 μm	ATLASGAL[b]	IRAS
C1	AGAL335.461-0.237	Dark	Dark	Bright	-
C2	AGAL335.441-0.237	Dark	Dark	Bright	16264-4841
C3	AGAL335.427-0.241	Green fuzzies[a]	Point source	Bright	-
C4	AGAL335.221-0.344	Green fuzzies[a]	Point source	Bright	-
C5	AGAL335.061-0.427	Green fuzzies[a]	Point source	Bright	16256-4905

[a] Green fuzzies: Enhancement at 4.5 μm.

[b] Bright emission: Peak emission > 1 Jy/beam; weak emission: Peak < 1 Jy/beam

within the width of the lines, suggesting that this filament is physically connected representing a single coherent structure.

The ^{13}CO(3-2) central line velocity, v_{LSR}, was used to derive the distance to the filament, using the model for the rotational curve of the Galaxy outlined in Section 1.4.3.2. Since this structure appears as dark against the extended Galactic background emission, we assume that it lies at the near kinematic distance. Under these assumptions the distance to this filament is 3.6 kpc. Using this distance, the radius of the filament is 0.56 pc and the length is 33 pc.

6.3 Properties of the embedded clumps within the filament

From the ATLASGAL point source catalog we identified five clumps embedded in filament C. Figure 6.5 shows the position of the clumps along the filament. The names of the clumps are taken from their denomination in the ATLASGAL catalog, but for simplicity we assign them an ID of C1, C2 etc. Three of these clumps are embedded in the molecular cloud located to the upper left end of this filament and the rest are evenly distributed along its main branch.

Clumps C1 and C2 appear dark in both GLIMPSE and MIPSGAL images suggesting that these clumps are in early stage of evolution. Clump C3 shows green fuzzies (enhancement at 4.5 μm) and point like emission at 24 μm, both indicators of star formation activity. Clumps C4 and C5 show bright emission at all infrared wavelengths, suggesting that both clumps are in a more evolve evolutionary stage. Table 6.1 summarizes the star formation activity based on their emission at IR and continuum. Column 6 gives the name y IRAS association to the clumps.

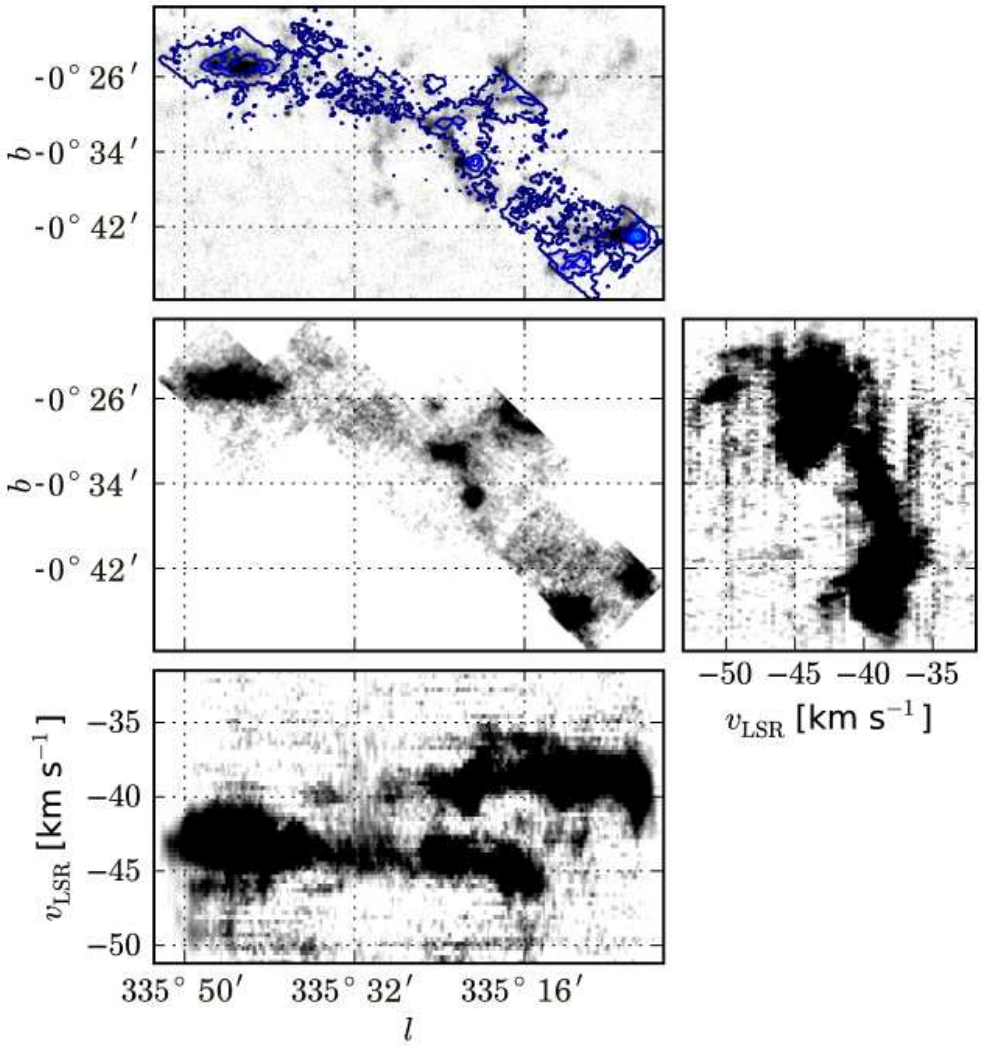

FIGURE 6.4: ^{13}CO(3-2) emission toward filament C. Top panel shows the integrated intensity map as contours over the dust thermal emission at 870 μm. The contours levels are from 3 to 50σ in steps of 3σ with σ = 3.3 K km s^{-1}. Lower and right panels shows the position velocity map (l,v) and (b,v) integrated over both Galactic latitude and longitude respectively of filament C. We see that this filament corresponds to a single coherent structure since the dispersion in velocity along it is similar to the line width observed.

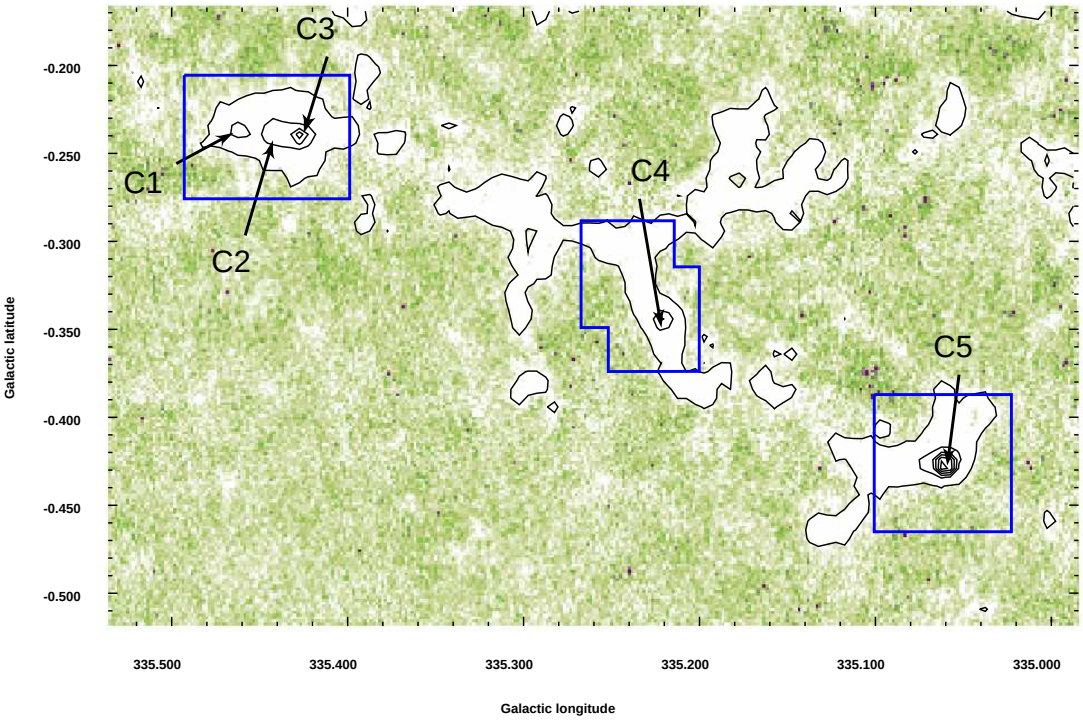

FIGURE 6.5: Color image 870 μm continuum emission toward filament C, contours from 3σ to peak emission in logarithmic scale. Arrows indicate the position of the clumps embedded within this filament and blue boxes shows the area covered by the MALT90 observations. Contours shows the emission > 3σ noise.

For each clump we derive the peak flux, diameter of the half peak emission and integrated intensity at both 870 μm and 350 μm. These values are given in Table 6.2. The spacings between the clumps were computed from their relative position (from the ATLASGAL catalog) and their angular separation. The spacing was measured between two consecutive clumps, starting with clump C1. The derived separations are listed in Table 6.5. The clumps embedded in this filament have a mean separation of $\sim$ 10 pc, with the exception of clumps C1, C2 and C3 which are located very close together within a giant molecular cloud, thus having a mean separation of $\sim$ 1 pc.

We also obtained their properties of the ^{13}CO(3-2) line emission, by fitting a Gaussian to the mean value of the 3σ ^{13}CO(3-2) emission covered by each clump, increasing in this way the signal to noise in each spectrum. From these fits we obtained the peak temperature (T_{peak}), central velocity (v_{LSR}), line width (Δv) and integrated intensity ($\int T_b dv$, II in the table) of each spectrum. The values obtained, from the continuum and molecular line emission, are listed in Table 6.2.

The clumps with higher fluxes at 870 μm, clumps C3, C4 and C5, were also observed in N_2H^+(3-2). Figure 6.6 shows the N_2H^+(3-2) spectra toward the clumps. Only in one of these three

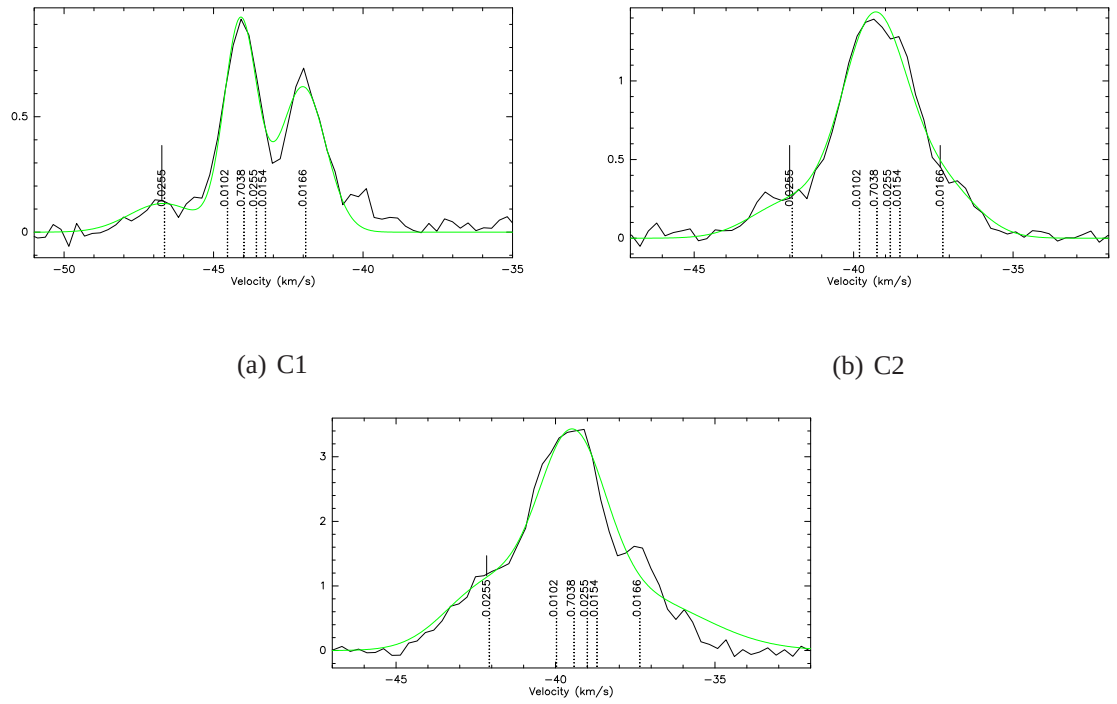

(a) C1

(b) C2

(c) C3

FIGURE 6.6: Spectra of the N_2H^+observations toward clumps C1, C2 and C3. Each plot shows the Gaussian fit (green line) and the position of the individual hyperfine component. The numbers indicate the relative intensity of the lines. Here is clearly seen that due to the large linewidth of the hyperfine components the hyperfine components appear blended.

clumps it is possible to distinguish the N_2H^+(3-2) hyperfine structure. For the other two clumps the large width in velocity of the hyperfine components makes it impossible to distinguish the hyperfine structure within the spectra. For all the N_2H^+(3-2) spectra we performed a three component Gaussian fit, with the position of each component fixed to the theoretical position of each hyperfine component. Table 6.2 shows the peak temperatures (T_{peak}), central velocities (v_{LSR}) and line widths (Δv) of the fits performed to each spectrum.

TABLE 6.2: Parameters of the clumps in filament C from their continuum and molecular emission.

	870 μm				**350 μm**				**^{13}CO(3-2)**					**N_2H^+(3-2)**			
ID	Peak Flux	Diameter		Int. Flux	Peak Flux	Diameter		Int. Flux	T_{peak}	v_{LSR}	Δv	II	Diameter	T_{peak}	v_{LSR}	Δv	τ
	Jy/Beam	’	pc	Jy	Jy/Beam	’	pc	Jy	km s^{-1}	km s^{-1}	K	K km s^{-1}	pc	km s^{-1}	km s^{-1}	K	
C1	1.15	0.4	0.4	1.2(0.1)	13.70	0.4	0.4	35.3(1.9)	3.72	-42.10	2.99(0.58)	11.88(2.32)	0.6				
C2	1.30	0.5	0.5	2.4(0.1)	9.09	0.3	0.3	21.9(1.4)	3.72	-42.40	2.55(0.42)	10.22(1.71)	0.3				
C3	2.53	0.7	0.7	5.5(0.3)	43.04	0.5	0.5	143.8(2.6)	3.71	-42.32	2.07(0.33)	8.18(1.30)	1.1	0.12	-46.69	2.65 (0.56)	-
														0.90	-44.09	1.29 (0.06)	-
														0.62	-42.01	1.79 (0.14)	-
C4	1.77	0.5	0.5	2.5(0.3)	21.08	0.5	0.5	80.8(1.4)	4.13	-39.55	2.21(0.33)	9.73(1.46)	0.7	0.22	-42.00	2.83 (0.34)	-
														1.36	-39.35	2.39 (0.06)	-
														0.32	-37.26	2.57 (0.20)	-
C5	5.18	0.8	0.8	12.1(0.5)	84.20	0.7	0.7	340.6(2.8)	4.90	-39.25	4.20(1.04)	21.95(5.45)	0.9	0.95	-42.157	3.09(0.37)	-
														2.80	-39.50	2.48 (0.15)	-
														0.80	-37.44	4.95 (0.56)	-

6.4 Chemistry, evolutionary stage and kinematics of the brightest clumps

To asses the chemistry and evolutionary stage of the clumps embedded in filament C, we performed MALT90 observations covering the five clumps detected in this filament. For clumps C1 and C2 we detected only N_2H^+ and HCN, both molecular transitions that traces dense gas. We didn't detect any hot chemistry molecules (e.g. CH_3CN, HNCO) which suggest that these clumps are in a early stage of evolution. These results agree with the lack of emission observed in both the GLIMPSE and MIPSGAL images toward these clumps.

Toward clump C3 we detected the largest number of molecular transitions, detecting emission (integrated intensity $> 3\sigma$ noise) in seven of the sixteen molecular lines observed. We detected: N_2H^+(1-0), HCO^+, $H^{13}CO^+$ and HCN which are molecular lines that trace dense gas. We also detected HC_3CN, observed typically toward hot cores, C_2H and SiO observed toward photodissociation region and shocked gas respectively. The molecular lines detected agree with the presence of the green fuzzies detected at infrared wavelength, suggesting that this clump is hot with signs of current star formation.

Toward clump C4, located at the center of the filament, we detected emission in five molecular lines, four of them correspond to high density tracers: N_2H^+(1-0), HNC, $H^{13}CO^+$ and HCO^+. In addition, we detected emission in C_2H and typicaly observed toward photodisociation regions. These detections and the 24 μm point source detected toward this clump suggest that it is hot and in an evolved evolutionary stage.

Clump C5 presents emission in five of the sixteen molecular lines observed. The only density tracer detected toward this clump are N_2H^+ and HCN. We also detected emission in HC_3CN, C_2H and SiO typically observed toward hot cores. The infrared emission and hot chemistry molecules detected toward this clump suggest that it is hot with signs of current star formation.

For each clump we made velocity integrated intensity maps of the molecules detected. Figure 6.7 shows the integrated intensity maps toward clumps C1, C2 and C3. The range of velocities was set from -52 km s^{-1} to -38 km s^{-1}, which include all the emission detected. This figure shows that clumps C1 and C2, which are dark at infrared wavelengths, only present some extended emission at HNC and N_2H^+. The emission toward clump C3 is the dominant in these maps, matching very well the position of the point source observed at 24 μm (Figure 6.7 upper panel)

Figure 6.8 shows the integrated intensity maps toward clump C4. The range in velocity used for all the transitions ranges from -45 km s^{-1}to -35 km s^{-1}. Only N_2H^+ and HNC shows significant emission. Their morphology traces very well the emission detected at 870 μm. Integrated intensity

maps of the detected molecular transitions toward clump C5 are shown in Figure 6.9. In these maps we see that the morphology of the gas correlates with the dust emission. The molecular emission from the hot chemistry molecules also matches very well the location of the 24 μm point source.

For each clump we fit a Gaussian to the peak position of the molecular lines detected, obtaining for each transition its central velocity (v_{LSR}), peak antenna temperature (T_{peak}), line width (Δv) and integrated intensity (II). We also obtained the (l,b) position of the peak spectrum expressed as offsets with respect to the position of the peak spectrum at N_2H^+(1-0) (Δl and Δb) and the total integrated intensity (I_T). The parameters derived from these observations are summarized in Table 6.3. We also fitted the hyperfine structure observed in the N_2H^+(1-0) emission. From these fits we obtained the excitation temperature, line widths and opacity toward each clump. These values are summarized in Table B.1.

The spectra of all the molecules detected at the position of the N_2H^+(1-0) peak emission for clumps C1, C2, C3, C4 and C5 are shown in Figures 6.10, 6.11, 6.12, 6.13 and 6.14 respectively. For clumps C1 and C2 we see that the peaks of the HCN molecular line have a blue shifted velocity to that observed at N_2H^+(1-0). For both clumps we also noticed a second component blue-shifted with respect to the main line in the ^{13}CO(3-2) spectra. For clump C2 we see self absorption in the ^{13}CO(3-2) spectrum, which is also noticeable in the N_2H^+(1-0) spectrum. For clump C3 there is a difference in velocities between the N_2H^+(1-0) and HCO^+ lines and auto absorption at ^{13}CO(3-2)with a double peaked red asymmetry, suggesting outward motions.

The spectra of clump C4 shows the HCO^+ peak at a lower velocity compared to the N_2H^+ peak. The rest of the transitions have their peaks at the same velocity. The profiles of the lines are symmetric. For clump C5 the spectra are also symmetric with all the peaks at the same velocity.

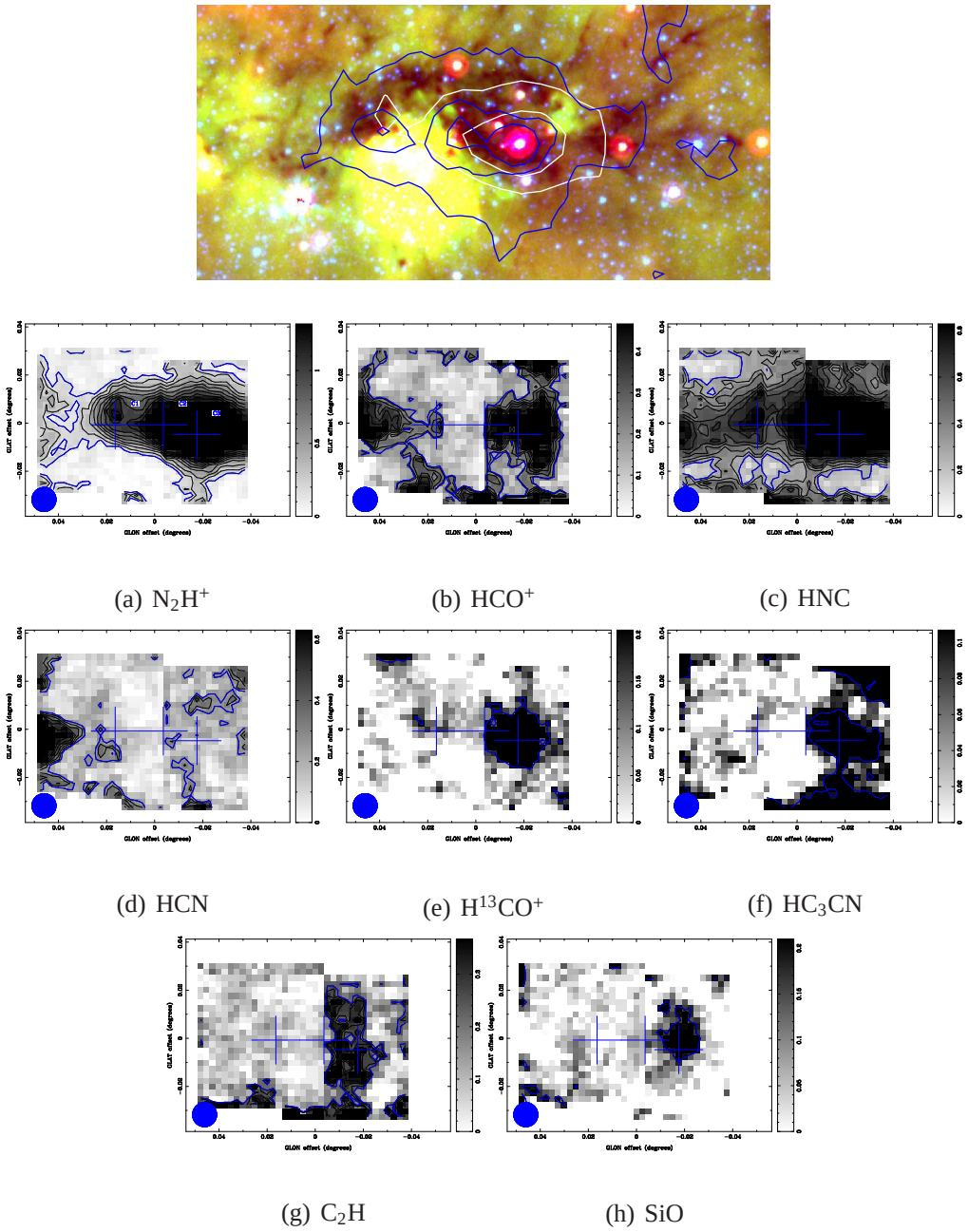

(a) N_2H^+ (b) HCO^+ (c) HNC

(d) HCN (e) $H^{13}CO^+$ (f) HC_3CN

(g) C_2H (h) SiO

FIGURE 6.7: Integrated intensity maps toward clumps C1, C2 and C3. Top panel: IRAC three color image of the region covered by the MALT90 data (Red: 24 μm, blue: 8 μm, green: 4.5 μm), blue contours show the emission at 870 μm, while the white contours N_2H^+(1-0) emission. Panels (a)- (h): Maps of integrated intensity of the detected molecular line transitions (II > 3σ). Contours represent the emission from 90% of the peak to 3σ noise emission (blue contour) in steps of 10%. The crosses indicate the positions of the clumps and the blue circle shows the beam size. The color bar shows the value of the peak in the integrated intensity for each molecular line.

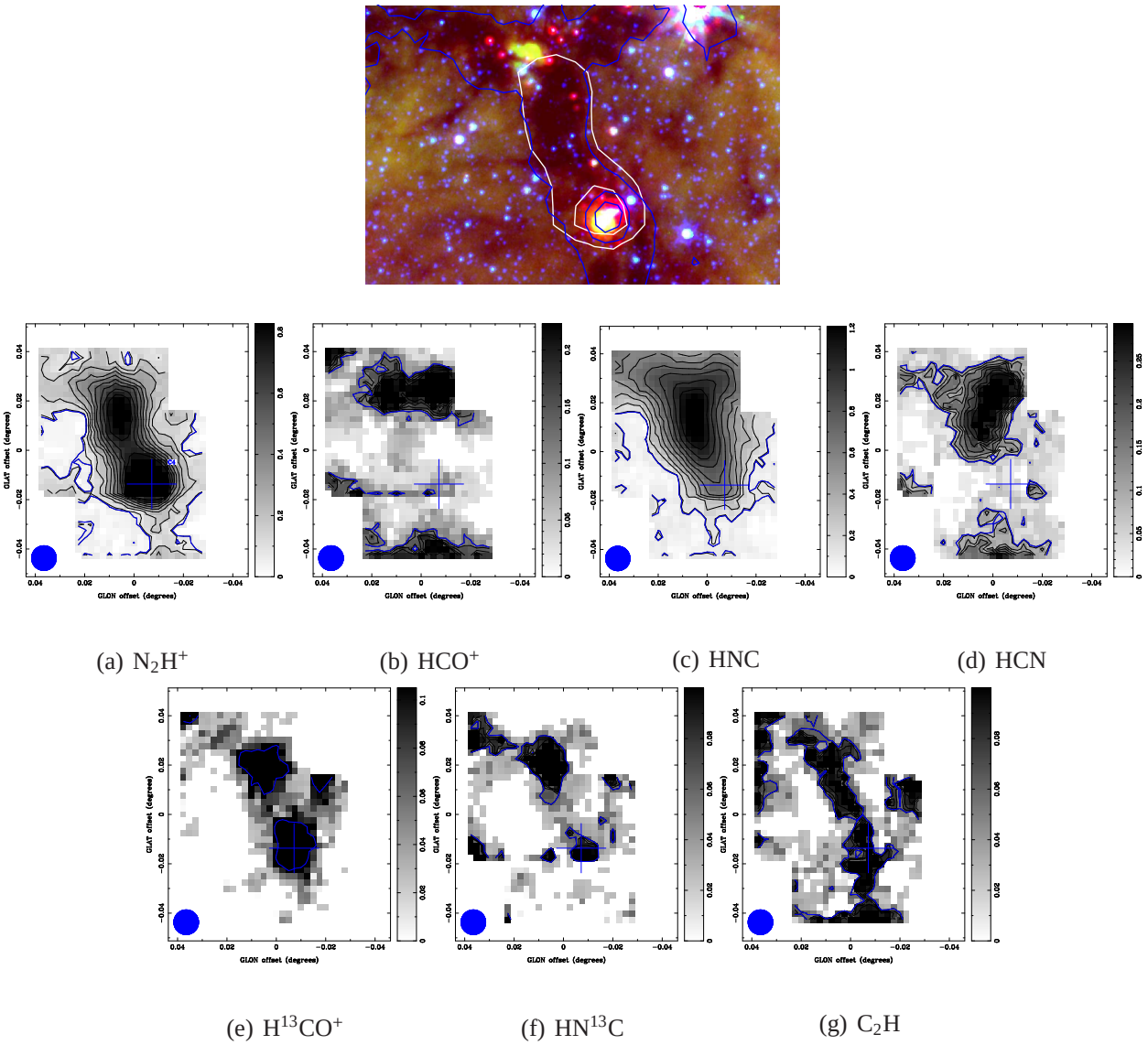

(a) N_2H^+ (b) HCO^+ (c) HNC (d) HCN

(e) $H^{13}CO^+$ (f) $HN^{13}C$ (g) C_2H

FIGURE 6.8: Integrated intensity maps toward clumps C4. Top panel: IRAC three color image of the region covered by the MALT90 data (Red: 24 μm, blue: 8 μm, green: 4.5 μm), blue contours show the emission at 870 μm, while the white contours N_2H^+(1-0) emission. Panels (a)- (g): Maps of integrated intensity of the detected molecular line transitions (II > 3σ). Contours represent the emission from 90% of the peak to 3σ noise emission (blue contour) in steps of 10%. The crosses indicate the positions of the clumps and the blue circle shows the beam size. The color bar shows the value of the peak in the integrated intensity for each molecular line.

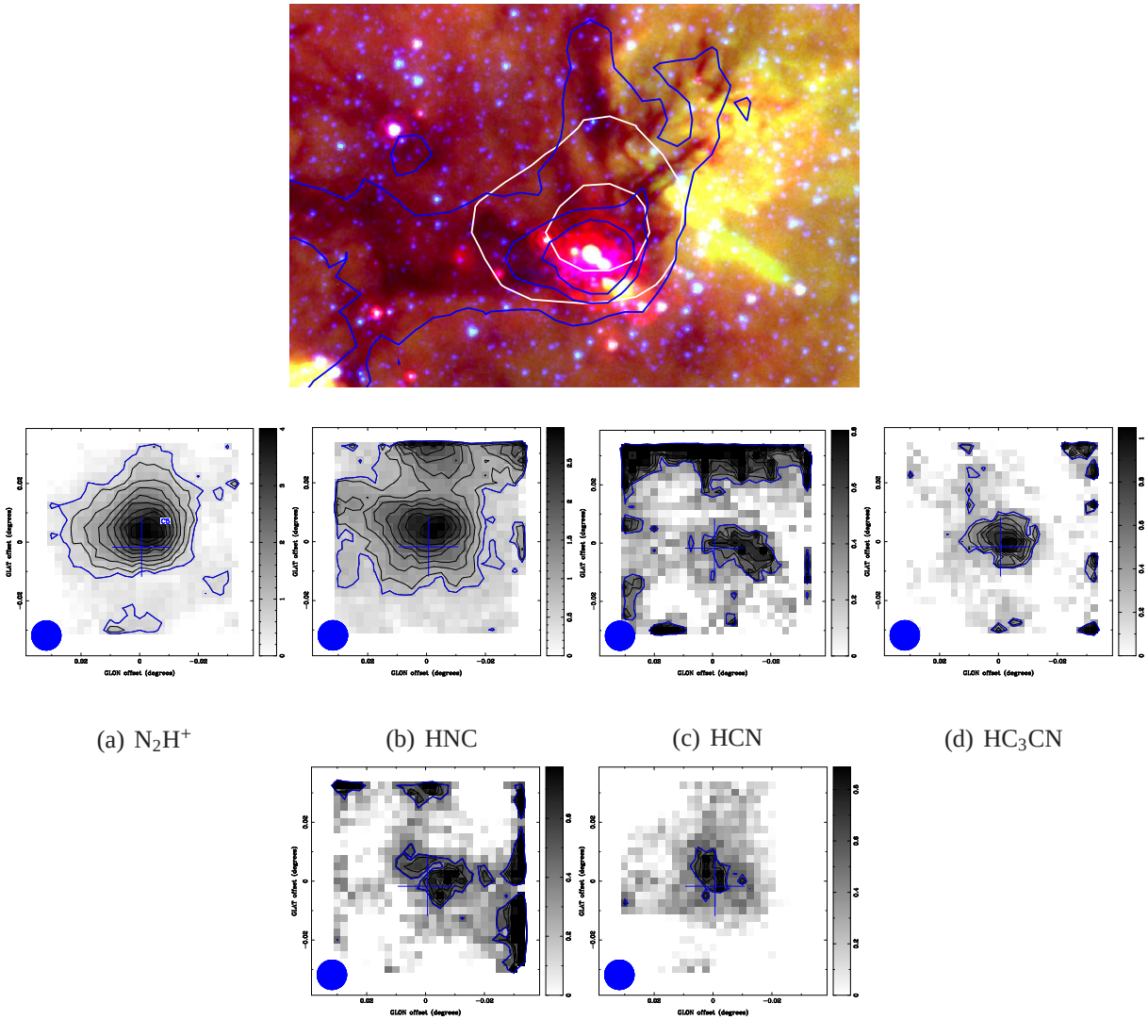

(a) N_2H^+ (b) HNC (c) HCN (d) HC_3CN

(e) C_2H (f) SiO

FIGURE 6.9: Integrated intensity maps toward clumps C5. Top panel: IRAC three color image of the region covered by the MALT90 data (Red: 24 μm, blue: 8 μm, green: 4.5 μm), blue contours show the emission at 870 μm, while the white contours N_2H^+(1-0) emission. Panels (a)- (f): Maps of integrated intensity of the detected molecular line transitions (II > 3σ). Contours represent the emission from 90% of the peak to 3σ noise emission (blue contour) in steps of 10%. The crosses indicate the positions of the clumps and the blue circle shows the beam size. The color bar shows the value of the peak in the integrated intensity for each molecular line.

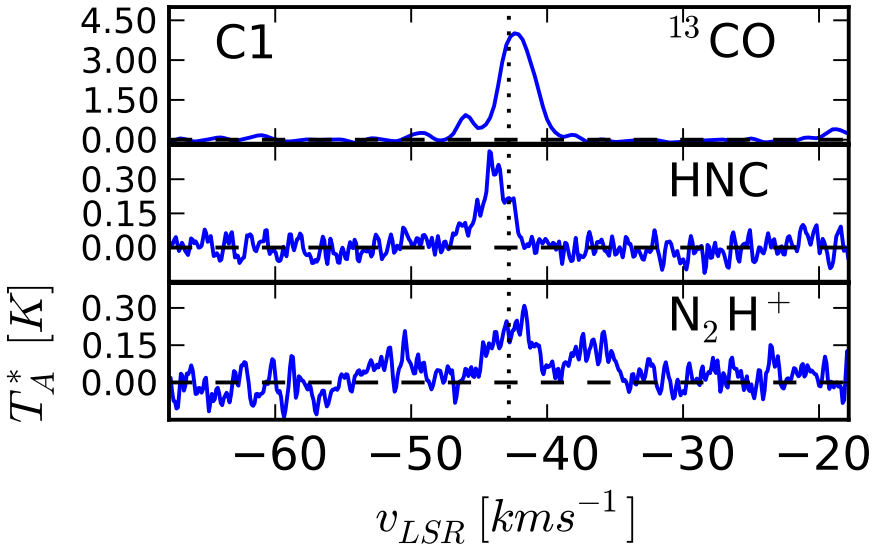

FIGURE 6.10: Spectra toward clump C1. Each spectrum are at the (l,v) position corresponding to the peak emission at N_2H^+. Dotted line shows the central velocity of the N_2H^+(1-0) emission.

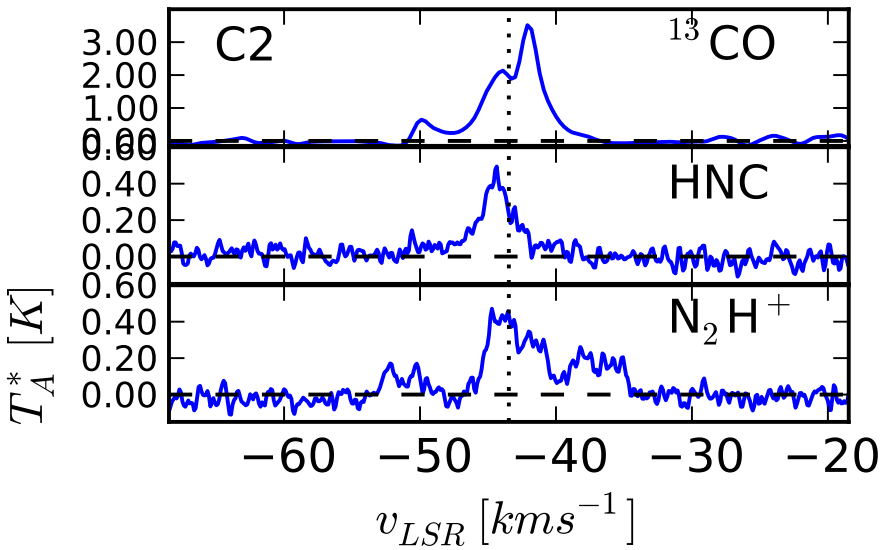

FIGURE 6.11: Spectra toward clump C2. Each spectrum are at the (l,v) position corresponding to the peak emission at N_2H^+. Dotted line shows the central velocity of the N_2H^+(1-0) emission.

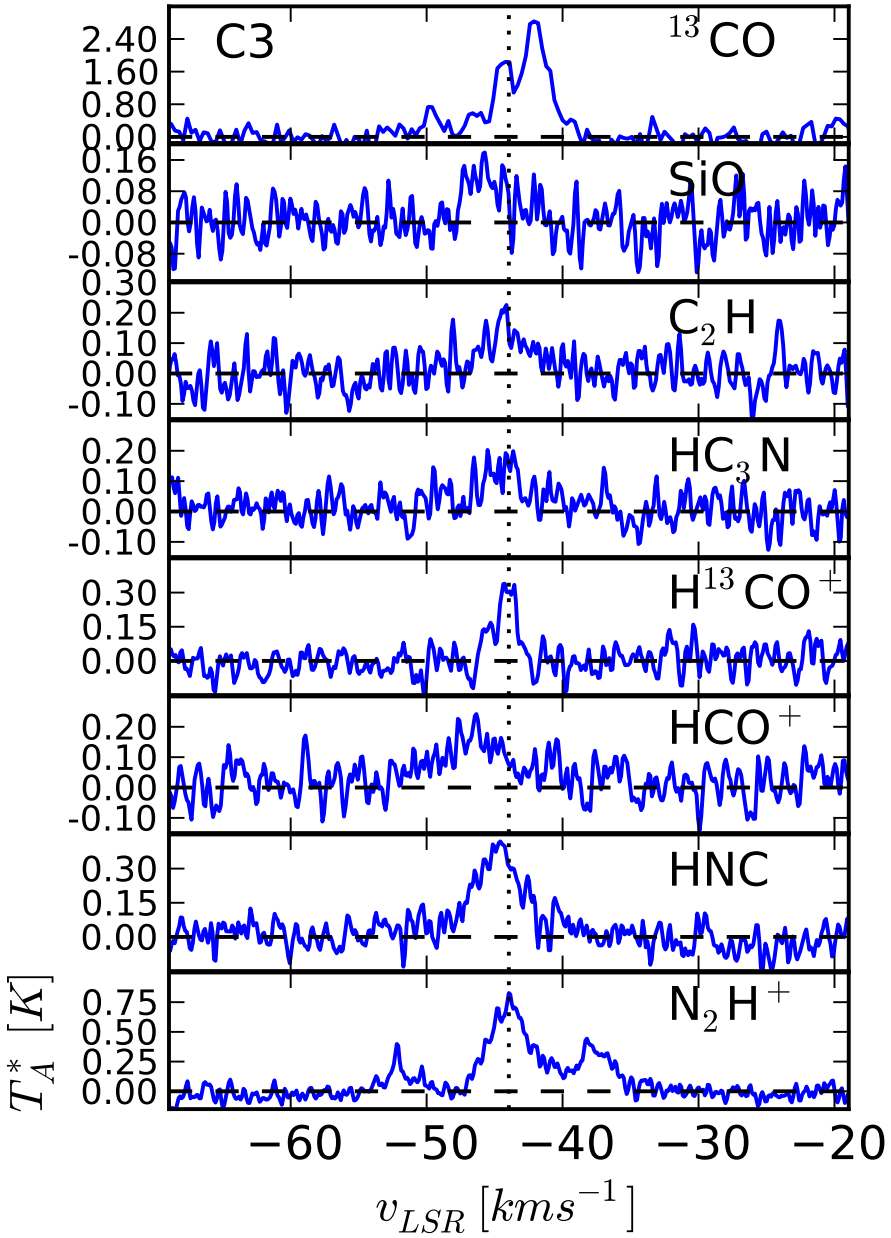

FIGURE 6.12: Spectra toward clump C3. Each spectrum are at the (l,v) position corresponding to the peak emission at N_2H^+. Dotted line shows the central velocity of the N_2H^+(1-0) emission.

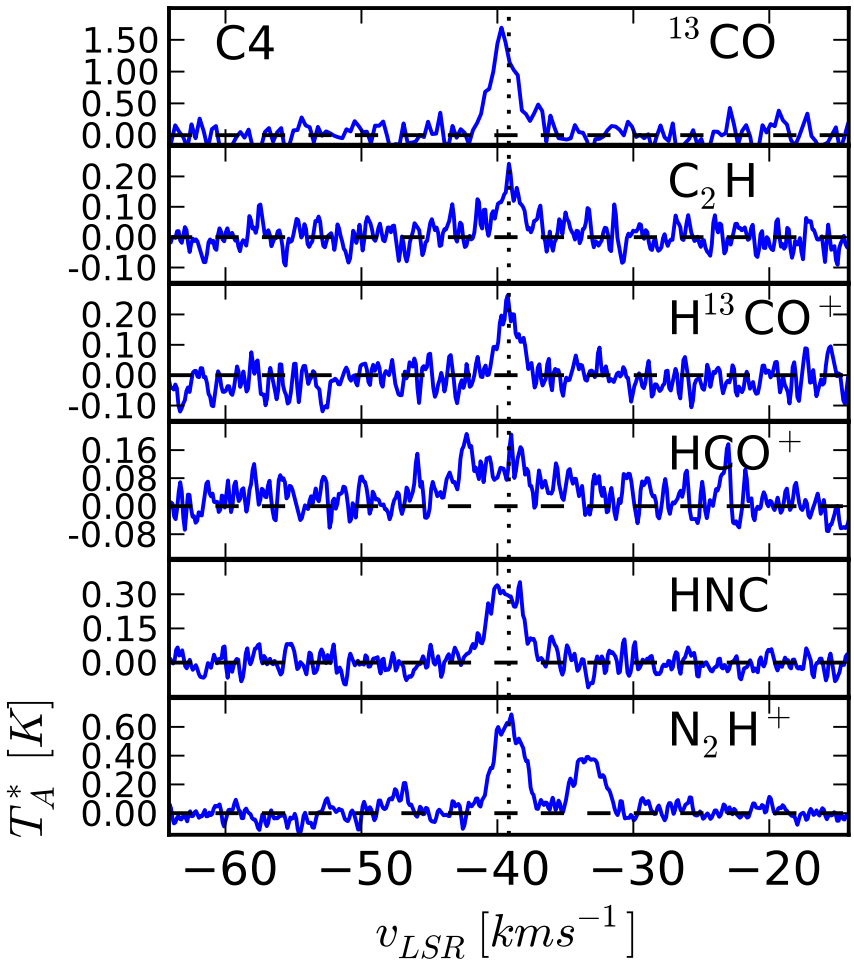

Figure 6.13: Spectra toward clump C4. Each spectrum are at the (l,v) position corresponding to the peak emission at N_2H^+. Dotted line shows the central velocity of the N_2H^+(1-0) emission.

TABLE 6.3: Filament C: Parameters derived from Gaussian fits to the MALT90 spectra

Source	Molecule	Δl[a]	Δb[a]	T_{peak}	V_{LSR}	Δv	II[b]	I_T[c]	*rms*
		"	"	K	km s^{-1}	km s^{-1}	K km s^{-1}	K km s^{-1}asec^2	K/channel
C1 AGAL335.461-0.237	$N2H^+$	0	0	0.27	-42.94	2.7	1.52	140	0.23
	HNC	0	0	0.33	-44.01	1.70	0.82	406	0.24
C2 AGAL335.441-0.237	$N2H^+$	0	0	0.38	-42.94	2.8	3.62	587	0.23
	HNC	18	18	0.42	-44.00	1.73	1.52	386	0.22
C3 AGAL335.427-0.241	$N2H^+$	0	0	0.94	-43.92	3.26	3.26	538	0.23
	HCO^+	-190	-7	0.36	-43.91	1.05	0.40	19	0.23
	$H^{13}CO^+$	-18	-9	0.40	-43.98	1.40	0.59	730	0.23
	HNC	-54	-9	0.63	-44.49	1.97	1.32	1950	0.22
	HC_3N	-18	0	0.17	-43.98	1.93	0.35	760	0.22
	C_2H	-18	-18	0.36	-43.55	2.06	0.79	690	0.23
	SiO	-18	-36	0.15	-44.87	3.97	0.63	600	0.23
C4 AGAL335.221-0.344	$N2H^+$	0	0	0.84	-39.06	2.35	2.10	312	0.24
	HCO^+	-12	-124	0.35	-40.30	1.24	0.46	21	0.23
	$H^{13}CO^+$	-30	-88	0.34	-39.67	1.15	0.42	1300	0.24
	HNC	-39	-97	0.83	-40.41	2.09	1.85	131	0.23
	C_2H	0	36	0.33	-39.79	0.87	0.31	650	0.24
C5 AGAL335.061-0.427	$N2H^+$	0	0	1.33	-39.34	2.06	2.92	416	0.21
	HNC	-18	0	0.95	-39.04	1.99	2.01	111	0.20
	HC_3N	9	18	0.52	-39.63	1.38	0.76	440	0.38
	C_2H	54	18	0.51	-40.18	0.7	0.38	295	0.20
	SiO	-18	18	0.25	-37.75	1.29	0.34	890	0.37

[a] Offset of the peak emission from the N_2H^+(1-0) peak.

[b] Integrated intensity at the peak.

[c] Total integrated intensity, from the MALT90 catalog.

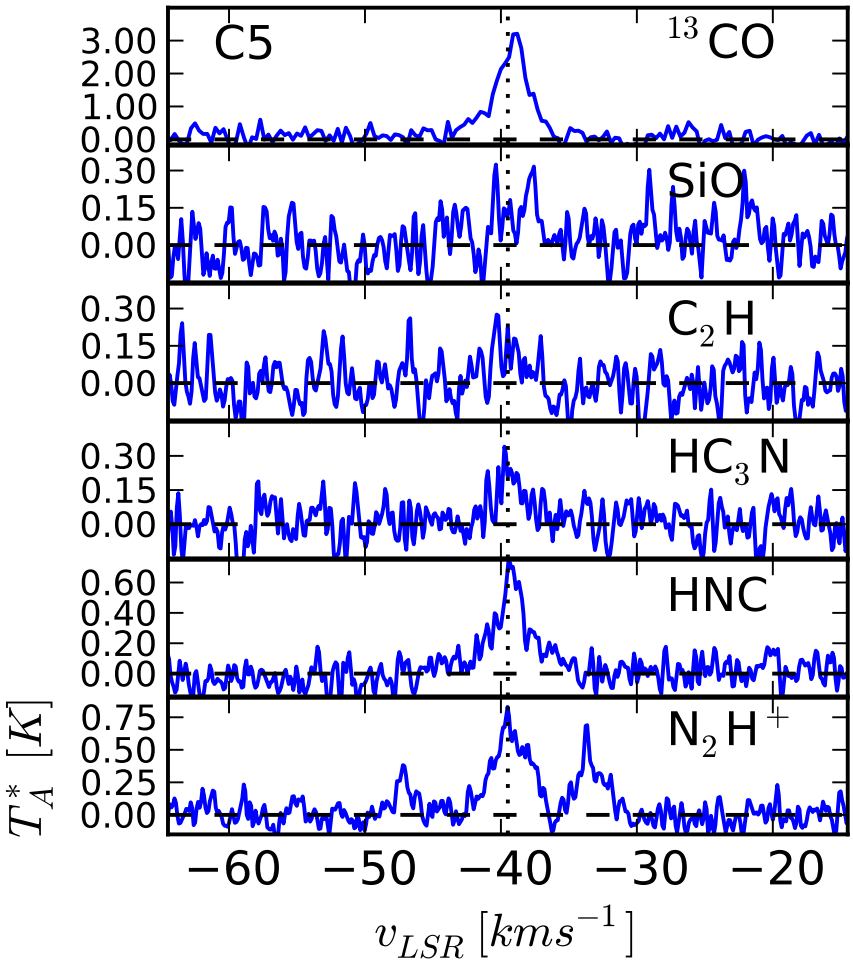

Figure 6.14: Spectra toward clump C5. Each spectrum are at the (l,v) position corresponding to the peak emission at N_2H^+. Dotted line shows the central velocity of the N_2H^+(1-0) emission.

6.5 Physical properties of the filament and its clumps

In this section we derive the physical properties (temperature, mass, internal and external pressure) of filament C and the clumps embedded in it using the observations, of both continuum and molecular line, described in the previous section.

6.5.1 Color temperature

From the observations at 350 μm and 870 μm we derived the *color temperature* of filament C. This was done from the ratio between the continuum emission at both wavelengths (see Section 1.4.2.2 for further details). Because the color temperature depends on the value of the spectral index β, we calculated the color temperature using different values of β. The average color temperature found toward this filament was 15 K, 12 K, 10 K and 8 K using a spectral index β =1, 1.5, 2 and 2.5 respectively, presenting higher temperatures locally toward the clumps. Figure 6.15 shows the map of temperatures obtained using different values of β. The temperature map obtained with β = 1.5 have a mean temperature similar to those observed toward cold molecular clouds, thus for the rest of the computations we use the color temperature derived with this spectral index.

The mean color temperatures derived using β = 1.5 toward clumps C3 and C4 is ~40 K, toward clumps C1 and C5 is ~27 K and ~15 K toward clump C2 (Table 6.5). These temperatures are consistent with the temperature observed toward clumps presenting the same characteristics in their infrared emission detected in the GLIMPSE and MIPSGAL images (Rathborne et al. 2010). We compared the derived color temperature, for each clumps, with the presence or absence of molecular emission. Clumps C3 and C5 presents SiO and HC_3CN typically observed toward hot cores, this emission and the infrared emission observed suggests that these clumps might be considerer as active clumps and thus the mean color temperature derived for these clumps (27 K and 42 K) agree with their expected dust temperatures.

Clump C4 presents C_2H observed toward photodissociation regions. We also detected a point source emission at 24 μm and at 8 μm suggesting that this clump corresponds to a hot core which is in agreement with its derived average color temperature of 46 K. Clumps C1 and C2 have mean temperatures of 29 K and 14 K, both clumps appear dark in the infrared images, suggesting that this clumps are quiescent, with low temperatures.

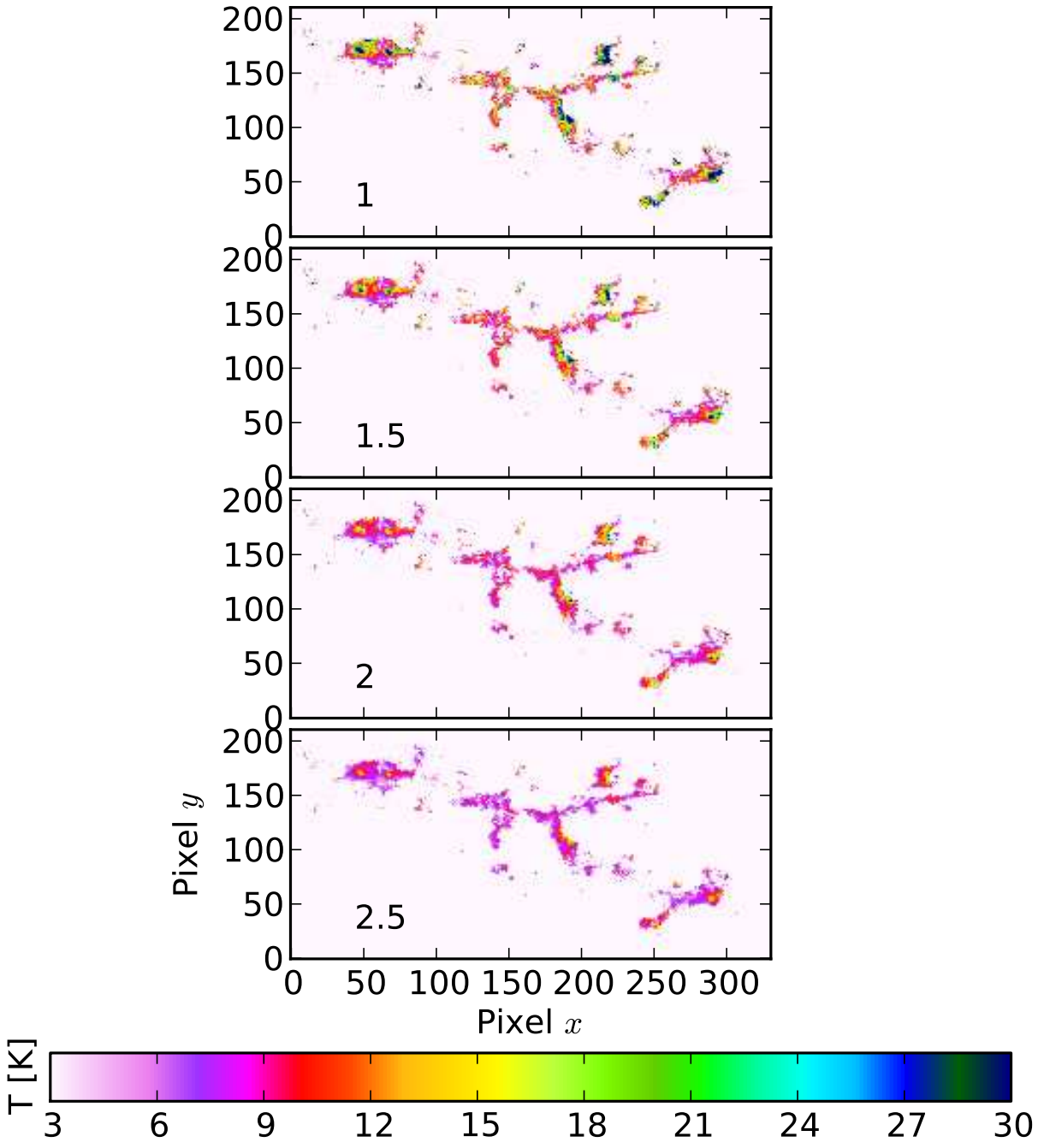

Figure 6.15: Derived color temperature for filament C. The panels show the derived color temperature using different values for the spectral index β. The temperature along the filament decreases with higher values of β, the average temperature ranges from ~15 to 8 K and in all cases the temperature peaks locally toward the clumps.

6.5.2 Column density and mass

In this section we describe the methods used to compute the column density and mass for filaments C. From the 870 μm continuum and ^{13}CO(3-2) molecular line emission we compute the mass and virial mass of the filament and the clumps embedded in it.

6.5.2.1 Column density and total mass of the filament

The radial column density was obtained from the 870 μm emission (see Section 1.4.2.2 for further details). The calculus was done over perpendicular emission along the path obtained for this filament (Figure 6.2). The temperature used is described in Section 6.5.1, which varies along the filament having an average temperature of 12 K and higher temperatures locally toward the clumps, using this temperature we attempt to avoid over estimation of the mass toward the clumps. The dust opacity used have a value of $k_{870} = 0.012$ cm^{2}gr^{-1}. Filament C has an average column density of 2×10^{22} cm^{-2}. The mass of the filament was obtained by integrating the radial column density over the diameter and length of the filament. The total mass derived for filament C was found to be 1.2×10^4 M$_\odot$.

The virial mass was obtained from the ^{13}CO(3-2) line width along the filament. Since this molecular cloud has a filamentary shape we compute the virial mass at each point along the path defined for this filament using Equation 1.6. The total virial mass was determined by adding the individual virial masses determined for each point along the filament, obtaining a value of 9×10^3 M$_\odot$.

There is agreement between the mass derived from the dust and the virial mass is this filament. The ratio between the total dust mass and total virial mass, m/m_{vir}, is 1.2. This ratio implies that on global scale filament C is found to be in virial equilibrium.

6.5.2.2 Mass of the clumps

For each clumps we derived their mass from the 870 μm dust continuum emission using Equation 1.32. The temperature used for each clump was the average color temperature derived in Section 6.5.1 and listed in Table 6.5. For all the clumps we assume a dust opacity of $k_{870} = 0.012$ cm^{2}gr^{-1}. Using these values, for clumps C1 and C4 we derived a mass of ~80 M$_\odot$ and ~90 M$_\odot$ respectively, clumps C2, C3 and C5 have higher masses obtaining a value of 464 M$_\odot$, 398 M$_\odot$ and 500 M$_\odot$ respectively.

The virial mass was derived from the ^{13}CO(3-2) molecular line observations using Equation

1.66. This equation assumes that the clumps have spherical geometry and that they are in virial equilibrium. The virial mass obtained for clump C1 is 670 $M_\odot$, clump C2 have a virial mass of 243 $M_\odot$, clump C3 589 $M_\odot$, clump C4 426 $M_\odot$ and clump C5 2000 $M_\odot$. Theses values and the dust mass obtained for each clump are shown in Table 6.5.

Using the opacity, excitation temperature and line widths derived from the fit to the hyperfine components observed in the N_2H^+(1-0) emission, we derived the mass of the clumps. The masses were obtained using equation 1.4.3.3. The values of the mass obtained for these clumps are summarized in Table 6.5

In general the ratio between the dust mass and the virial mass, m/m_{virial}, is low, suggesting that clumps C1, C4 and C5 are not in virial equilibrium. Clump C2 have a lower virial mass than the dust mass indicating that this clump also has not reached virial equilibrium. The only clump that appears to be near virial equilibrium is clump C3 with a ratio m/m_{virial} of ~ 0.7

6.5.2.3 Lineal mass along the filament

We use the radial column density obtained from the dust continuum emission at 870 μm to derive the lineal mass of the filament. This was done by integrating the radial column density over the diameter of the filament at each point along the path previously defined. The mean lineal mass derived is ~360 $M_\odot$ pc^{-1}, having higher values at the position of the clumps (Figure 6.16).

The lineal virial mass was derived from Equation 1.6 using the mean line width of the ^{13}CO(3-2) emission at each point along the path previously determined. This mass has an average value of 615 $M_\odot$ pc^{-1} and in general follows the same morphology distribution observed at the lineal dust mass, having higher values than the lineal mass (from the dust) at some points along the filament. This can be due to an under estimation of the lineal dust mass due to an over estimation of the color temperature. To analyze what would be the effect in the lineal dust mass of a lower temperature we re-compute the lineal dust mass using a lower temperature (11 K). The lineal dust mass obtained with this temperature raised from a mean value of ~360 $M_\odot$ pc^{-1} to ~450 $M_\odot$ pc^{-1}, however, this value is still lower than the mean value of the lineal virial mass. Therefore, the effect of an over estimation in the temperature does not explains the discrepancy observed between the lineal virial mass and the dust mass considering that the temperature at the clumps cannot lower than 10 K.

6.5.3 External and internal pressure

The surface pressure exerted on this filament was derived from the external pressure of this filament, by assuming that the external pressure should be the same at the boundary of the filament. The

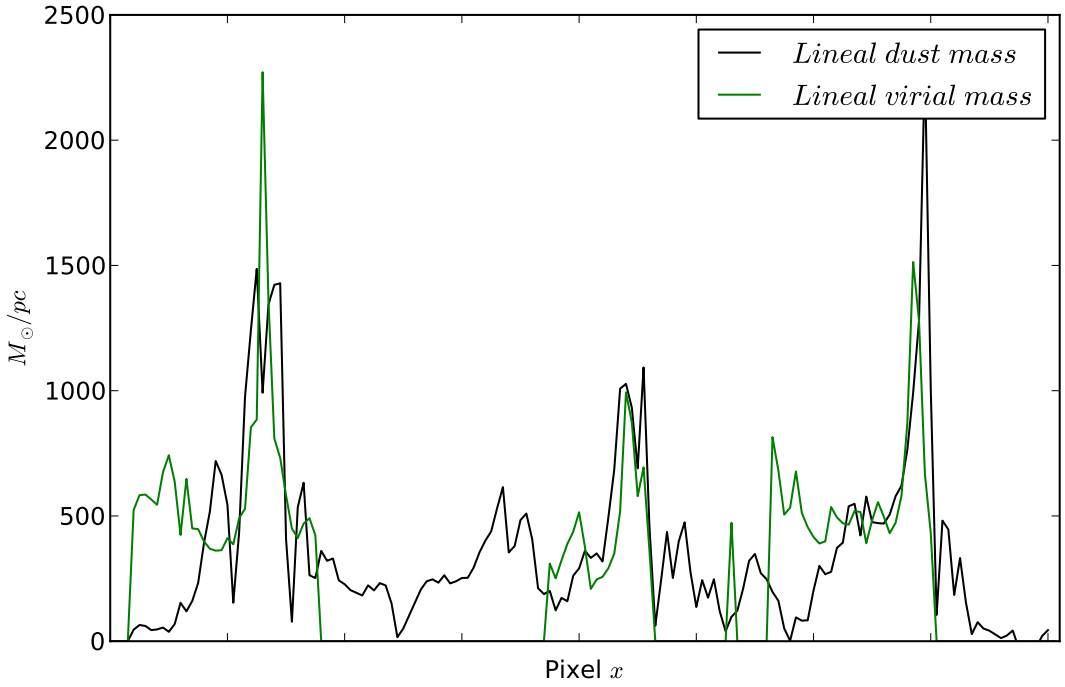

FIGURE 6.16: Lineal dust and virial mass distribution along the filament. Top panel: Black line, lineal mass from thermal dust emission at 870μm; Green line, virial mass form ^{13}CO(3-2). This figure show how both masses have the same morphology along the filament.

external pressure was estimated from the ^{13}CO(3-2) molecular line and dust continuum emission observed toward the region clearly located outside the boundaries defined for this filament. The mean velocity dispersion observed at ^{13}CO(3-2) is σ = 0.9 km s^{-1} and the average density is $\langle\rho\rangle$= 5.86×10^{-22} gr cm^{-3} giving a external pressure of $P_s/k = 3.5 \times 10^4$ K cm^{-3}. This value is similar to the values found on filamentary molecular clouds surrounded by atomic gas (Fiege and Pudritz 2000).

The internal pressure was obtained from the molecular line and dust continuum emission. The velocity dispersion, $\langle\sigma\rangle$, was derived from the ^{13}CO(3-2) line width at each point along the path defined. For this filament $\langle\sigma\rangle$ has a mean value of 1.15 km s^{-1}. The density at each point along the filament was derived from the lineal dust mass. At each point the lineal mass was divided by the volume per unit length, obtaining a mean density of 1.6×10^{-20}gr cm^{-1}. With these values we derived at each point the internal pressure, which has an average value of $\langle P\rangle/k = 1.4 \times 10^6$ K cm^{-3}.

6.6 Stability of the filament: magnetic field support

In this section we discuss the stability of the filament through two different methods. First, we study the stability of filament C by analyzing its radial intensity profile obtained from the continuum observations at 870 μm and 350 μmand second we study its virial equilibrium. To analyze its virial equilibrium, we used the values of the lineal dust mass, lineal virial mass, internal pressure and external pressure and compared them with the expected values in presence of different scenarios of magnetic field support (Fiege and Pudritz 2000).

6.6.1 Radial density profile analysis

This study is based on the assumption that the shape observed at the radial intensity from the dust continuum emission, is determined by the presence of a magnetic field that contribute to the support of the filament. To analyze the behavior the radial intensity profile we divided the the filament into two groups: the emission containing the clumps and the group containing the inter-clump material. Since we only are interested in the shape of the radial intensity, this was averaged and normalized for both regions at both wavelengths.

The normalized mean radial intensity of the clumps and inter-clumps material was fitted by a column density profile given by Equation 1.34. In this fit we use as free parameters: the central density, ρ_c, inner flat radius, R_{flat} and the parameter p. This parameter (p) depends on the shape of the column density profile and is indicative of the presence of a magnetic field. A value of $p = 4$, represents a filament in hydrostatic equilibrium and a value of $p \sim 2$ represent a filament with magnetic support, described by Fiege and Pudritz (2000) (see Section 1.3.2).

The radial intensity profile toward the clumps is best fitted by a column density profile with $p \sim 3.9$ and 5 for the 870 μm and 350 μm emission respectively (Figure 6.17), the fit at 350 μm is not a very good fit, but we see that the intensity profile at this wavelength is very similar to the profile with $p = 4$. This suggests that on the clumps the shape in the radial intensity can be explained by models that only include hydrostatic equilibrium, without the presence of an additional magnetic field support. On the inter-clump material the normalized mean intensity, although the profiles are not very well defined, shows wings more opened than the wings observed toward the clumps, looking more similar to a profile with $p = 2$. The radial intensity profile from the 870 μm emission present bumps which make it impossible to perform a god fit to this profile, however, we see that the emission is more flattened compared to a column density profile with $p = 4$ being the best fit to this emission the one corresponding to $p = 3.1$. The radial intensity profile obtained from the 350 μm emission is more defined and it is best fitted by a column density profile with $p = 2.1$, which corresponds to a profile expected for a filamentary molecular clouds with magnetic support.

The same procedure was done to the emission at each point along the path defined for this filament. At each point the radial intensity was fitted by a column density profile given by Equation 1.34 obtaining the central density, internal radius, and p. The values of p that best fitted the radial column density along the filament are shown in Figure 6.19. This plot shows only the point with a χ^2 between the fit and the observed radial intensity lower than 2. In general the points corresponding to the inter-clumps material (black dots) have values that range from 2.5 to 1. The points corresponding to the clumps (red diamonds) have, in general, higher values for p. This results and the fits made to the averaged column density suggest that while the shape of the radial intensity toward the clumps are well characterized by hydrostatic equilibrium toward the inter-clumps material the shape observed suggest the presence of a magnetic field to explain its stability.

6.6.2 Virial equilibrium analysis

Following the analysis described by Fiege and Pudritz (2000) we study the effect of a magnetic field by evaluating the relationship between $\langle P \rangle / P_s$ and m/m_{vir} at each point along the filament. We plot $\langle P \rangle / P_s$ against m/m_{vir} in a diagram with constant values of $\mathcal{M}/|\mathcal{W}|$. This plot allow us to estimate the value of $\mathcal{M}/|\mathcal{W}|$ which, depending of its sign, represents a magnetic field either toroidal or poloidal in the virial equilibrium equation given by Equation 1.4. In this diagram values of $\mathcal{M}/|\mathcal{W}|$ negatives represent a toroidal dominated magnetic field, positives values represent a poloidal dominated magnetic field and $\mathcal{M}/|\mathcal{W}|$=0 corresponds to the non-magnetic solution.

Figure 6.20 shows the distribution of $\langle P \rangle / P_s$ and m/m_{vir} derived for each point along filament C. The mean value of $\langle P \rangle / P_s$ and m/m_{vir} are 0.025 and 0.5 respectively which give $\mathcal{M}/|\mathcal{W}| = -0.8$, suggesting that the virial equilibrium for this filaments is given by the presence of a magnetic field that is dominated by a toroidal component, similar to the results obtained for filaments A and B. The clumps have values of $\langle P \rangle / P_s$ and m/m_{vir} of 0.001 and 1.06, thus $\mathcal{M}/|\mathcal{W}|$=0.06 very close to the solution that represents the non magnetic stability. The values obtained from the emission of the inter-clump material are distributed preferentially to the toroidal dominated magnetic field region of this diagram, for this region $\langle P \rangle / P_s$=0.004 and m/m_{vir}=0.33 which give $\mathcal{M}/|\mathcal{W}|$=-2.01.

The global values of m/m_{vir} and $\langle P \rangle / P_s$ obtained for this filament suggest that for its stability it is needed a toroidal dominated magnetic field that prevents the filament from expansion. It is also shown that locally, at the clumps region, the presence of the magnetic field is not very important and the stability in this regions can be explained only by their hydrostatic equilibrium.

6.7 Fragmentation

In this section we discuss the fragmentation on filament C. To do this we considered the filament as a cylinder. Theory predicts that the fragmentation can be due to fluid, or *"sausage"*, instabilities in a self-gravitating cylinder. The spacing between the cores, predicted by this theory, is given by the wavelength of the fastest growing unstable mode of fluid instability (Jackson et al. 2010). This spacing depends whether the filament is treated as an incompressible fluid (Chandrasekhar and Fermi 1953) or as an isothermal gas cylinder.

On filament C, the mean radius and the central density derived from the 870 μm are 0.56 pc and $\rho_c \sim 1.2\times10^{-19}$ gr cm^{-3} respectively. The average value of the ^{13}CO(3-2) line width is 2.69 km s^{-1}. From the 870 μm we derived that the average spacing observed between two consecutive clumps is 6.8 pc. If we considerer that this filament is an incompressible fluid, then, the expected separation between the clumps is $\lambda_{max} = 11 * 0.56\ pc = 6.16\ pc$ which is close to the value observed toward the clumps embedded in this filament.

If we considerer this filament as a infinite isothermal turbulent dominated cylinder (as Nessie), observations of the molecular line width and central density give an estimated value of the scale heigh $H = 0.27$ ($\ll R = 0.5pc$). Using this value for the scale height, the expected separation between the clumps is ~5.9 pc, also in agreement with the typical separation observed between the embedded clumps. This suggests that for filament C we can assume that it is either an incompressible fluid or an isothermal cylinder. In both cases the *"sausage"* instabilities gives a plausible scenario of the fragmentation of this filament.

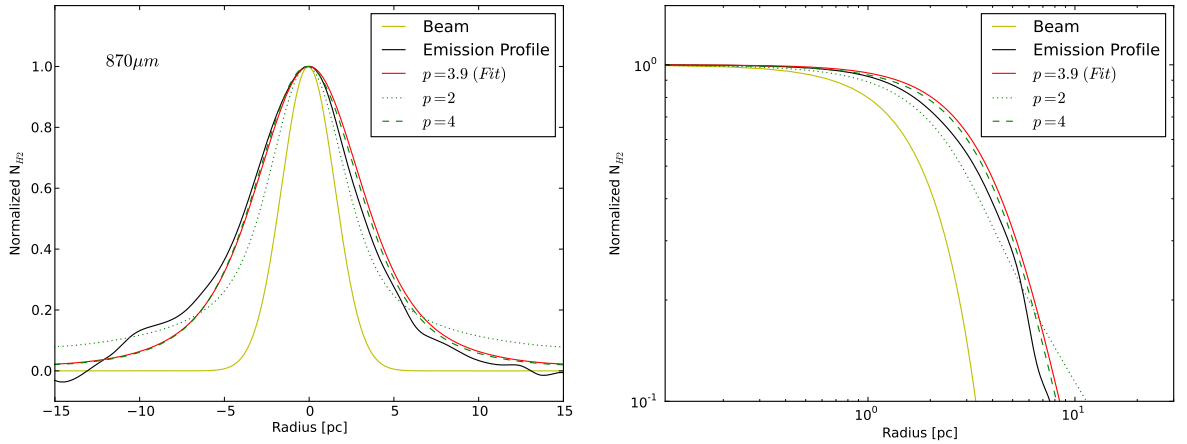

(a) 870 μm

(b) 870 μm

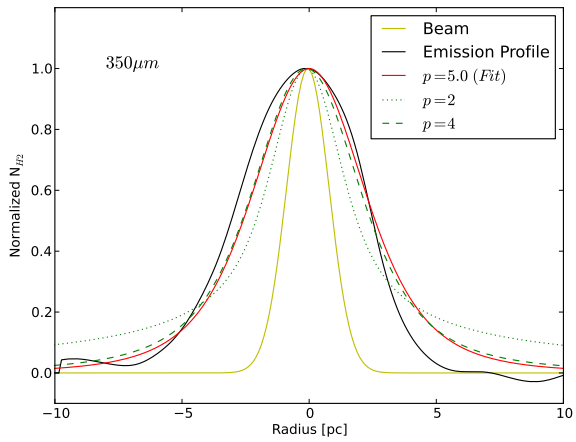

(c) 350 μm

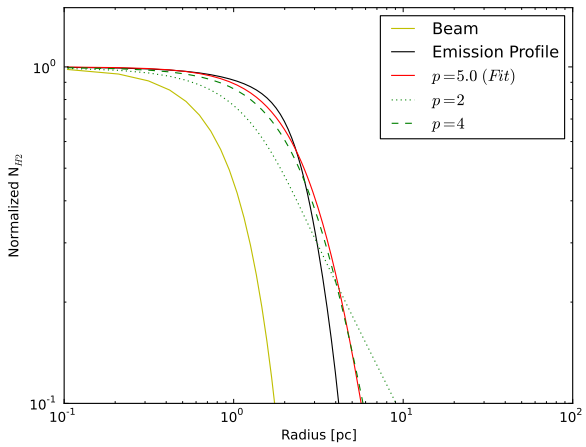

(d) 350 μm

FIGURE 6.17: Column density profile of the normalized mean column density of the clumps in filament C. Top panels show the 870 μm emission, bottom panels show the 350 μm emission. The left panels show lineal plot of the profiles and right panels shown the profiles in logarithmic scales. The red solid lines represents the best fit to the radial intensity, the beam profile is shown with the solid yellow line, the hydrostatic solution p=4 (green dashed line) and magnetized solution p=2 (green dotted line) are also shown. We can see that in general the shape of the radial intensity follows the shape of a column density profile with $p = 4$.

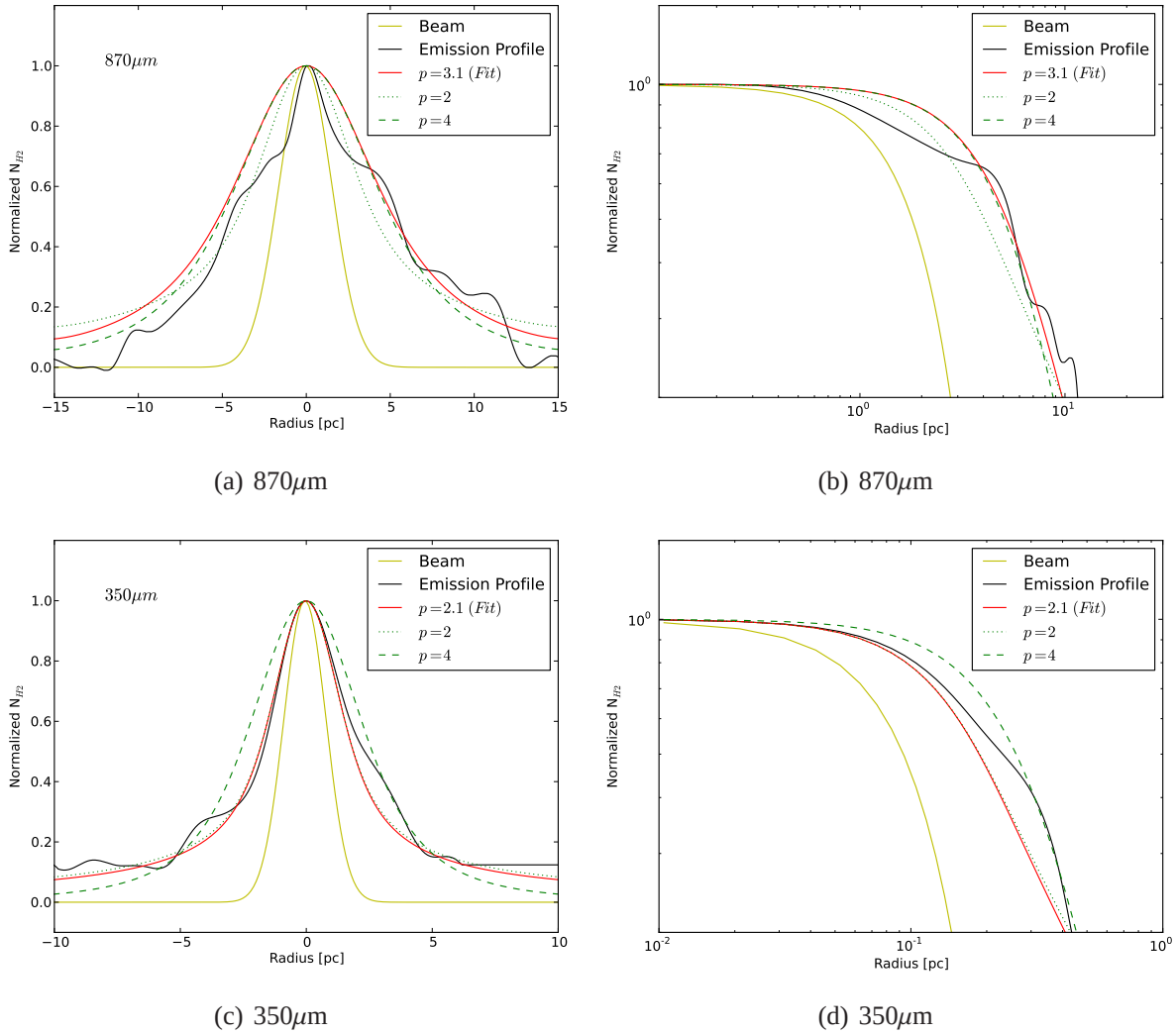

(a) 870μm (b) 870μm

(c) 350μm (d) 350μm

FIGURE 6.18: Column density profile of the normalized mean radial column density of the inter-clump material in filament C. Top panels show the 870 μm emission, bottom panels show the 350 μm emission. The left panels show lineal plot of the profiles and right panels shown the profiles in logarithmic scales. The beam profile is shown with the solid yellow line, the hydrostatic solution (green dashed line) and magnetized solution (green dotted line) are also shown. We can see that the shape of the radial intensity differs from the observed at the clump looking more similar to a column density profile with $p \sim 2$ at both wavelengths.

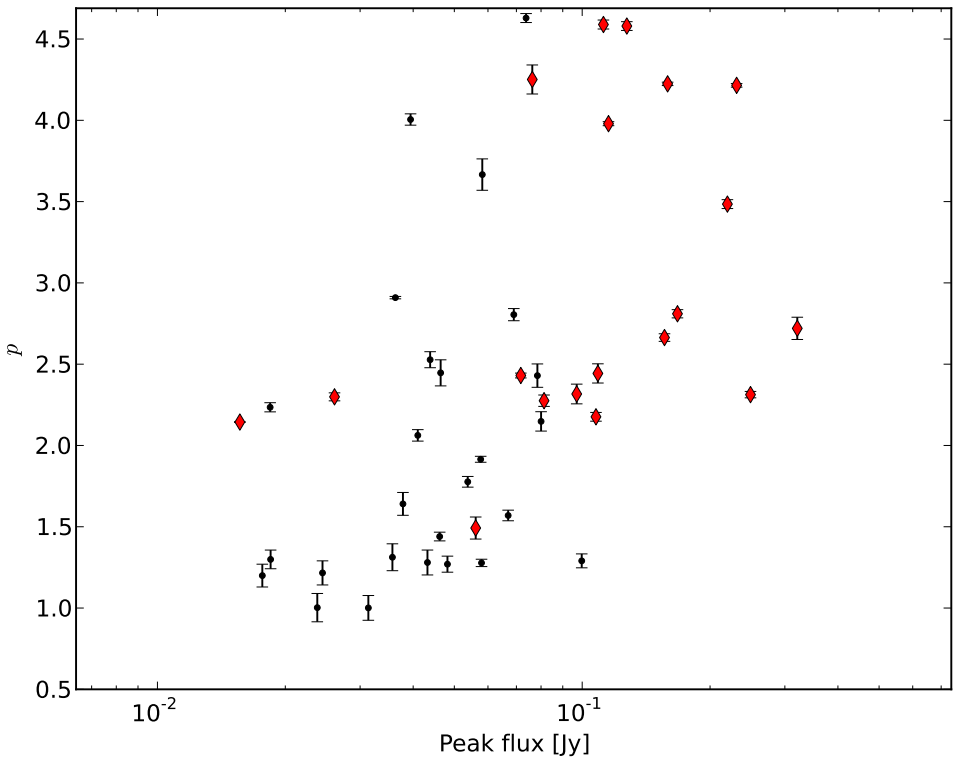

FIGURE 6.19: Plot of p, the parameter that define the shape of the density profile, vs peak flux for the clump (red point) and inter-clump (black points) material. The error bars show the χ^2 between the fit and the observed radial density. We can see that in general the inter-clump regions have values of p lower than the clumps.

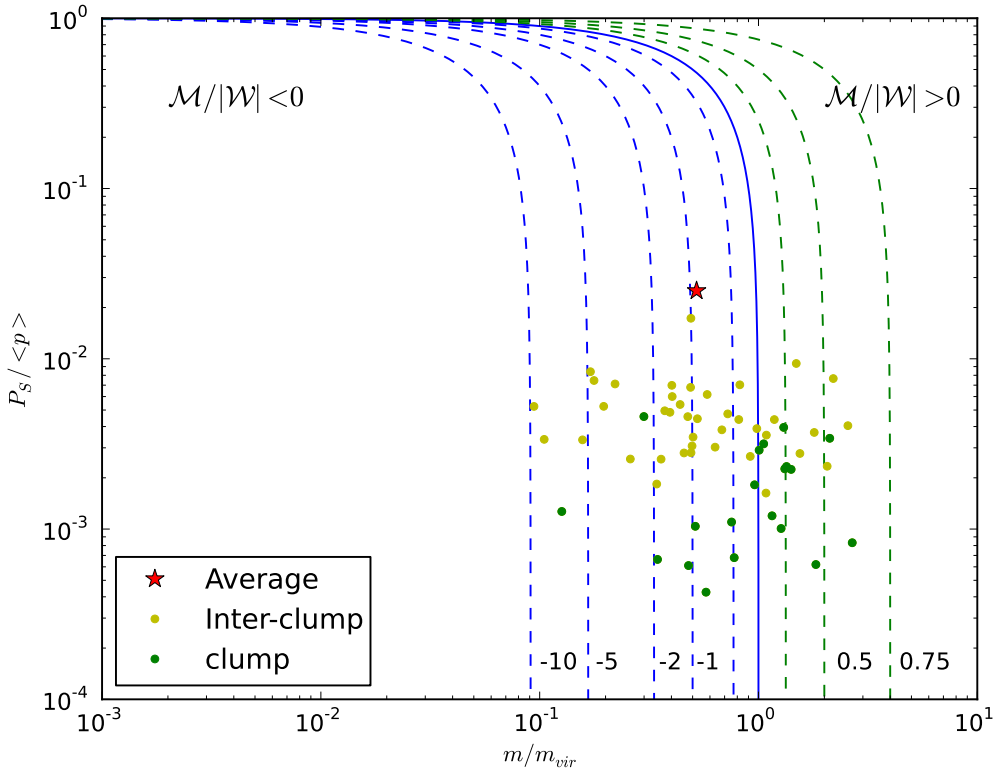

FIGURE 6.20: Plot of the $\langle P \rangle / P_s$ vs m/m_{vir} for the clumps and inter-clumps material for filament C. Blue dashed lines: toroidal models for magnetic fields, blue solid line: unmagnetized solution, green dashed lines: poloidal magnetic field models. Yellow dots: values found for the inter-clump region of the filament; black dots: values found for the regions were clumps are located and the red star: mean value for the filament.

TABLE 6.4: Filament C: derived properties of the filament.

Distance	**Length**	**Radius**	**N clumps**	**Δv**	**Temperature**	**Total mass**			**Lineal mass**			**P_s/k**	**$\langle P \rangle/k$**
				^{13}CO		**m**	**m_{vir}**	**m/m_{vir}**	**m**	**m_{vir}**	**m/m_{vir}**		
pc	pc	pc		km s^{-1}	K	$M_\odot$	$M_\odot$		$M_\odot$	$M_\odot$		10^4 K cm^{-3}	10^4 K cm^{-3}
3600	33	0.56	5	2.69	11	11700	9400	1.2	366	615	0.46	3.5	137

Table 6.5: Filament C, properties of the clumps

	Temperature		$\mathbf{m_{dust}}$	$\mathbf{m_{vir}}$	$\mathbf{m_{N2H+}}$	$\mathbf{m_{dust}/m_{vir}}$	**Spacing**
	Color	Assumed					
	K		$M_\odot$	$M_\odot$	$M_\odot$		pc
C1	29	-	79	670	106	0.1	1.4
C2	14	-	464	243	-	1.9	0.9
C3	27	-	398	589	1100	0.66	14
C4	46	-	92	426	437	0.20	11
C5	42	-	500	1984	209	0.24	-

7

Filament D: AGAL332.294-0.094

Filament D, AGAL332.294-0.094, shows a clear filamentary structure at 870 μm, with a length of ~28 arc minutes. However, such structure is not evident in the GLIMPSE or MIPSGAL images. Figure 7.1 (panel a) shows a three color image of the *Spitzer*/GLIMPSE observations at 3.6 μm (blue), 4.5 μm (green) and 8 μm (red). In this figure we see significant amount of infrared emission at 8 μm along this structure. At this wavelength the filamentary morphology seen at 870 μm is not evident due to the extended 8 μm emission, particularly toward the left part of the filament. The high levels of infrared emission are also observed in the *Spitzer*/MIPSGAL image at 24 μm (Figure 7.1 panel b), where we observe a bright zone that matches the bright emission seen at the IRAC bands. The IR features indicates the presence of several regions with current star formation, which provides an opportunity to investigate the connection between this filament and the star formation occurring within it.

At 870 μm the filament appears as a continuous structure harboring several clumps. Near its central part we observe a bifurcation of the main stream and also several clumps at the side of this complex. The dust continuum emission at 350 μm, observed with SABOCA, follows the same morphology seen at 870 μm identifying clearly the clumps embedded in this filament and thus its fragmentation (Figure 7.1 panels c and d).

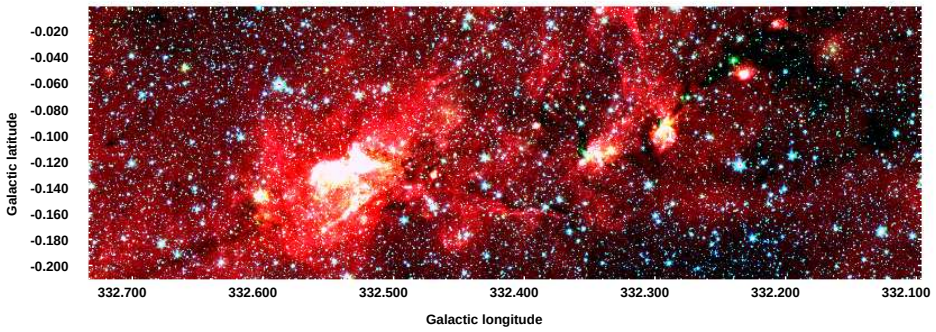

(a) *Spitzer*/GLIMPSE 3.5 μm - 8 μm

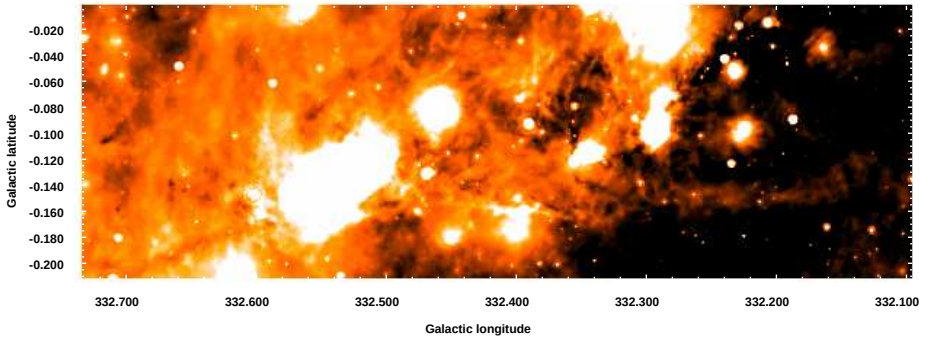

(b) *Spitzer*/MIPSGAL 24 μm

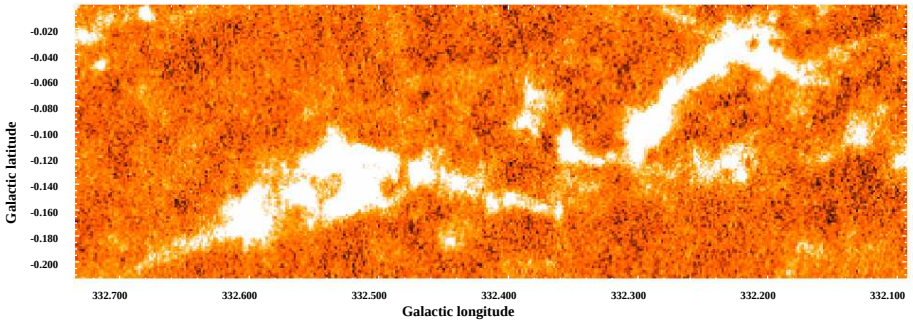

(c) APEX/LABOCA 870 μm

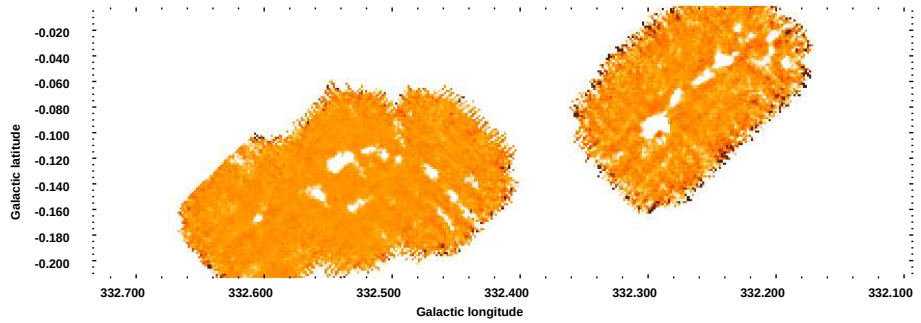

(d) APEX/SABOCA 350 μm

FIGURE 7.1: Multi wavelength continuum images of filament D. *Spitzer* color image of filament D (Blue: 3.6 μm, green: 4.5 μm and red: 8 μm) shows considerable emission at 8 μm. MIPSGAL 24 μmimages shows this structure as a collection of bright clouds embedded in a diffuse extended emission at 24 μm. However at 870 μm and 350 μm we can see how this structure appears as connected.

7.1 Defining the Filament

The name of this filament corresponds to the ATLASGAL denomination of the the brightest clump observed at 870 μm. To define this filament, we followed peaks in the 870 μm emission. This was done using a Python algorithm that interpolates the emission between the peaks (see Section 1.4.1.1 for further details). The width of the region was set to 20 pixels to each side to the path obtained, this width was chosen to enclose all the emission observed at 870 μm. The same region was used to define the filament at 350 μm. The path defined for this region is shown in Figure 7.2, in this figure the black line marks the path as it follow the 870 μm peaks.

Figure 7.3 also shows the flux density at 870 μm and 350 μm along the path previously defined. In this figure we clearly identify the location of the clumps embedded, which corresponds to the sectors with the highest flux density, even seen when embedded in extended emission. The flux density distribution at both wavelengths present the same morphology and the overall emission is higher than the typically noise in these images showed by the red dotted line (4.7 mJy at 870 μm and 0.29 Jy at 350 μm)

From the 870 μm dust continuum emission we determined the mean projected diameter of the filament. This was obtained from the radial dispersion of the dust emission observed along the path, by fitting a Gaussian. The FWHM of the fit, corresponds to the diameter of the filament. The mean radius of the filament (FWHM/2) has a value of ~32 arc seconds.

7.2 Physical coherence of the observed filamentary structure

Although at 870 μm this structure seem to be connected. Since the dust thermal emission takes into account all the emission along the line of sight, what we see can be only the projection of two or more molecular clouds in the same line of sight. Therefore, to determine if this structure is physically coherent we performed observations at ^{13}CO(3-2). Figure 7.4 (upper panel) shows the integrated intensity map overlayed to the dust continuum emission at 870 μm, we see that there is an agreement between the morphology of the gas traced by ^{13}CO(3-2) and the dust thermal emission toward this filamentary structure.

Position-velocity map (l,v) and (b,v) integrated over its Galactic longitude and latitude respectively are shown in Figure 7.4 (lower and right panels). In these maps we observe that the central velocity, v_{LSR}, at ^{13}CO(3-2) is similar along all the filamentary structure suggesting that this structure is physically connected and thus from now on we can call it a filament.

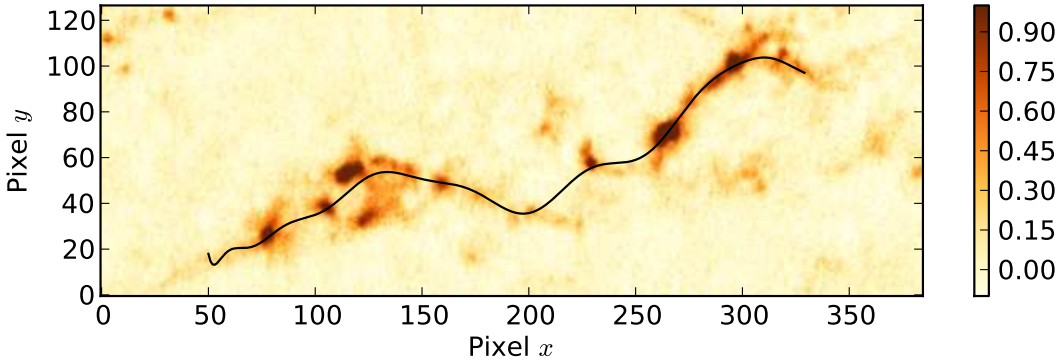

FIGURE 7.2: Path defined for filament D. Color scale show the 870 μm emission (scale in Jy/beam) toward filament D in black is shown the path used to define the filament, which follows the peaks at 870 μm. The region containing the filament was set to 20 pixel to each side of this path.

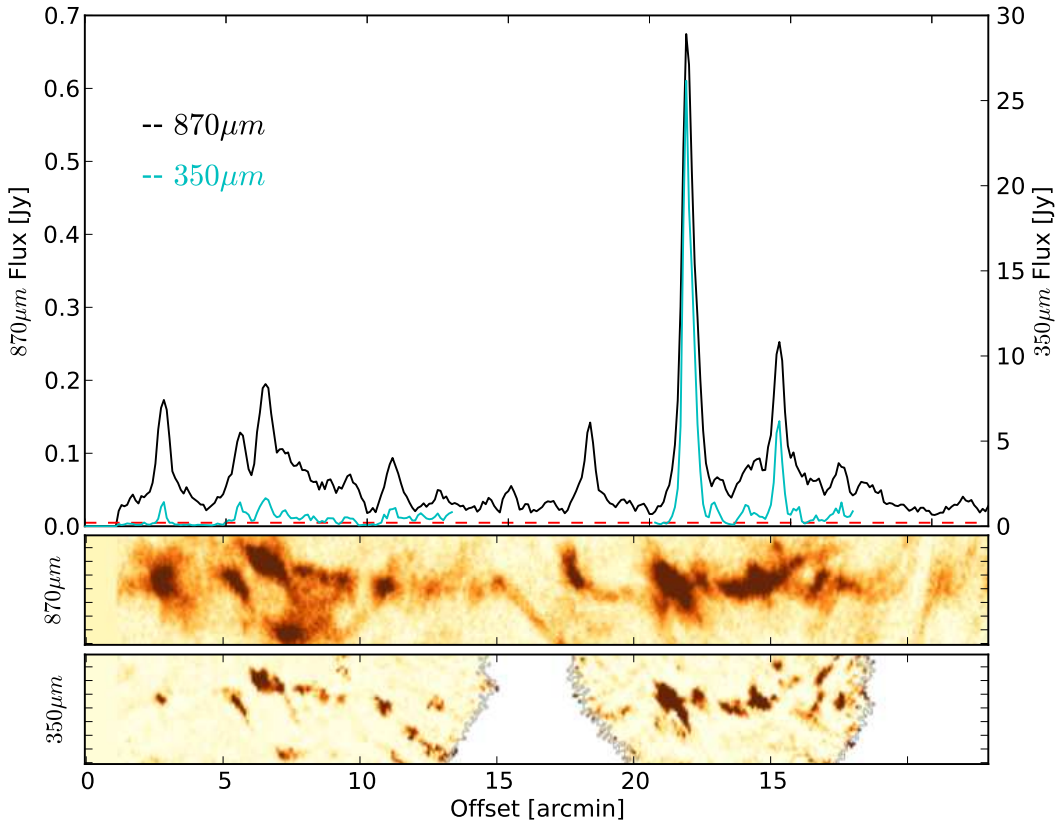

FIGURE 7.3: Distribution of dust continuum emission along the filament. Upper panel: Flux along the path defined for filament D for both 870 μm (black line) and 350 μm (blue line) dust continuum emission, red dotted line represents the mean noise in the map (4.7 mJy at 870 μm and 0.29 Jy at 350 μm).Lower panels: Color images of the filament at 870 μm and 350 μm.

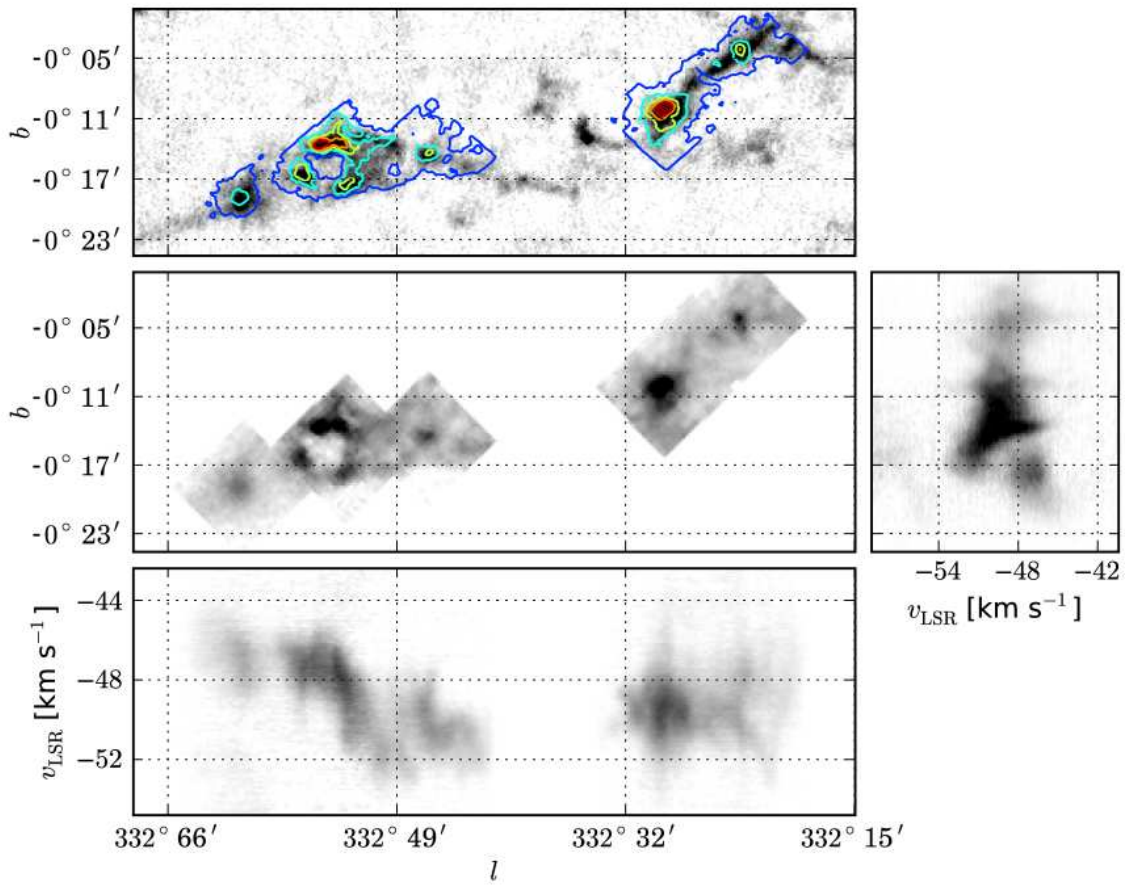

FIGURE 7.4: ^{13}CO(3-2)emission toward filament D. Top panel: dust emission at 870 μm overlaid with contours of the ^{13}CO(3-2) integrated intensity from 3 to 30 σ with σ = 3.3. Middle panel: ^{13}CO(3-2) integrated intensity. Lower and right panels: position velocity maps (l,v) and (b,v) integrated over both Galactic latitude and longitude respectively. These images reveal that the ^{13}CO(3-2) emission toward this filament reveals that this filament is a single coherent structure.

From the molecular line observations we determined the distance to the filament, using the mean central velocity of the line and a model for the rotational curve in the Galaxy (see section 1.4.3.2 for further details). Some part of this structure that are very bright at sub millimeter but dark at infrared (at the ends of this filament), which can be interpret as that the filament is obscuring foreground emission, because of this we choose the near kinematic distance for this filament. We find a mean distance of 3.3 Kpc to filament D. This implies that the length and diameter of this filament are 26.6 pc and 0.52 pc respectively. Table 7.4 summarizes the global properties found for filament D.

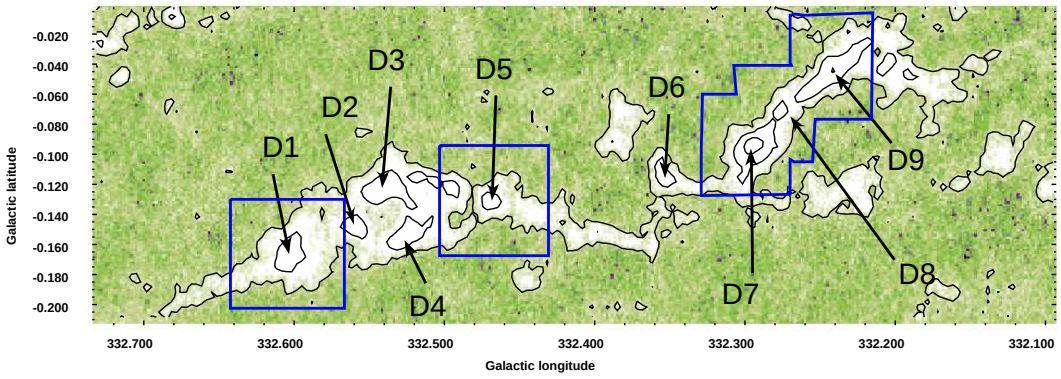

FIGURE 7.5: Color image 870 μm emission toward filament D. Arrows indicate the position of the clumps embedded within the filament and boxes shows observations with MALT90. Contours shows the emission from $> 3\sigma$ to the peak in logarithmic scale. We can see that the clumps are evenly distributed along the filament.

7.3 Properties of the embedded clumps within the filament

From the ATLASGAL point source catalog we identified 8 clumps. Five of them are located in the region of the filament that show significant emission at infrared wavelengths and the rest are evenly distributed along the filament. The name of the clumps correspond to their ATLASGAL denomination in the catalog, but for simplicity we assign to each core an ID (i.e. D1, D2, D3 etc). Figure 7.5 shows a color image of the 870 μm emission with the location of the clumps along the filament and their respective IDs. This figure also shows the region of the filament covered by the MALT90 observations.

Figure 7.6 (upper panel) shows a three color image composed of IRAC 4.5 μm (blue), 8 μm (green) and MIPS 24 μm (red) bands. In contours it is overlaid the 870 μm dust continuum emission. This figure shows that clumps D1, D2, D3, D4 and D5 are immersed in a extended region with high emission at 8 μm and 24 μm, from these clumps only clump D1 (Figure 7.6 lower panel) is the one with the least emission at 24 μm identifying this clump with a green fuzzy (enhancement at 4.5 μm). Clumps D6, D7, D8 and D9 are embedded in a dark molecular cloud, however, they also show emission at infrared (8 μm emission, 24 μm point sources, etc.) suggesting current star formation. Therefore in this filament most of the clumps are in a late stage of evolution with star formation currently taken place. Table 7.1 summarizes the global star formation activity of the clumps based on their emission at infrared and sub-millimeter wavelengths and their association with IRAS sources.

For each clump we derive their properties from the dust continuum emission, at both 870 μm and

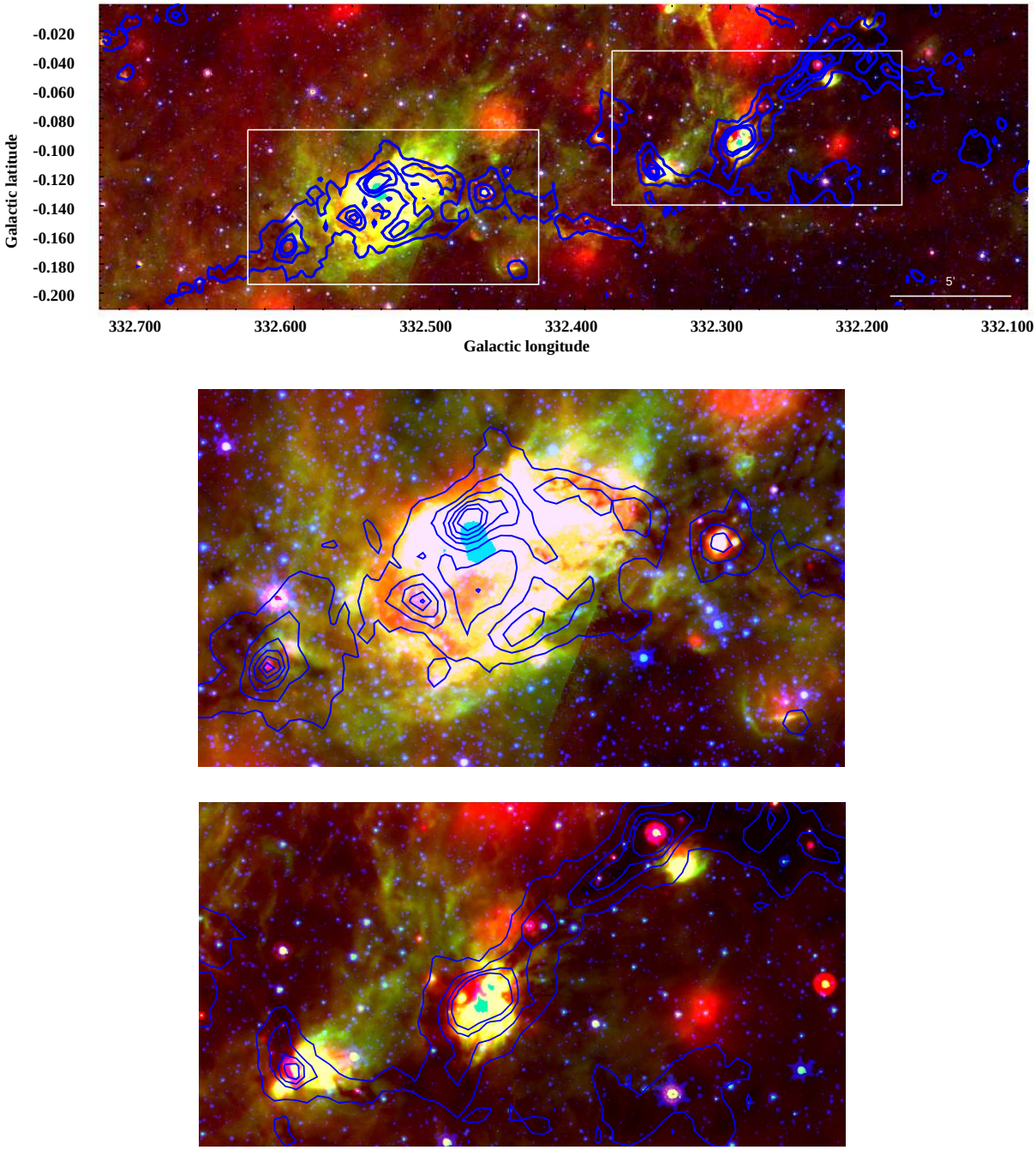

Figure 7.6: Color image filament D. Red: 24 μmMIPSGAL, green: IRAC 8 μm and blue IRAC 4.5 μm. The white boxes shows the region showed in the lower panels. Middle panel zoom into the region containing clumps D1, D2, D3, D4 and D5, we see the high levels of emission toward these clumps which is saturated at 24 μm. Lower panel zoom into the region containing clumps D6, D7, D8 and D9. These clumps are embedded in a dark region but they show localized infrared emission.

TABLE 7.1: Filament D, star formation activity of the observed clumps

ID	ATLASGAL Name	GLIMPSE 3.6 - 8 μm	MIPSGAL 24 μm	ATLASGAL[b]	IRAS
D1	AGAL332.604-0.167	Green fuzzies[a]	Point Source	Bright	16136-5038
D2	AGAL332.559-0.147	Bright 8 μm	Bright	Bright[b]	-
D3	AGAL332.544-0.124	Bright 8 μm	Bright	Bright	16132-5039
D4	AGAL332.529-0.157	Bright 8 μm	Bright	Bright	-
D5	AGAL332.469-0.131	Bright 8 μm	Bright	Bright	-
D6	AGAL332.352-0.116	Bright 8 μm	Bright	Bright	-
D7	AGAL332.294-0.094	Bright 8 μm	Bright	Bright	16119-5048
D8	AGAL332.277-0.072	Green fuzzies[a]	Point source	Weak	-
D9	AGAL332.241-0.044	Green fuzzies[a]	Point source	Bright	-

[a] Green fuzzies: Enhancement at 4.5 μm.

[b] Bright emission: Peak emission > 1 Jy/beam; weak emission: Peak < 1 Jy/beam

350 μm. From these emissions we calculate the peak flux, the diameter of the clump and integrated intensity for each clump. The parameters obtained are listed in Table 7.2. From the ^{13}CO(3-2) molecular line observations we obtained the mean spectrum over the region containing the 3σ emission toward each clump. To these spectrum we fit a Gaussian obtaining: the peak antenna temperature (T_{peak}), central velocity (v_{LSR}), line width (Δv) and integrated intensity ($\int T_b dv$, II in the table). We also obtained the diameter of each source defined by the region containing the emission at half of the peak. Table 7.2 gives the values obtained from these observations. For clumps D6 and D8 we don't have observations at 350 μm or ^{13}CO(3-2).

We performed N_2H^+(3-2) observations toward five of the eight clumps that presented the highest emission at 870 μm. The hyperfine components of this transition appear blended due to the large width in velocity in each component. Only for two clumps, D3 and D5, it is possible to distinguish more than one component in the N_2H^+(1-0) emission. Figure 7.7 shows the spectra obtained for each clump embedded in the filament D. In these spectra we show the position of the hyperfine components. We try to fit the hyperfine component to each clump with CLASS but this was only possible for clump D9, however even this fit is not very good, thus we did not use the τ obtained from this fit to derive the mass of this clump. For the rest of the clumps we fitted a three component Gaussian to each spectrum using a fixed position for each component. From these fits we derived the peak temperature (T_{peak}), central velocity (v_{LSR}), line width (Δv) for each spectrum. Table 7.2 shows the parameter obtained at each position, we have to notice that due to the blending of the hyperfine components the width of the line is likely to be overestimated.

7.4 Chemistry, evolutionary stage and kinematics of the brightest clumps

To asses the chemistry and evolutionary stage of the clumps embedded in filament D, we performed observations of sixteen molecular lines as part of the MALT90 project. The observations from MALT90 covered four of the eight clumps identified along this filament: D1, D5, D7, D8 and D9. For clump D1 we detected (integrated intensity > 3σ) six of the sixteen molecular lines observed. Most of the molecules detected toward this clump corresponds to density tracers such as HCO^+, N_2H^+,HCN, HNC and $H^{13}CO^+$. We also detected C_2H usually found toward photodissociation regions. The molecular transition with the highest peak temperature is HCO^+, 1.22 K followed by N_2H^+. For clump D5 we detected the same six molecular lines observed toward clump D1, this agrees with the fact that both clumps are the ones with lower emission at 8 μm and 24 μm.

Clump D7 is the only clump that shows HC_3CN molecular line emission which is usually detected toward hot cores. This suggests that this clump is in a more evolve evolutionary stage which agrees with the significant amount of emission observed at the GLIMPSE and MIPSGAL images. The molecular line transitions detected toward this clump are HCO^+, $H^{13}CO^+$, N_2H^+, HCN, HNC, HC_3CN and C_2H. For clump D8 and D9 we detected HCO^+, N_2H^+, HCN, HNC and C_2H. The molecular transitions detected indicate that these clumps are warm and dense which also coincide with their emission at 24 μm observed at mid-IR.

For all the clumps we made velocity integrated intensity maps of the molecular lines detected. Figure 7.8 (panels a to f) shows the integrated intensity map of the molecular transitions detected towards clump D1. The range in velocity used ranges from -41 km $s^{-1}$to -36 km s^{-1}. In this figure we see that at HCO^+, N_2H^+(1-0) and HNC the emission matches well the morphology observed at the dust thermal emission (see Figure 7.8 upper panel). HCN is the more extended of all the molecules and the emission at $H^{13}CO^+$ and C_2H is concentrated toward the position of the 24 μm point source.

Figure 7.9 (panels **a** to **f**) shows the integrated intensity maps toward clump D5 using a range in velocity from -55 km $s^{-1}$to -45 km s^{-1}. These maps show the molecular line emission at HCO^+, HNC and HCN quite extended increasing towards the part of the filament with higher infrared emission (Figure 7.9 upper panel). The emission at $H^{13}CO^+$, N_2H^+ and C_2H seem localized to the 24 μm point source detected toward this clump.

Velocity integrated intensity maps of the detected molecules toward clumps D7, D8 and D9 are shown in Figure 7.10. The range in velocity used for these maps ranges from -55 km s^{-1} to -45 km s^{-1}. These maps show the emission detected at HCO^+, N_2H^+ and HNC is continuous form clump to clump tracing very well the morphology of the filament observed at 870 μm. $H^{13}CO^+$,

HCN, C_2H and HC_3CN have their emission localized toward each clump with little emission visible in the inter-clump region.

For each clump we fit a Gaussian to the peak position of all the molecules detected. From this fit we obtained the central velocity of the emission (v_{LSR}), its peak antenna temperature (T_{peak}), line width (Δv) and integrated intensity ($\int T_b dv$, II in the table). We also obtained the (l,b) position of the peak spectrum expressed as the offset with respect to the position of the peak spectrum of N_2H^+(1-0) (Δl and Δb) and the total integrated intensity (I_T). For all the clumps the detections were defined as the emission of II > 3σ. The list of the parameters derived are summarized in Table 7.3. We also fitted the hyperfine structure observed in the N_2H^+(1-0) emission. From these fits we obtained the excitation temperature, line widths and opacity toward each clump. These values are summarized in Table B.1.

The spectra of the molecules detected toward clumps D1, D5, D7, D8 and D9 are shown in Figures 7.11, 7.12, 7.13, 7.14 and 7.14 respectively. For clumps D1 we see that in general the molecular line emission is symmetric with the exception of HCO^+. In this molecule we see that the peak is slightly blue shifted respect to the peak at N_2H^+(1-0) and the spectrum also shows a blue asymmetry with some auto absorption, suggesting the presence of infall motions in this clump. For clump D5 we see some asymmetry in the profiles of HCN and ^{13}CO(3-2). In this last one (^{13}CO(3-2)) we also observe some auto absorption with a red asymmetry which is commonly observed toward molecular clouds with outward motions. The channel maps of HCO^+ toward clumps D1 and D5 are show in Figures E.11 and E.13 respectively, and N_2H^+(1-0) in Figures E.12 and E.14 respectively.

For clumps D7 the spectrum at HCN shows its peak blues shifted respect to N_2H^+. We also see in the ^{13}CO(3-2) spectrum a blue asymmetry with broad wings suggesting inward turbulent motions. The profiles in the spectra of the molecules detected toward clumps D8 and D9 are very symmetric, with the peak at HCO^+ also blue shifted respect to N_2H^+, in both cases. The skewed red profile observed toward both clumps suggests inward motions. Figures E.15 and E.16 show the channel maps of HCO^+ and N_2H^+(1-0) respectively toward clumps D7, D8 and D9.

Table 7.2: Parameters of the clumps in filament D from their continuum and molecular emission.

ID	870 μm				350 μm				^{13}CO(3-2)					N_2H^+(3-2)			
	Peak Flux	Diameter		Int. Flux	Peak Flux	Diameter		Int. Flux	T_{peak}	v_{LSR}	Δv	II	Diameter	T_{peak}	v_{LSR}	Δv	
	Jy/Beam	’	pc	Jy	Jy/Beam	’	pc	Jy	km s^{-1}	km s^{-1}	K	K km s^{-1}	pc	km s^{-1}	km s^{-1}	K	
D1	1.80	0.7	0.7	4.21(0.27)	5.71	0.3	0.3	7.28(0.45)	4.54	-47.05	3.25(0.40)	15.74(1.94)	1.4	1.42	-46.47	4.26(0.12)	0.1(0.25)
D2	1.33	0.7	0.7	3.38(0.26)	5.68	0.2	0.2	5.33(0.41)	10.03	-47.45	2.38(0.73)	25.45(7.83)	1.0	-	-	-	-
D3	2.02	0.8	0.8	5.85(0.28)	6.81	0.4	0.4	22.71(0.46)	15.53	-47.45	2.33(0.45)	38.81(7.54)	0.6	0.70	-49.88	1.21(0.04)	-
														1.99	-47.17	1.69(0.04)	-
														0.83	-45.14	1.41(0.07)	-
D4	1.05	0.6	0.6	2.61(0.26)	3.39	0.2	0.2	2.78(0.52)	6.89	-47.65	2.30(0.98)	16.93(7.25)	0.8	-	-	-	-
D5	0.97	0.6	0.6	1.66(0.45)	4.49	0.2	0.2	5.09(0.58)	8.30	-50.20	2.94(0.27)	20.01(2.36)	1.0	0.55	-51.32	3.01(0.23)	-
														1.77	-48.67	2.72(0.09)	-
														0.67	-46.61	2.52(0.19)	-
D6	1.48	0.4	0.4	1.73(0.24)	-	-	-	-	-	-	-	-	-	-	-	-	-
D7	7.02	1.0	0.9	19.69(0.56)	104.86	0.5	0.5	334.86(2.56)	10.96	-49.35	3.52(0.15)	41.21(1.72)	0.8	0.55	-51.32	3.008(0.22)	-
														1.77	-48.67	2.72(0.10)	-
														0.67	-46.61	2.52(0.19)	-
D8	0.71	0.3	0.34	8.09(0.90)	-	-	-	-	-	-	-	-	-	-	-	-	-
D9	2.63	0.7	0.7	5.92(0.38)	29.91	0.4	0.4	67.61(2.45)	5.34	-48.00	4.11(0.28)	23.45(1.59)	0.7	1.99	-47.66	4.35(0.03)	4.04(0.05)

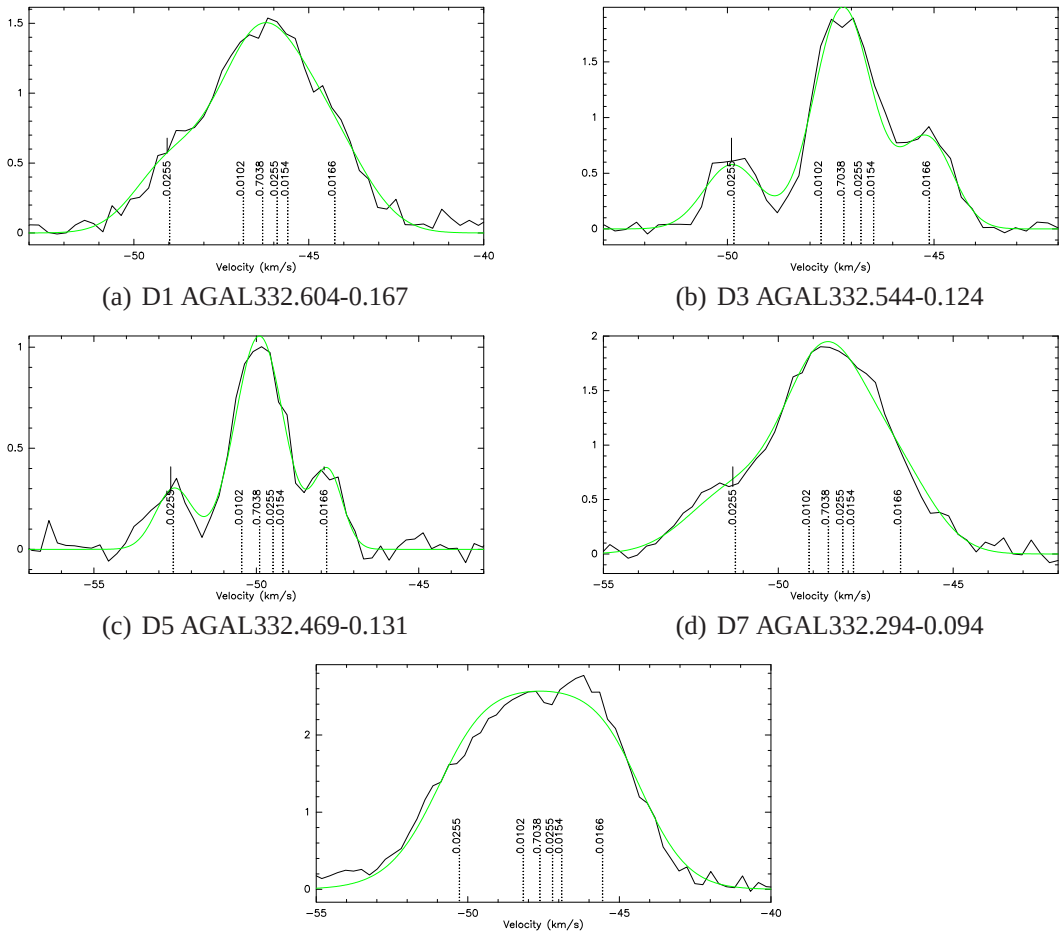

(a) D1 AGAL332.604-0.167

(b) D3 AGAL332.544-0.124

(c) D5 AGAL332.469-0.131

(d) D7 AGAL332.294-0.094

(e) D9 AGAL332.241-0.044

FIGURE 7.7: Spectra of the N_2H^+observations toward clumps D1, D3, D5, D7 and D9. Each plot show the fit (green line) and position of the hyperfine structure component for each spectra. The numbers indicate the relative intensity of the lines. Here is clearly seen that due to the large linewidth of the hyperfine components is not possible to distinguish them.

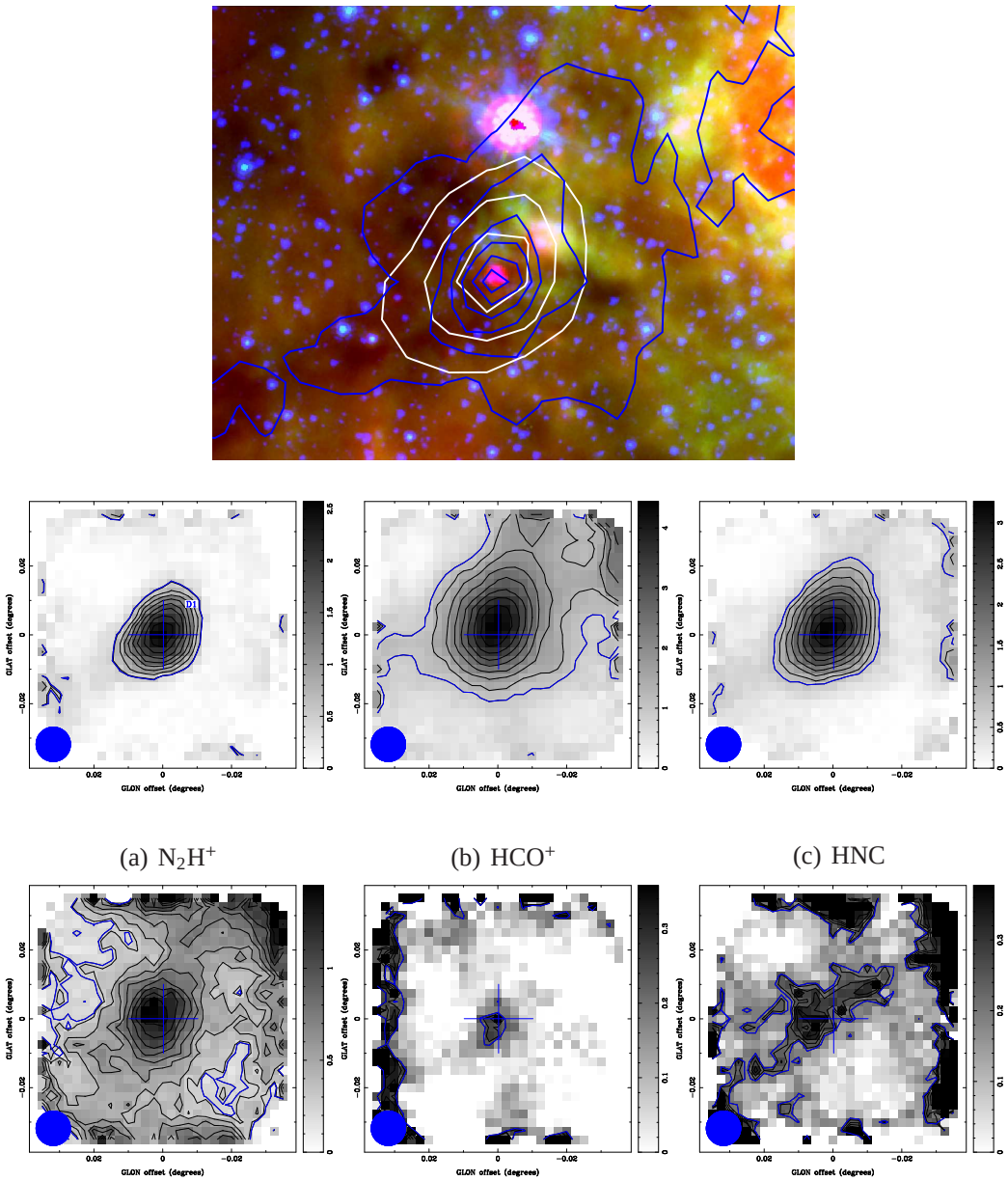

(a) N_2H^+ (b) HCO^+ (c) HNC

(d) HCN (e) $H^{13}CO^+$ (f) C_2H

FIGURE 7.8: II images of the molecules detected toward D1 from the MALT90 survey. Top panel: Three color *Spitzer*/IRAC (Red: 24 μm, blue: 8 μm, green: 4.5 μm, blue contours: 870 μm, white contours: N_2H^+(1-0)). Lower panels (a)-(f): Maps of integrated intensity from each of the detected lines (II > 3σ). Contours represent the emission from 90% of the peak to 3σ noise emission (blue contour) in steps of 10%. The cross shows the position of the clumps and the blue circle shows the beam size. The color bar shows the value of the peak at each molecule.

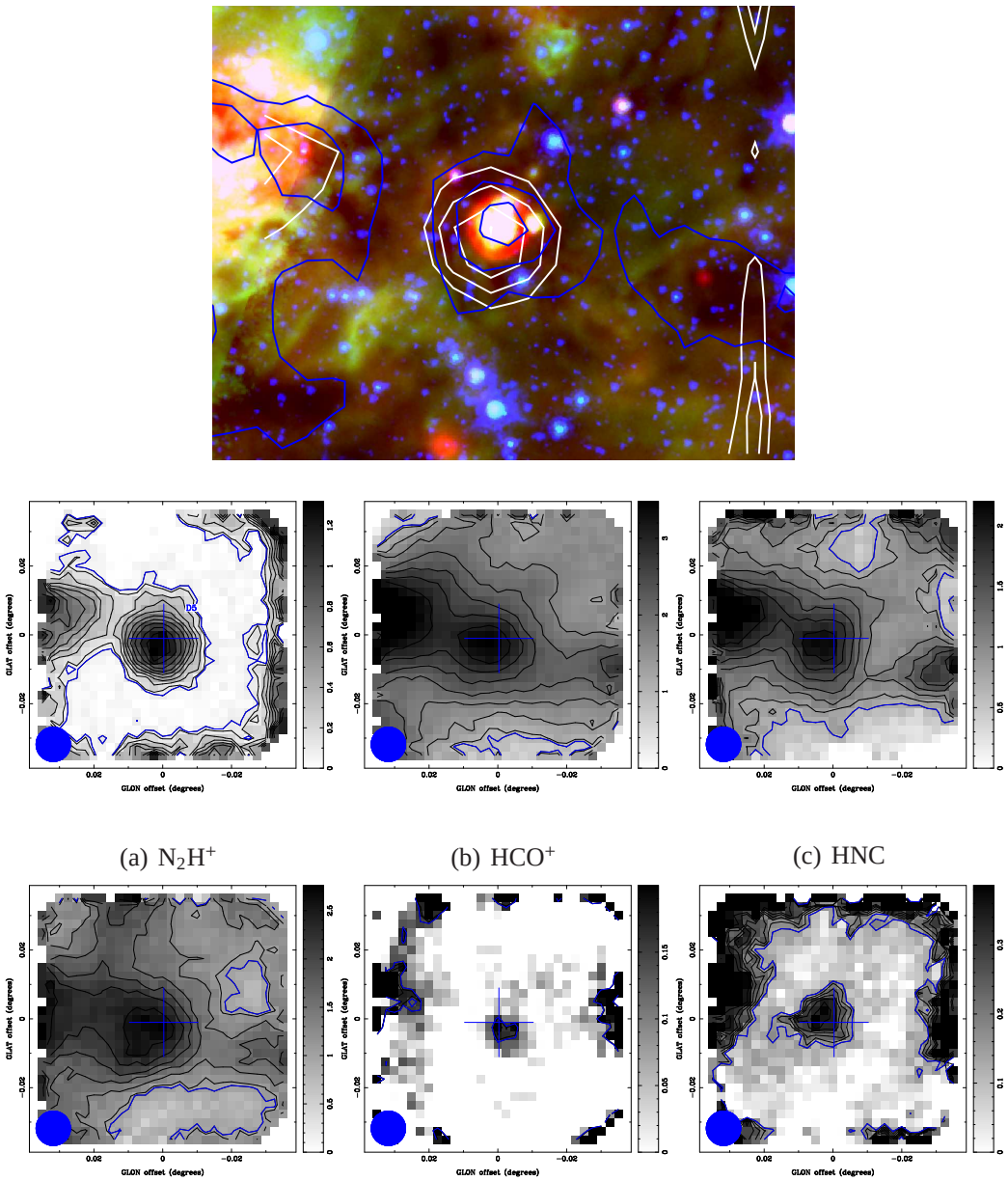

(a) N_2H^+ (b) HCO^+ (c) HNC

(d) HCN (e) $H^{13}CO^+$ (f) C_2H

FIGURE 7.9: II images of the molecules detected toward D5 from the MALT90 survey. Top panel: Three color *Spitzer*/IRAC (Red: 24 μm, blue: 8 μm, green: 4.5 μm, blue contours: 870 μm, white contours: N_2H^+(1-0)). Lower panels (a)-(f): Maps of integrated intensity from each of the detected lines (II > 3σ). Contours represent the emission from 90% of the peak to 3σ noise emission (blue contour) in steps of 10%. The cross shows the position of the clumps and the blue circle shows the beam size. The color bar shows the value of the peak at each molecule.

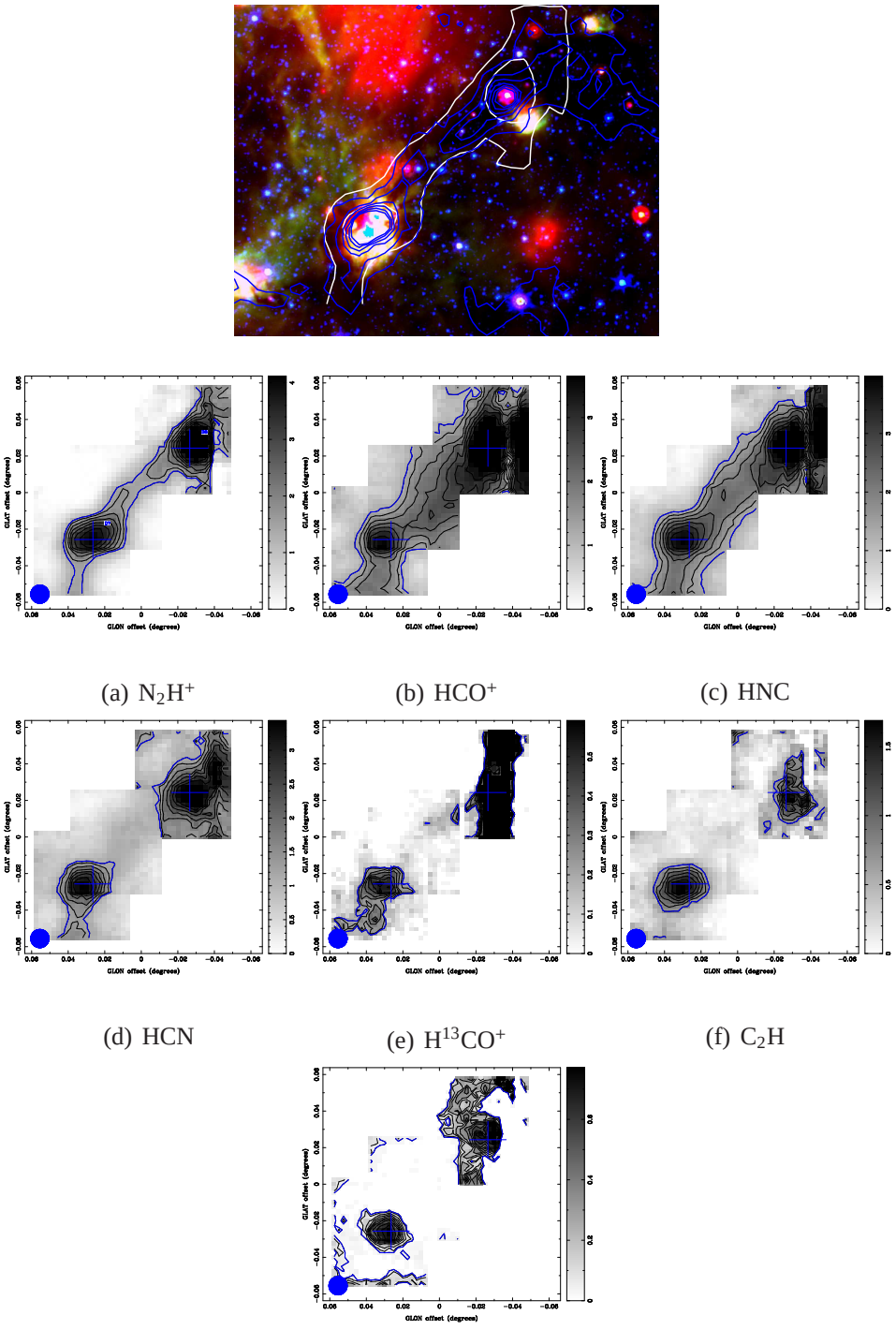

(a) N_2H^+ (b) HCO^+ (c) HNC

(d) HCN (e) $H^{13}CO^+$ (f) C_2H

(g) HC_3CN

FIGURE 7.10: II images of the molecules detected toward D7 and D9 from the MALT90 survey. Top panel: Three color *Spitzer*/IRAC (Red: 24 μm, blue: 8 μm, green: 4.5 μm, blue contours: 870 μm, white contours: N_2H^+(1-0)). Lower panels (a)-(f): Maps of integrated intensity from each of the detected lines (II > 3σ). Contours represent the emission from 90% of the peak to 3σ noise emission (blue contour) in steps of 10%. The cross shows the position of the clumps and the blue circle shows the beam size. The color bar shows the value of the peak at each molecule.

TABLE 7.3: Filament D: Parameters derived from Gaussian fits to the MALT90 spectra

Source	Molecule	Δl[a]	Δb[a]	T_{peak}	V_{LSR}	Δv	II[b]	I_T[c]	*rms*
		"	"	K	km s^{-1}	km s^{-1}	K km s^{-1}	K km s^{-1}asec^2	K/channel
D1 AGAL332.604-0.167	$N2H^+$	0	0	0.85	-46.55	2.79	2.52	244	0.23
	HCO^+	-9	-9	1.22	-48.27	2.13	2.77	928	0.23
	$H^{13}CO^+$	0	9	0.16	-45.85	1.64	0.27	118	0.23
	HCN	0	-9	0.46	-46.77	1.29	0.63	510	0.23
	HNC	0	-9	0.65	-47.35	3.94	2.73	246	0.22
	C_2H	-27	0	0.21	-46.22	2.20	0.49	400	0.23
D5 AGAL332.469-0.131	$N2H^+$	0	0	0.52	-50.08	2.89	1.60	75	0.18
	HCO^+	-9	9	1.12	-51.19	2.04	2.43	1589	0.19
	$H^{13}CO^+$	9	0	1.12	-50.33	2.04	2.43	249	0.19
	HCN	0	0	0.65	-50.90	2.27	1.57	950	0.19
	HNC	0	0	0.74	-50.78	1.59	1.25	522	0.20
	C_2H	0	-9	0.21	-50.45	1.38	0.31	650	0.19
D7 AGAL332.294-0.094	$N2H^+$	0	0	1.37	-48.71	2.63	2.84	947	0.18
	HCO^+	72	-27	1.11	-49.58	1.88	2.08	111	0.34
	$H^{13}CO^+$	-18	0	0.38	-48.95	1.19	0.48	1300	0.18
	HCN	-9	0	0.76	-49.75	2.84	2.30	1118	0.56
	HNC	0	0	1.09	-49.31	2.79	3.24	981	0.10
	HC_3N	0	0	0.39	-49.06	1.69	0.70	29	0.09
	C_2H	-9	0	0.58	-49.48	2.74	1.69	163	0.10
D8 AGAL332.277-0.072	$N2H^+$	0	0	1.12	-48.7	2.6	6.6	1082	0.21
	HCO^+	10	10	1.03	-50.5	4.7	5.4	1551	0.22
	HCN	10	10	0.1	-53.2	10.2	11	1045	0.21
	HNC	10	10	1.17	-49.3	3.9	4.9	1185	0.23
	C_2H	10	20	0.1	-49.3	3.3	14.4	124	0.23
D9 AGAL332.241-0.044	$N2H^+$	0	0	1.76	-47.61	2.04	3.83	1481	0.25
	HCO^+	45	-18	1.63	-48.08	2.81	4.88	1748	0.25
	HCN	0	9	0.59	-47.11	2.15	1.35	1311	0.24
	HNC	45	-36	1.82	-47.41	2.35	4.56	1372	0.24
	C_2H	9	9	0.47	-48.94	2.93	1.47	730	0.24

[a] Offset of the peak emission from the N_2H^+(1-0) peak.

[b] Integrated intensity at the peak.

[c] Total integrated intensity.

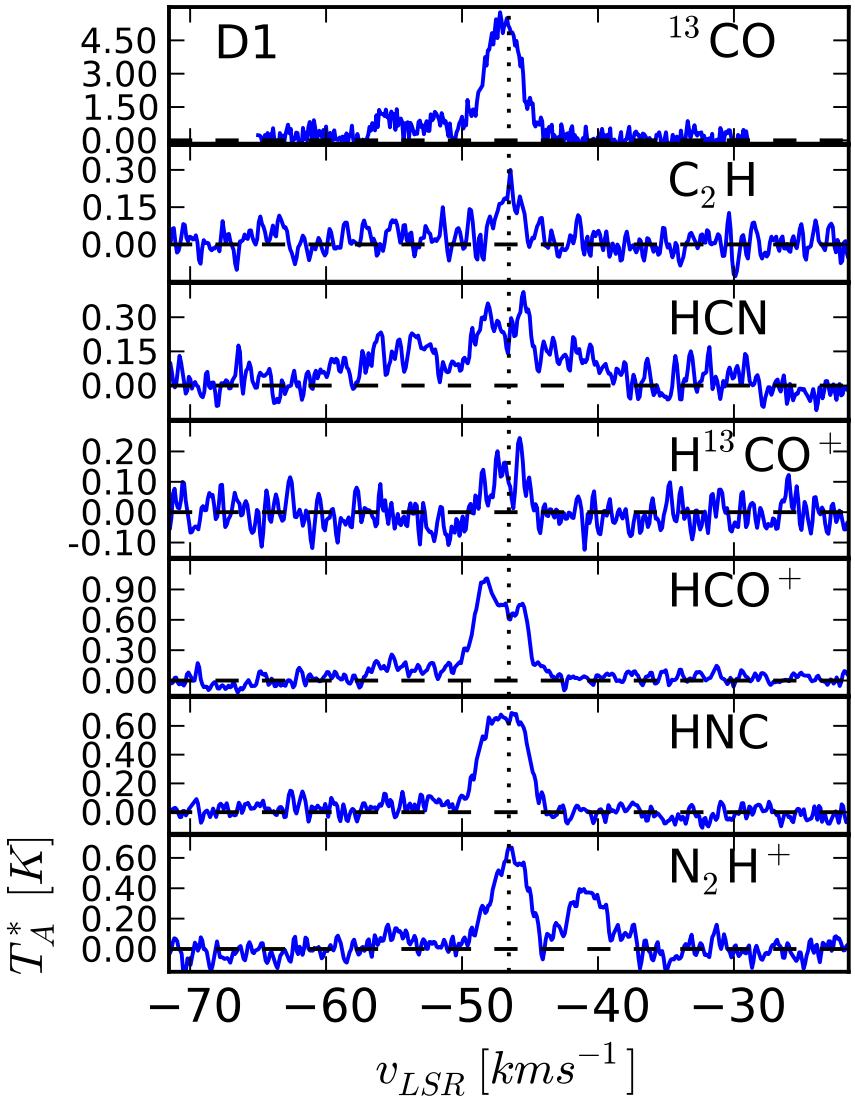

Figure 7.11: Spectra toward clump D1. Each spectrum are at the (l,v) position corresponding to the peak emission at N_2H^+. Dotted line shows the central velocity of the N_2H^+(1-0) emission.

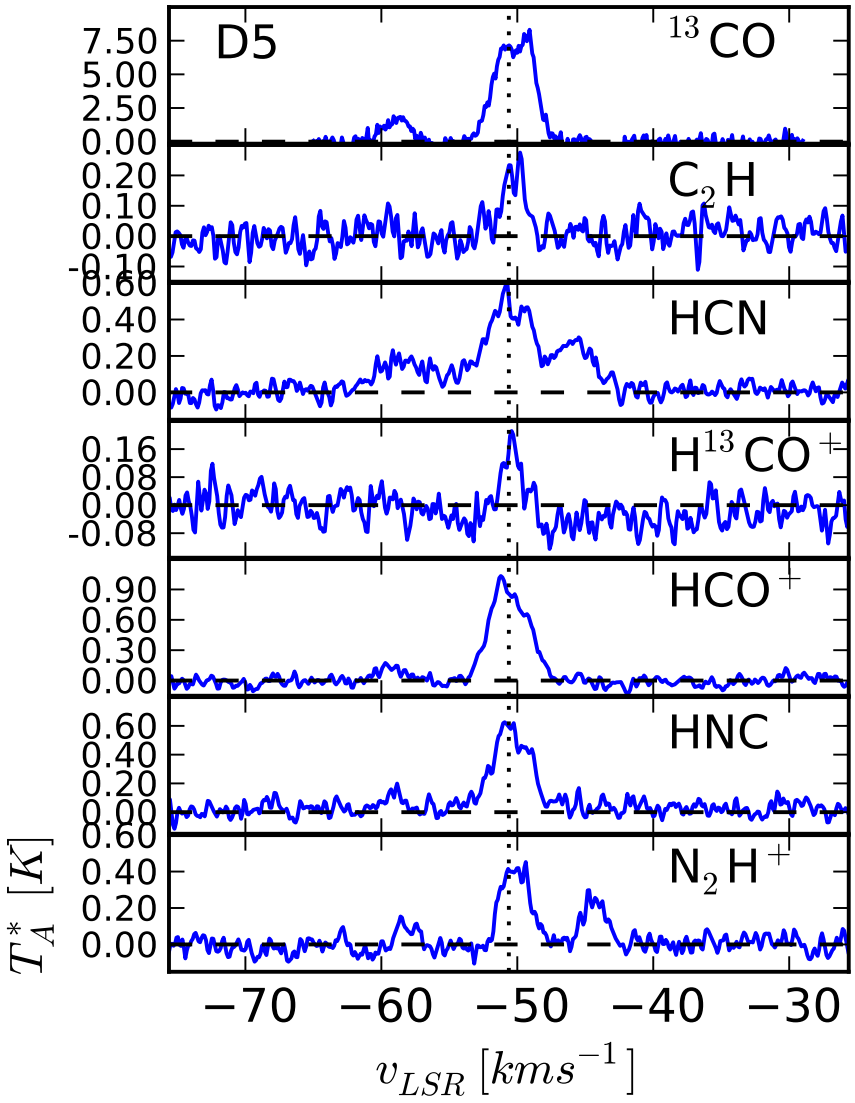

FIGURE 7.12: Spectra toward clump D5. Each spectrum are at the (l,v) position corresponding to the peak emission at N_2H^+. Dotted line shows the central velocity of the N_2H^+(1-0) emission.

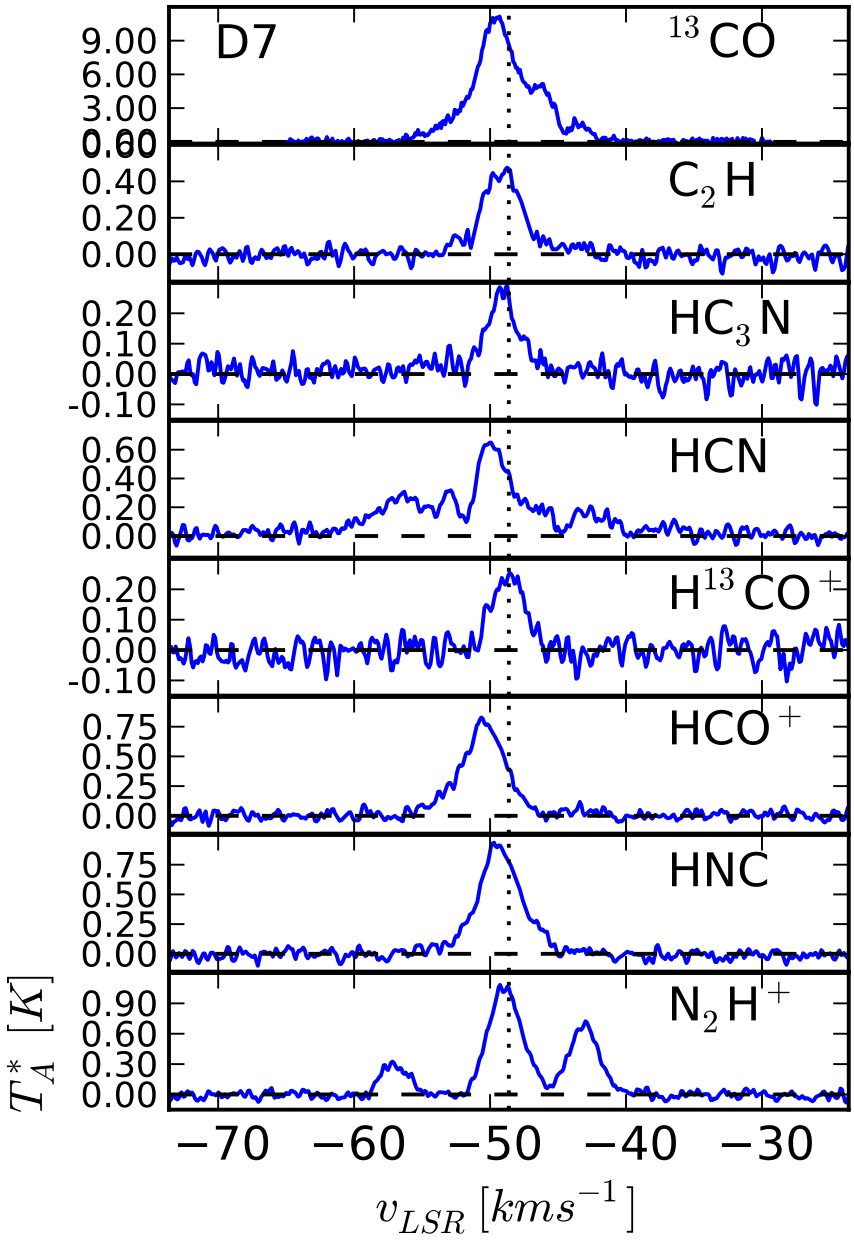

Figure 7.13: Spectra toward clump D7. Each spectrum are at the (l,v) position corresponding to the peak emission at N_2H^+. Dotted line shows the central velocity of the N_2H^+(1-0) emission.

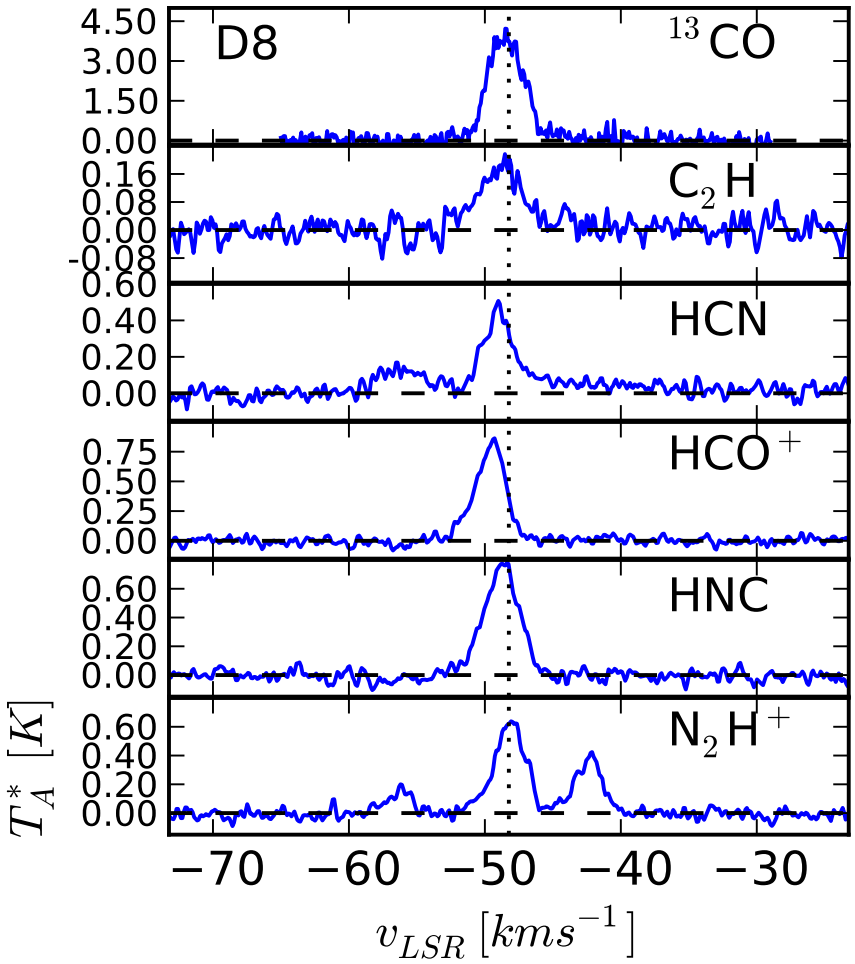

FIGURE 7.14: Spectra toward clump D8. Each spectrum are at the (l,v) position corresponding to the peak emission at N_2H^+. Dotted line shows the central velocity of the N_2H^+(1-0) emission.

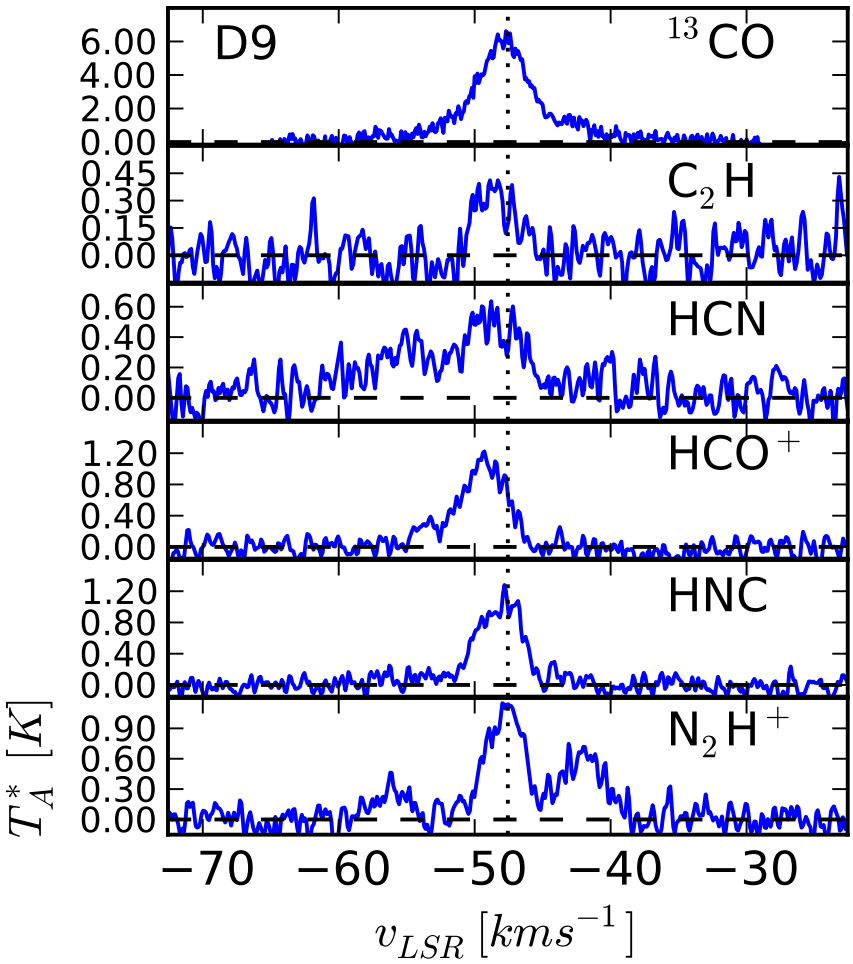

Figure 7.15: Spectra toward clump D9. Each spectrum are at the (l,v) position corresponding to the peak emission at N_2H^+. Dotted line shows the central velocity of the N_2H^+(1-0) emission.

7.5 Physical properties

In this section we derive the physical properties (temperature, masses, internal and external pressure) of filament D and the clumps embedded within it, using the multi wavelength data described in the previous section.

7.5.1 Color temperature

The *color temperature* was derived from the 870 μm and 350 μm dust thermal continuum emission detected toward filament D, using the method described is Section 1.4.2.2. This color temperature represents a good estimation of the dust temperature only toward the regions of the filament were there is no considerable emission at the GLIMPSE and MIPSGAL images. On the regions of this filament where the infrared emission is significant, the color temperatures derived are not representatives to the true temperature of the dust, because the assumptions made for this calculus are not longer valid in this regime. This explains why the color temperatures derived in these regions are too cold (6 K to 8 K).

Since the color temperature depends on the value of the spectral index, β. We computed the color temperature using different values of β. At the infrared dark regions of filament D, the mean color temperature derived are 14 K, 12 K, 10 K and 9 K using a spectral index β of 1, 1.5, 2 and 2.5 respectively. The mean temperatures obtained for the clumps D6, D7 and D9, locate in this infrared dark part of the filament, are 30 K for $\beta = 1.5$. This temperature is similar to the dust temperatures observed toward warm and hot clumps (Rathborne et al. 2010), thus we used the temperatures obtained with an spectral index $\beta = 1.5$ for further calculations. Figure 7.16 shows the temperature maps derived for the different values of β.

Based on the molecular lines detected from the observation of MALT90, the lack of detection of hot chemistry molecules and the emission observed at 8 μm we can infer that clumps D1, D5 and D9 are proto-stellar objects having temperatures 30 K, which is in agreement with the color temperatures derived from the dust thermal continuum. On clump D6 we detect HC_3CN and considerable more emission at 8 μm and 24 μm indicating a more evolved stage, however we don't detect many hot chemistry molecules thus we assumed a temperature of 35 K usually observed toward hot clumps (Rathborne et al. 2010). Toward the regions where there is significant emission at infrared, we use ~50 K which is a dust temperature typically observed toward regions with similar characteristics.

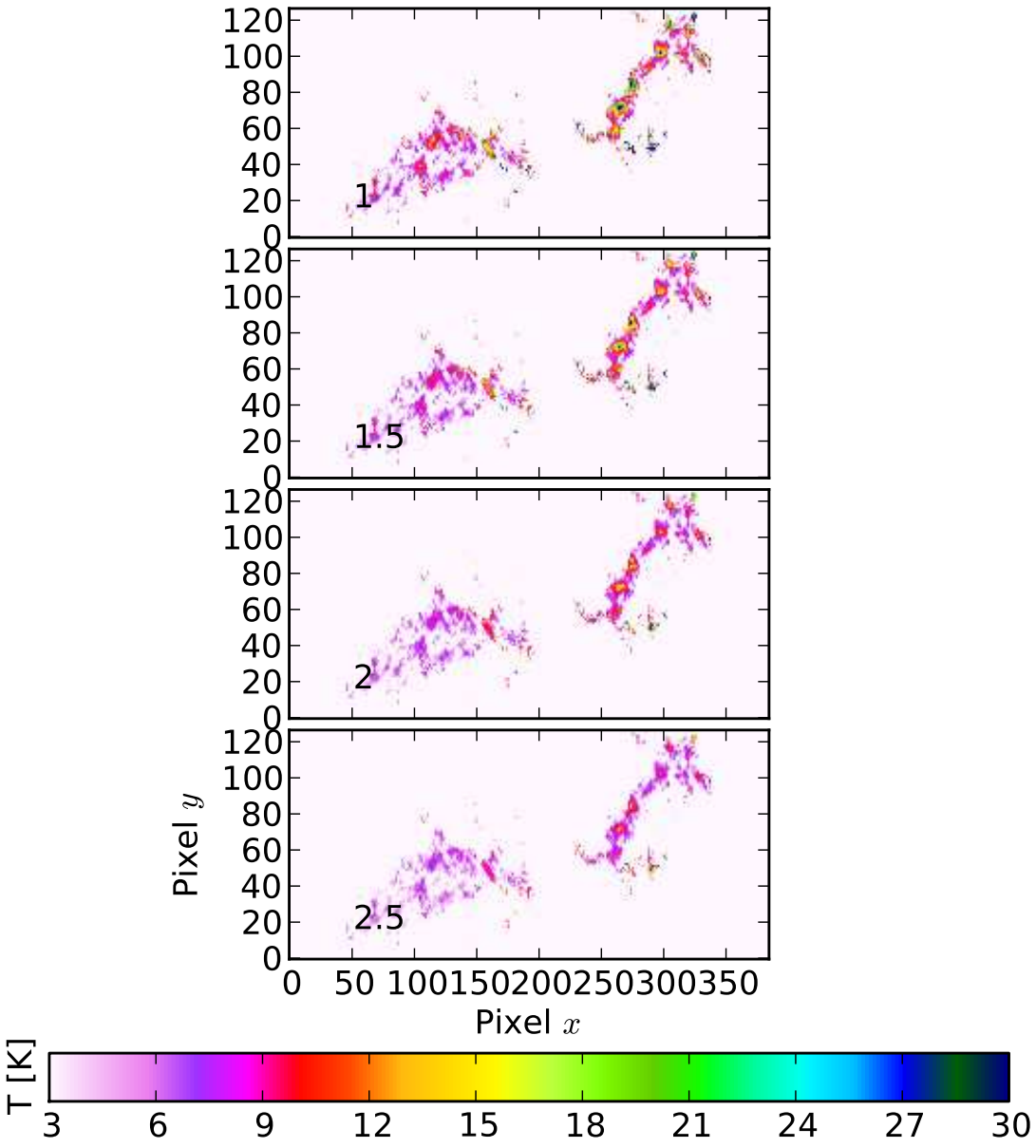

Figure 7.16: Derived color temperature for filament B. The panels show the derived color temperature using different values for the spectral index β. The temperature along the filament decreases with higher values of β, the average temperature is ~12 K and in all cases the temperature peaks locally toward the clumps.

7.5.2 Column density and mass

In this section we describe the methods used to obtain the total and lineal dust mass from the 870 μm continuum emission and the lineal and virial mass from the ^{13}CO(3-2) molecular line observations. We also describe how we obtained the total and virial masses for all the clumps embedded in this filament.

7.5.2.1 Column density and total mass of the filament

From the 870 μm dust continuum emission we calculated the radial column density at each point along the path defined for this filament, using Equation 1.31. For this calculus we used a dust opacity coefficient of $k_{870} = 0.012$ cm^{2}gr^{-1}and the temperature profile obtained in Section 7.5.1, which have a mean temperature of 12 K over all the filament and higher temperatures toward the clumps. The mean column density has a value of 5×10^{21} cm^{-2} reaching to 10^{23} locally toward the clumps. The total dust mass was obtained by integrating the radial column density along the diameter and length of the filament. We found that the total mass has a value of $\sim 7 \times 10^3$ M$_\odot$.

The virial mass was computed from the ^{13}CO(3-2) molecular line observation using Equation 1.6 at each point along the filament, taking into account the filamentary shape of this molecular cloud. The total virial mass was obtained by adding all the values of the virial mass calculated at each point along the filament. For filament D, the total virial mass has a value of $\sim 7 \times 10^3$ M$_\odot$.

Using the opacity, excitation temperature and line widths derived from the fit to the hyperfine components observed in the N_2H^+(1-0) emission, we derived the mass of the clumps observed in MALT90. The masses were obtained using equation 1.4.3.3. The values of the mass obtained for these clumps are summarized in Table 7.5.

Both virial and total mass are in agreement. The ratio between the total dust and virial mass is ~ 1. This value suggest that this filament is in virial equilibrium. However, due to the shape of this filament is better to analyze the virial equilibrium through the lineal total and virial mass.

7.5.2.2 Mass of the clumps

For each clump we calculated their total mass from their emission at continuum and molecular lines. The dust mass, from their emission at 870 μm, was computed using the integrated flux observed toward each clump using a dust opacity coefficient of $k_{870} = 0.012$ cm^{2}gr^{-1}. The temperature used for each clumps was obtained from the map of temperatures obtained in Section 7.5.1 using a spectral

index $\beta = 1.5$, when this temperature was not representative we used instead the assumed temperature for those clumps immersed in bright infrared emission. The clumps have masses ranging from ~ 70 $M_\odot$ to ~ 1200 $M_\odot$. Table 7.5 summarizes the total masses obtained for each clump.

The virial mass was derived from the ^{13}CO(3-2) molecular line emission, using Equation 1.66. This equation assumes that the clumps have a spherical geometry, which is a good approximation for the clumps embedded in this filament and are in virial equilibrium. We found that the virial masses range from ~ 400 $M_\odot$ to $\sim$1200 $M_\odot$, having in general higher values than the dust mass.

The ratio between the dust mass and virial mass is ~0.1 for clumps D1, D2 and D4. For clumps D3 and D9 this ratio is ~0.4. These values suggest that these clumps are not in virial equilibrium. For clump D7 we found that the dust and virial mass have almost the same value, suggesting that this clump is in virial equilibrium being the only clump embedded in this filament with this characteristic.

7.5.2.3 Lineal mass along the filament

At each point of the filament we obtained the total flux from the dust thermal emission at 870 μm. From this flux we obtained the radial column density. The lineal mass was computed by integrating the observed radial column density across the diameter of the filament, at each point along the path defined. We found that filament D has a mean lineal dust mass of 291 $M_\odot$.

Using the ^{13}CO(3-2) molecular line emission we derived the lineal virial mass. To do this we used the path defined for this filament to calculate lineal virial mass from the ^{13}CO(3-2) line width at each point. The mean line width of this observations is $\Delta v = 2.12$ km s^{-1} which gives a mean lineal virial mass of 380 $M_\odot$ pc^{-1}. The overall distribution of the lineal virial mass is similar to the one observed for the lineal dust mass. Figure 7.17 shows the distribution of both lineal masses along the filament, we see in this figure that overall both masses follow the same distribution.

7.5.3 External and internal pressure

The external pressure was computed from the ^{13}CO(3-2) molecular line and 870 μm continuum emission detected toward the regions located clearly outside the boundaries defined for filament D. The mean density in this external region is $\langle\rho\rangle = 3.7 \times 10^{22}$ gr cm^{-3} and the mean velocity dispersion of the ^{13}CO(3-2) molecular line is σ is 1.35 km s^{-1}. We assume that the external pressure is equal to the pressure at the surface of the filament, then these values give a mean value for the surface pressure of $Ps/k = 4.9 \times 10^4$ K cm^{-3}, which is similar to values obtained toward filaments surrounded by atomic gas (Fiege and Pudritz 2000).

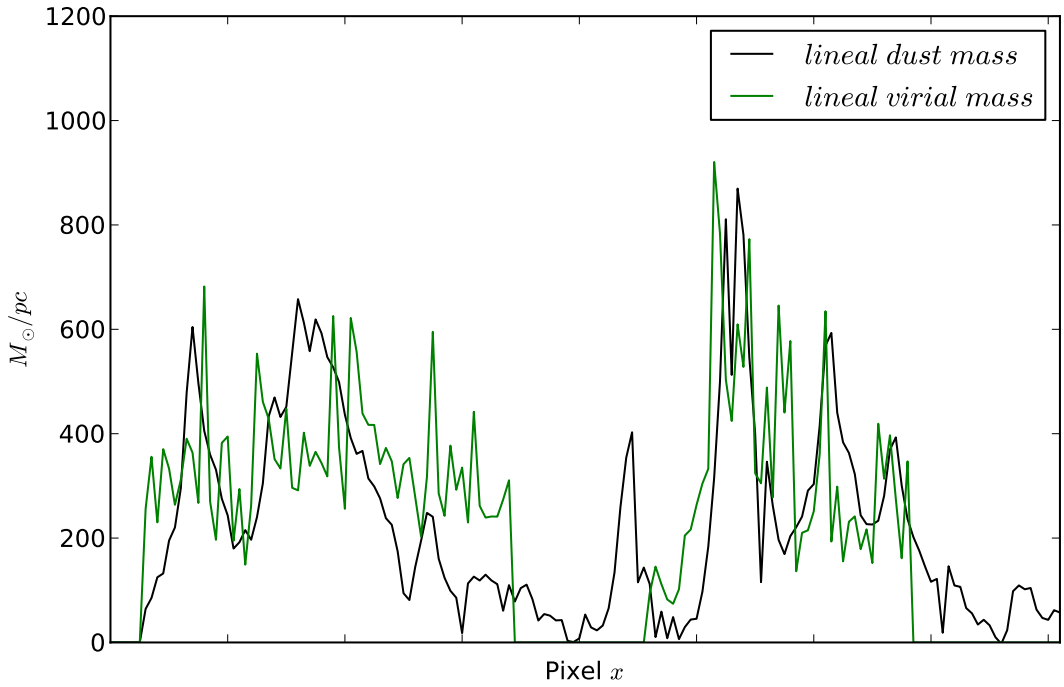

FIGURE 7.17: Lineal dust and virial mass distribution along the filament. Top panel: Black line, lineal mass obtained from the 870 μm thermal dust emission; Green, lineal virial mass derived from the ^{13}CO(3-2) molecular line emission. Overall both lineal masses have a similar morphology.

The internal pressure was calculated at each point along the filament using the line width, obtained from the ^{13}CO(3-2) emission, and the density per unit length derived from the 870 μm emission. We fit a Gaussian to the averaged ^{13}CO(3-2) spectrum obtained at each point along the filament and retrieve from this fit the line width of each spectrum. Then, the lineal density, at each point, was obtained by dividing the lineal mass over the volume per unit length (see Section 1.4.2.2 for further details). For filament D, the internal pressure have a mean value of $\langle P \rangle / k = 510 \times 10^4$ K cm^{-3}.

7.6 Stability of the filament: magnetic field support

In this section we study the stability of the filament in a twofold way. Firstly we study the influence of the presence of a magnetic field over the radial profile observed at 870 μm and 350 μm. Secondly, we analyze the extended form of the virial equilibrium, which include magnetic support, to determine if it is needed a magnetic field to explain the stability of this filament.

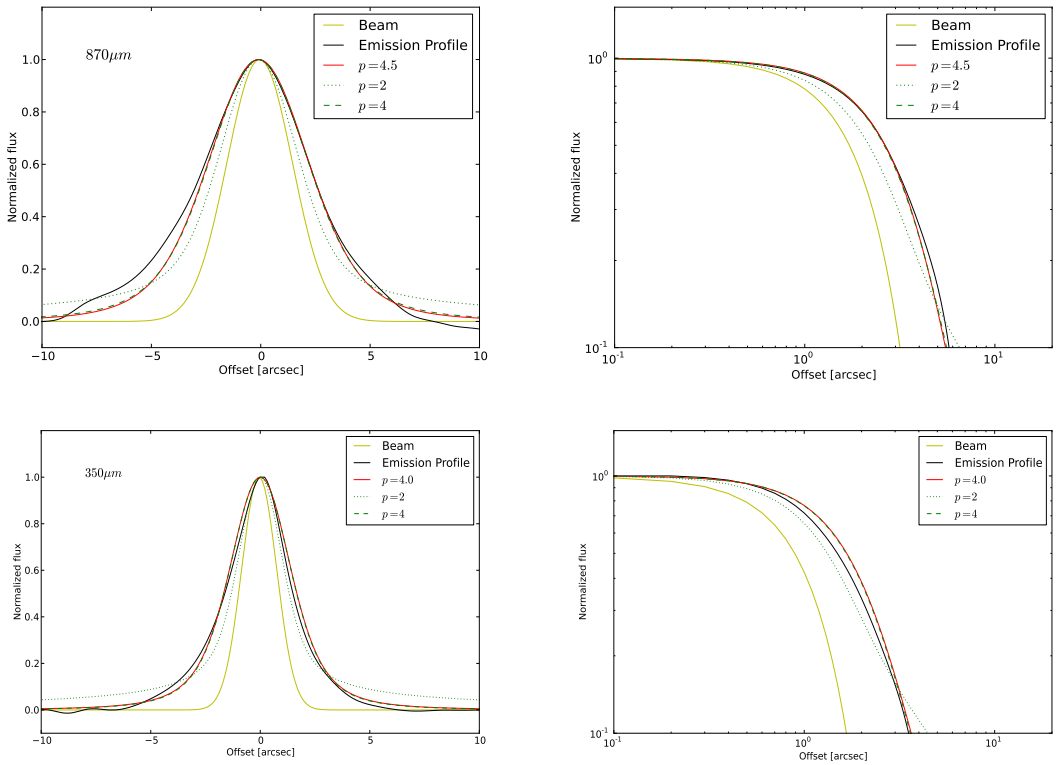

FIGURE 7.18: Density profile of the normalized mean density of the clumps in filament D. Top panels show the 870 μm emission, bottom panels show the 350 μm emission. The left panels show lineal plot of the profiles and right panels shown the profiles in logarithmic scales. The red solid lines represents the best fit to the density profile, the beam profile is shown with the solid yellow line, the hydrostatic solution p=4 (green dashed line) and magnetized solution p=2 (green dotted line) are also shown. We can see that in general the shape of the radial density follows the shape of a profile with $p = 4$.

7.6.1 Radial density profile analysis

To analyze the radial intensity profile we separate the dust emission into two groups: emission coming from the clumps embedded in the filament and emission from the inter-clumps material. Because we are only interested on the overall shape of the radial intensity, the dust continuum emission on both groups (clumps and inter-clumps) was averaged and normalized.

To the normalized radial intensity, at both 870 μm and 350 μm, we fit a density profile that satisfy Equation 1.34. For this fit we use as free parameter the central density, ρ_c, inner flat radius, R_{flat} and p. In this equation p varies according to the shape of the filament, $p = 4$ represents the radial density profile for a non-magnetic filament (Ostriker case) and $p \sim 2$ corresponds to a

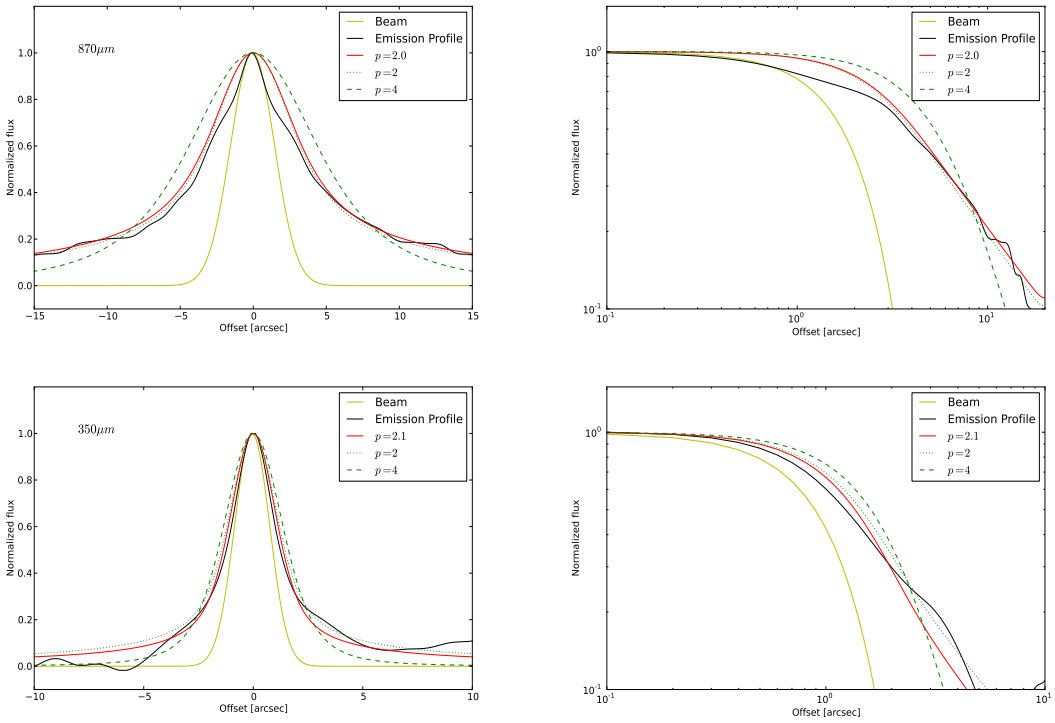

FIGURE 7.19: Density profile of the normalized mean radial density of the inter-clump region in filament D. Top panels show the 870 μm emission, bottom panels show the 350 μm emission. The left panels show lineal plot of the profiles and right panels shown the profiles in logarithmic scales. The beam profile is shown with the solid yellow line, the hydrostatic solution (green dashed line) and magnetized solution (green dotted line) are also shown. We can see that the shape of the radial density differs from the observed at the clump looking more similar to a solution with $p \sim 2$ at both wavelengths.

filamentary molecular cloud with magnetic field support (Fiege and Pudritz 2000).

On the clumps, the best fit to the radial intensity for both wavelengths is shown in Figure 7.18. The value of p obtained from the best fits are 4.5 and 4 at 870 μm and 350 μm respectively. This suggests that the shape of the radial intensity observed toward the clumps can be explained only by hydrostatic equilibrium, which corresponds to the non magnetic solution of a radial density profile with $p = 4$. Figure 7.19 shows the mean normalized column density and their corresponding fit toward the inter-clump material. In general the radial column density have wider wings that the one obtained for the clumps region. The non magnetic profile, $p = 4$, doesn't seems to fit the radial density profile at either wavelengths whereas the solution with $p = 2$ corresponding to a filament with magnetic support looks more similar to the shape on the radial density profile obtained for this region. The best fit to the radial column density is $p = 2.1$ and 2 for the emission at 870 μm and 350 μm respectively.

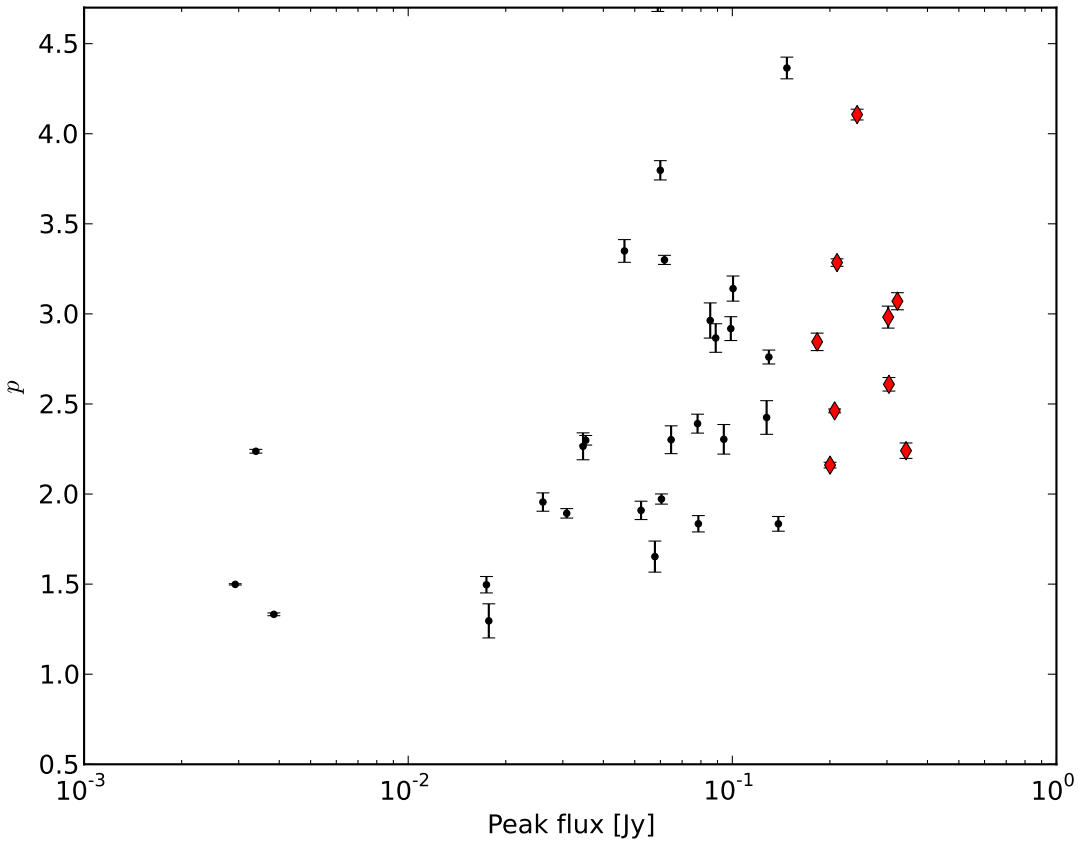

FIGURE 7.20: Plot of p, parameter that define the shape of the density profile, vs peak flux for the clump (red point) and inter-clump (black points) region. The error bars show the χ^2 between the fit and the observed radial density. We can see that in general the inter-clump regions have values of p lower than the clumps.

To analyze how the shape of the radial intensity changes along the filament we fit the 870 μm emission at each point along the path defined for this filament. We considered a *"good fit"* if the χ^2 between the observations and the fit is lower than 2. The values of p obtained from these good fits are shown in Figure 7.20. For this filament is not so clear the difference in the distribution of p between the region corresponding to the emission at clumps (red dots) and the inter-clump material (yellow dots). However, in general the values of p for the clumps are well distributed having many points in the range $2 < p < 4.5$, while for the inter-clump region they spread until $p = 1.5$. This result together with the previous analysis suggest that globally for the filament is needed an additional support explain its stability (magnetic field), while toward the clumps the stability can be explained only by hydrostatic equilibrium (non magnetic solution).

7.6.1.1 Virial equilibrium analysis

We analyze the stability of the filament following the work of (Fiege and Pudritz 2000) who uses an extended version of the virial equilibrium which includes external pressure and magnetic field support. With the values obtained from the lineal dust mass, lineal virial mass, internal pressure and surface pressure we compute $\langle P \rangle / P_s$ and m/m_{vir} for this filament. We plot $\langle P \rangle / P_s$ against m/m_{vir} over a diagram with constants values of $\mathcal{M}/|\mathcal{W}|$ to visualize the values of $\mathcal{M}/|\mathcal{W}|$ needed for the stability of this filament. Values of $\mathcal{M}/|\mathcal{W}|$¡0 implies that the support of the filament is given by a toroidal dominated magnetic field while values of $\mathcal{M}/|\mathcal{W}|$¿0 implies a poloidal dominated magnetic field as the additional support for the filament. The non-magnetic solution is given by $\mathcal{M}/|\mathcal{W}|$=0.

In this diagram we see that most of the values of $\langle P \rangle / P_s$ and m/m_{vir} obtained for this filament lay into the region of the diagram representing the solution of support via a toroidal dominated magnetic field. The mean value of $\langle P \rangle / P_s$ and m/m_{vir} are 0.015 and 0.7 respectively for the entire filament giving $\mathcal{M}/|\mathcal{W}|$=-0.3, which represents a solution to the virial equilibrium with a toroidal dominated magnetic field. For the clumps the values derived are $\langle P \rangle / P_s$=0.01 and m/m_{vir}=1.0 giving $\mathcal{M}/|\mathcal{W}|$=0.09 which is close to the non magnetic solution of the virial equilibrium. For the inter-clump region $\langle P \rangle / P_s$=0.02 and m/m_{vir}=0.4 which gives $\mathcal{M}/|\mathcal{W}|$=-1.3 suggesting that the inter-clump region of the filament is best represented also by the toroidal dominated magnetic field solution of the virial equilibrium.

This result is similar to the one obtained from the analysis of the mean radial column density, suggesting that while at the clump the magnetic field is negligible if we considerer the entire filament its stability is given by the presence of a magnetic field, in this case a toroidal dominated magnetic field.

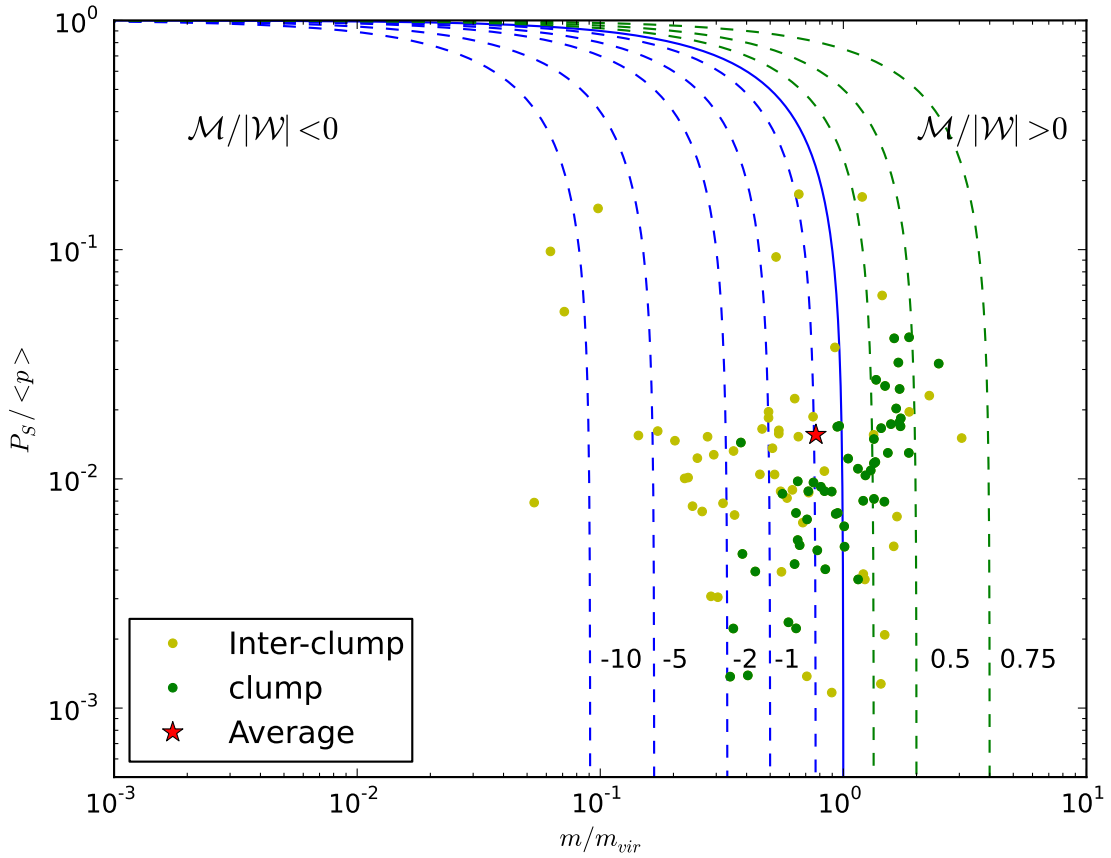

FIGURE 7.21: Plot of the $\langle P \rangle / P_s$ vs m/m_{vir} for the clumps and inter-clumps regions for filament D. Blue dashed lines: toroidal models for magnetic fields, blue solid line: unmagnetized solution, green dashed lines: poloidal magnetic field models. Yellow dots: values found for the inter-clump region of the filament; black dots: values found for the regions were clumps are located and the red star: mean value for the filament

TABLE 7.4: Filament D: derived properties of the filament.

Distance	**Length**	**Radius**	**N clumps**	**Δv**	**Temperature**	**Total mass**			**Lineal mass**			**P_s/k**	**$\langle P \rangle/k$**
				^{13}CO		**m**	**m_{vir}**	**m/m_{vir}**	**m**	**m_{vir}**	**m/m_{vir}**		
pc	pc	pc		km s^{-1}	K	$M_\odot$	$M_\odot$		$M_\odot$	$M_\odot$		10^4 K cm^{-3}	10^4 K cm^{-3}
3270	26.6	0.52	9	2.11	12	6800	6900	0.98	291	380	0.76	4.9	510

TABLE 7.5: Filament D, derived properties

	Temperature		$\mathbf{m_{dust}}$	$\mathbf{m_{vir}}$	$\mathbf{m_{N2H+}}$	$\mathbf{m_{dust}/m_{vir}}$	**Spacing**
	Color	Assumed					
	K		$M_\odot$	$M_\odot$	$M_\odot$		pc
D1	7	30	218	1848	183	0.12	2.98
D2	8	50	94	708	-	0.13	1.53
D3	9	50	162	407	-	0.39	0.77
D4	7	50	72	528	-	0.14	2.06
D5	12	-	349	1080	455	0.32	3.64
D6	-	35	180	-	246	-	-
D7	26	-	1238	1239	304	1.00	1.5
D8	15	-	15	-	40	-	1.6
D9	19	-	581	1478	2000	0.39	-

8

Filament E: AGAL332.094-0.421

Filament E, AGAL332.094-0.421, shows considerable mid infrared emission suggesting that it is an active region of star formation and could be an example of a late stage for filamentary molecular clouds where the fragmentation processes are over. At infrared wavelengths the structure studied doesn't appear as an infrared dark cloud. *Spitzer*/GLIMPSE images shows two sign spots of high emission at 8 μm and an extended region surrounded by considerable emission at 4.5 μm and 8 μm. At 4.5 μm we see a diffuse sheet like structure (green color in the images) in the upper left corner that matches the bright emission seen at 24 μm. The brightest part observed at the *Spitzer*/IRAC bands correlates well with the bright 24 μm cloud observed in the *Spitzer*/MIPSGAL maps (Figure 8.1 panel b). In general at 24 μm the emission is very extended covering almost entirely this region.

The dust continuum emission at 870 μm traces well the bright infrared regions. The morphology at 870 μm is complex, showing a filament that could be connected to the big molecular cloud observed to the upper right side and a string of clumps running parallel, but above, the main filament. At 350 μm the emission follows the morphology seen at 870 μm. The continuum emission suggests that the string of clumps observed cloud be a final stage of the fragmentation of a filamentary molecular cloud.

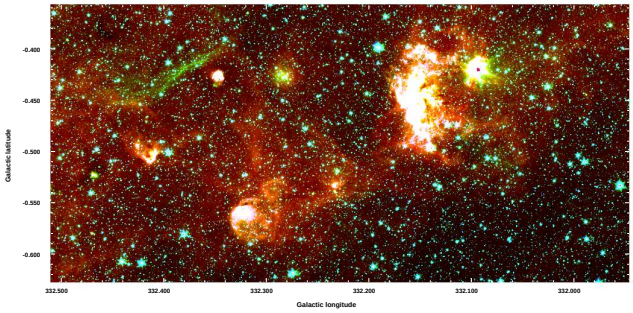

(a) *Spitzer*/GLIMPSE 3.5 μm - 8 μm

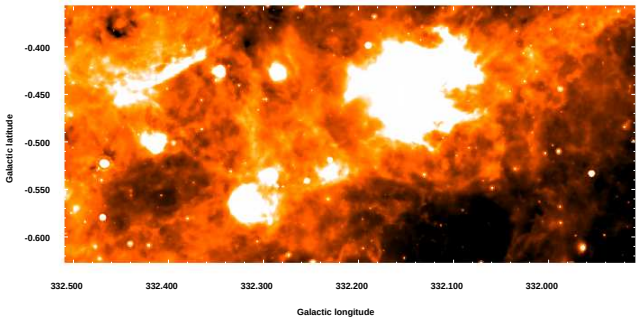

(b) *Spitzer*/MIPSGAL 24 μm

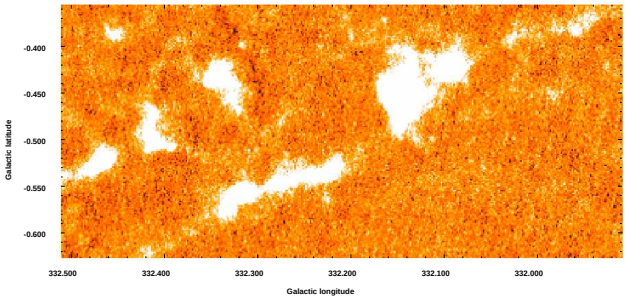

(c) APEX/LABOCA 870 μm

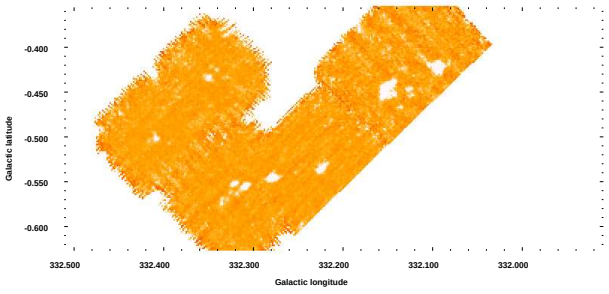

(d) APEX/SABOCA 350 μm

FIGURE 8.1: Multi-wavelength image of region E. *Spitzer* images show high levels of emission at infrared corresponding to bright structures at dust continuum with several regions with active star formation occurring (e.g. green fuzzies, bright 8 μm , 24 μm emission). We also can observe a small filamentary structure that does not to seem connected when we look at its infrared counterpart but it does at 870 μm.

8.1 Defining the Filament

This region was named after the brightest clump within it, using the ATLASGAL catalog denomination. Due to the complex structure observed in this region we will focus on a small portion of it where we see clearly at 870 μm an apparently connected filamentary structure. The path of the potential filament was determined by following the peaks in the 870 μm emission. To do this we use a Python algorithm that interpolates the emission between the peaks obtaining the path shown in Figure 8.2 (for further details see Section 1.4.1). Once the path was defined the width of the region containing the filament was set to 15 pixels (180 arc seconds) to each side of this path, enclosing all the continuum emission detected toward this filament. This region was also used to define the filament at 350 μm.

Figure 8.3 shows the flux density of the 870 μm and 350 μm dust continuum emission along the path defined for this filament. In this figure we can clearly identify the position of the clumps embedded. This is even more evident at the 350 μm emission where the clumps are more evident because the extended emission of this filament is not very high. In this figure we also see that overall the filament have a intensity much higher than the mean *rms* observed in this maps (4.7 mJy at 870 μm and 0.09 Jy at 350 μm, red dotted line).

From the 870 μm emission we derived the projected radius of this filament. This was done by fitting a Gaussian to the radial dispersion of the emission at each point along the filament. This filament has an average projected radius of 14".

8.2 Physical coherence of the observed filamentary structure

Although the small filament observed in this region appears to be connected, since the dust continuum emission traces all clouds along the line of sight we need additional molecular line information to determined its physical coherence. To determine if this filament is a single coherent structure and if the string of clumps detected are related to this filament, we performed ^{13}CO(3-2) observations covering this region almost entirely.

Figure 8.4 (middle panel) shows the velocity integrated intensity map of the ^{13}CO(3-2) emission. This map was made using a range in velocity from -65 km s^{-1} to -40 km s^{-1}. The upper panel in this figure shows the velocity integrated intensity contours overploted to the 870 μm continuum emission. We see that the ^{13}CO(3-2) emission traces well the morphology observed in the continuum. Figure 8.4 (lower and right panels) shows the position-velocity (l,v) and (b,v) maps

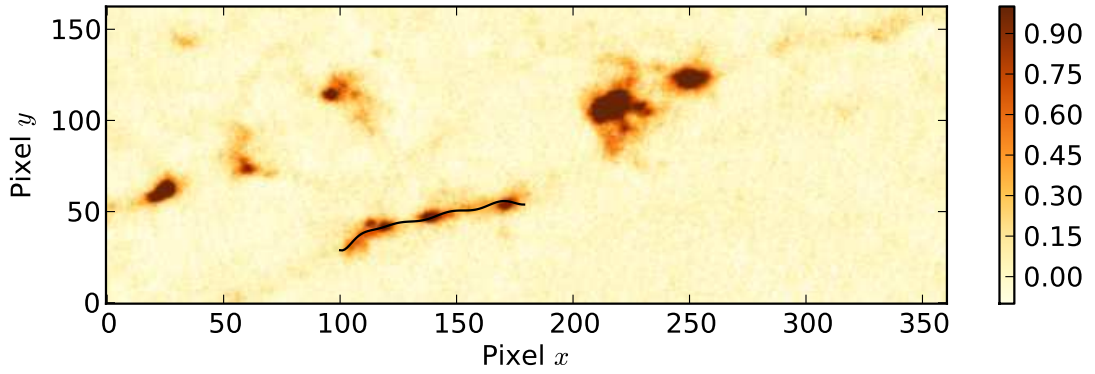

FIGURE 8.2: Path defined for filament E. Color scale showing the 870 μm emission (scale in Jy/beam) toward filament E. The black line shows the path defining the filament, based on the Python algorithm that follows the 870 μm peaks. The region containing the filament was set to 15 pixel to each side of this path.

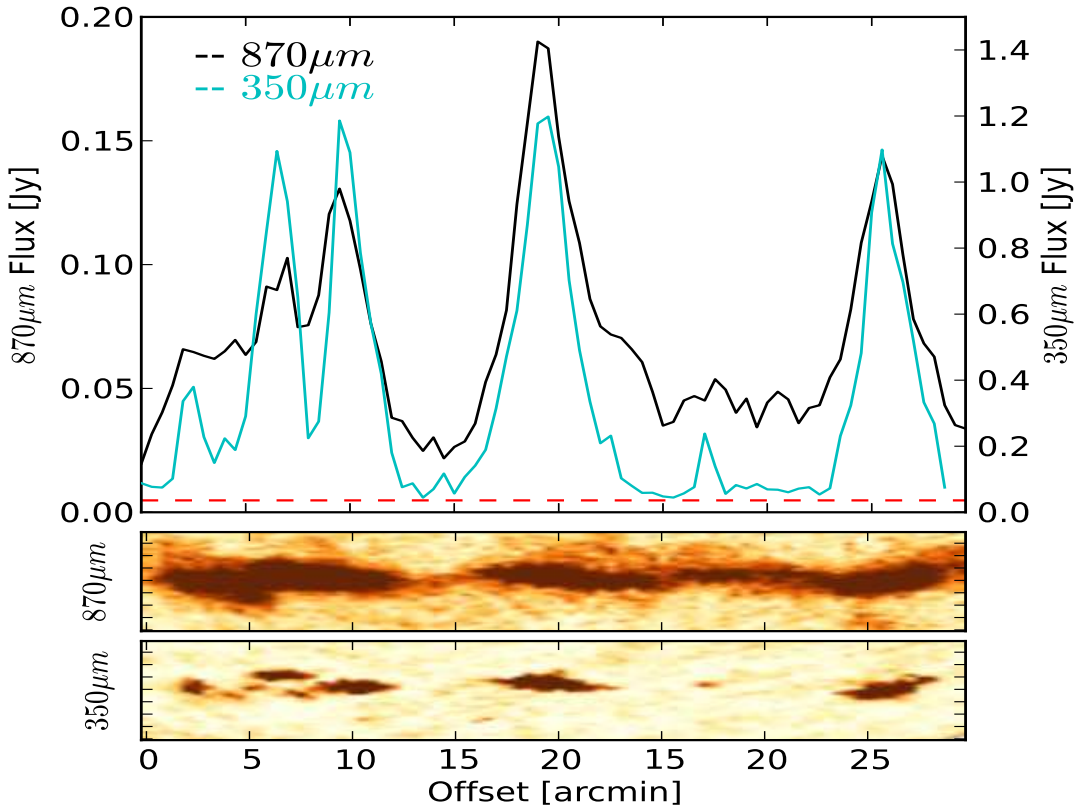

FIGURE 8.3: Distribution of dust continuum emission along the filament. Top panel: Flux along the path defined for filament E for both 870 μm (black line) and 350 μm (blue line), red dotted line represents the mean noise in the map (4.7 mJy at 870 μm and 0.09 Jy at 350 μm). Lower panels: Color scale of the emission at 870 μm and 350 μm. We see how the clumps are well defined in the 350 μm emission.

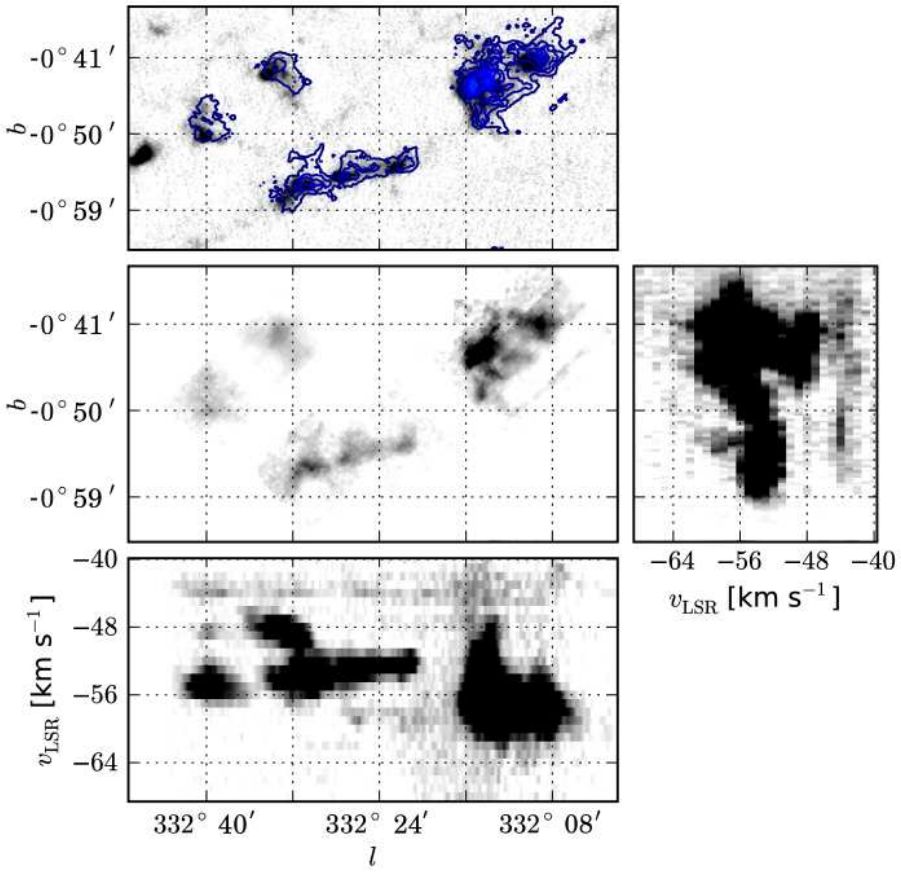

FIGURE 8.4: ^{13}CO(3-2)emission toward filament E. Top panel: dust emission at 870 μm overlaid with contours of the ^{13}CO(3-2) integrated intensity from 3 to 30 σ, with σ = 3.4 K km s^{-1}. Middle panel: ^{13}CO(3-2) integrated intensity. Lower and right panels: position velocity maps (l,v) and (b,v) integrated over both Galactic latitude and longitude respectively. These images reveal that the ^{13}CO(3-2) emission toward this filament reveals three discrete molecular clouds along the line of sight ((l,v) lower panel).

of the ^{13}CO(3-2) emission integrated along the Galactic latitude and longitude respectively. These position-velocity maps show how the central velocity on the string of clumps varies from -48 km s^{-1} to -56 km s^{-1}. The small filament has the same velocity indicating that it is a single coherent structure. The molecular cloud observed to the upper right side of the image, has a similar velocity to the small filament. Thus, this cloud might have been initially connected to the filament.

From the ^{13}CO molecular line emission we also derived the distance to the small filament, using the model of the rotation of the Galaxy described in Section 1.4.3.2. This filament does not appear dark at infrared, thus, we cannot disentangle between it near and far kinematic distance using this

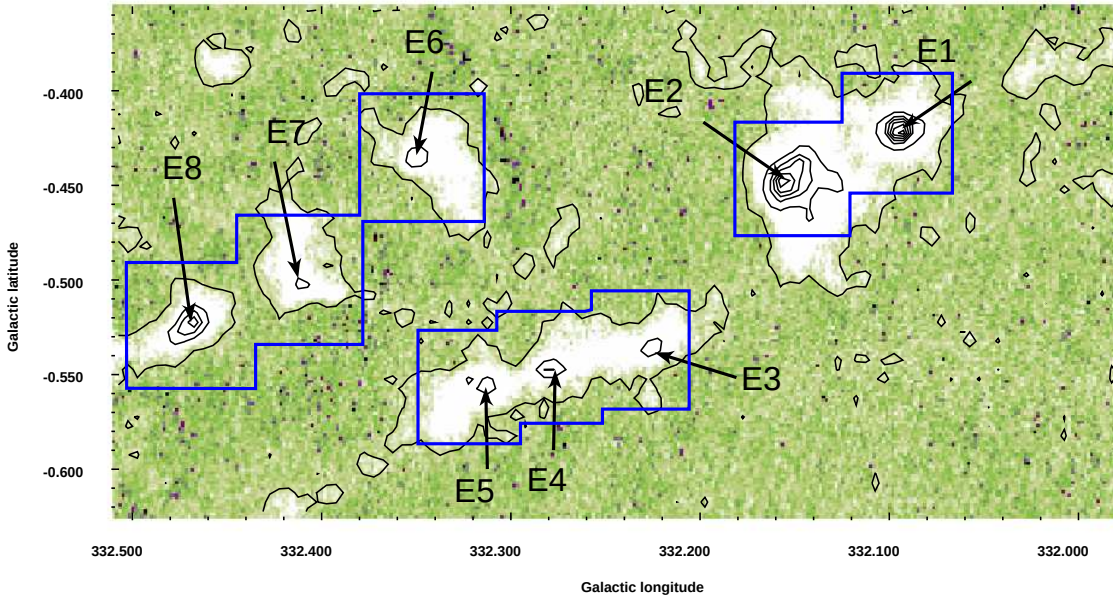

FIGURE 8.5: Color image of the emission at 870 μm, contours from 3σ to peak emission in logarithmic scale. Arrows indicated the position of the clumps identified within this filament. Boxes shows the region of the filament covered by the MALT90 observations. Contours shows the emission > 3σ

method. In the catalog of (Caswell and Haynes 1987) of HII region, the molecular cloud observed in this region (upper right side of the image) correspond to a HII cataloged with a distance of 4 kpc, which correspond to the near kinematic distance. In this catalog the near kinematic distance was chosen based on 21 cm absorption line data toward the HII region. Thus, for the filament we will use its near kinematic distance. This distance to the small filament is ~3.7 Kpc which gives it a length of 36.6 pc and a radius of 0.23 pc.

8.3 Properties of the embedded clumps within the filament

From the ATLASGAL point source catalog we identify eight clumps. The location of these clumps are shown in Figure 8.5. The names of the clumps are taken from their ATLASGAL denomination, but for simplicity, in this work we assign them the IDs E1, E2, E3 etc ordered by Galactic longitude. In the small filament we detected three embedded clumps (E3, E4 and E5). Clumps E1 and E2 are located in the molecular cloud observed toward the upper right side of the image, and the rest of the clumps corresponds to the string of clumps above and parallel to the small filament.

Table 8.1: Filament E, star formation activity of the observed clumps.

ID	ATLASGAL Name	GLIMPSE 3.6 - 8 μm	MIPSGAL 24 μm	ATLASGAL [b]	IRAS
E1	AGAL332.094-0.421	Bright 8 μm	Bright	Bright	16124-5110
E2	AGAL332.156-0.449	Bright 8 μm	Bright	Bright	16128-5109
E3	AGAL332.226-0.536	Green fuzzies[a]	Point source	Bright	-
E4	AGAL332.279-0.547	Green fuzzies[a]	Point source	Bright	-
E5	AGAL332.312-0.556	Diffuse 8 μm	Diffuse	Bright	16141-5107
E6	AGAL332.351-0.436	Bright 8 μm	Bright	Bright	16137-5100
E7	AGAL332.411-0.502	Bright 8 μm	Bright	Bright	16143-5101
E8	AGAL332.469-0.522	Green fuzzies[a]	Point source	Bright	16147-5100

[a] Green fuzzies: Enhancement at 4.5 μm.

[b] Bright emission: Peak emission > 1 Jy/beam; weak emission: Peak < 1 Jy/beam

Clumps E1, E2, E5, E6 and E7 show extended emission at infrared wavelengths. Toward clumps E3, E4 and E8 the infrared emission is localized to the center of each clump (green fuzzies and 24 μmpoint sources), suggesting a less evolved stage of evolution. Table 8.1 summarizes the observational properties based on the level of infrared and sub millimeter emission found in the GLIMPSE, MIPSGAL and ATLASGAL images. In this table *Bright* at infrared means that the emission found is extended around the region containing the clump. Column 6 of this table show the association of the clumps with IRAS sources. Almost all the clumps in this region are associates with an IRAS source.

From the 870 μm and 350 μm continuum emission we derive the properties of the eight clumps identified obtaining: the peak flux, integrated flux and the size enclosing the emission at the half peak. The values obtained are listed in Table 8.2.

For the clumps observed at ^{13}CO(3-2) we derive the average spectrum of the $> 3\sigma$ noise emission. To the mean spectra we fit a Gaussian obtaining: peak temperature (T_{peak}), central velocity (v_{LSR}), line width (Δv) and integrated intensity ($\int T_b dv$, II in the table). The values gathered from these fits are summarized in Table 8.2.

Toward the eight clumps identified at 870 μmwe performed N_2H^+ observations. Due to the large width in velocity observed in these sources the hyperfine structure is not always resolved and in most of the clumps observed we only see a single broad emission. Only for clump E7 it was possible to fit the hyperfine structure using CLASS, obtaining from this fit the opacity toward this clump, however, the fit is not very good, thus, we will not use this opacity to calculate the

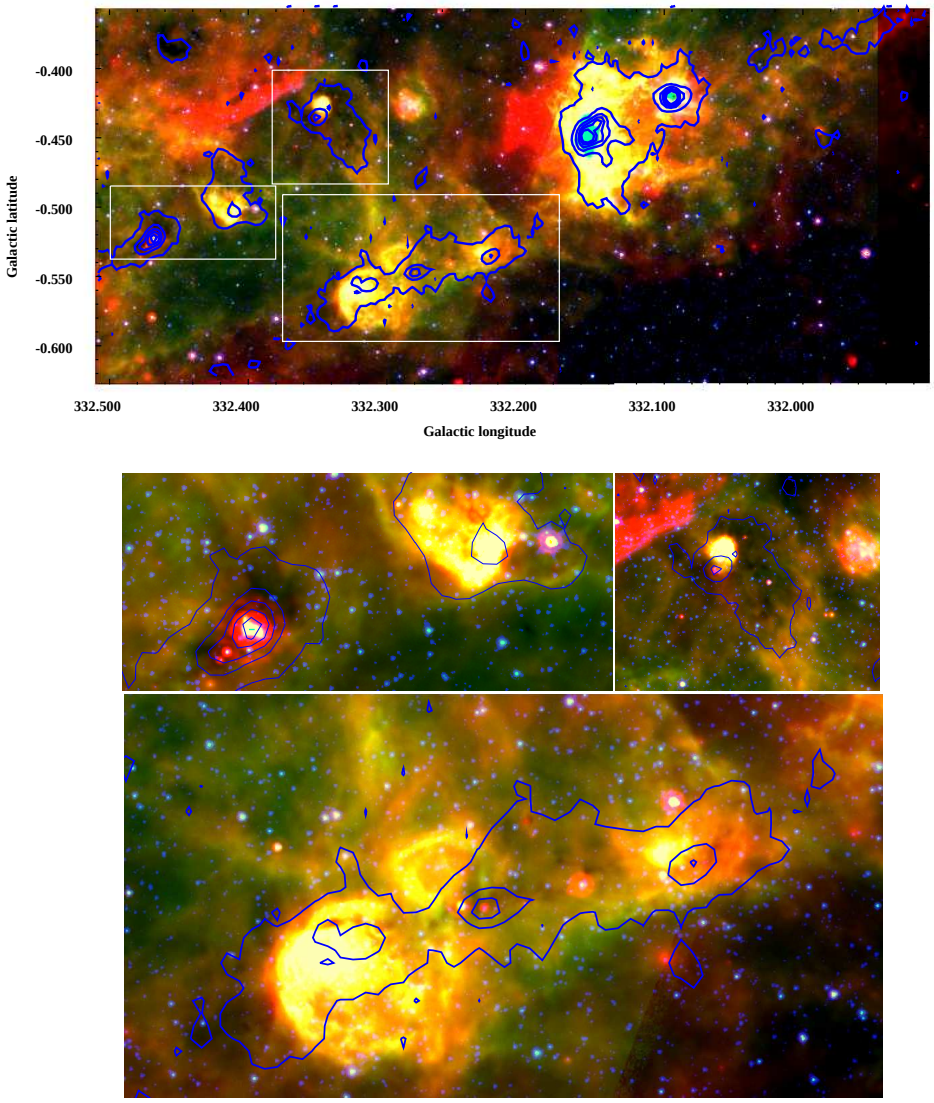

FIGURE 8.6: Infrared emission toward filament E. Top panel: Color image of filament E (red: 24 μm, green: 8 μm and blue: 4.5 μm); blue contours dust thermal emission at 870 μm. Lower panels: Zoom into the regions indicated by white boxes at the top panel image. We can see that although at infrared wavelength the filament does not appear as a connected structure their counterpart at 870 μm does, we also can see how this filament is in a late evolutionary stage due to the high emission at 8 μm and 24 μm characteristic of star formation regions.

mass of this clump. For the remaining clumps, we fit a three component Gaussian centered in the theoretical position of the hyperfine component. From these fits we obtained the peak temperature (T_{peak}), central velocity (v_{LSR}), line width (Δv) and integrated intensity (II). Table 8.2 listed the values obtained from these fits. Figure 8.7 shows the spectra of the N_2H^+(3-2) observations with

their fit (green line) and the position of the hyperfine components.

8.4 Chemistry, evolutionary stage and kinematics of the brightest clumps

To assess the chemistry and evolutionary stage of the clumps embedded in this region, we performed molecular line observation of sixteen molecular lines as part of the MALT90 survey. These observations were carried out toward the eight clumps detected in this region and covered entirely the small filament. For all the clumps we detected (velocity integrated intensity > 3σ noise) HCO^+, N_2H^+, HCN, HNC which are transitions typically found toward dense molecular clouds. We also detected C_2H observed toward photodissociation regions.

Toward clumps E1 and E8 we detected eight of the sixteen molecular lines observed: N_2H^+, HNC, $HN^{13}C$, HCO^+, $H^{13}CO^+$, HCN, HC_3CN and C_2H. HC_3CN is usually detected toward hot cores and C_2H is a photodissociation tracer, boths detection are in agreement with the infrared emission observed toward these clumps. Toward E2, E5 and E6 we detected molecular transitions that traces dense gas (N_2H^+, HNC, HCO^+, $H^{13}CO^+$ and HCN) and C_2H also in agreement with their infrared emission. Toward clumps E3, E4 and E7 we detected the density tracer: N_2H^+, HNC, HCO^+ and HCN, and C_2H.

Integrated intensity maps were made for all the transitions detected toward each clump. Figure 8.8 shows the integrated intensity maps of HCO^+, HCN, HNC, C_2H, HC_3CN and N_2H^+ toward clumps E6, E7 and E8 using a velocity range of -62 km s^{-1} to -36 km s^{-1}. We see that the emission is localized toward the clumps with no visible emission between them. From these three clumps, E6 is the one with higher emission at all the transitions.

Figure 8.10 shows the velocity integrated intensity maps toward the filament containing clumps E3, E4 and E5. The molecules detected toward this region are HCO^+, N_2H^+, HCN, HNC and C_2H which have a range in velocity from -58 km s^{-1} to -48 km s^{-1}. This figure shows that the emission of HCO^+, HNC and HCN covers the entire filament while at N_2H^+ we the emission in localized towards the clumps. From the six molecular transitions showed in these maps C_2H in the one with lower intensity. This C_2H emission matches well the morphology observed at the dust and others molecules. Toward the region containing clumps E1 and E2 we made integrated intensity maps of HCO^+, HCN, HNC, N_2H^+, C_2H and HC_3CN using a range in velocity from -67 km s^{-1} to -45 km s^{-1} (Figure 8.11). We see that the emission of HCO^+ and HCN is more extended while at the rest of the molecular lines show localized emission towards the central part of the clumps.

The spectra of the molecular lines detected toward clump E1 is shown in Figure 8.12. In this

figure we see a red asymmetry in the ^{13}CO(3-2), HCO$^+$ and HNC lines. In these line we also see self-absorption. These profile suggest outward movement in the clump. The spectra also suggest turbulent motions due to the large line widths ($\sim$ 2-3 km s^{-1}).

Toward clump E2 the line width of the lines is also large suggesting turbulent motions in the clump. The spectra toward this clump are also more complex, and most of them show self-absorption. For this clump the N_2H^+(1-0) emission is very weak compared with the emission observed toward the other clumps. Figure E.17 and E.18 show the channel map of N_2H^+(1-0) and HCO$^+$ for clumps E1 and E2.

For clump E3 the spectra are more symmetric are narrow distinguishing clearly the hyperfine components at N_2H^+(1-0) and HCN. The spectra toward clump E4 are also very symmetric and narrow. For clump E5 the line width of the spectra are wider, we see some auto absorption at ^{13}CO(3-2) which presents a red asymmetry suggesting outward motions. Figure E.19 and E.20 show the channel map of N_2H^+(1-0) and HCO$^+$ for clumps E3, E4 and E5.

The spectra toward clumps E6 and E7 are rather symmetric. Since the signal to noise in this emission is not very high, the hyperfine components at N_2H^+ and HCN are not very clear. Toward clump E8 the spectra are asymmetric with a clear wing to the blue side of the spectra, suggesting outflows. We can also distinguish some self absorption in the HNC line. Figure E.21 and E.22 show the channel map of N_2H^+(1-0) and HCO$^+$ for clumps E6, E7 and E8.

For each clump, we perform a Gaussian fit to the peak position in all the molecular lines detected. From these fits we obtained the central velocity of the emission (v_{LSR}), its peak antenna temperature (T_{peak}), line width (Δv) and integrated intensity (II). We also obtained the (l,b) position of the peak spectrum expressed as the offset with respect to the position of the peak spectrum of N_2H^+(1-0) (Δl and Δb) and the total integrated intensity (I_T). For all the clumps, the detections were defined as the emission of II > 3σ. The results of these fits for each of the detected molecules are summarized in Table 8.3. We also fitted the hyperfine components of the N_2H^+ emission. From these fits we obtained the excitation temperature, line width and opacity of the line. These values are listed in Table B.1.

Table 8.2: Parameters of the clumps in filament E from their continuum and molecular emission.

	870 μm				350 μm				^{13}CO(3-2)					N_2H^+(3-2)			
ID	Peak Flux	Diameter		Int. Flux	Peak Flux	Diameter		Int. Flux	T_{peak}	v_{LSR}	Δv	II	Diameter	T_{peak}	v_{LSR}	Δv	τ
	Jy/Beam	’	pc	Jy	Jy/Beam	’	pc	Jy	km s^{-1}	km s^{-1}	K	K km s^{-1}	pc	km s^{-1}	km s^{-1}	K	
E1	6.99	1.4	1.5	23.9 (0.7)	18.68	0.6	0.6	85.77(3.68)	9.13	-56.20	5.87(0.33)	57.14(3.25)	1.5	1.34	-53.80	2.99(0.26)	
														3.69	-50.92	3.04(0.26)	
														1.35	-48.84	2.75(0.26)	
E2	5.23	2.0	2.1	47.8 (0.9)	9.22	0.5	0.5	35.82(2.25)	14.51	-56.00	4.82(0.17)	74.54(2.59)	1.1	0.18	-56.62	1.29(0.17)	
														0.62	-53.98	1.56(0.12)	
														0.22	-51.91	1.42(0.42)	
E3	1.49	1.9	2.0	10.1 (0.9)	4.38	0.4	0.4	13.84(0.84)	8.30	-52.23	2.25(0.19)	19.90(1.69)	0.8	0.15	-50.89	0.79(0.03)	
														0.67	-48.24	2.06(0.03)	
														0.08	-46.17	2.06(0.03)	
E4	1.98	1.2	1.3	7.9 (0.5)	4.95	0.5	0.5	18.99(0.98)	6.59	-53.11	3.08(0.28)	21.65(1.99)	0.9	0.82	-55.08	3.47(0.15)	
														2.43	-52.45	2.59(0.04)	
														1.05	-50.32	2.24(0.07)	
E5	1.36	1.3	1.4	8.3 (0.6)	5.15	0.3	0.3	9.53(0.55)	10.27	-53.50	3.51(0.19)	38.45(2.17)	0.8	0.13	-57.80	2.63(0.74)	
														0.32	-55.13	2.91(0.26)	
														0.08	-52.99	7.66(1.99)	
E6	1.65	1.6	1.7	10.8 (0.7)	2.90	0.4	0.4	6.01(0.96)	7.94	-48.01	2.33(0.20)	19.69(1.71)	1.3	1.36	-59.13	2.76(0.05)	
														3.15	-56.49	2.55(0.03)	
														1.18	-54.41	2.53(0.08)	
E7	1.68	1.7	1.8	7.9 (0.8)	4.62	0.4	0.4	9.17(0.89)	3.84	-54.68	2.75(0.46)	11.25(1.88)	0.9	0.21	-53.30	0.87(0.08)	11.0(1.38)
E8	3.11	1.5	1.6	17.4(0.8)	-	-	-	-	-	-	-	-	-	0.37	-55.15	1.45(0.20)	
														1.16	-52.51	1.98(0.69)	
														0.52	-50.43	1.66(0.11)	

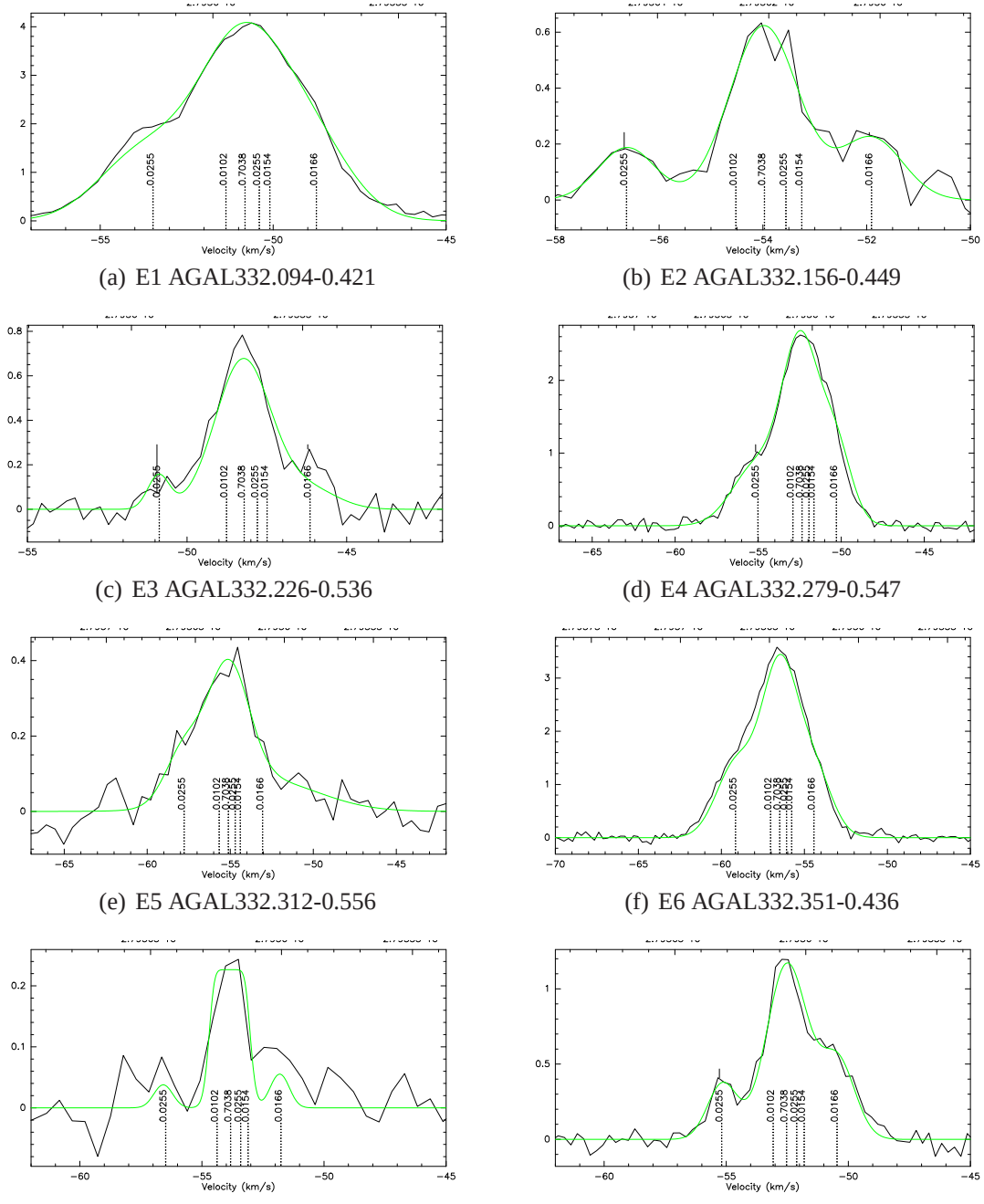

(a) E1 AGAL332.094-0.421

(b) E2 AGAL332.156-0.449

(c) E3 AGAL332.226-0.536

(d) E4 AGAL332.279-0.547

(e) E5 AGAL332.312-0.556

(f) E6 AGAL332.351-0.436

(g) E7 AGAL332.411-0.502

(h) E8 AGAL332.469-0.522

FIGURE 8.7: Spectra of the N_2H^+observations. Each plot show the Gaussian fit (green line) and position of the individual hyperfine component for each spectra. The numbers indicate the relative intensity of the lines. The fit is shown in green. Here is clearly seen that due to the large linewidth of the hyperfine components they are blended in almost all the spectra.

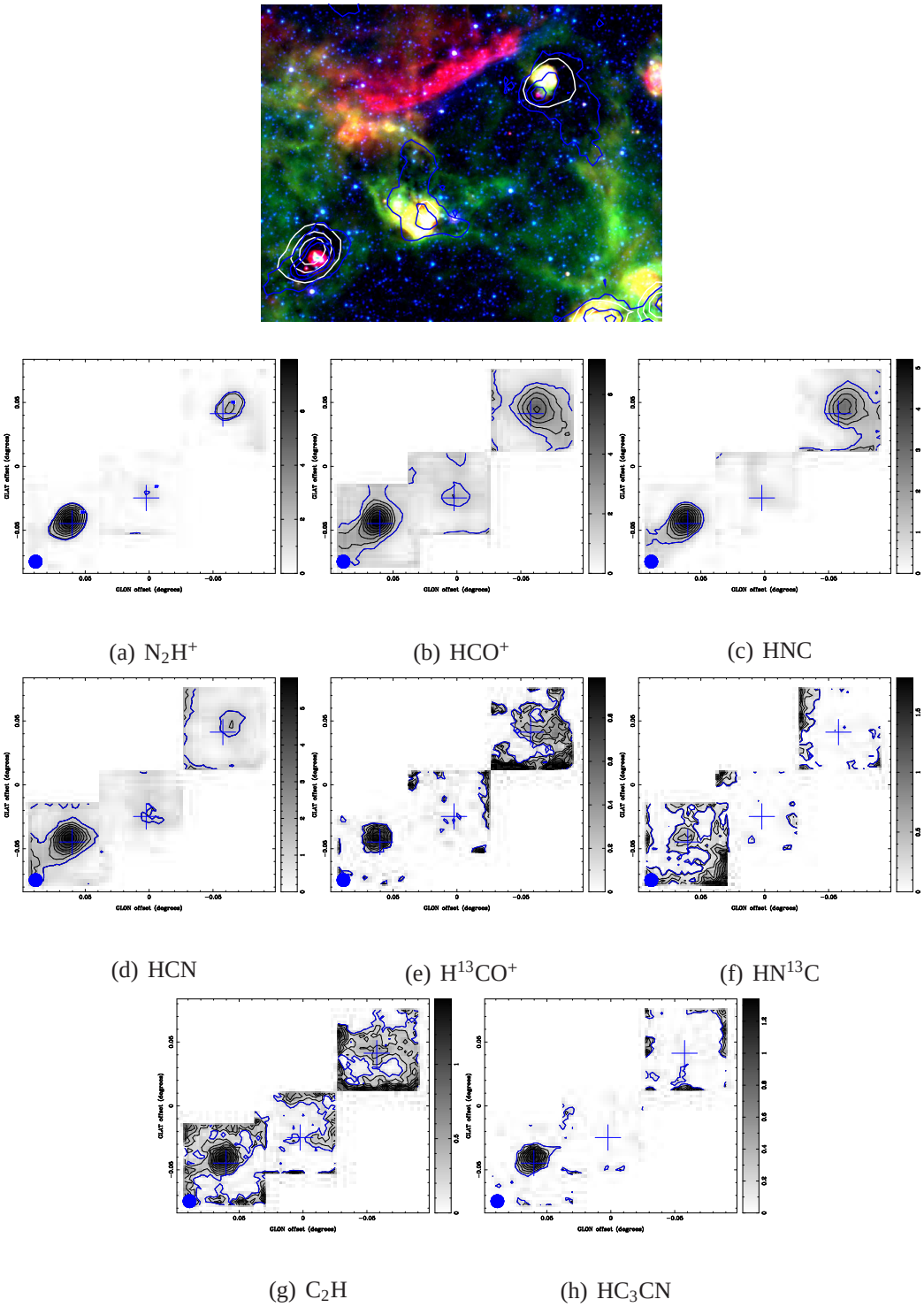

FIGURE 8.8: II images of the molecules detected toward E6, E7 and E8 from the MALT90 survey. Top panel: Three color *Spitzer*/IRAC (Red: 24 μm, blue: 8 μm, green: 4.5 μm, blue contours: 870 μm, white contours: N_2H^+(1-0)). Lower panels (a)-(h): Maps of integrated intensity from each of the detected lines (II $> 3\sigma$). Contours represent the emission from 90% of the peak to 3σ noise emission (blue contour) in steps of 10%. The crosses shows the position of the clumps and the blue circle shows the beam size. The color bar shows the value of the peak at each molecule.

FIGURE 8.9: Zoom of filament toward the region covered by clumps E3, E4 and E5. Color image composed of blue: IRAC 4.6 μm, green IRAC 8 μm and red MIPS 24 μm. Blue contours integrated intensity of C_2H molecular line emission and black contours integrated intensity of N_2H^+(1-0) molecular line emission.

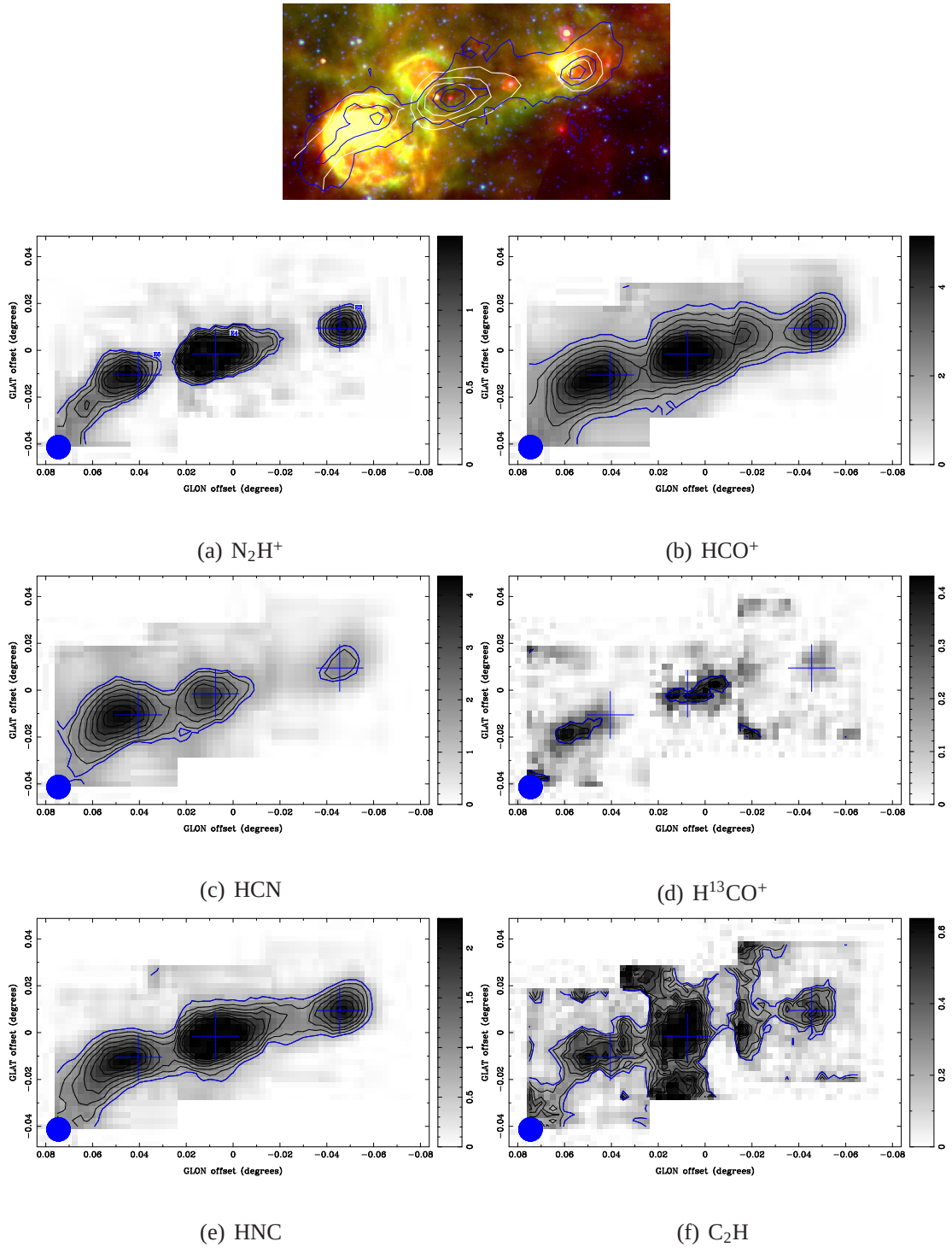

(a) N_2H^+ (b) HCO^+

(c) HCN (d) $H^{13}CO^+$

(e) HNC (f) C_2H

FIGURE 8.10: II images of the molecules detected toward E3, E4 and E5 from the MALT90 survey. Top panel: Three color *Spitzer*/IRAC (Red: 24 μm, blue: 8 μm, green: 4.5 μm, blue contours: 870 μm, white contours: N_2H^+(1-0)). Lower panels (a)-(f): Maps of integrated intensity from each of the detected lines (II $> 3\sigma$). Contours represent the emission from 90% of the peak to 3σ noise emission (blue contour) in steps of 10%. The crosses shows the position of the clumps and the blue circle shows the beam size. The color bar shows the value of the peak at each molecule.

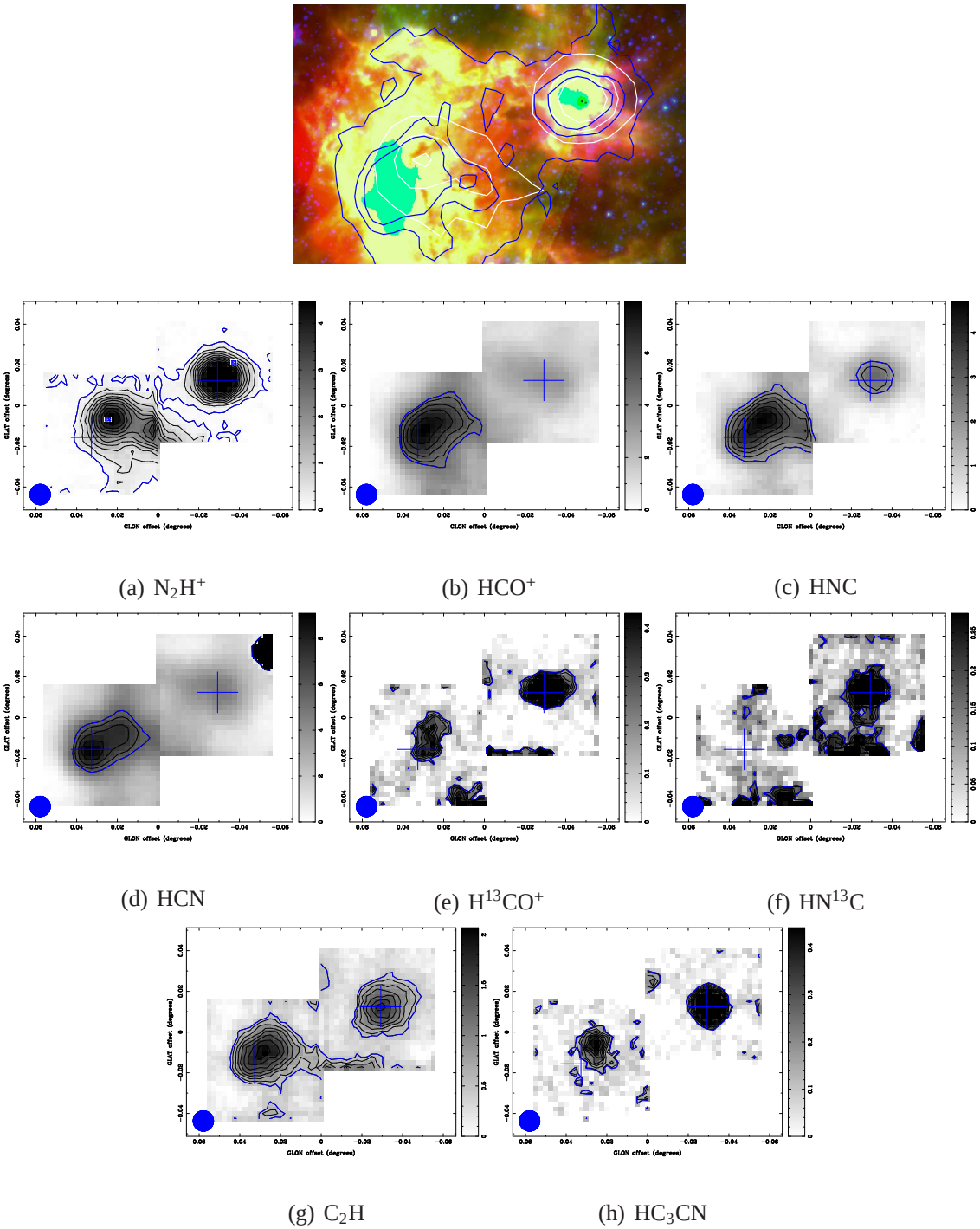

(a) N_2H^+ (b) HCO^+ (c) HNC

(d) HCN (e) $H^{13}CO^+$ (f) $HN^{13}C$

(g) C_2H (h) HC_3CN

FIGURE 8.11: II images of the molecules detected toward E1 and E2 from the MALT90 survey. Top panel: Three color *Spitzer*/IRAC (Red: 24 μm, blue: 8 μm, green: 4.5 μm, blue contours: 870 μm, white contours: N_2H^+(1-0)). Lower panels (a)-(h): Maps of integrated intensity from each of the detected lines (II > 3σ). Contours represent the emission from 90% of the peak to 3σ noise emission (blue contour) in steps of 10%. The crosses shows the position of the clumps and the blue circle shows the beam size. The color bar shows the value of the peak at each molecule.

Table 8.3: Properties of the MALT90 observations

Source	Molecule	Δl[1]	Δb[1]	Peak	Width	Velocity	I_P[2]	I_T[3]	*rms*
		"	"	K	km s^{-1}	km s^{-1}	K km s^{-1}	K km s^{-1}asec^2	km s^{-1}
E1 AGAL332.094-0.421	$N2H^+$	0	0	1.33	3.52	-56.42	4.99	87	0.19
	HCO^+	9	0	0.71	2.56	-54.94	1.93	432	2.69
	$H^{13}CO^+$	0	0	0.43	3.57	-56.88	1.63	20	0.19
	HCN	0	0	0.43	2.37	-55.77	1.08	2514	8.17
	$HN^{13}C$	0	0	0.34	2.30	-57.00	0.83	29	0.18
	HNC	18	0	0.75	2.96	-55.63	2.36	306	0.18
	HC_3N	9	0	0.47	2.89	-56.88	1.45	22	0.18
	C_2H	0	0	0.54	2.28	-56.83	1.31	218	0.19
E2 AGAL332.156-0.449	$N2H^+$	0	0	0.65	3.21	-57.80	2.22	489	0.20
	HCO^+	-45	18	1.19	3.47	-55.95	4.40	1683	0.49
	$H^{13}CO^+$	-18	27	0.19	2.18	-55.41	0.44	944	0.20
	HCN	-45	27	1.17	3.34	-56.12	4.16	2226	0.22
	HNC	0	0	0.81	1.95	-58.61	1.68	1057	0.20
	C_2H	-18	9	0.47	2.67	-57.76	1.33	246	0.20
E3 AGAL332.226-0.536	$N2H^+$	0	0	0.57	2.93	-51.89	1.78	78	0.11
	HCO^+	0	-9	1.42	2.96	-52.33	4.48	747	0.11
	HCN	0	-9	0.70	2.47	-52.26	1.84	546	0.11
	HNC	0	0	0.84	2.49	-52.35	2.23	133	0.11
	C_2H	0	0	0.36	1.40	-52.44	0.53	156	0.12
E4 AGAL332.279-0.547	$N2H^+$	0	0	0.96	2.96	-52.80	3.03	227	0.29
	HCO^+	0	0	1.87	3.69	-52.78	7.36	979	0.27
	HCN	0	9	0.71	2.37	-53.46	1.79	931	0.27
	HNC	9	0	1.18	5.19	-52.58	6.53	126	0.26
	C_2H	9	0	0.31	2.44	-53.21	0.80	114	0.27
E5 AGAL332.312-0.556	$N2H^+$	0	0	0.59	1.73	-53.75	1.08	41	0.11
	HCO^+	0	-9	1.46	3.03	-53.38	4.71	1704	0.12
	$H^{13}CO^+$	-18	9	0.33	1.19	-53.78	0.41	457	0.12
	HCN	0	-9	0.86	3.54	-53.44	3.24	1592	0.21
	HNC	-9	0	0.69	3.40	-53.87	2.50	184	0.11
	C_2H	-18	-18	0.36	1.66	-53.48	0.63	14	0.21
E6 AGAL332.351-0.436	$N2H^+$	0	0	0.80	2.12	-48.25	1.80	172	0.21
	HCO^+	-9	0	1.57	2.02	-48.66	3.38	851	0.21
	$H^{13}CO^+$	36	27	0.34	1.41	-48.24	0.51	682	0.22
	HCN	0	-9	0.66	1.83	-47.75	1.28	168	0.22
	HNC	0	0	1.18	2.16	-48.46	2.71	424	0.21
	C_2H	-18	0	0.36	1.65	-48.40	0.63	250	0.22
E7 AGAL332.411-0.502	$N2H^+$	0	0	0.51	1.65	-54.23	0.89	50	0.21

Continued on next page

[1]Offset of the peak emission from the N_2H^+(1-0)peak.

[2]Integrated intensity

[3]Total integrated intensity, from the MALT90 catalog

Table 8.3 – *Continued from previous page*

Source	Molecule	Δl	Δb	Peak	Width	Velocity	I_P	I_T	*rms*
	HCO^+	9	18	0.58	2.87	-53.33	1.77	15	0.21
	HCN	18	26	0.32	3.94	-53.59	1.34	182	0.21
	HNC	0	0	0.41	1.74	-54.32	0.76	975	0.20
	C_2H	0	0	0.15	1.67	-94.58	0.27	400	0.21
E8 AGAL332.469-0.522	$N2H^+$	0	0	1.29	3.94	-51.18	5.42	443	0.19
	HCO^+	0	0	1.36	2.70	-50.37	3.91	1166	0.19
	$H^{13}CO^+$	0	0	0.43	2.63	-51.58	1.21	15	0.20
	HCN	9	0	0.67	3.29	-46.67	2.35	866	0.20
	$HN^{13}C$	-9	9	0.34	2.47	-51.15	0.89	522	0.20
	HNC	0	0	1.12	2.75	-50.74	3.28	464	0.19
	HC_3N	9	0	0.49	2.77	-51.42	1.44	43	0.19
	C_2H	9	0	0.49	2.35	-51.45	1.22	63	0.20

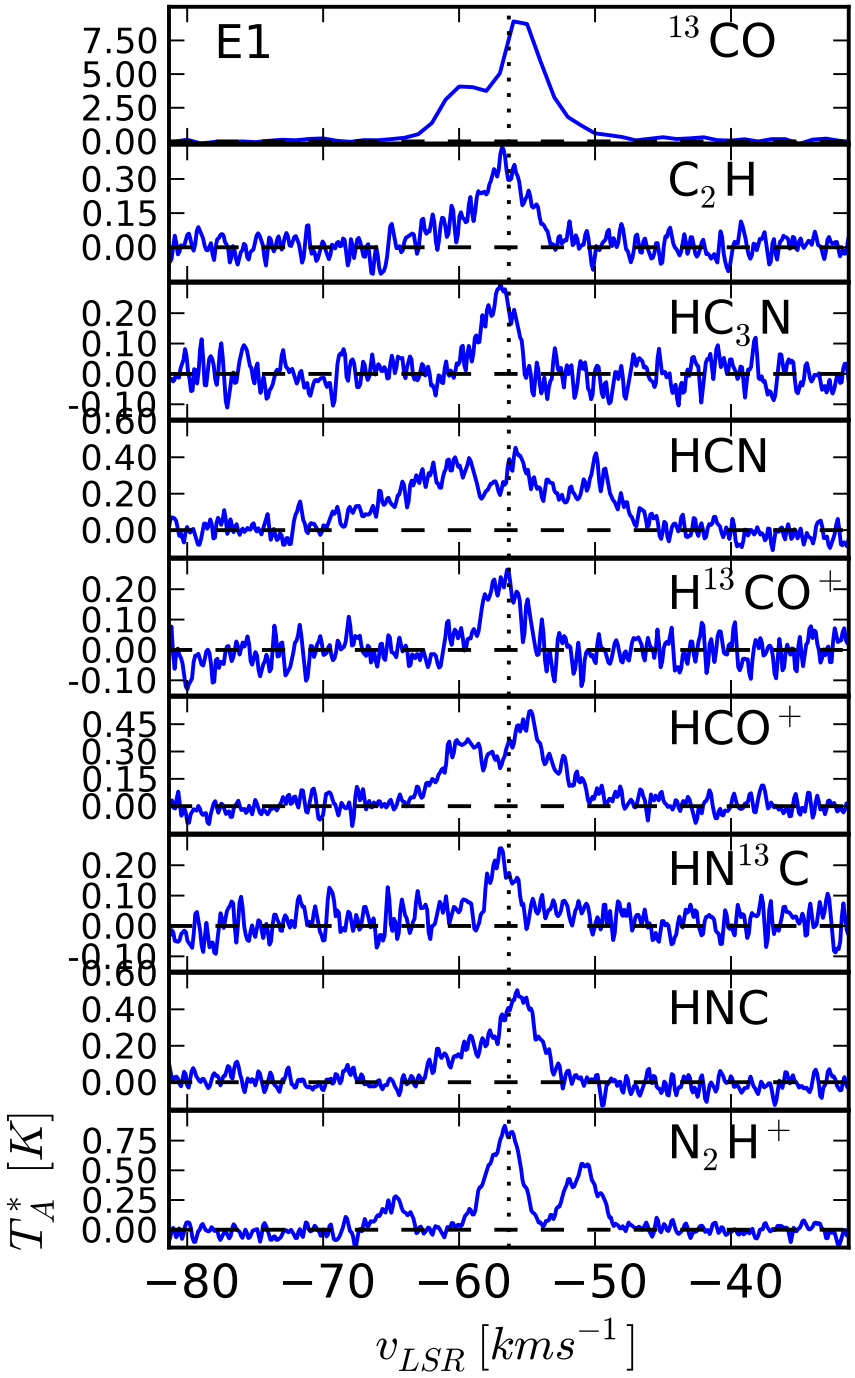

Figure 8.12: Spectra toward clump E1. Each spectrum are at the (l,v) position corresponding to the peak emission at N_2H^+.

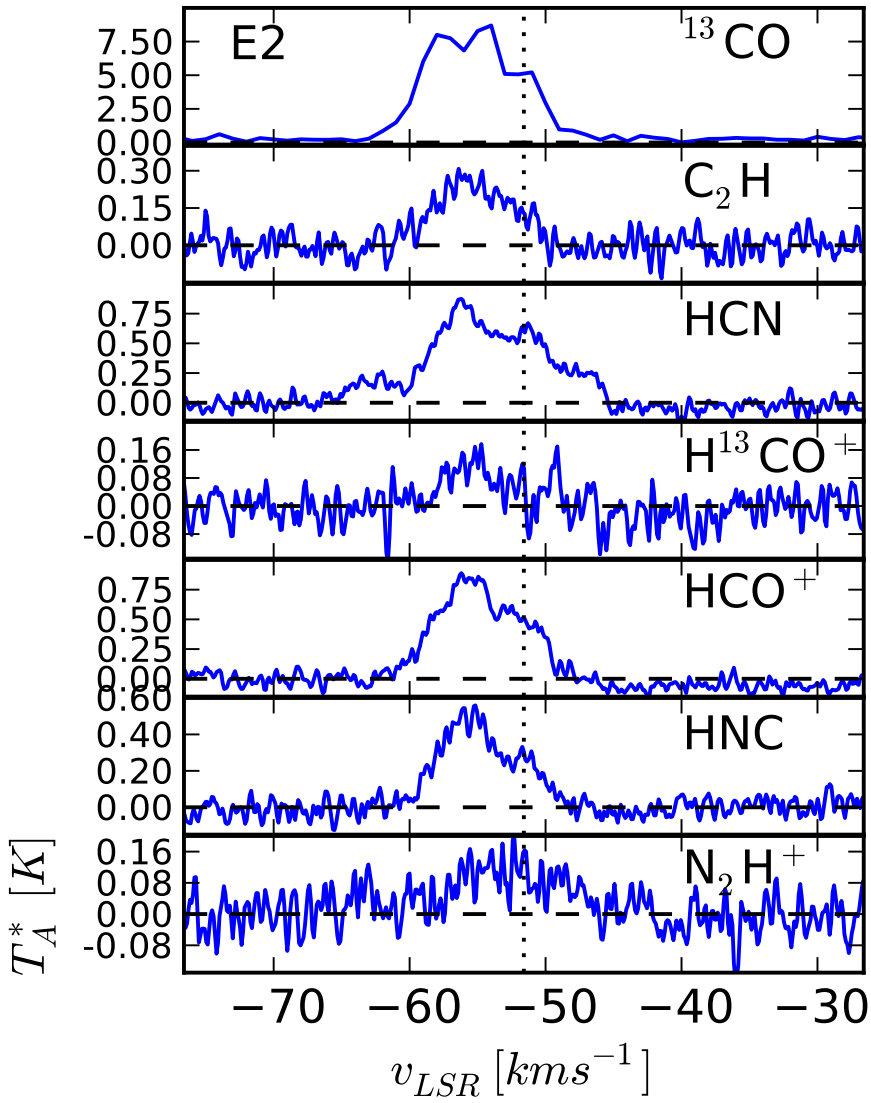

FIGURE 8.13: Spectra toward clump E2. Each spectrum are at the (l,v) position corresponding to the peak emission at N_2H^+.

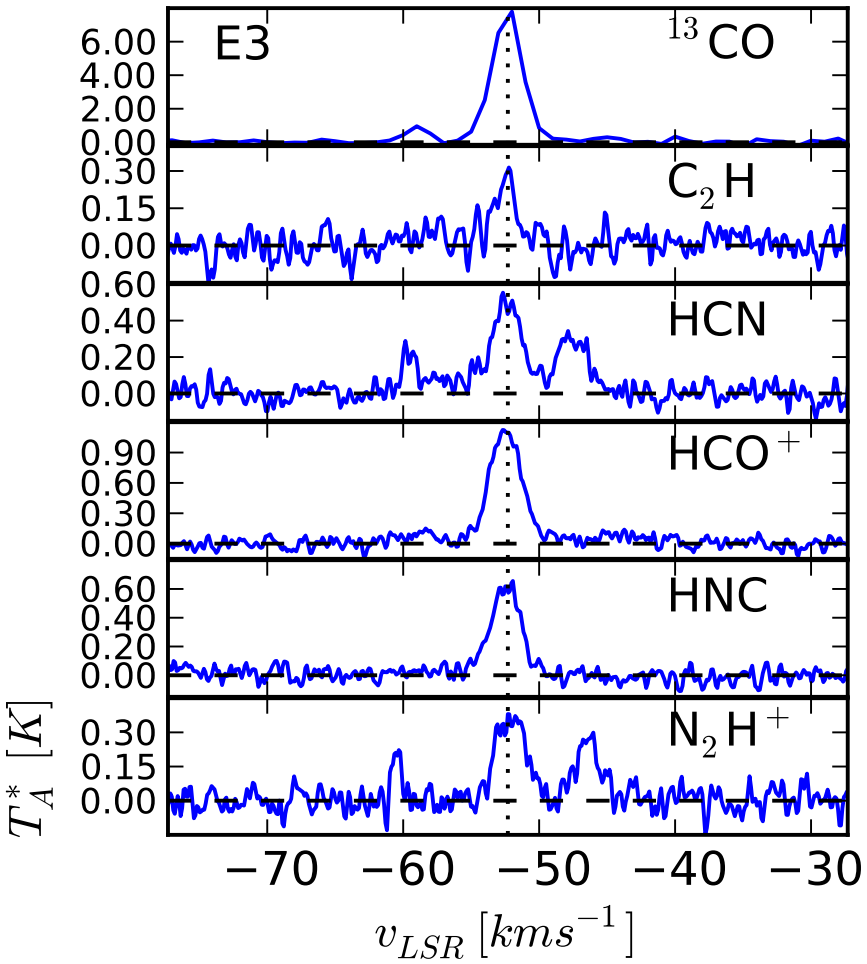

FIGURE 8.14: Spectra toward clump E3. Each spectrum are at the (l,v) position corresponding to the peak emission at N_2H^+. Dotted line shows the central velocity of the N_2H^+(1-0) emission.

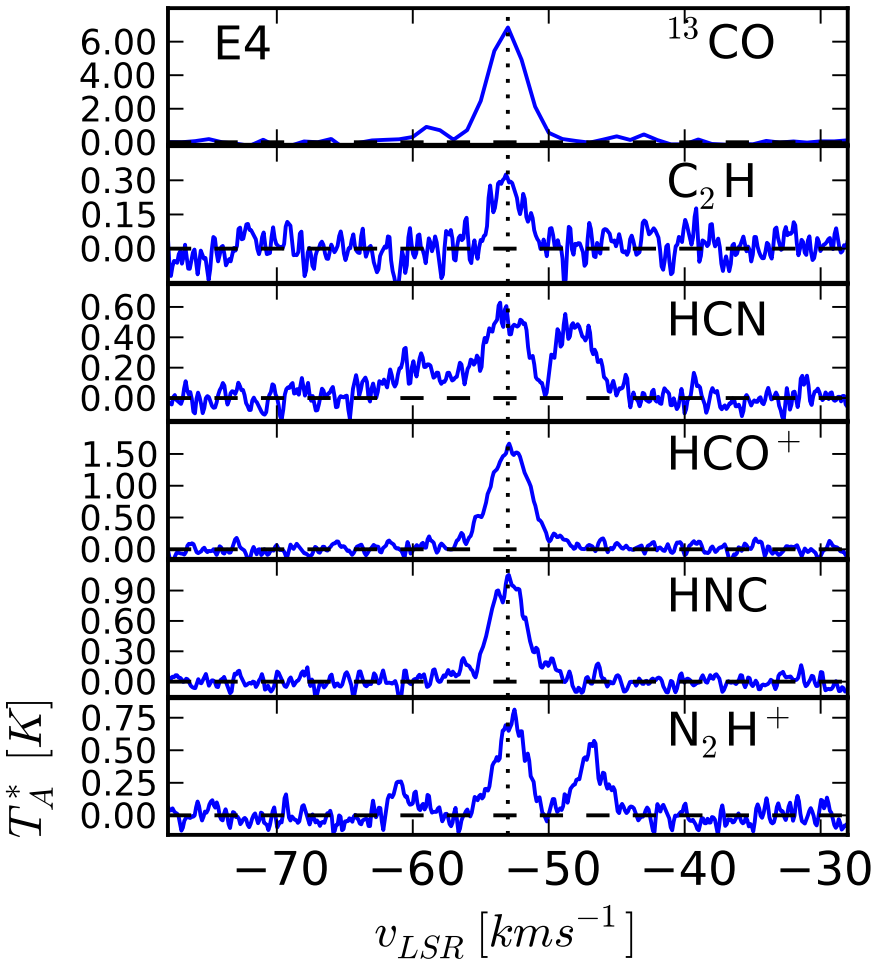

FIGURE 8.15: Spectra toward clump E4. Each spectrum are at the (l,v) position corresponding to the peak emission at N_2H^+. Dotted line shows the central velocity of the N_2H^+(1-0) emission.

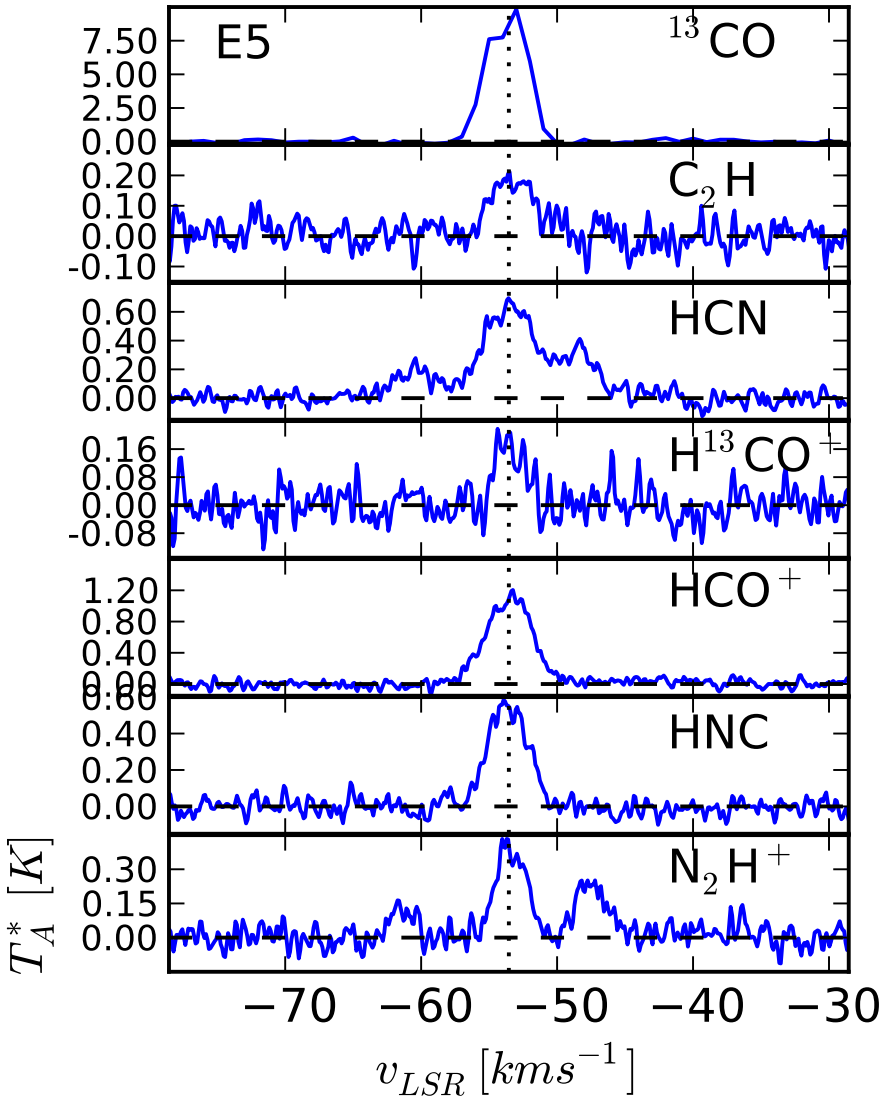

Figure 8.16: Spectra toward clump E5. Each spectrum are at the (l,v) position corresponding to the peak emission at N_2H^+. Dotted line shows the central velocity of the N_2H^+(1-0) emission.

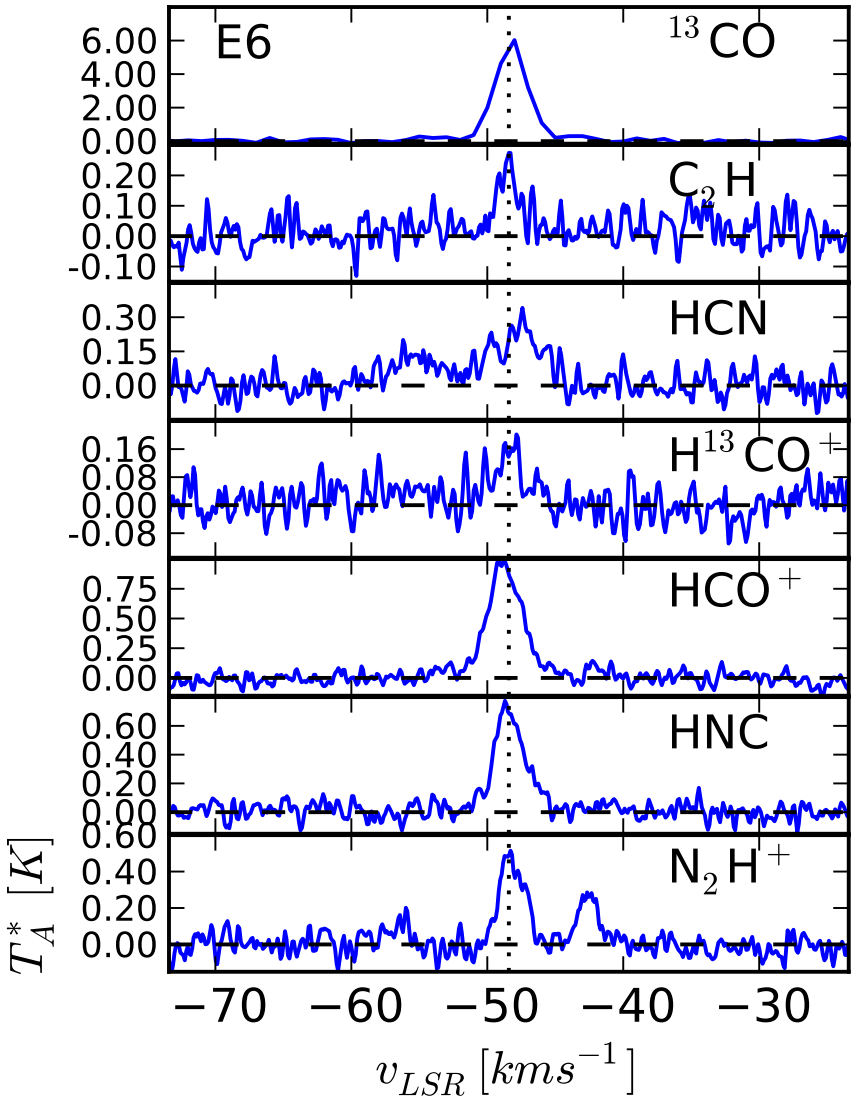

FIGURE 8.17: Spectra toward clump E6. Each spectrum are at the (l,v) position corresponding to the peak emission at N_2H^+. Dotted line shows the central velocity of the N_2H^+(1-0) emission.

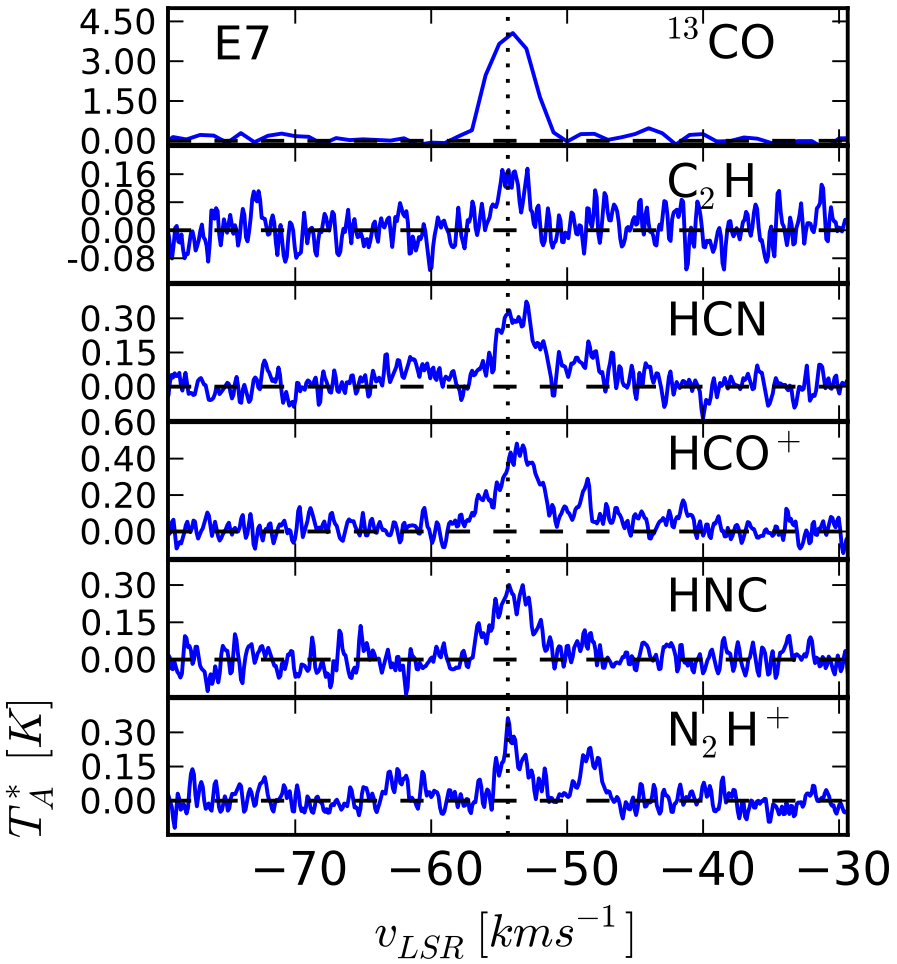

Figure 8.18: Spectra toward clump E7. Each spectrum are at the (l,v) position corresponding to the peak emission at N_2H^+. Dotted line shows the central velocity of the N_2H^+(1-0) emission.

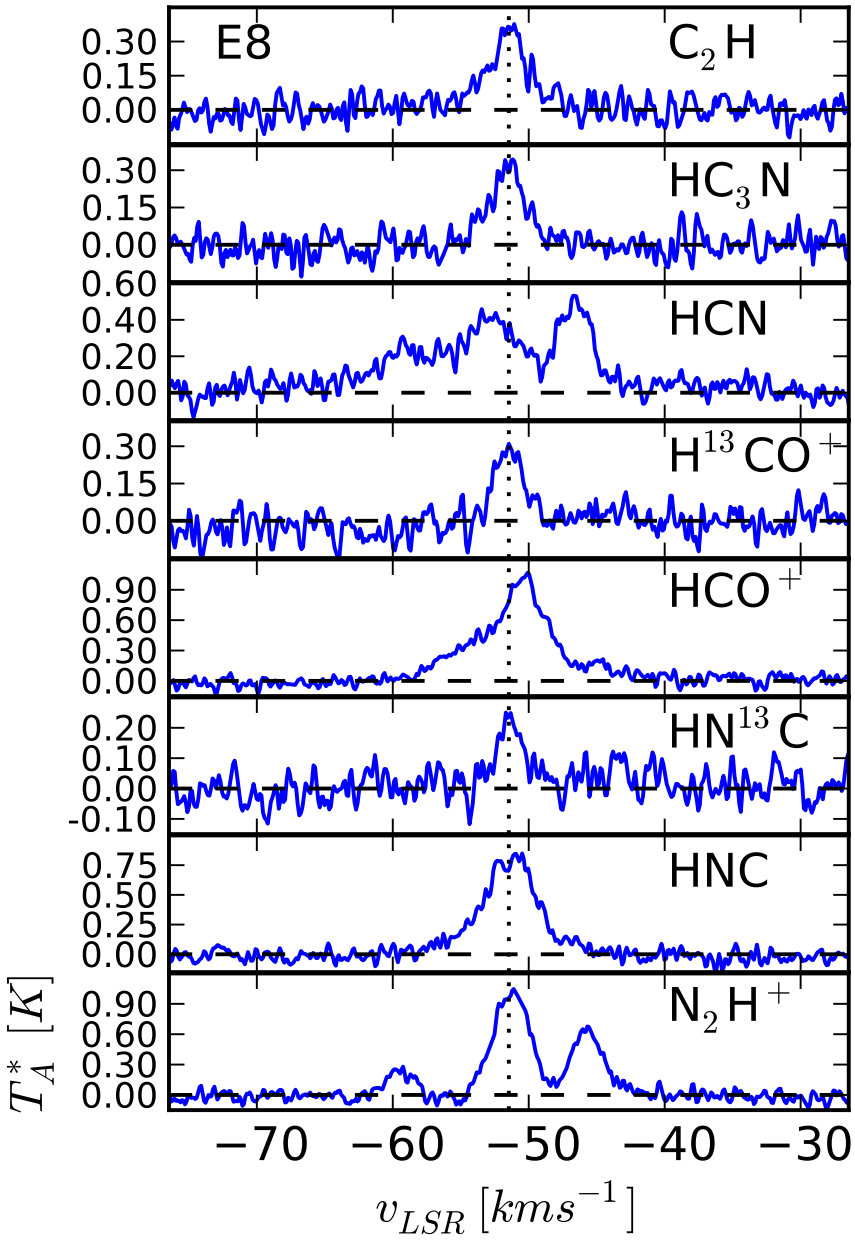

FIGURE 8.19: Spectra toward clump E8. Each spectrum are at the (l,v) position corresponding to the peak emission at N_2H^+. Dotted line shows the central velocity of the N_2H^+(1-0) emission.

8.5 Physical properties of the filament and its clumps

In this section we derive the physical properties (temperature, masses, external and internal pressure) of filament E and the clumps embedded within it, using the multi wavelength data described in the previous section.

8.5.1 Color temperature

The color temperature was obtained from the 870 μm and 350 μm continuum emission. GLIMPSE and MIPSGAL show that the majority of this region exhibit considerable infrared emission. The assumptions made for the calculus of the color temperature may not be valid in a vast part of this region. Thus, we only use the color temperature determined over the region where the infrared emission is low, which corresponds to most of the region covered by the small filament.

The color temperature depends on the spectral index β. Since β is unknown, we calculated the color temperature using four different values of the spectral index β. The mean temperatures derived for the filament are 13 K, 11 K, 9 K and 8 K using β = 1, 1.5, 2 and 2.5 respectively, having a gradient of temperatures that increases locally towards the clumps. For consistency with the results obtained for the other filaments we use a spectral index β = 1.5, which give temperatures similar to those observed in other typical molecular clouds. On the clumps the peak temperatures are ~20 K using this spectral index, which is low compared to the dust temperature (~ 35 – 60 K) typically observed toward clumps with star formation indicators, such as green fuzzies and 24 μm point sources (Rathborne et al. 2010).

Most of the clumps exhibit considerable infrared emission, thus, we assume a dust temperature based on this emission. Toward clumps E1, E2, E7 and E8 we detected bright extended infrared emission at 24 μm, suggesting high temperatures. For these clumps we assumed a temperature of 60 K, typically found toward clumps exhibiting similar infrared emission (Rathborne et al. 2010). Toward clump E3, E4 and E5 the infrared emission is in the form of green fuzzies and 24 μm point sources. For these clumps we assume a temperature of 35 K, which is usually observed toward clumps with similar characteristics (Rathborne et al. 2010). E6 exhibit low levels of infrared emission, thus for this clump we use it derived color temperature (18 K).

8.5.2 Column density and mass

In this section we derive the column density, total and lineal mass for filament E (the small filament observed in this region), using both their continuum and molecular line emission. We also calculate

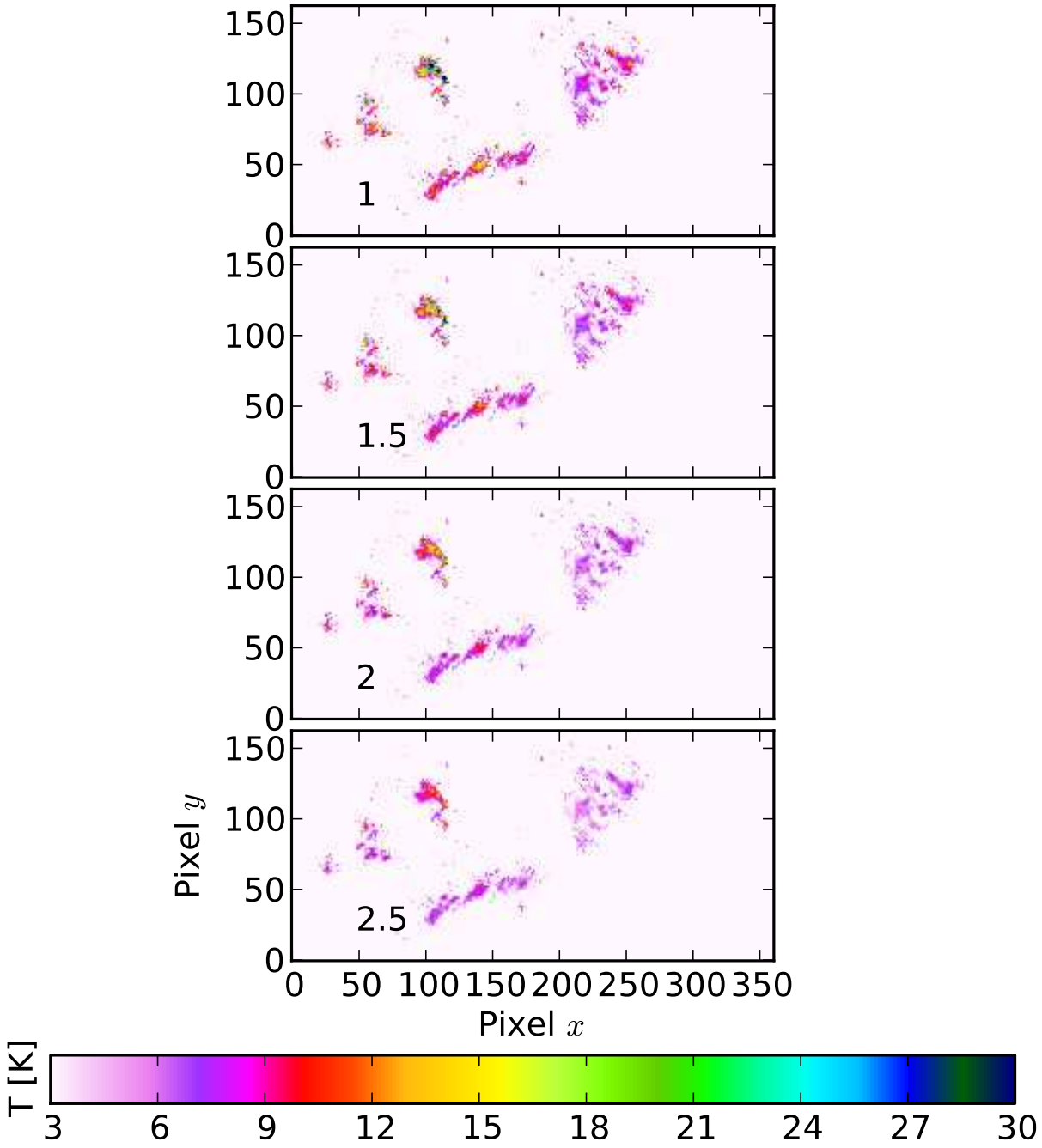

FIGURE 8.20: Derived color temperature for filament E. The panels show the derived color temperature using different values for the spectral index β. The temperature along the filament decreases with higher values of β, the average temperature is ~10 K and in all cases the temperature peaks locally toward the clumps.

the mass for each individual clump embedded within this region.

8.5.2.1 Column density and total mass of the filament

The radial column density of the filament was computed from the emission at 870 μm along the small filament, using Equation 1.31 .The temperature used was calculated in the previous section, assuming an spectral index $\beta = 1.5$. This temperature has an average value of 13 K and higher values locally toward the clumps. The mean column density found for this filament is 2×10^{22} cm^{-2}. The total mass was obtained by integrating the radial column density along the diameter and length of the filament. We found that filament E has a total dust mass of 4.6×10^3 M$_\odot$.

Since this filament has a filamentary shape to estimate the total virial mass we calculated the *lineal virial mass* (Equation 1.6) at each point along the filament. This was done by measuring the line width of the ^{13}CO(3-2) emission along it. The total virial mass of this filament was obtained by integrating all the values obtained along the filament. The total virial mass is 8.2×10^3 M$_\odot$. The ratio between the total mass and total virial mass is ~ 0.6. This value implies that globally the filament is close to the virial equilibrium. However, since the shape of this filament is filamentary is better to do stablish its stability via the analisys of its lineal dust mass and lineal virial mass.

8.5.2.2 Mass of the clumps

For each clump we calculate their total and virial mass. The dust mass was obtained from the integrated flux over the 3σ emission toward each clump and their distance. The integrated fluxes used for each clump are listed in Table 8.2. The temperatures used for each clump are the temperature assumed (or derived) based on their characteristics at infrared (see Table 8.5). The mass of the clumps ranges from ~ 200 M$_\odot$ to ~ 1400 M$_\odot$.

The virial mass was computed by assuming that the clumps are in virial equilibrium and that their geometry is spherical. We calculate the average line width at each clump from the ^{13}CO(3-2) molecular line emission within the region that enclosed their emission above 3σ noise. The virial masses found for the cores ranges from ~ 500 M$_\odot$ to ~ 6000 M$_\odot$.

Using the opacity, excitation temperature and line widths derived from the fit to the hyperfine components observed in the N_2H^+(1-0) emission, we derived the mass of clumps observed in MALT90. The masses were obtained using equation 1.4.3.3. The values of the mass obtained for these clumps are summarized in Table 8.5

Table 8.5 summarizes the values of dust and virial mass found for each clump. The ratio between the dust mass and virial mass for clumps E1, E2, E4, E5 and E7 range from 0.1 to 0.3. These values suggest that these clumps are not in virial equilibrium. For clump E3 and E6 the ratio between th total mass and virial mass is close to 1 suggesting that these clumps are gravitationally bound.

8.5.2.3 Lineal mass along the filament

The lineal dust mass was obtained by integrating the radial column density over the projected diameter of the filament at each point along it, using the 870 μm dust continuum emission. Figure 8.21 shows the lineal mass distribution along the filament which presents higher values at the position of the clumps. The average lineal dust mass is ~490 $M_\odot$ pc^{-1}.

From the ^{13}CO(3-2) molecular line emission we estimate the lineal virial mass. The ^{13}CO(3-2) line width was obtained from a Gaussian fit to the average emission across the diameter of the filament, to increase the signal to noise of the spectra. The lineal virial mass was obtained using Equation 1.6 at each point along the filament. The mean value of the lineal virial mass is 942 $M_\odot$ pc^{-1}. The distribution of lineal virial mass along the filament is also shown in Figure 8.21, in this figure we see that the overall distribution of both masses is similar.

8.5.3 External and internal pressure

The external pressure was calculated from the ^{13}CO(3-2) molecular and 870 μm continuum emission detected toward the region defined outside the boundaries of the filament. The mean velocity dispersion, σ, obtained is 2.28 km s^{-1} which is higher than the values found for the other filaments (A, B, C and D) suggesting that the environment surrounding filament E is more turbulent. The mean density obtained from this region is $\langle\rho\rangle = 7.27 \times 10^{-22}$ gr cm^{-3}. These values give a surface pressure of $P_s/k = 2.8 \times 10^5$ K cm^{-3}.

The internal pressure was computed at each point along the filament using the corresponding value of σ from the ^{13}CO(3-2) molecular line emission and the lineal mass obtained from the dust continuum emission. The mean value along the filament is $\langle P\rangle /k = 2.5 \times 10^7$ K cm^{-3}, also larger than the averaged value found toward the other filaments.

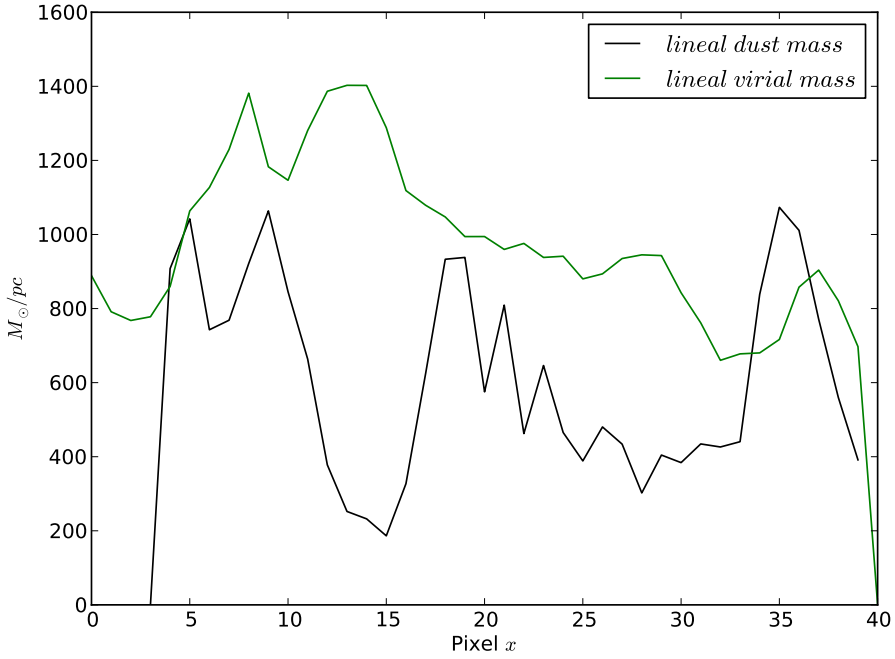

FIGURE 8.21: Lineal dust and virial mass distribution along the filament. Top panel: Black, lineal mass derived from the 870 μm dust thermal emission; Green, virial mass derived form the ^{13}CO(3-2) molecular line emission detected toward this filament.

8.6 Stability of the filament: magnetic field support

In this section we compare the properties derived for filament E with prediction from theories that describe the stability of filamentary molecular clouds, in particular whether the existence of a magnetic field contributes to their overall support. The presence of a magnetic field is analyzed by two methods: its influence over the radial column density profile and by a virial equilibrium analysis.

8.6.1 Radial density profile analysis

To analyze the influence of the magnetic field over the radial intensity profile of the filament, we separated its emission into two groups: the clumps and inter-clump material. Since we are only interested in the analysis of the shape of the radial intensity profile, this was averaged and normalized in both groups. The average radial intensity corresponding to the clumps, at both 870

μm and 350 μm, are shown in Figure 8.22. For the 870 μm emission the best fit was a profile with p = 3.4 and for the 350 μm emission the radial intensity was best fitted by a profile with p = 3.9. In both cases the emission out of the clumps is close to a profile with $p \sim 4$, which is the value obtained by Ostriker for the hydrostatic equilibrium in the non magnetic scenario.

On the inter-clump material of this filament we found that the mean normalized radial intensity have wings that are more opened than that toward the clumps. Although the fit to the emission at 870 μm is not perfect due to the bumps seen on the radial profile, the best fit to the radial intensity is given by a column density profile with p = 2.6. At 350 μm the radial intensity is more defined and the best fit is density profile with p = 3, which is closer to the values found for filaments supported by magnetic fields.

The same fit was done to the radial intensity at each point along filament. Figure 8.24 shows the values of p corresponding to the best fits, we only use in this plot the fits with a $\xi^2 < 2$. Here we see that since this filament is very small, using this criteria we have only 5 point with a good fit. In general the values are uniformly distributed between 1.5 and 3. The point corresponding to the clumps (red diamonds) are clearly separated having higher values, but the low number of points obtained for this filament makes difficult to interpret this result.

The analysis to the mean radial intensity shows that, like in the previous filaments (A, B, C and D), the stability toward the clumps can be explained only by hydrostatic support but inter-clump material of the filament the radial column density observed suggests that we need an additional mechanism of support that could be a magnetic field.

8.6.2 Virial equilibrium analysis

The stability of this filament was also studied via an analysis of its virial equilibrium. To analyze the virial equilibrium we plot $\langle P \rangle / P_s$ against m/m_{vir} in a diagram with constant values of the ratio between the total magnetic energy per unit length, $\mathcal{M}$, and lineal gravitational energy, $|\mathcal{W}|$ ($\mathcal{M}/|\mathcal{W}|$), following the same analysis of Fiege and Pudritz (2000). We found that, in general, the mean values of $\langle P \rangle / P_s$ and m/m_{vir} for the whole filament lies in the sector of the diagram that represents the presence of a toroidal dominated magnetic field (Figure 8.25). The values of $\langle P \rangle / P_s$ and m/m_{vir} obtained for the inter-clump region of the filament are 0.009 and 0.6 respectively which gives $\mathcal{M}/|\mathcal{W}|$=-2.0. This value corresponds to a toroidal dominated magnetic field. For the clumps we found $\langle P \rangle / P_s$=0.003 and m/m_{vir}=0.3, these values implies that $\mathcal{M}/|\mathcal{W}|$=-0.5 which also suggest the presence of a toroidal dominated magnetic field, however, we see that, in general, the points corresponding to the clump tend to be closer to the non-magnetic solution (green dotted line).

The average values obtained for the entire filament are $\langle P \rangle / P_s$=0.009 and m/m_{vir}=0.58 giving

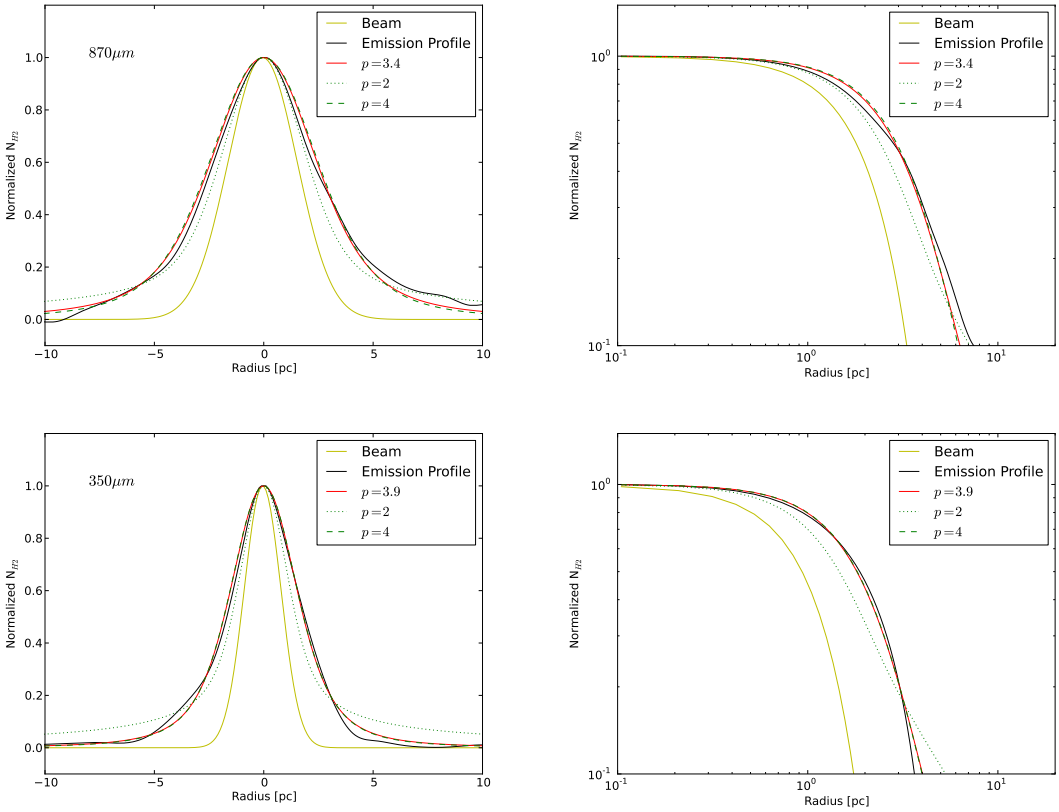

FIGURE 8.22: Density profile of the normalized mean density of the clumps in filament E. Top panels show the 870 μm emission, bottom panels show the 350 μm emission. The left panels show lineal plot of the profiles and right panels shown the profiles in logarithmic scales. The red solid lines represents the best fit to the density profile, the beam profile is shown with the solid yellow line, the hydrostatic solution p=4 (green dashed line) and magnetized solution p=2 (green dotted line) are also shown. We can see that in general the shape of the radial density follows the shape of a profile with p = 4.

$\mathcal{M}/|\mathcal{W}|$=-0.7. This result suggest that if we considerer the filament as a whole, the stability is due to the presence of a toroidal dominated magnetic field that prevent the filament to expand.

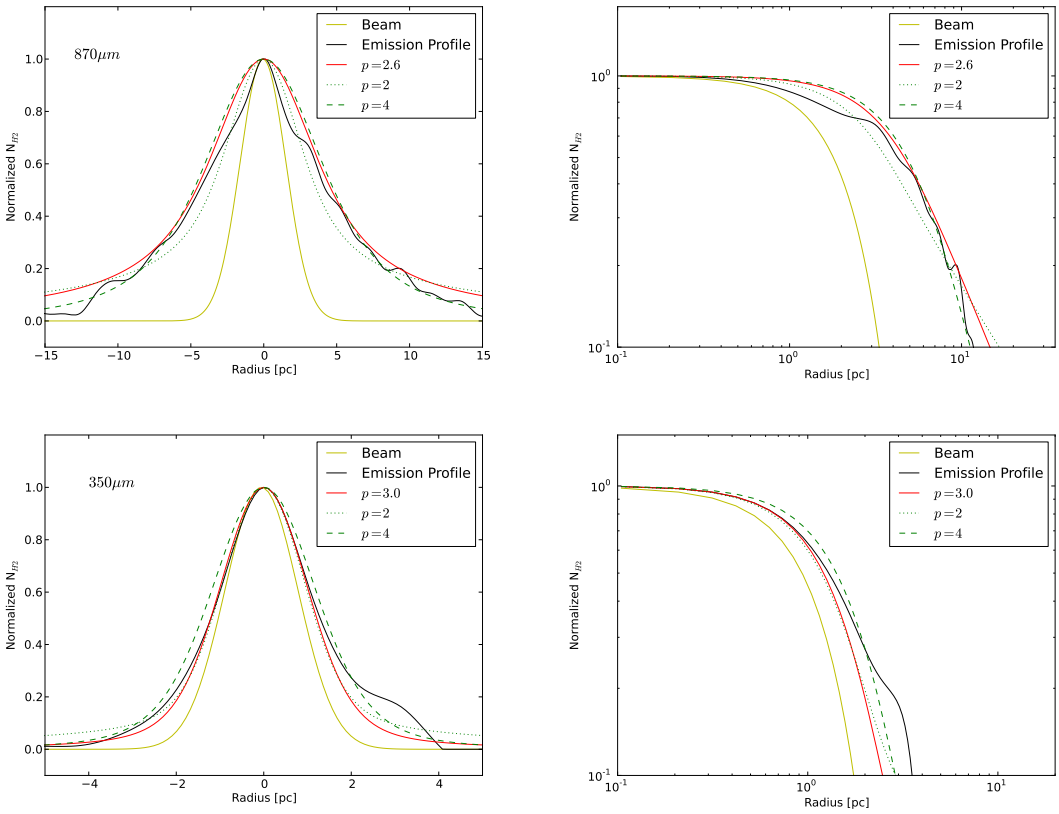

FIGURE 8.23: Density profile of the normalized mean radial density of the inter-clump region in filament E. Top panels show the 870 μm emission, bottom panels show the 350 μm emission. The left panels show lineal plot of the profiles and right panels shown the profiles in logarithmic scales. The beam profile is shown with the solid yellow line, the hydrostatic solution (green dashed line) and magnetized solution (green dotted line) are also shown. We can see that the shape of the radial density differs from the observed at the clumps. At 870 μm the emission has several bumps making the fit not perfect, we see that the peak of the emission is more similar to a profile with $p = 2$ but to the lower part the shape is more similar to $p = 4$. At 350 μm the column density is very well traced by a profile with $p = 3$.

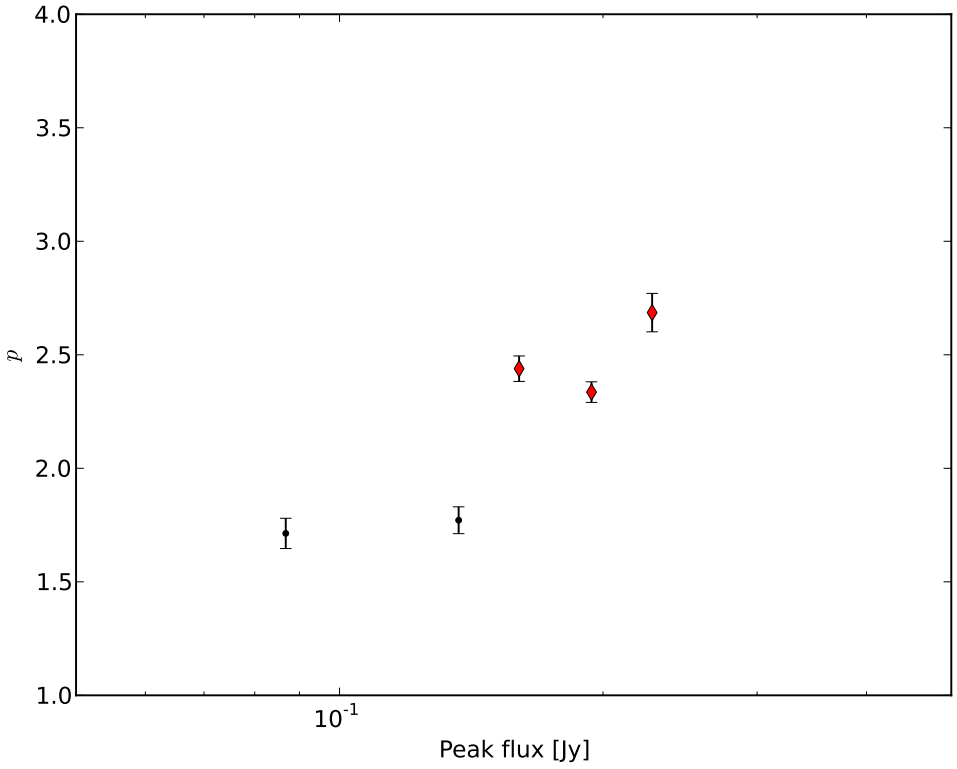

FIGURE 8.24: Plot of p, the parameter that define the shape of the density profile, vs peak flux for the clump (red points) and inter-clump (black points) material in filament E. The error bars show the χ^2 between the fit and the observed radial density. We can see that in general the inter-clump regions have values of p lower than the clumps.

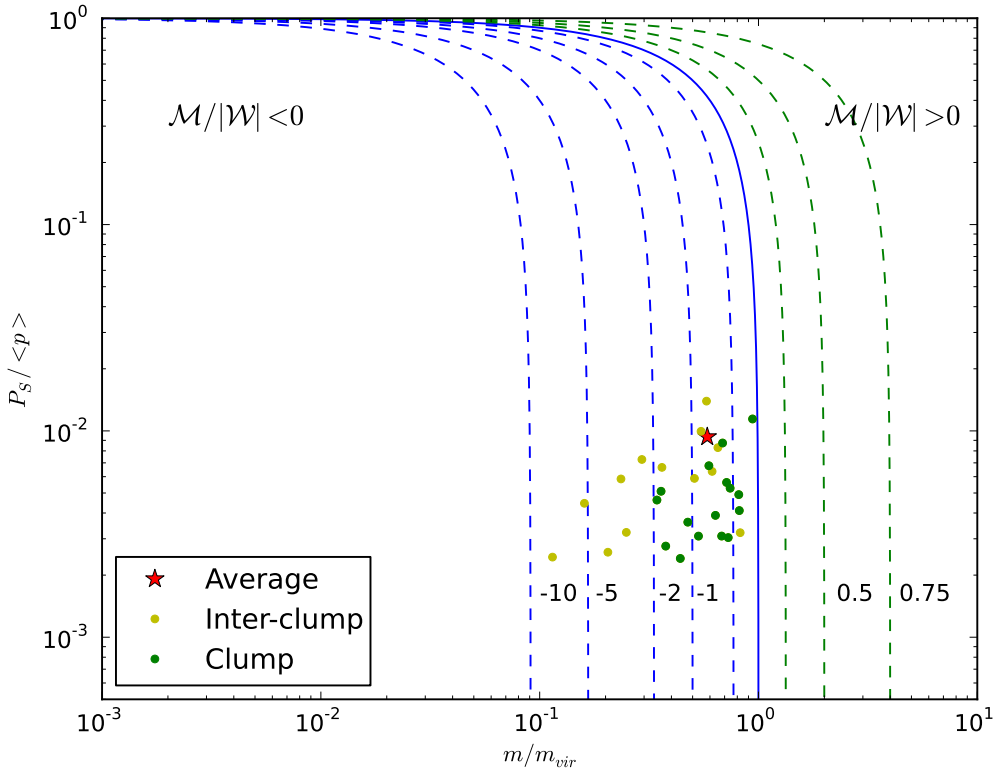

FIGURE 8.25: Plot of the $\langle P \rangle / P_s$ vs m/m_{vir} for the clumps and inter-clumps regions for filament E. Blue dashed lines: toroidal models for magnetic fields, blue solid line: unmagnetized solution, green dashed lines: poloidal magnetic field models. Yellow dots: values found for the inter-clump region of the filament; black dots: values found for the regions were clumps are located and the red star: mean value for the filament.

TABLE 8.4: Filament E: derived properties of the filament.

Distance	**Radius**	**Width**	**N clumps**	**Δv**	**Temperature**	**Total mass**			**Lineal mass**			**P_s/k**	**$\langle P \rangle/k$**
				^{13}CO		**m**	**m_{vir}**	**m/m_{vir}**	**m**	**m_{vir}**	**m/m_{vir}**		
pc	pc	pc		km s^{-1}	K	$M_\odot$	$M_\odot$		$M_\odot$	$M_\odot$		10^4 K cm^{-3}	10^4 K cm^{-3}
3690	36.6	0.23	8	3.33	12	4600	8200	0.6	489	942	0.52	28	2515

TABLE 8.5: Filament E, properties of the clumps

	Temperature		$\mathbf{m_{dust}}$	$\mathbf{m_{vir}}$	$\mathbf{m_{N2H+}}$	$\mathbf{m_{dust}/m_{vir}}$	**Spacing**
	Color	Assumed					
	K		$M_\odot$	$M_\odot$	$M_\odot$		pc
E1	10	60	650	6029	649	0.1	1.5
E2	8	60	1300	3194	2150	0.4	1.1
E3	9	35	522	506	1270	1.0	0.8
E4	10	60	214	1067	600	0.2	0.9
E5	9	35	429	1232	454	0.3	0.8
E6	18	-	1394	882	-	1.5	1.3
E7	-	60	214	850	460	0.3	0.9
E8	-	35	900	-	890	-	-

9

Discussion & Conclusions

In this chapter I discuss the main results obtained in my thesis. In §9.1, I discuss the global properties of the observed filamentary molecular clouds: their masses and temperatures. In §9.2 I discuss the stability of the filamentary molecular clouds in the context of theories that include magnetic field support. In §9.3 I analyze the fragmentation of the filaments based on theories that predict the typical observed separation between individual clumps. In section 9.4 I discuss the properties of the clumps embedded within the filaments and their proposed stage of evolution, with the aim of addressing the question of whether these clumps will form high mass stars and clusters.

9.1 Filamentary molecular clouds

From the ATLASGAL survey, which observed the dust continuum emission at sub-millimeter wavelengths, I found that filamentary structures are ubiquitous along the Galactic Plane. Within the ~150 degrees square region observed in the first years of ATLASGAL, I found ~7000 compact sources, with ~80% of them having no association with either *MSX* or *IRAS* sources. Because they are compact and devoid of infrared emission, that is commonly associated with active star formation, they may represent clumps that are in a very early evolutionary phase. This makes them excellent candidates for starless clumps, thus, their detailed study with next generation facilities

like ALMA, will shed light on the star formation process.

The ATLASGAL images revealed that most of the detected clumps and compact regions are usually embedded in a more extended molecular cloud with filamentary shapes. To determine the physical and kinematical properties of these filamentary structures I analyzed five filamentary molecular clouds located in the inner region of the Galactic Plane. These filamentary structures exhibit a wide range in the properties of their infrared and sub-millimeter emission, from filaments showing little or no infrared emission to filaments that are bright at 8 μm and 24 μm. The infrared emission in this wavelength range can be interpreted as emission from protostellar objects or HII regions, where the dust has been heated by UV radiation from newly formed stars. Hence, the lack of infrared emission suggest that the clumps embedded in the filaments are in a very early evolutionary stage. Thus, the chosen filaments allow us to investigate the characteristics of filaments in different stages of evolution. Having a sample of filaments that span a range in star formation activity is important to determine whether or not filaments are connected with star formation.

Although it is clear that filamentary structures are ubiquitous in Galactic Plane surveys, the dust continuum emission producing these *"filaments"* may not arise from a single coherent molecular cloud, but instead may be the superposition of two or more molecular clouds along the same line of sight. Therefore, it is not possible to establish their physical properties until we determine whether or not the emission arises from a single physical entity. We do this by measuring the velocities along the filament observing the emission in molecular line (e.g. ^{13}CO(3-2)). In four of the five filaments studied in this work the velocities along the filaments are similar, suggesting that the emission arises from a single molecular cloud. For filament B we found that the observed structure is in fact the superposition of three discrete molecular clouds along the line of sight. Thus, although the emission appears connected in the sub-millimeter images, the *filaments* in this case is not a coherent structure. Thus, molecular line observations are key to determine if filaments are single coherent structures.

The color temperatures of the filaments which show little infrared emission (A, B and C), thus potentially in an early stage of evolution, are similar to the temperatures of cold molecular clouds. In all the filaments, the average temperature in the inter-clump regions range from 10 to 15 K, increasing locally toward the clumps.

The column density of the filaments, derived from the dust continuum emission, ranges from $\sim 10^{22} - 10^{24}$ cm^{-2} with the higher values derived toward the clumps. These column densities are similar to values found toward dense star forming molecular clouds, and toward other filaments such as IC5146 (Arzoumanian et al. 2011), IRDCs (Simon et al. 2006), or the high star formation region of Orion, which has peak column densities of about 10^{23} cm^{-2} (Bally et al. 1987).

The total mass of the filaments derived from the dust continuum emission ranges from $1 - 4 \times 10^4$ M$_\odot$

for filaments A, B, C and D and is 5×10^3 $M_\odot$ for filament E, which is the smallest filament. The virial masses are similar to the ones obtained from the dust emission, and range from 7×10^3 to 10^4 $M_\odot$. In general, for each filament, the mass derived from the dust emission is close to the virial mass, suggesting that the filaments are close to the virial equilibrium. However, due to the filamentary shape of these structures it is more appropriate to analyze the virial equilibrium through an analysis of their lineal dust and lineal virial masses.

The lineal mass derived from the dust emission ranges from 260 $M_\odot$ pc^{-1} to 500 $M_\odot$ pc^{-1}. The critical lineal mass of the filaments, below which the filaments is unable to radially collapse, is given by $M_{lineal,crit} = 2v^2/G$, where v corresponds to the sound speed, c_s in the case of thermal support (Ostriker 1964) and σ in the case of turbulent support (Fiege and Pudritz 2000). The molecular line emission from the filaments exhibit large line widths ($\sim 2-3$ km s^{-1}), suggesting that turbulent motions dominate. Considering this, the critical lineal mass corresponds to $M_{lineal,crit} = 2\sigma_v^2/G$. In general, the lineal virial masses range from 400 to 1000 $M_\odot$ pc^{-1}, being larger than the lineal *dust* mass by a factor of 2. This suggest that there is an additional mechanism that supports the filaments against expansion, possibly external pressure or magnetic fields.

The pressure exerted at the surface of the filaments was calculated from the emission of the molecular gas located outside the boundaries of each filament. The derived surface pressure ranged from $P_s/k = 4 \times 10^4$ K cm^{-3} to 5×10^5 K cm^{-3}. Boulares and Cox (1990) estimated that the total pressure of atomic gas in the ISM surrounding molecular clouds is $P/k \sim 10^4$ K cm^{-3} . However, if a molecular cloud is associated with an HI complex then this value can be higher by an order of magnitude. The values we derived for the surface pressure on the filaments are comparable to these. The internal pressure derived for the filaments ranges from $\langle P \rangle$/k=$10^6 - 10^9$ K cm^{-3}, and are also similar to values found for other filamentary molecular clouds.

9.2 The stability of filaments: magnetic support

A comparison of the lineal dust mass and the lineal virial mass of all filaments, shows that the former has lower values than the latter, suggesting that an additional mechanism is needed to make these filaments stable against expansion. We investigated whether or not magnetic fields are needed to support filamentary molecular clouds using two different approaches: via the shape of the radial column density and the virial equilibrium. In this section I discuss the major findings from these two analyses.

First, I found that the radial intensity profile of the dust emission at both 870 μm and 350 μm are similar. Second, I found that the radial intensity toward regions where the clumps are located have

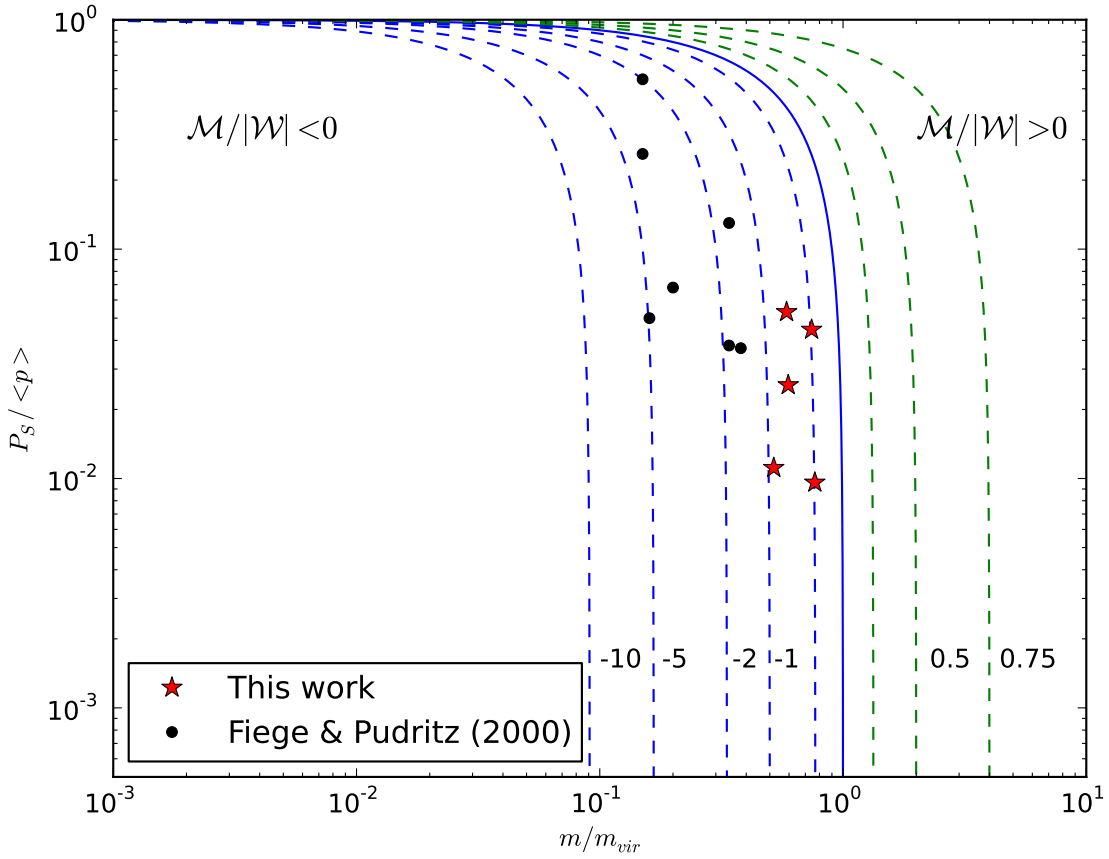

Figure 9.1: Plot of the average $\langle P \rangle / P_s$ vs m/m_{vir} for filaments. Blue dashed lines: toroidal models for magnetic fields, blue solid line: unmagnetized solution, green dashed lines: poloidal magnetic field models. Black dots: values $\langle P \rangle / P_s$ vs m/m_{vir} from Fiege and Pudritz (2000) toward seven filaments and the red star: values found for the filaments studied in this work

profiles that are well fit by a column density profile of the form:

$$\Sigma_\rho(r) = A_p \frac{\rho_c R_{flat}}{[1 + (r/R_{flat})^2]^{\frac{3}{2}}}. \tag{9.1}$$

This equation describes the classical model of an isothermal filament in hydrostatic equilibrium without magnetic field for their stability (Ostriker 1964), suggesting that clumps may not need a magnetic field support. Third, I found that for all filaments, the radial profile of the emission from the inter-clump regions exhibit a distinctive shape, different from that observed toward the clumps. In general, the column density of the inter-clump regions is well fit by a profile with the following

shape:

$$\Sigma_{\rho}(r) = A_p \frac{\rho_c R_{flat}}{[1 + (r/R_{flat})^2]^{\frac{1}{2}}}. \tag{9.2}$$

This relation, first studied by Fiege and Pudritz (2000), describes an isothermal filament with magnetic support. These results suggest that in order to be stable, the inter-clump region of the filaments need a magnetic field for support while for clumps, the presence of a magnetic field is not required. If we don't distinguish between clump and inter-clump regions and since the majority of the filament corresponds to inter-clump region, we expect that the mean shape of the radial density at larger radii will have values similar to r^{-2}, suggesting magnetic fields are needed for support. This is the case for other filamentary molecular clouds reported in the literature such as IC5146 (Lada et al. 1999) or L977 (Alves et al. 1998).

I also analyzed the stability and magnetic field support of the filaments via their *virial equilibrium*. For this analysis I use an extended version of the virial equation including pressure and magnetic support, given by the following equation (see section D.1 for further details):

$$\frac{P_S}{\langle P \rangle} = 1 - \frac{m}{m_{vir}} \left(1 - \frac{\mathcal{M}}{|\mathcal{W}|} \right). \tag{9.3}$$

For all filaments, we calculated the values of $\langle P \rangle / P_s$ and m/m_{vir} at each point along their major symmetry axis and also determined their average value. The average values found for the filaments ranged from:

$$0.52 < \quad m/m_{vir} \quad < 0.76 \tag{9.4}$$

$$0.009 < \quad P_s/\langle P \rangle \quad < 0.34 \tag{9.5}$$

These values imply a ratio between the lineal total magnetic energy ($\mathcal{M}$) and the lineal gravitational energy $\mathcal{W}$, of $\mathcal{M}/|\mathcal{W}| < 0$. This suggests that the equilibrium requires the presence of a toroidal dominated magnetic field (see Figure 9.1). This result is similar to that found by Fiege and Pudritz (2000) toward the ρ Oph, Taurus, and Orion regions. Even though for the filaments studied by Fiege and Pudritz (2000), the presence of a toroidal dominated magnetic field was implied, the values of m/m_{vir} are slightly lower than the ones determined for the filaments studied in this work.

In summary, the analysis of the radial column density and of the *virial equilibrium*, suggest that filaments are best modeled as isothermal (really constant velocity dispersion) filamentary molecular clouds wrapped by an helical, toroidal dominated magnetic field. This magnetic field would support the filamentary molecular cloud preventing its expansion and also allow the formation of the clumps

within it. One suggestion is that the clumps form along the filaments at the location where the magnetic field crosses the filaments, however, direct measurements of the magnetic field would be useful to corroborate this hypothesis.

9.3 From filaments to clumps: Fragmentation scale

In this section I discuss the fragmentation of filamentary molecular clouds. Since filaments are ubiquitous along the Galactic plane and most of them have embedded clumps that may give rise to stars, it is important to understand the processes that lead to the fragmentation of filaments and the formation of clumps. Assuming that filaments can be represented as a self-gravitating cylinders, theory predicts that fragmentation can occur due to a fluid, or *"sausage"*, instability. This instability may produce several clumps with a characteristic spacing (which may be roughly periodic) given by the wavelength of the fastest growing unstable mode of the fluid instability (Jackson et al. 2010). The actual value will depend on whether the filament is an incompressible fluid (Chandrasekhar and Fermi 1953) or an isothermal gas cylinder.

Jackson et al. (2010) used molecular line observations of HNC(1-0) to detect clumps within the Nessie nebula, an extreme example of a filamentary molecular cloud. Assuming that Nessie is an isothermal cylinder where the turbulent pressure dominates, then the spacing expected for this filament due to the *"sausage"* instability matches well the observed clump separation. This suggest that fluid instabilities may be the mechanism responsible for the fragmentation in the Nessie nebula. To assess whether or not this result applies to our filaments, we investigated the clump separations in them. Because the fragmentation of filaments may be related closely to the processes of formation of the filamentary structure, it is best to study filaments which show very little evidence of star formation. Because of this, we focused our analysis on filaments A, B and C since they exhibit little infrared emission and, therefore, are likely to be in an early stage of evolution.

I found that the observed spacing between clumps is ∼2.5 pc in filaments A and B and ∼6 pc in filament C. If these filaments are treated as incompressible fluids, only for filament C the expected separation between the clumps is in agreement with the observations. For the other two filaments, the clumps appear more closely spaced than that predicted by this theory.

However, a more realistically assumption is that filaments are isothermal cylinders with turbulent pressure as support, as in the case of Nessie. In this case, the observed molecular line widths together with the central density can be used to predict the spacing of the clumps. For the filaments, the effective scale of height is $H_{eff} \sim 0.1 - 0.2 pc$, smaller than the radius of the cylinder (∼ 0.5 pc), giving an expected separation between the clumps of $\lambda_{max} = 22 H_{eff}$. Assuming that the filaments

are infinite isothermal cylinders with turbulent support, we found that for *all the filaments* the spacing observed between the clumps is in agreement with the values expected from the *"sausage"* instability fragmentation of filaments with a finite radius $R \gg H$.

This result suggests that the fragmentation of filamentary molecular clouds can be due to this fluid, or *"sausage"*, instability and that this fragmentation leads to the formation of star forming clumps. This is also supported by the roughly periodic spacing observed between the clumps embedded in the filaments. This theory also predicts a critical mass per unit length of $M_{crit} = 2v^2/G$ and a maximum mass of the clumps of $M \sim \lambda_{max} M_{crit}$. For our filaments, the critical mass (virial mass) have values ranging from 400 to 1000 $M_\odot$ with $\lambda \sim 2$ pc, which implies a maximum mass for the clumps of 800 to 2000 $M_\odot$. This values are in agreement with the masses derived for the clumps in the filaments, suggesting that turbulence has an important role in the physics of these filamentary structures.

9.4 Characteristics of the embedded clumps

In this section I discuss the properties of the clumps embedded within the filaments. All the filaments harbor several clumps, many of which are regularly spaced. Infrared images reveal that some of these clumps already contain active star formation, as evidenced by their association with star formation indicators such as green fuzzies (enhancement at 4.5 μm indicative of shocked gas), 8 μm emission or 24 μm emission (which reveal the presence of an embedded proto-stellar object).

The temperatures of the clumps, derived from the sub-millimeter emission or estimated based on their infrared emission, reveal that the clumps are both "cold" and "hot" (temperatures of 10 to 50 K). The mass of the clumps range from ~20 $M_\odot$ to ~4000 $M_\odot$. Kroupa (2007) suggest that, in order to form at least one star with a mass > 8 $M_\odot$, a high mass protostellar clump should have at least a mass of 200 $M_\odot$ and show no evidence for active star formation . Thus, to generate a sample of clumps in a very early stage of evolution, before high mass star formation has begun, we should look for cold clumps with masses of a few 100 to a few 1000 $M_\odot$ (Beuther et al. 2002; Williams et al. 2004; Faúndez et al. 2004). Moreover, they need to be relatively compact (~ 0.5 pc) reaching densities of 10^6 cm^{-3}. Some of the filaments contain clumps with masses higher than 200 $M_\odot$ and cold temperatures (<20 K), likely to be the precursors of high mass stars. The filaments also contain high-mass clumps exhibiting bright infrared emission, which due to the sensitivity of *Spitzer*, likely correspond to high mass protostars.

Since the clumps we detected display a wide range in their properties, from low to high mass cores with low and high temperatures, we can use them to help determine an evolutionary sequence for high mass star formation. We divided the clumps found into four broad categories: *quiescent* ,

protostellar, HII and PDR.

We have found 14 quiescent cores (with no infrared emission). Two of them were observed by MALT90 detecting only $N_2H^+$and HNC (see Table 9.1). Once the clumps starts contraction, they begin the *"protostellar"* phase. The central star will heat the surroundings and immediately produce shocked gas. This phase should be characterized by the detection of an enhancement at 4.5 μm and point source emission at 24 μm. In this stage we also can detect molecules that are released to the gas phase, via shocks, such as HCO^+, HCN and C_2H. As the protostar evolves, more energy is released to its surrounding and molecules are release to the gas phase such as $H^{13}CO^+$, $HN^{13}C$, HC_3CN. At this stage, shocked gas can also be inferred by the presence of SiO. About $\sim$ 35% of the clumps embedded in our filaments are classified as *"protostellar"*.

In the later stages of their evolution, we observe HII regions, characterized by bright emission at 8 and 24 μm. In this phase, we also detect molecules like those observed toward hot cores (e.g $HN^{13}C$, CH_3CN or HC_3CN). We found that 23% of the clumps show these characteristics. Toward the clumps associated with PDRs (about 23%) we found rich chemistry, detecting most of the molecules observed. Also, toward these clumps we found that the line profiles are broad indicative of turbulent motions.

These result show that the molecular line information combined with infrared images, can be used to asses the evolutionary stage of the clumps, identifying each stage with certain observed characteristics. To obtain a clearer picture of how the clumps evolve, it is necessary to extend this study to include more clumps. This is the aim of MALT90 survey, which will observe more than 2000 clumps, to determine an characterize the evolutionary sequence of high mass star formation.

9.5 Evolution of filamentary molecular clouds

The characteristics of the clumps embedded in filaments suggest that these structures are closely connected to high mass star formation. The evolution of the clumps within the filament drive the evolution of the filaments. "Young" filaments are often seen as infrared dark structures while more evolved filaments have several bright HII regions and OB associations scattered along their lengths. In these cases its often difficult to see the original filamentary molecular cloud.

In filaments that are predominantly infrared dark (e.g. A and C), most of the clumps embedded within them are either quiescent (dark at infrared wavelengths) or protostellar (showing green fuzzies and 24 μm emission). Once the clumps evolve, they start to heat their surroundings. As a result, they are no longer infrared dark, however, they often still appear connected in the dust continuum emission. This suggests that filaments classified as IRDCs may be similar to the other

filaments, but are simply in an earlier evolutionary stage. In the more evolved filaments, the clumps embedded are in either the protostellar or HII regions phases.

Once the clumps are in a late evolutionary stage, the filaments likely break up completely. In these cases the clumps may no longer be connected at (sub)millimeter wavelengths. Filament E is an example of this late evolutionary stage. Other star forming complexes with filamentary shape such as Orion, or NGC6334 may be also examples of this stage. Surrounding these regions it is also possible to see some remnant of the initial filament.

Table 9.1: Clump properties. Density tracers refer to molecular lines: N_2H^+(1-0) ,HCO^+, HCN and HNC. Density tracers isotopomers refer to: $H^{13}CO^+$, $HN^{13}C$ and ^{13}CS. Hot cores refers to CH_3CN, HC_3CN, $HC^{13}CCN$ and HNCO. PDR shows the detection of $C_2H$and Schock shows the detection of SiO.

Source	*Spitzer*	IRAS, Masers	Class.	Mass	T	Radius	Density tracers	D. T. isotopomers	Hot core	PDR	Shocks
C1	Dark	-	Qscent.	80	30	0.4	Y	-	-	-	-
C2	Dark	16264-4841	Qscent.	464	14	0.4	Y	-	-	-	-
D8	GF, 24 μmPS	-	Prst.	-	15	0.3	Y	-	-	Y	-
E3	GF, 24 μmPS	-	Prst.	522	35	2.0	Y	-	-	Y	-
E4	GF, 24 μmPS	-	Prst.	214	60	1.3	Y	-	-	Y	-
D1	GF, 24 μmPS	16136-5038, Maser	Prst.	218	30	0.7	Y	Y	-	Y	-
A24	GF, 24 μmPS	-	Prst.?	113	40	0.9	Y	-	-	-	-
C3	GF, 24 μmPS	-	Prst.	398	27	0.7	Y	Y	Y	Y	Y
D9	GF, 24 μmPS	-	Prst.	581	19	0.7	Y	Y	Y	Y	-
C5	GF, 24 μmPS	16256-4905, Maser	Prst.	500	42	0.8	Y	-	Y	-	-
B6	GF, 24 μmPS	16351-4722	Prst.	698	14	0.6	Y	-	-	-	-
E8	GF, 24 μmPS	16147-5100	Prst.	900	35	1.6	Y	Y	Y	Y	-
C4	GF, 24 μmPS	-	Prst.	92	46	0.5	Y	Y	-	Y	-
A25	GF, 24 μmPS	16390-4637	Prst.	225	25	0.9	Y	-	-	-	-
B2	GF, 24 μmPS	16340-4732, Maser	Prst.	1960	30	1.2	Y	Y	Y	Y	Y
E6	Bright 8,24 μm	16137-5100	HII	1394	18	1.7	Y	Y	-	Y	-
B1	Bright 8,24 μm	-	HII	462	30	0.8	Y	Y	Y	Y	-
D5	Bright 8,24 μm	-	HII	349	12	0.6	Y	Y	-	Y	-
D7	Bright 8,24 μm	16119-5048, Maser	HII	1238	26	0.9	Y	Y	Y	Y	-
E1	Bright 8,24 μm	16124-5110	HII	650	60	1.5	Y	Y	Y	Y	-
E7	Bright 8,24 μm	16143-5101	HII	214	60	1.8	Y	-	-	Y	-
A37	Bright 8,24 μm	-	PDR	516	40	0.5	Y	Y	Y	Y	Y
E2	Bright 8,24 μm	16128-5109	PDR	1300	60	2.1	Y	Y	Y	Y	-
E5	Diffuse 8,24 μm	16141-5107	PDR	214	60	1.4	Y	Y	-	Y	-

10

Summary

In this thesis I performed a multi wavelength study of filamentary molecular clouds to determine their physical characteristics and their connection to star formation. This section highlights the main results obtained in this thesis:

- ATLASGAL project is an unbiased survey of dust emission at 870 μm in the Galactic Plane. From these data I made a compact source catalog containing more than ~7000 objects. I found that more than half of the objects are not associated with *IRAS* or *MSX* sources, suggesting that they might be clumps in an early evolutionary state. These are excellent candidates for high mass starless clumps and their detailed study with next generation telescopes like ALMA will help understand the initial stages of high mass star formation.

- ATLASGAL, as well as other recent (sub)millimeter surveys show that filamentary molecular clouds are ubiquitous along the Galactic Plane. These data show that clumps are usually embedded within the more extended emission associated with filaments.

- Since the observed dust continuum emission correspond to the emission from all sources along the line of sight, a filament appearing connected may be produced by the superposition of several molecular clouds at different depth. To establish the physical coherence of a filaments we made molecular lines observations to determine the velocity along the filaments.

We found most, but not all, filamentary structures observed correspond to single coherent structures.

- The column densities derived for the filaments are similar to that of IRDCs and typical cold molecular clouds. The column densities obtained are high enough to form high mass stars (McKee and Ostriker 2007) and are similar to values obtained toward other filamentary molecular clouds.

- The column density profile of the filaments are consistent with models that describe filamentary molecular clouds supported by magnetic field. Moreover, the mass and pressures derived from the continuum and molecular line emission suggest that these structures are stables due to the presence of a *toroidal dominated magnetic field* that prevents the filament from expansion. However, once the clumps are formed the magnetic field is not needed to support them as they appear stable as a result of hydrostatic equilibrium.

- The observed characteristic separations between the clumps are in agreement with the separation predicted by theories that explain the fragmentation of isothermal filaments by fluid or *"sausage"* instability. This theory can also explain the origin of the filamentary structures.

- Some of the clumps embedded within the filaments have high masses (>200 $M_{\odot}$), high densities (10^5 to 10^6 cm^{-3}) and cold temperatures (<20 K), suggesting that they may be in a very early evolutionary phase in the formation of a high mass stars.

The results of this thesis show that filaments are likely supported by toroidal dominated magnetic field that prevents the filaments from expansion and that fluid instabilities may provoke localized regions of the filaments to collapse, given rise to star-forming clumps. Many of these clumps may give rise to high mass stars, as they evolve they will disrupt their environment and destroy the original filament. Therefore, the characterization of filaments gives us information about the earliest stages of high mass star formation, which is important because high-mass stars are on of the most important objects in the Galaxy and yet the least understood.

A

Observations Details

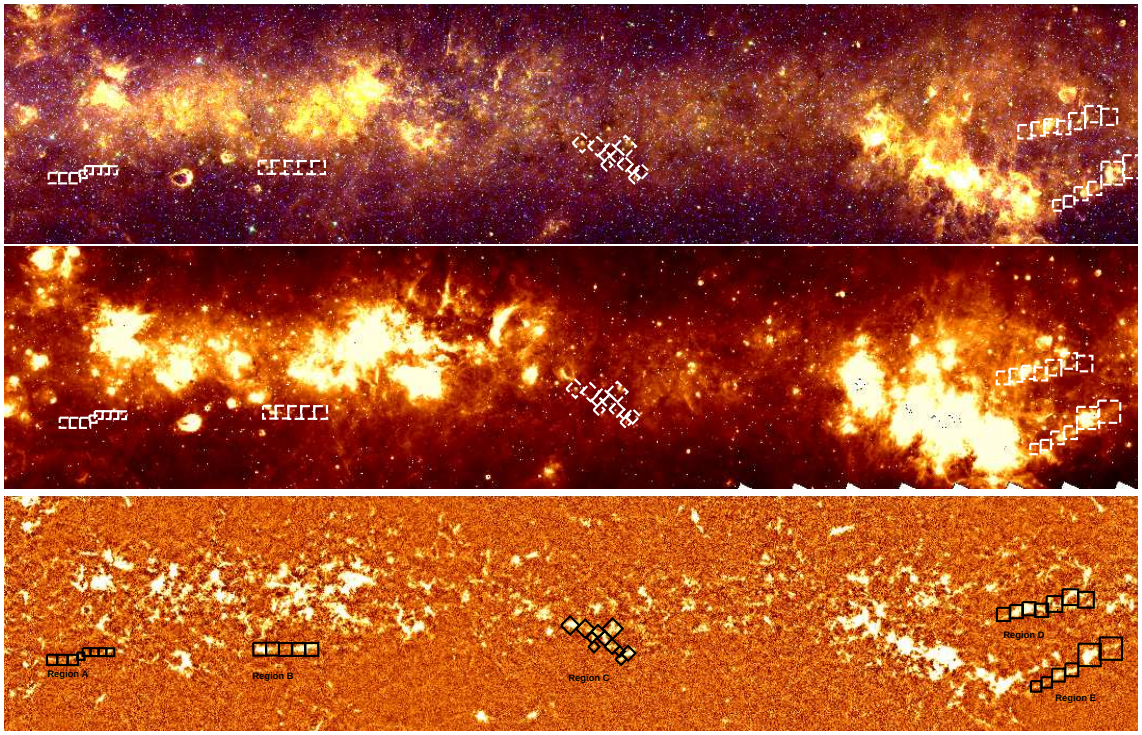

FIGURE A.1: Color image of the region selected for this work, shown at different wavelegths. Upper panel: *Spitzer*/GLIMPSE three color image (Blue: 3.6 μm, green: 5.8 μm and red: 8 μm). Middle panel: Color image of *Spitzer*/MIPSGAL 24 μm. Lower panel: Mosaic of ATLASGAL data at 870 μm. Boxes on all images indicate the regions with follow up observations at continuum and molecular lines.

Table A.1: Observations made with SABOCA/APEX

Source	RA J2000	DEC J2000	Size X arc min	Size Y arc min	Date
B1	16:37:36.239	-47:41:35.55	5.5	5.8	Aug 2010
B2	16:38:35.321	-47:30:15.21	5.4	5.8	Aug 2010
B3	16:38:16.645	-47:33:52.82	5.6	5.8	Aug 2010
B4	16:37:57.028	-47:37:47.75	5.4	5.7	Aug 2010
B5	16:38:54.673	-47:26:33.94	7.7	7.5	Aug 2010
C1	16:30:11.362	-48:48:02.33	9.3	7.9	Jul 2010
C2	16:29:52.647	-48:53:20.96	7.5	9.1	Jul 2010
C3	16:29:54.612	-48:57:25.34	5.3	5.8	Jul 2010
C4	16:29:35.924	-48:57:51.62	5.7	6.1	Jul 2010
C5	16:29:36.951	-49:01:39.07	5.7	6.2	Jul 2010
C7	16:29:06.652	-49:00:33.41	7.3	8.5	Jul 2010
C8	16:29:41.523	-49:05:42.80	5.7	6.4	Jul 2010
C9	16:29:35.917	-49:09:01.85	4	5.2	Jul 2010
D1	16:17:28.991	-50:46:18.41	4	4	Oct 2011
D2	16:17:01.467	-50:48:01.81	4.5	4.5	Oct 2011
D3	16:16:42.847	-50:50:16.61	4	4	Oct 2011
D4	16:15:45.126	-50:55:57.62	4	4	Oct 2011
D5	16:15:34.656	-50:55:42.83	4	4	Oct 2011
D6	16:15:16.842	-50:55:59.55	4	4	Oct 2011
E1	16:16:26.205	-51:17:45.83	8.9	9.2	Aug 2010
E2	16:18:04.701	-51:08:27.65	4	4	Oct 2011
E3	16:17:56.116	-51:15:07.07	5.5	5.5	Oct 2011
E4	16:17:23.778	-51:17:10.16	5.5	5.5	Oct 2011

Table A.2: Observation at 13CO(3-2)

Source	RA J2000	DEC J2000	Size X arc min	Size Y arc min	I. Time min	Date
A1	16:43:18.07	-46:37:31.5	4.6	4.6	15	Jun 2010
A2	16:43:05.61	-46:39:50.5	5	5	15	Jun 2010
B1	16:38:54.67	-47:26:33.9	7.7	7.5	43	Jun 2010
B2	16:38:35.32	-47:30:15.2	5.3	5.9	43	Aug 2010
B3	16:38:16.64	-47:33:52.8	5.7	5.9	23	Aug 2010
B4	16:37:57.03	-47:37:47.7	5.5	5.5	43	Aug 2010
B5	16:37:36.24	-47:41:35.5	5.4	5.8	42	Aug 2010
C1	16:30:02.80	-48:50:32.7	4.9	10.6	94	Jul 2010
C2	16:29:32.19	-49:01:07.2	10.4	11.5	198	Jul 2010
C3	16:29:33.10	-49:12:19.3	4.5	6.6	51	Jul 2010
D1	16:17:28.991	-50:46:18.41	4	4	30	Oct 2011
D2	16:17:01.467	-50:48:01.81	4.5	4.5	38	Oct 2011
D3	16:16:42.847	-50:50:16.61	4	4	15	Oct 2011
D4	16:15:45.126	-50:55:57.62	4	4	30	Oct 2011
D5	16:15:34.656	-50:55:42.83	4	4	30	Oct 2011
D6	16:15:16.842	-50:55:59.55	4	4	29	Oct 2011
E1	16:17:56.11	-51:15:07.0	5.4	5.7	42	Oct 2010
E2	16:17:23.78	-51:17:10.2	5.9	5.3	21	Oct 2010
E3	16:16:26.20	-51:17:45.8	8.9	9.3	62	Oct 2010
E4	16:17:23.778	-51:17:10.16	5.5	5.5	42	Oct 2011

TABLE A.3: List of point positions observed at N_2H^+

Source	ATLASGAL Source	RA J2000	DEC J2000	I. Time min	Date
A P1	AGAL338.394-0.406	16:42:43.86	-46:43:35.0	4.4	Jul
A P2	AGAL338.476-0.429	16:43:05.37	-46:41:02.6	5.7	Jul
A P3	AGAL338.551-0.419	16:43:21.77	-46:37:20.6	8.2	Jul
A P4	AGAL338.616-0.441	16:43:39.30	-46:35:25.0	16	Jul
B P2	AGAL337.406-0.402	16:38:49.95	-47:28:02.5	6.2	Jul
B P6	AGAL337.153-0.394	16:37:48.06	-47:38:46.1	5.6	Jul
C P1	AGAL335.441-0.237	16:30:08.77	-48:48:11.6	31	Jul
C P2	AGAL335.221-0.344	16:29:42.23	-49:01:54.9	26	Jul
C P3	AGAL335.061-0.427	16:29:23.71	-49:12:18.2	17	Jul
D P1	AGAL332.604-0.167	16:17:29.99	-50:46:20.5	5	Jul
D P3	AGAL332.544-0.124	16:17:01.01	-50:46:41.8	5	Jul
D P5	AGAL332.469-0.131	16:16:42.08	-50:50:17.5	5.6	Jul
D P7	AGAL332.294-0.094	16:15:45.19	-50:56:07.2	5.7	Jul
D P8	AGAL332.241-0.044	16:15:17.08	-50:56:01.4	5.6	Jul
E P1	AGAL332.469-0.522	16:18:26.87	-51:07:07.3	5	Jul
E P2	AGAL332.411-0.502	16:18:05.35	-51:08:26.2	4.4	Jul
E P3	AGAL332.351-0.436	16:17:29.79	-51:08:30.0	5	Jul
E P4	AGAL332.156-0.449	16:16:40.55	-51:17:05.2	4.8	Jul
E P5	AGAL332.094-0.421	16:16:15.71	-51:18:26.6	5	Jul
E P6	AGAL332.312-0.556	16:17:55.70	-51:14:59.4	5	Jul
E P7	AGAL332.226-0.536	16:17:24.37	-51:17:46.5	5	Jul

Table A.4: List of regions observed with MOPRA as part of the MALT90 project

Source	RA J2000	DEC J2000
AGAL332.094-0.421	16:16:16.655	-51:18:25.24
AGAL332.156-0.449	16:16:39.330	-51:17:10.17
AGAL332.226-0.536	16:17:23.225	-51:17:52.51
AGAL332.241-0.044	16:15:16.842	-50:55:59.55
AGAL332.276-0.071	16:15:34.656	-50:55:42.83
AGAL332.279-0.547	16:17:40.752	-51:16:07.97
AGAL332.294-0.094	16:15:45.126	-50:55:57.62
AGAL332.312-0.556	16:17:54.681	-51:15:01.02
AGAL332.351-0.436	16:17:29.542	-51:08:23.13
AGAL332.411-0.502	16:18:04.701	-51:08:27.65
AGAL332.469-0.131	16:16:42.847	-50:50:16.61
AGAL332.469-0.522	16:18:26.978	-51:07:08.72
AGAL332.604-0.167	16:17:29.450	-50:46:14.18
AGAL335.061-0.427	16:29:23.123	-49:12:19.77
AGAL335.221-0.344	16:29:42.016	-49:02:01.39
AGAL335.232-0.314	16:29:38.128	-49:00:20.52
AGAL335.427-0.241	16:30:05.698	-48:48:40.71
AGAL335.461-0.237	16:30:13.156	-48:47:01.93
AGAL337.139-0.382	16:37:39.422	-47:39:12.21
AGAL337.153-0.394	16:37:49.858	-47:38:41.25
AGAL337.371-0.399	16:38:41.308	-47:29:23.12
AGAL337.406-0.402	16:38:50.893	-47:27:56.18
AGAL337.437-0.399	16:38:57.908	-47:26:20.44
AGAL338.394-0.406	16:42:42.370	-46:43:38.44

Table A.5: Calibrators used for SABOCA observations

Source	RA J2000	DEC J2000	Flux [Jy]
B13134	13:16:43.15	-62:58:31.6	180
IRAS 16293	16:32:22.9	-24:28:35.6	135
G34.3	18:53:18.5	01:14:58.6	430
G5.88	18:00:30.38	-24:04:00.5	230

B

Additional parameters

B.1 Parameters used for computations

TABLE B.1: Parameters used for calculus of mass from n2hp. Excitation temperature, line width and opacity obtained from fitting to the hyperfine component with CLASS. Diameter derived from gaussian fitting to the integrated intensity maps.

Clump	Diameter	T_{ex}	Δv	τ
	pc	K	km s^{-1}	
A25	0.9	3.9	1.5 ±0.4	4.40
A38	0.4	77.8	3.1 ±0.1	0.10
B1	0.7	71.3	2.2 ±0.1	0.10
B2	1.7	5.37	2.8 ±0.1	0.10
B6	0.6	7.3	2.6 ±0.0	1.15
C1	0.6	4.5	3.9 ±0.4	0.92
C3	0.7	24.9	3.5 ±0.2	0.10
C4	0.5	29.8	2.1 ±0.2	0.10
C5	0.8	5.1	2.3 ±0.1	0.10
D1	0.7	5.0	2.9 ±0.2	1.32
D5	0.6	26.6	1.7 ±0.1	0.10
D6	0.4	29.0	1.9 ±0.2	0.10
D7	0.9	5.6	2.4 ±0.1	0.10
D8	0.3	6.6	2.6±0.1	1.12
D9	0.7	47.8	3.2±0.1	0.10
E1	1.5	4.3	2.4±0.1	0.10
E2	2.1	3.8	4.6±0.1	0.10
E3	2.0	4.3	1.8±0.2	2.3
E4	1.3	6.2	2.2 ±0.3	1.16
E5	1.4	5.6	2.5 ±0.3	0.79
E7	1.8	3.8	1.35 ±0.1	0.10
E8	0.5	44.1	2.9 ±0.1	0.10

Table B.2: Line parameters for molecules used to calculate N_{tot}

Transition	Frequency [MHz]	B (MHz)	μ (D)
N_2H^+(1-0)	93173.4035[a]	46586.867	3.4
N_2H^+(3-2)	279511.9375[b]		

[a] Caselli et. al. 1995
[b] Caselli et. al. 2002a

Table B.3: Frequencies of N_2H^+(3-2) hyperfine structure

F'_1F'	F_1F	Frequency (MHz)	Relative Velocity (km s^{-1})	Relative Intensity
3 4	3 4	279509.8785±0.0062	2.0120	0.0166
2 2	1 2	279511.1328±0.0064	0.6690	0.0154
2 2	1 1	279511.3445±0.0061	0.4424	0.0479
2 1	1 0	279511.3847±0.0061	0.3993	0.0222
3 3	2 3	279511.4305±0.0063	0.3503	0.0140
2 3	1 2	279511.5089±0.0062	0.2663	0.0945
3 3	2 2	279511.6858±0.0061	0.0769	0.0885
3 2	2 1	279511.7978±0.0061	-0.0430	0.0610
4 3	3 2	279511.8097±0.0061	-0.0557	0.1005
4 4	3 3	279511.8114±0.0061	-0.0576	0.1356
3 4	2 3	279511.8083±0.0061	-0.0542	0.1249
2 1	1 1	279511.8486±0.0063	-0.0974	0.0187
4 5	3 4	279511.8621±0.0061	-0.1118	0.1746
4 3	3 3	279512.3171±0.0065	-0.5990	0.0102
2 2	2 2	279514.2219±0.0063	-2.6385	0.0114
2 3	2 3	279514.3427±0.0063	-2.7678	0.0141

TABLE B.4: Frequencies of N_2H^+(1-0) hyperfine structure (Daniel et al. 2006)

F'_1F'	F_1F	Frequency (MHz)	Relative Intensity
10	11	93171.617	0.333
12	11	93171.913	0.417
12	12	93171.913	1.250
11	10	93172.048	0.333
11	11	93172.048	0.250
11	12	93172.048	0.417
22	11	93173.475	1.250
22	12	93173.475	0.417
23	12	93173.772	2.330
21	10	93173.963	0.556
21	11	93173.963	0.417
21	12	93173.963	0.028
01	10	93176.261	0.111
01	11	93176.261	0.333
01	12	93176.261	0.556

TABLE B.5: Frequencies of HCN hyperfine structure (Bhattacharya and Gordy 1960)

F'_1F'	F_1F	Frequency (MHz)	Relative Intensity
10	11	88630.42	1.000
10	21	88631.85	1.667
10	01	88633.94	0.333

TABLE B.6: Frequencies of HNC hyperfine structure

F'_1F'	F_1F	Frequency (MHz)	Relative Intensity
10	01	90663.417	3
10	21	90663.556	5
10	11	90663.622	1

Table B.7: Frequencies of C_2H hyperfine structure (Padovani et al. 2009)

F'$_1$F'	F_1F	Frequency (MHz)	Relative Intensity
3/2, 1	1/2, 1	87284.105	0.042
3/2, 2	1/2, 1	87316.898	0.416
3/2, 1	1/2, 0	87328.585	0.207
1/2, 1	1/2, 1	87401.989	0.208
1/2, 0	1/2, 1	87407.165	0.084
1/2, 1	1/2, 0	87446.470	0.043

Table B.8: Molecular transition parameters

Line	Transition	Frequency MHz	A_l
^{13}CO(3-2)	J=3-2	330587.97	-5.65776[b]
N_2H^+	J=3-2	279511.701	-2.86895[a]
N2H$^+$	J=1-0	93173.480	-5.02536[b]
^{13}CS	J=2-1	92494.303	-4.84834[a]
H	41α	92034.475	-
CH_3CN	J_K=5_1-4_1	91985.316	-4.23806[a]
HC_3N	J= 10-9	91199.796	-4.23810[b]
$^{13}C^{34}S$	J=2-1	90926.036	-4.92479[c]
HNC	J=1-0	90663.572	-4.57032[c]
HC^{13}CCN	J=10-9,F=9-8	90593.059	-4.72312[c]
HCO$^+$	J=1-0	89188.526	-4.37812[b]
HCN	J=1-0	88631.847	-5.09559[b]
HNCO	J_{K_a,K_b}=$4_{1,3}$-$3_{1,2}$	88239.027	-4.44770[c]
HNCO	J_{K_a,K_b}=$4_{0,4}$-$3_{0,3}$	87925.238	-4.20850[a]
C2H	N=1-0,J=3/2-1/2, F=2-1	87316.925	-5.65605[a]
SiO	J=2-1	86847.010	-4.53632[b]
H^{13}CO$^+$	J=1-0	86754.330	-5.14556[a]
H^{13}CN	J=1-0	86340.167	-5.31569[a]

[a] JPL
[b] SLAIM
[c] CDMS

C

ATLASGAL compact source catalog

TABLE C.1: The ATLASGAL compact source catalogue. The columns are as follows: (1) name derived from Galactic coordinates of the maximum intensity in the source; (2)-(3) Galactic coordinates of maximum intensity in the catalogue source; (4)-(5) Galactic coordinates of emission centroid; (6)-(8) major and minor axis $1/e$ widths and position angle of source; (9) effective radius of source; (10)-(13) peak and integrated flux densities and their associated uncertainties; (14) `SExtractor` detection flag (see text for details).

Name	$\ell_{\rm max}$	$b_{\rm max}$	ℓ	b	$\sigma_{\rm maj}$	$\sigma_{\rm min}$	PA	$\theta_{\rm R}$	$S_{\rm peak}$	$\Delta S_{\rm peak}$	$S_{\rm int}$	$\Delta S_{\rm int}$	Flag
	(°)	(°)	(°)	(°)	(″)	(″)	(°)	(″)	(Jy beam^{-1})		(Jy)		
(1)	(2)	(3)	(4)	(5)	(6)	(7)	(8)	(9)	(10)	(11)	(12)	(13)	(14)
AGAL019.486−00.199	19.486	-0.199	19.487	-0.198	27	17	163	20	0.80	0.13	10.63	1.90	2
AGAL019.508−00.447	19.508	-0.447	19.509	-0.447	22	13	71	14	0.48	0.10	4.62	0.98	0
AGAL019.526−00.086	19.526	-0.086	19.526	-0.089	11	7	104	···	0.35	0.08	1.81	0.51	0
AGAL019.539−00.456	19.539	-0.456	19.538	-0.458	26	14	177	16	0.76	0.13	8.78	1.62	2
AGAL019.572−00.101	19.572	-0.101	19.574	-0.100	18	14	94	14	0.71	0.13	4.70	0.99	2
AGAL019.581−00.069	19.581	-0.069	19.582	-0.068	13	8	86	5	0.48	0.10	4.44	0.95	3
AGAL019.582−00.091	19.582	-0.091	19.582	-0.091	12	6	52	···	0.59	0.13	2.06	0.55	3
AGAL019.589−00.079	19.589	-0.079	19.589	-0.079	18	12	60	12	0.73	0.14	10.55	1.89	3
AGAL019.601−00.092	19.601	-0.092	19.601	-0.094	8	6	114	···	0.40	0.11	1.69	0.49	0
AGAL019.606−00.072	19.606	-0.072	19.607	-0.074	17	12	112	12	0.46	0.11	7.22	1.38	3
AGAL019.609−00.137	19.609	-0.137	19.609	-0.138	15	11	79	10	2.79	0.43	8.63	1.59	3
AGAL019.609−00.234	19.609	-0.234	19.609	-0.234	22	19	61	19	19.20	2.88	51.02	7.97	3
AGAL019.611−00.121	19.611	-0.121	19.611	-0.120	13	10	57	7	1.17	0.20	3.25	0.75	3
AGAL019.612−00.259	19.612	-0.259	19.612	-0.258	28	16	63	19	1.88	0.29	16.93	2.85	3
AGAL019.628−00.264	19.628	-0.264	19.626	-0.264	14	7	150	···	0.46	0.10	1.84	0.52	3
AGAL019.631−00.162	19.631	-0.162	19.630	-0.162	12	9	85	6	0.70	0.14	6.60	1.28	3
AGAL019.641−00.172	19.641	-0.172	19.641	-0.172	19	13	122	13	0.53	0.12	12.58	2.20	2
AGAL019.686−00.127	19.686	-0.127	19.684	-0.129	25	14	13	17	0.70	0.14	8.56	1.59	2
AGAL019.694−00.174	19.694	-0.174	19.694	-0.175	10	8	152	···	0.44	0.10	1.16	0.39	0
AGAL019.699−00.266	19.699	-0.266	19.699	-0.262	26	21	48	22	1.97	0.30	14.44	2.48	3
AGAL019.706−00.239	19.706	-0.239	19.706	-0.239	27	14	46	17	0.88	0.15	10.88	1.94	3
AGAL019.716−00.171	19.716	-0.171	19.717	-0.172	12	8	148	4	0.44	0.10	2.98	0.72	0
AGAL019.726−00.114	19.726	-0.114	19.726	-0.114	14	11	100	10	1.09	0.18	8.66	1.60	0
AGAL019.746−00.171	19.746	-0.171	19.745	-0.172	18	14	178	14	0.40	0.09	4.47	0.95	2
AGAL019.754−00.129	19.754	-0.129	19.755	-0.128	22	11	26	13	1.87	0.29	12.77	2.22	2
AGAL019.771−00.114	19.771	-0.114	19.770	-0.113	22	7	135	···	0.54	0.10	3.17	0.74	2
AGAL019.811−00.342	19.811	-0.342	19.812	-0.340	16	9	5	6	0.37	0.08	3.72	0.83	19
AGAL019.817−00.516	19.817	-0.516	19.816	-0.515	8	6	158	···	0.33	0.08	1.36	0.43	0
AGAL019.829−00.329	19.829	-0.329	19.830	-0.331	22	18	110	18	1.15	0.19	11.26	2.00	2
AGAL019.874−00.092	19.874	-0.092	19.874	-0.092	10	6	103	···	0.32	0.08	1.23	0.40	0
AGAL019.882−00.534	19.882	-0.534	19.885	-0.534	30	17	88	21	7.43	1.12	31.13	4.99	2
AGAL019.899−00.441	19.899	-0.441	19.896	-0.439	11	9	146	4	0.35	0.08	2.86	0.69	18
AGAL019.902−00.582	19.902	-0.582	19.902	-0.582	13	7	125	···	0.38	0.09	3.68	0.83	16
AGAL019.906−00.241	19.906	-0.241	19.906	-0.238	13	10	134	8	0.45	0.10	3.78	0.84	0
AGAL019.911−00.206	19.911	-0.206	19.911	-0.205	11	10	135	6	0.33	0.08	2.61	0.65	0
AGAL019.922−00.259	19.922	-0.259	19.926	-0.258	25	15	13	18	2.51	0.38	15.88	2.69	0
AGAL019.961−00.092	19.961	-0.092	19.961	-0.094	9	6	60	···	0.35	0.08	1.61	0.48	0
AGAL019.967−00.106	19.967	-0.106	19.970	-0.105	11	9	26	6	0.45	0.09	2.60	0.65	0
AGAL019.977−00.214	19.977	-0.214	19.976	-0.216	16	10	68	9	0.87	0.15	3.54	0.80	0
AGAL019.991−00.169	19.991	-0.169	19.991	-0.169	10	7	176	···	0.55	0.11	1.72	0.49	3
AGAL020.004−00.167	20.004	-0.167	20.002	-0.168	13	10	25	8	0.40	0.09	5.27	1.08	18
AGAL020.019−00.151	20.019	-0.151	20.018	-0.152	9	6	29	···	0.37	0.09	2.23	0.58	16
AGAL020.022−00.169	20.022	-0.169	20.024	-0.170	18	7	170	···	0.38	0.09	6.60	1.29	19
AGAL020.081−00.136	20.081	-0.136	20.080	-0.136	18	16	16	15	7.68	1.15	20.96	3.46	0

Notes: Only a small portion of the data is provided here, the full table is only available in electronic form at the CDS via anonymous ftp to cdsarc.u-strasbg.fr (130.79.125.5) or via http://cdsweb.u-strasbg.fr/cgi-bin/qcat?J/A+A/.

D

D.1 Derivation of the virial equation for filamentary molecular clouds

Here we derive the general form of the virial equation including magnetic field support based on the work of Fiege and Pudritz (2000). The general for of the tensor virial theorem in Cartesian coordinates, x_i, is given by (Chandrasekhar 1961):

$$\frac{1}{2}\frac{d^2 I_{i,k}}{dt^2} = 2T_{i,k} + \delta_{i,k}\left[\int_V P dV + M_V\right] + W_{i,k} - 2M_{i,k} + \int_S x_k \left(\frac{B_i B_j}{4\pi} dS_j - \frac{B^2}{8\pi} dS_i\right) - \int_S P x_k dS_i \quad \text{(D.1)}$$

where the integration is done over the volumen V of a cloud bounded by a surface S, P is the total pressure and $I_{i,k}$, $T_{i,k}$, $W_{i,k}$ and $M_{i,k}$ are the Cartesian tensors for moment of inertia, kinetic energy, gravitational energy and magnetic energy respectively. These are given by:

$$\begin{aligned} I_{i,k} &= \int dV \rho x_i x_k \\ T_{i,k} &= \frac{1}{2}\int dV \rho v_i v_k \\ W_{i,k} &= -\int dV \rho x_k \frac{\partial \phi}{\partial x_i} \\ M_{i,k} &= \frac{1}{8\pi}\int dV B_i B_k \end{aligned} \tag{D.2}$$

where ρ is density, P is pressure, v_i is the component of velocity, B_i is the component of the magnetic field and ϕ is the gravitational potential. The magnetic term M_v in equation D.1 is the bulk component of the magnetic energy given by:

$$M_v = \frac{1}{8\pi}\int B^2 dV \tag{D.3}$$

where B is the magnitude of the magnetic field. Filamentary molecular clouds are treated as idealized cylinder whose length is much larger that its radius. For such objects the scalar virial equation is given by the sum of the diagonal terms x and y, ignoring the z component since we are concerned in the radial equilibrium. Using equations D.2 and D.3 equation D.1 becomes:

$$\begin{aligned} \frac{1}{2}\frac{d^2 I_{ii}}{dt^2} &= \int_V \rho v_i^2 dV + \int_V P dV + \frac{1}{8\pi}\int B^2 dV - \int_V \rho x_i \frac{\partial \phi}{\partial x_i} - \frac{1}{4\pi}\int_V B_i^2 dV \\ &\quad + \frac{1}{4\pi}\int_S (x_i B_i)(B_j dS_j) - \frac{1}{8\pi}\int_S B^2 x_i dS_i - \int_S P x_i dS_i \end{aligned}$$

Since the velocity is everywhere is zero, then $\int_V \rho v_i^2 dV = 0$. Summing over x and y (11 and 22 component) and setting $\ddot{I_{11}} = \ddot{I_{22}} = 0$ for a filamentary molecular cloud in equilibrium, we obtain:

$$\begin{aligned} 0 &= 2\int_V P dV + \frac{1}{4\pi}\int B^2 dV - \int_V \rho \mathbf{r}\cdot\nabla\phi - \frac{\mathbf{1}}{\mathbf{4\pi}}\int_{\mathbf{V}} (\mathbf{B_x^2} + \mathbf{B_y^2})\mathbf{dV} \\ &\quad + \frac{1}{4\pi}\int_S (\mathbf{r}\cdot\mathbf{B})(\mathbf{B}\cdot d\mathbf{S}) - \frac{1}{8\pi}\int_S B^2 \mathbf{r}\cdot d\mathbf{S} - \int_S P\mathbf{r}\cdot d\mathbf{S} \end{aligned}$$

where the vector $\mathbf{r}$ and $d\mathbf{S}$ are defined by:

$$\begin{aligned} \mathbf{r} &= x\hat{x} + y\hat{y} \\ d\mathbf{S} &= dS_x\hat{x} + dS_y\hat{y} \end{aligned} \tag{D.4}$$

If the magnetic field is helical in cylindrical coordinates will only have component in z and ϕ, then $B \cdot d\mathbf{S} = 0$. Simplifying equation D.4 by using cylindrical coordinates and dividing by the length, we obtain:

$$0 = 2\int_V P d\mathcal{V} + \frac{1}{4\pi}\int B_z^2 d\mathcal{V} - \int_V \rho r \frac{\partial\phi}{\partial r} d\mathcal{V} - \frac{(B_{Sz}^2 + B_{S\phi}^2)}{4\pi}\mathcal{V} - 2P_S\mathcal{V}$$

$$2P_S\mathcal{V} = 2\int_V P d\mathcal{V} - \int_V \rho r \frac{\partial\phi}{\partial r} d\mathcal{V} + \left[\frac{1}{4\pi}\int B_z^2 d\mathcal{V} - \frac{(B_{Sz}^2 + B_{S\phi}^2)}{4\pi}\mathcal{V}\right]$$

Defining the sum of all the magnetic term, $\mathcal{M}$, as:

$$\mathcal{M} = \frac{1}{4\pi}\int B_z^2 d\mathcal{V} - \frac{(B_{Sz}^2 + B_{S\phi}^2)}{4\pi}\mathcal{V} \tag{D.5}$$

and given that the gravitational energy per unit legth,$\mathcal{W}$, is given by $\mathcal{W} = -\int \rho \frac{\partial\phi}{\partial r} d\mathcal{V}$, equation D.5 becomes:

$$2P_S\mathcal{V} = 2\int_V P d\mathcal{V} + \mathcal{W} + \mathcal{M} \tag{D.6}$$

The mass per unit length of a filament is obtained by integrating the density over the cross-sectional area:

$$m = 2\pi\int r\rho(r) dr \tag{D.7}$$

In cylindrical coordinates the Poisson's equation is given by:

$$\frac{1}{r}\frac{d}{dr}\left(r\frac{d\phi}{dr}\right) = 4\pi G\rho \tag{D.8}$$

Using this equation, the mass of a filaments becomes:

$$\begin{aligned} m(r) &= \frac{2\pi}{4\pi G}\int r\frac{1}{r}\frac{d}{dr}\left(r\frac{d\phi}{dr}\right)dr \\ &= \frac{1}{2G}r\frac{d\phi}{dr}\Big|_r \end{aligned} \tag{D.9}$$

And the gravitational energy per unit length becomes:

$$\mathcal{W} = -2G \int_0^m m' dm' = -m^2 G \tag{D.10}$$

For a filament we also have that, the average density and pressure within the cloud are given by:

$$\begin{aligned} \langle \rho \rangle &= \frac{m}{\mathcal{V}} \\ \langle P \rangle &= \frac{\int_V P d\mathcal{V}}{\mathcal{V}} \end{aligned} \tag{D.11}$$

In general is possible to write the effective pressure inside a molecular cloud as $P = \sigma^2 \rho$, where σ is the velocity dispersion. The average squared velocity dispersion is defined by:

$$\langle \sigma^2 \rangle = \frac{\langle P \rangle}{\langle \rho \rangle} = \frac{\int_{\mathcal{V}} \sigma^2 \rho d\mathcal{V}}{\int_{\mathcal{V}} \rho d\mathcal{V}} \tag{D.12}$$

With these definitions:

$$\frac{1}{2\int P d\mathcal{V}} = \frac{1}{2}\left[\frac{\mathcal{V}}{\int P d\mathcal{V}}\right]\left[\frac{m}{\mathcal{V}}\right]\frac{1}{m} \tag{D.13}$$

$$= \frac{1}{2}\frac{\langle \rho \rangle}{\langle P \rangle}\frac{1}{m} \tag{D.14}$$

$$= \frac{1}{2\langle \sigma^2 \rangle m} \tag{D.15}$$

Since, the virial mass per unit length is defined as:

$$m_{vir} = \frac{2\langle \sigma^2 \rangle}{G} \tag{D.16}$$

Using equation D.15 and D.16, we can re write equation D.6 as:

$$\begin{aligned}
\frac{2P_s\mathcal{V}}{2\int P d\mathcal{V}} &= \frac{2\int P d\mathcal{V} + (\mathcal{W}+\mathcal{M})}{2\int P d\mathcal{V}} \\
&= 1 + \frac{1}{2\int P d\mathcal{V}}(\mathcal{W}+\mathcal{M}) \\
&= 1 + \frac{1}{2\langle\sigma^2\rangle m}\frac{G}{G}(\mathcal{W}+\mathcal{M}) \\
&= 1 + \frac{1}{m_{vir}mG}(\mathcal{W}+\mathcal{M}) \\
&= 1 + \frac{(-m)}{m_{vir}(-m)mG}(-m^2G+\mathcal{M}) \\
&= 1 - \frac{m}{m_{vir}(-m^2G)}(-m^2G+\mathcal{M}) \\
&= 1 - \frac{m}{m_{vir}}\left(1 - \frac{\mathcal{M}}{m^2G}\right) \\
&= 1 - \frac{m}{m_{vir}}\left(1 - \frac{\mathcal{M}}{|\mathcal{W}|}\right) \qquad \text{(D.17)}
\end{aligned}$$

But, using the definition for the average internal pressure given by Equation D.11, we have:

$$\frac{2P_s\mathcal{V}}{2\int P d\mathcal{V}} = \frac{P_s}{\langle P\rangle} \qquad \text{(D.18)}$$

Obtaining, the extended version of virial equation to include magnetic field support:

$$\frac{P_s}{\langle P\rangle} = 1 - \frac{m}{m_{vir}}\left(1 - \frac{\mathcal{M}}{|\mathcal{W}|}\right) \qquad \text{(D.19)}$$

E

Channel Maps MALT90 observations

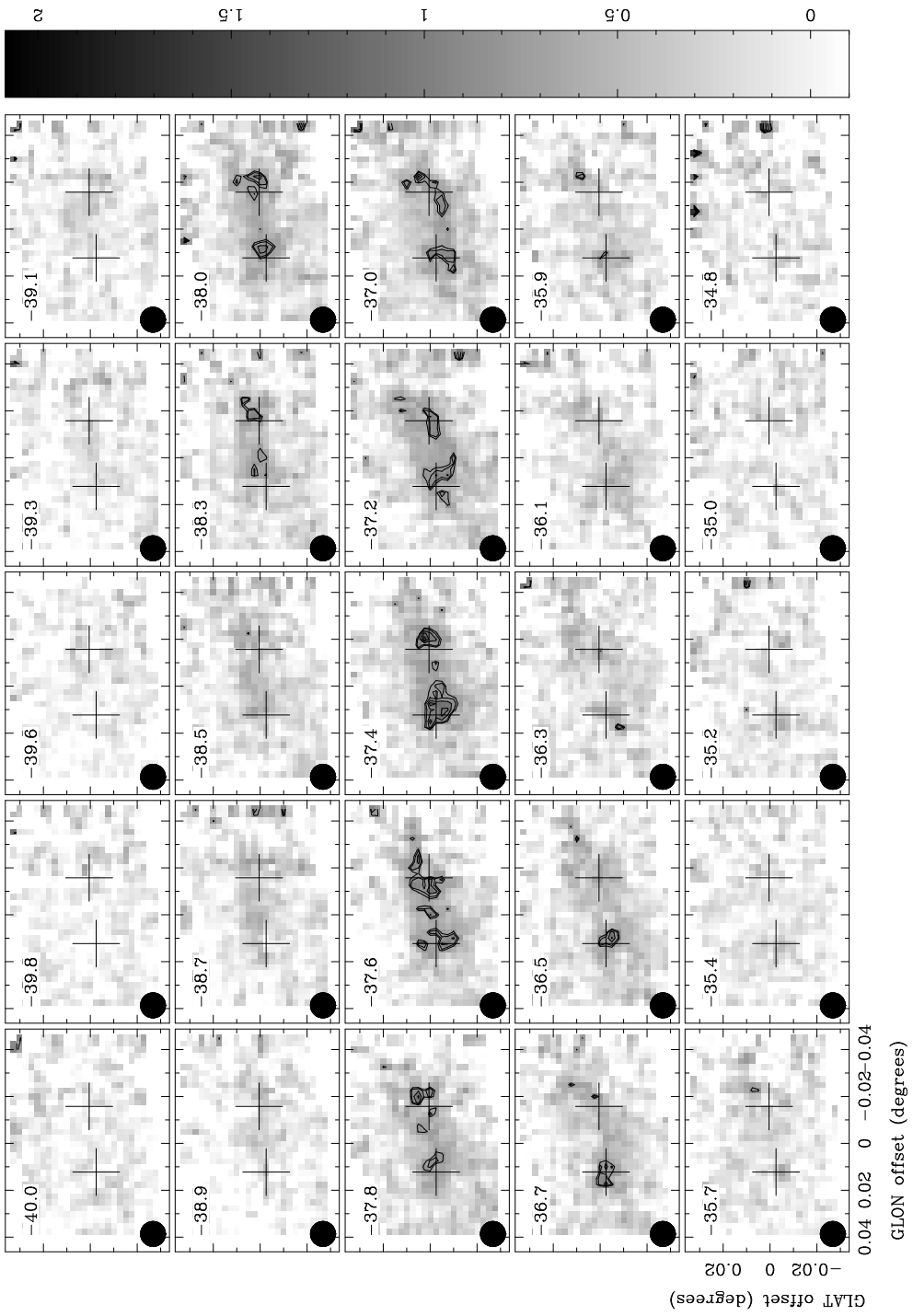

FIGURE E.1: Channel map of N_2H^+(1-0)molecular line emission toward clumps A24 and A25.

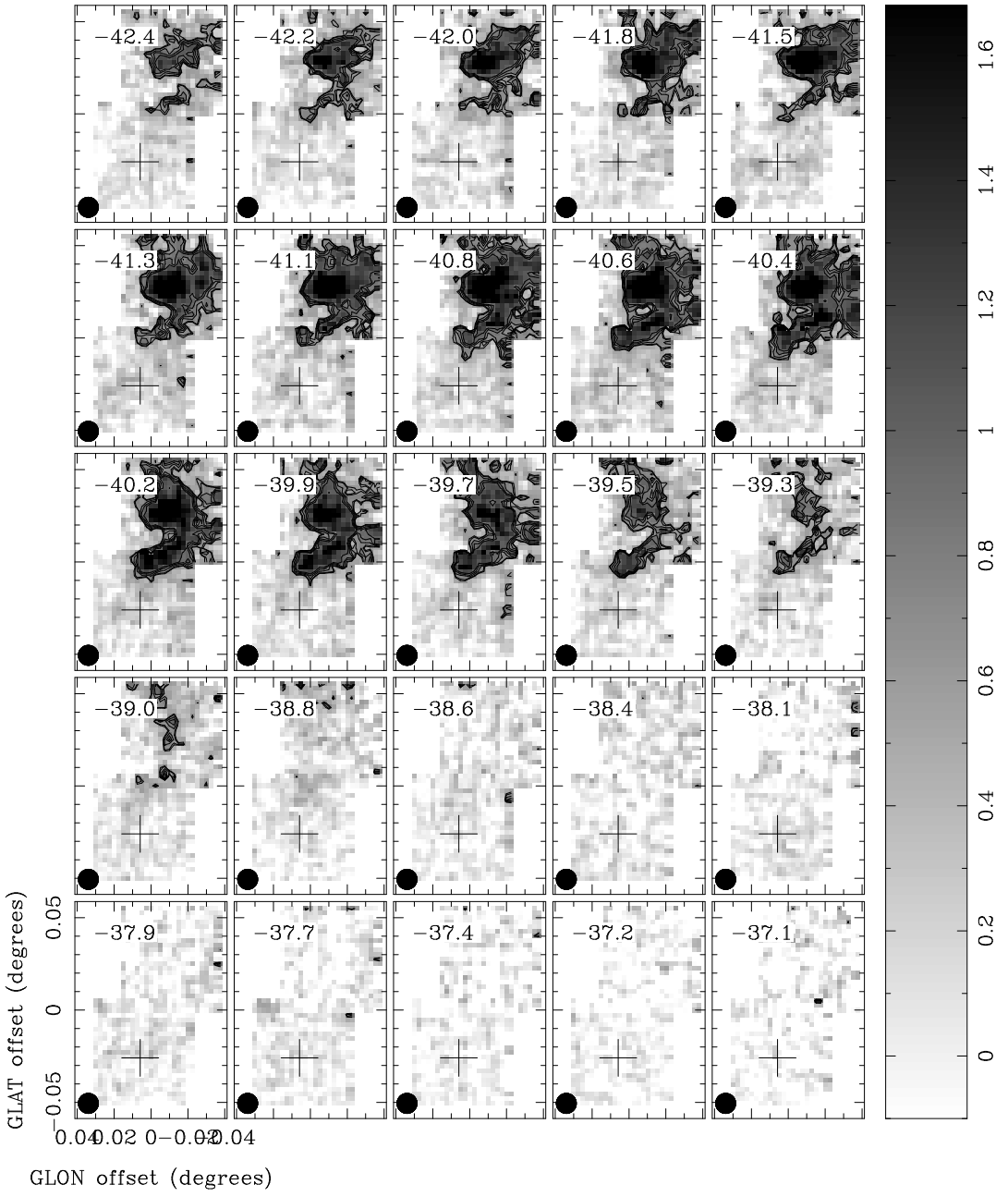

FIGURE E.2: Channel map of HCO^+molecular line emission toward clump A37.

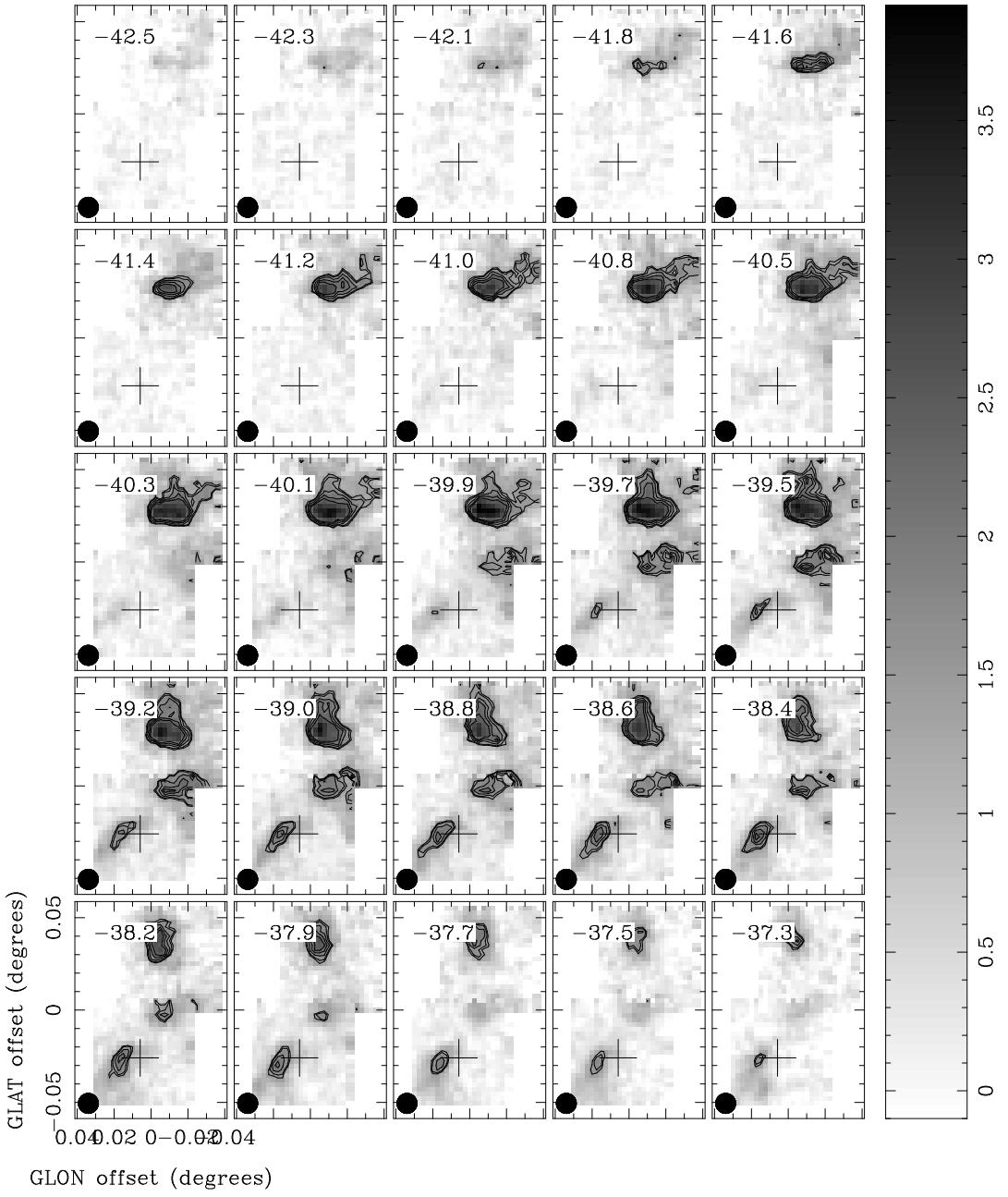

FIGURE E.3: Channel map of N_2H^+(1-0)molecular line emission toward clump A37.

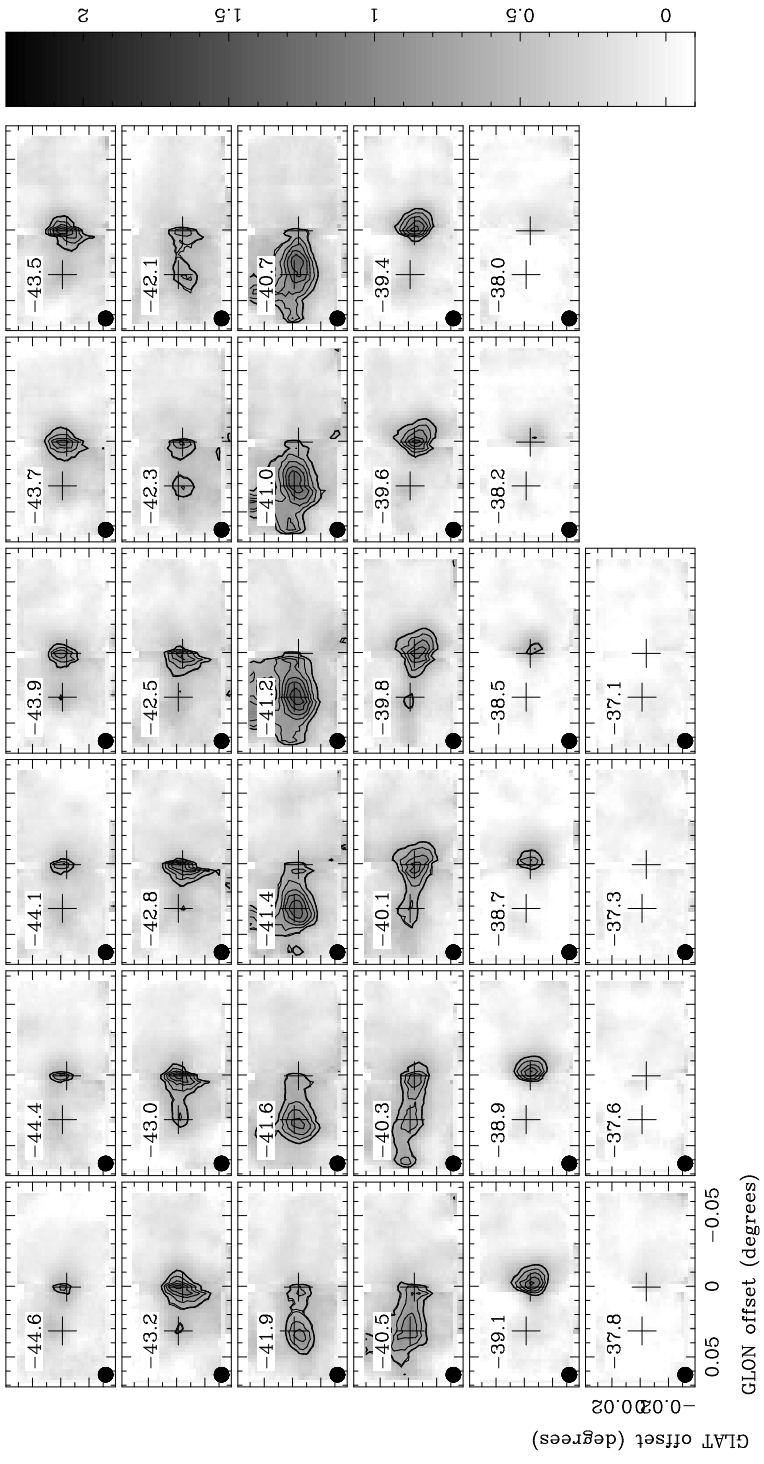

FIGURE E.4: Channel maps of HCO^+at region covering clumps B1 and B2.

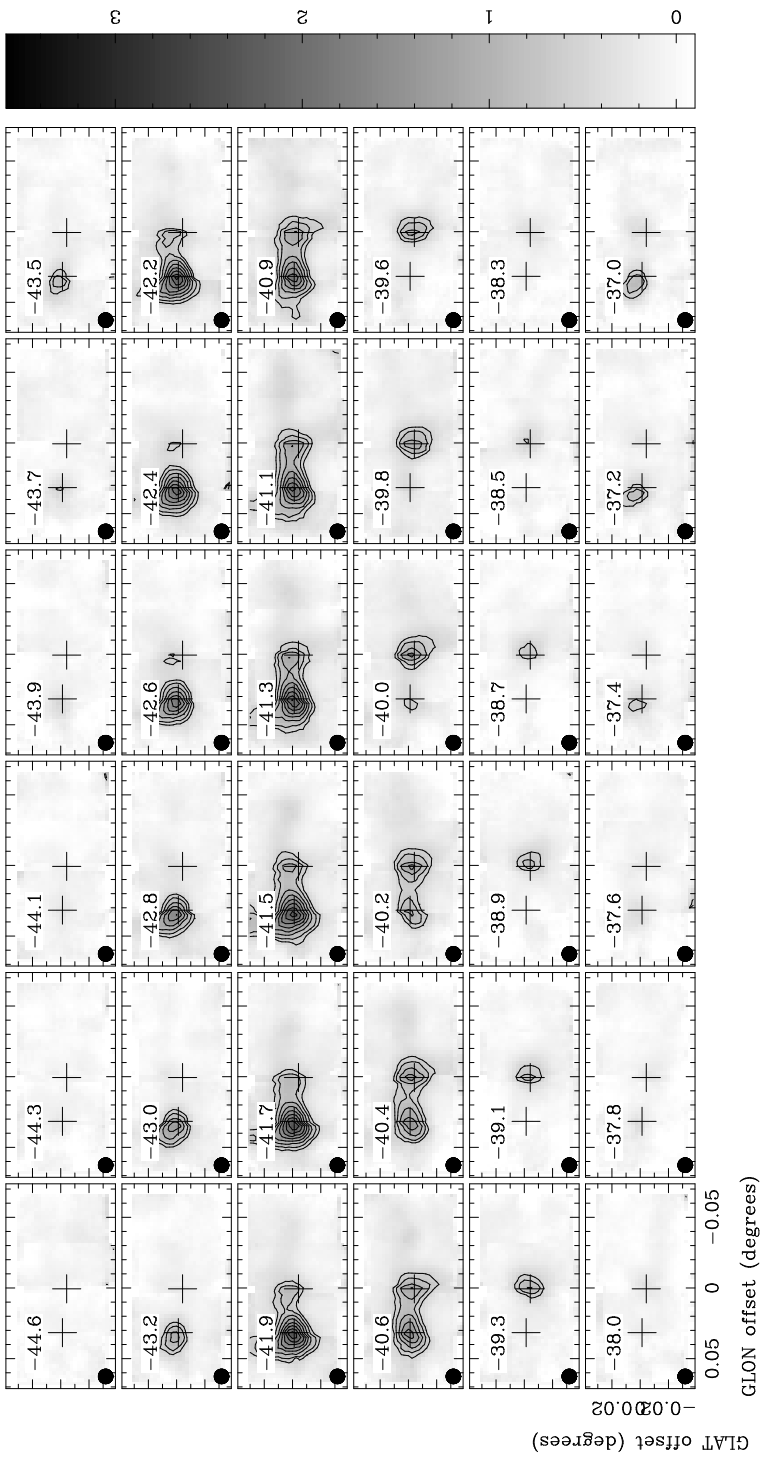

FIGURE E.5: Channel maps of N_2H^+(1-0) at region covering clumps B1 and B2.

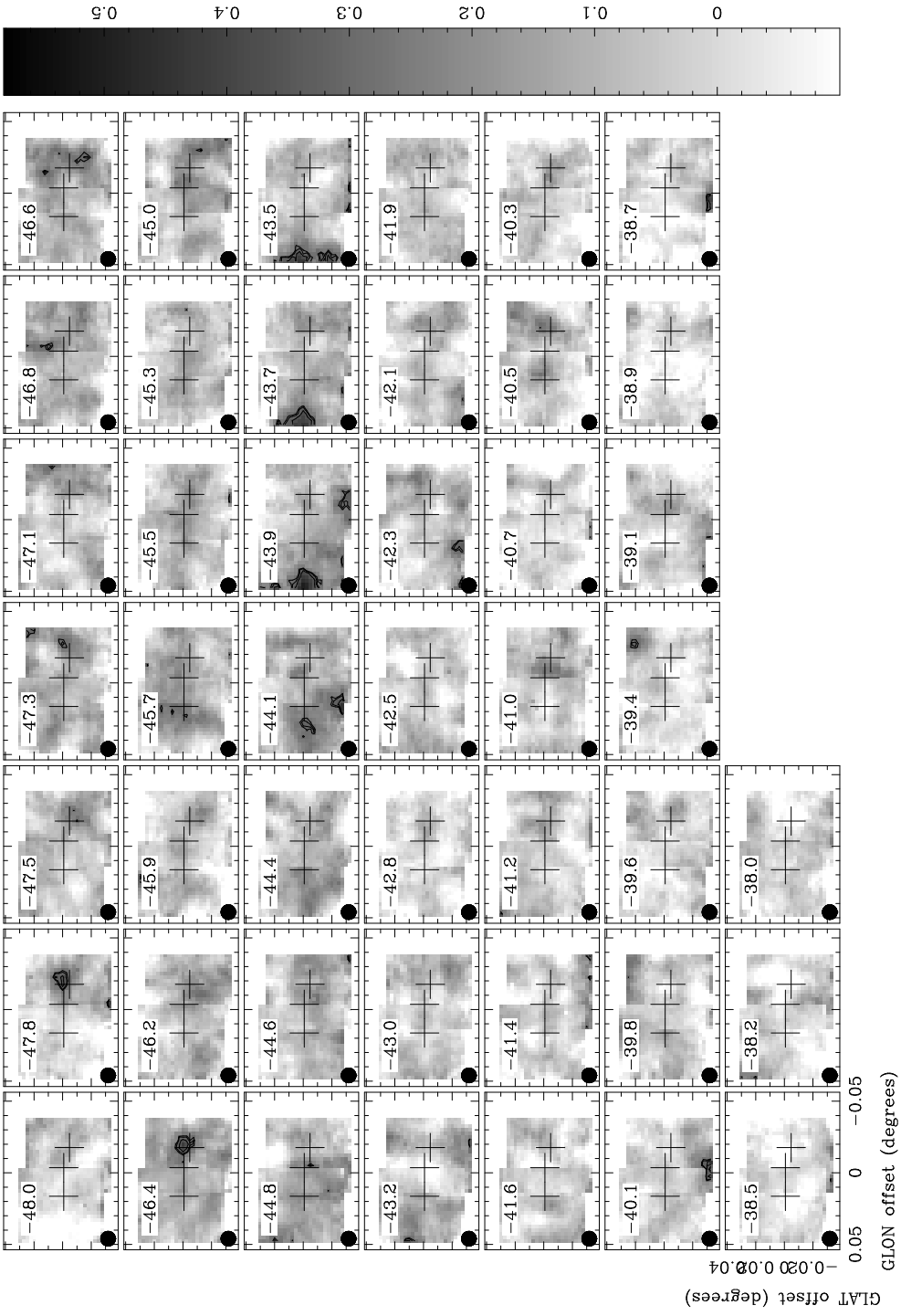

FIGURE E.6: Channel map of HCO^+ at region covering clumps C1, C2 and C3. The crosses show the position of the clumps C1, C2 and C3 from left to right. Here we see that HCO^+ is only observed toward clump C3 and it very localized.

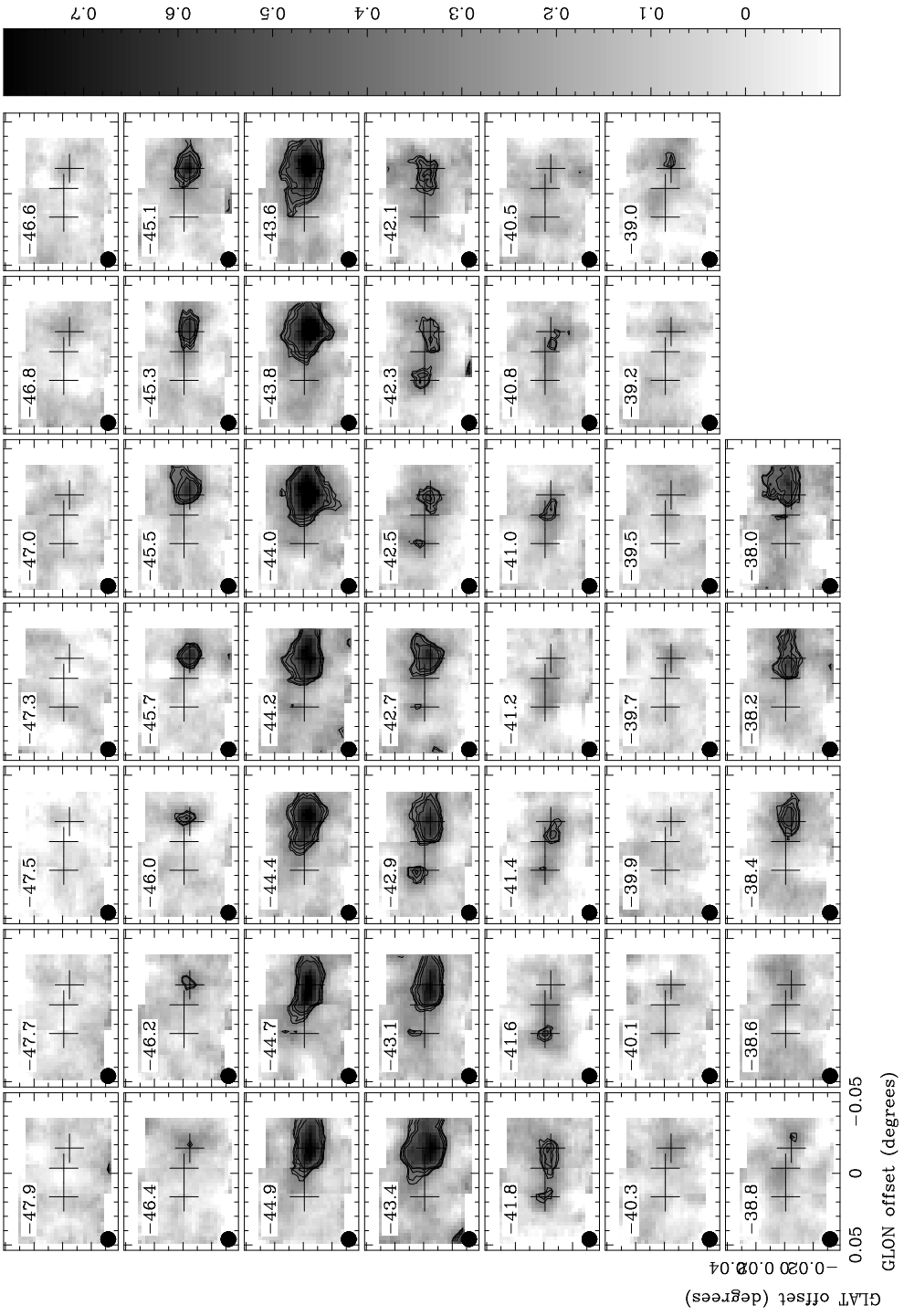

FIGURE E.7: Channel map of N_2H^+(1-0) at region covering clumps C1, C2 and C3. The crosses show the position of the clumps C1, C2 and C3 from left to right. At this transition the morphology is well traced by N_2H^+(1-0).

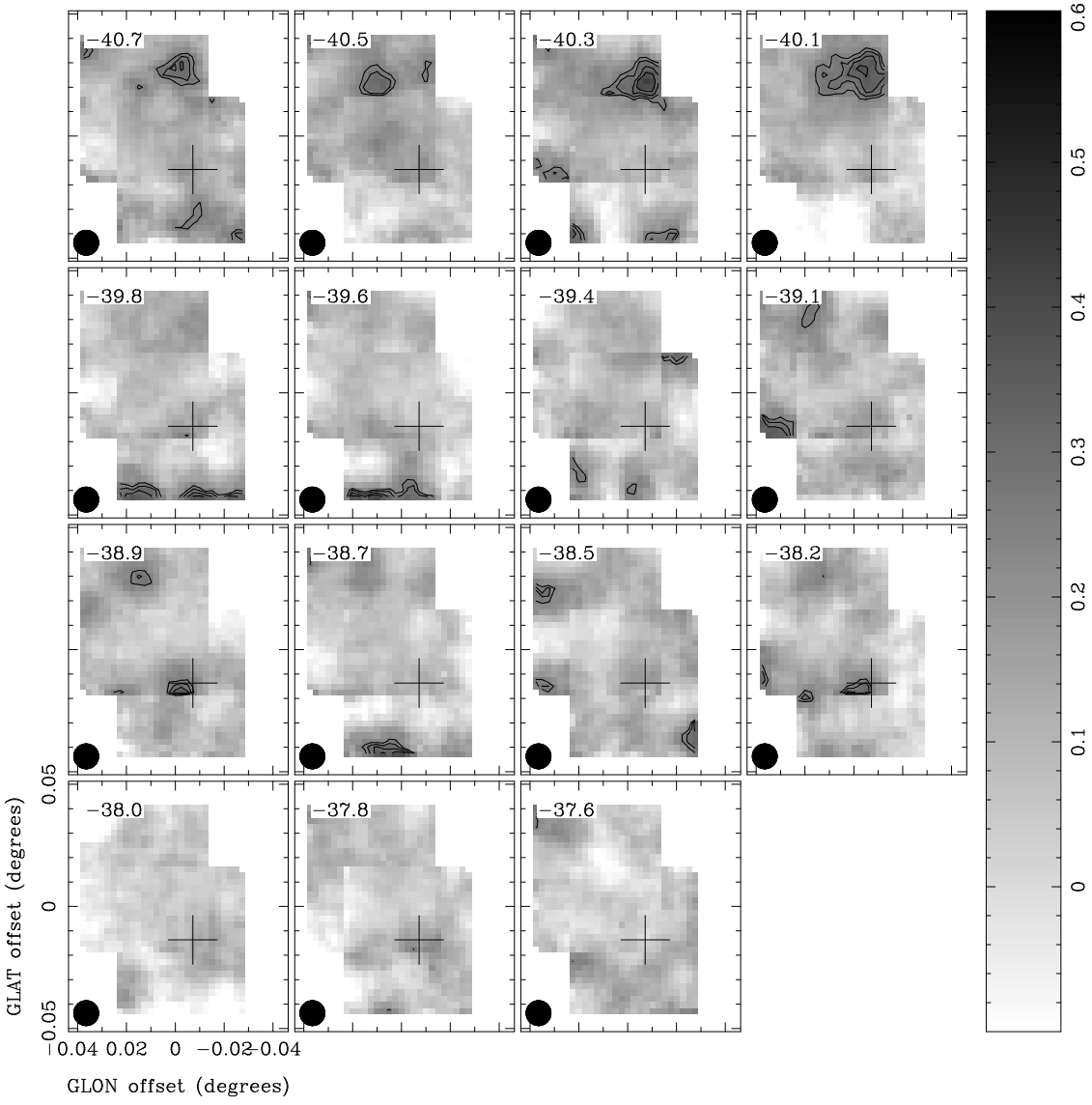

FIGURE E.8: Channel maps of HCO^+ at region covering clump C4. The cross shows the position of the clump.

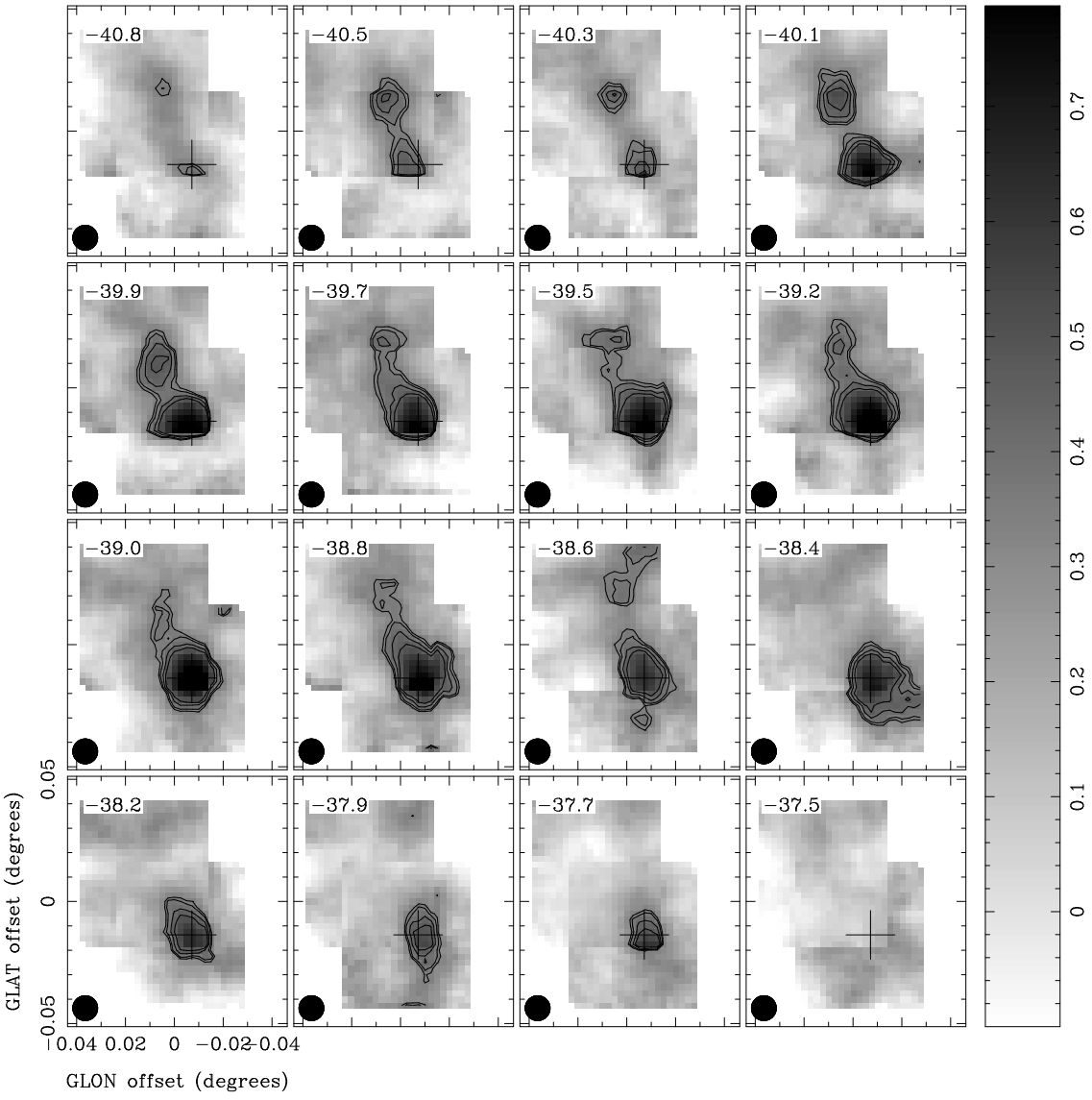

FIGURE E.9: Channel maps of N_2H^+(1-0) at region covering clump C4. The cross shows the position of the clump.

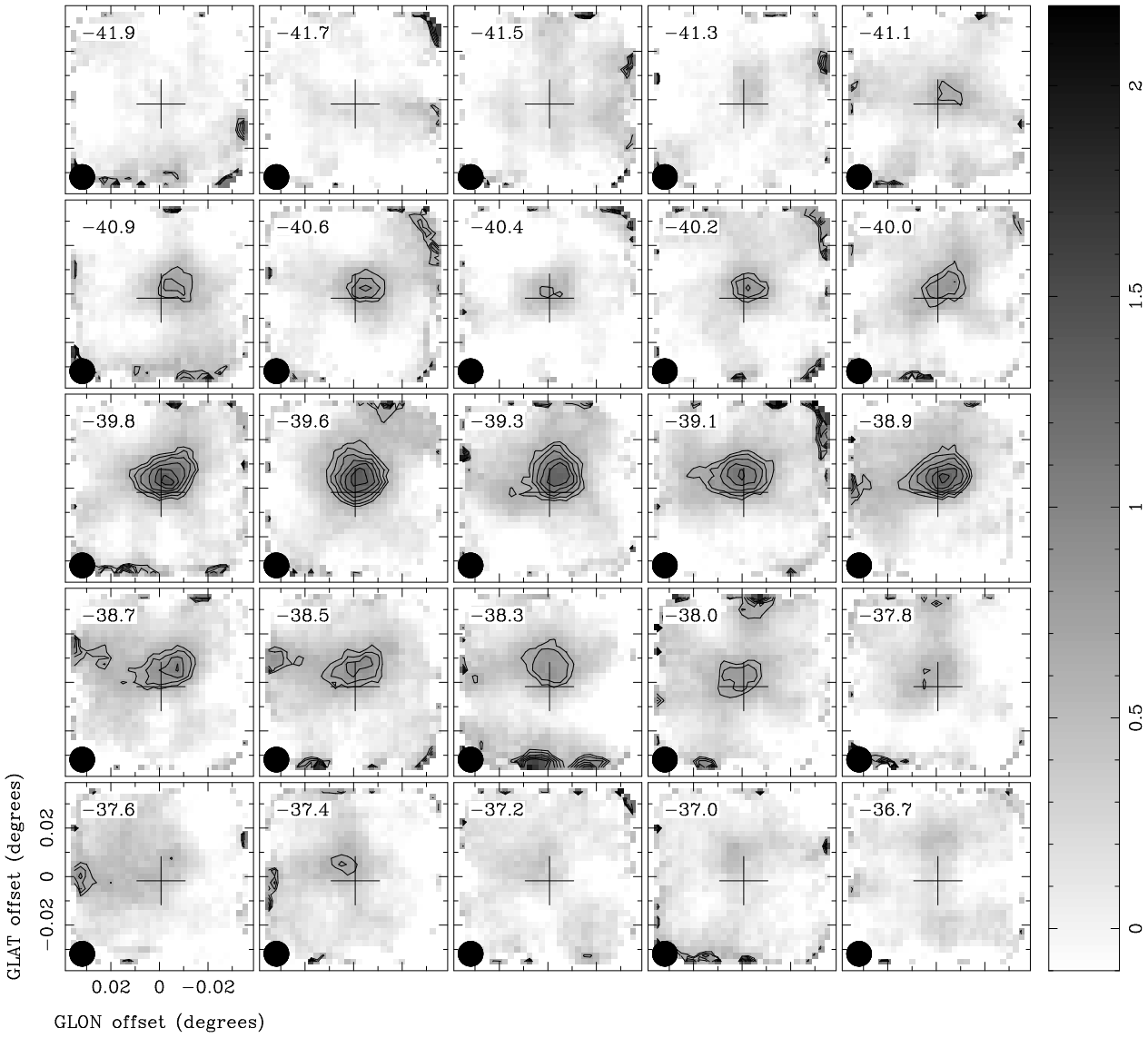

FIGURE E.10: Channel maps of N_2H^+(1-0) at region covering clumps C5. The cross shows the position of the clump.

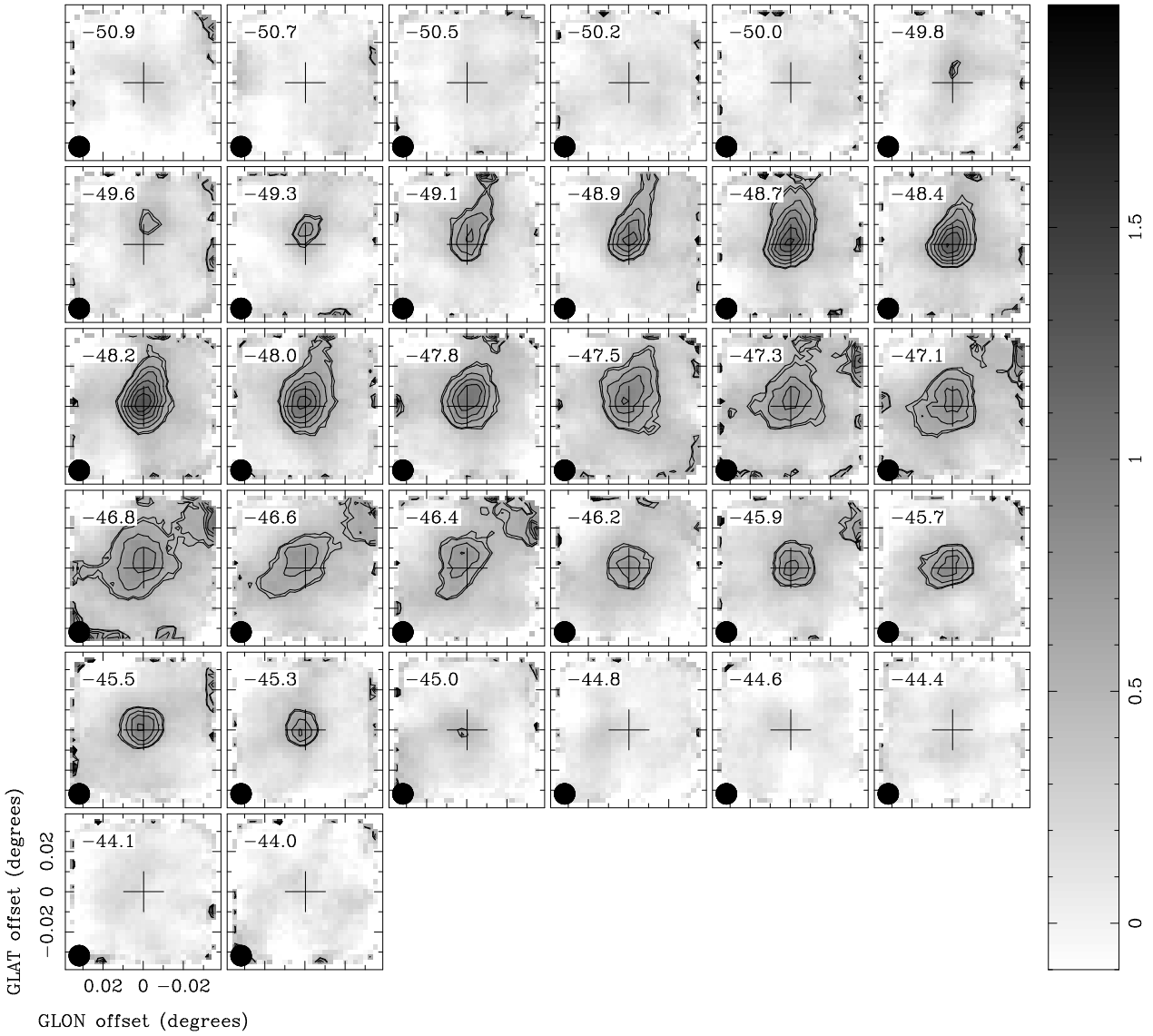

FIGURE E.11: Channel maps of HCO^+ at region covering clumps D1.

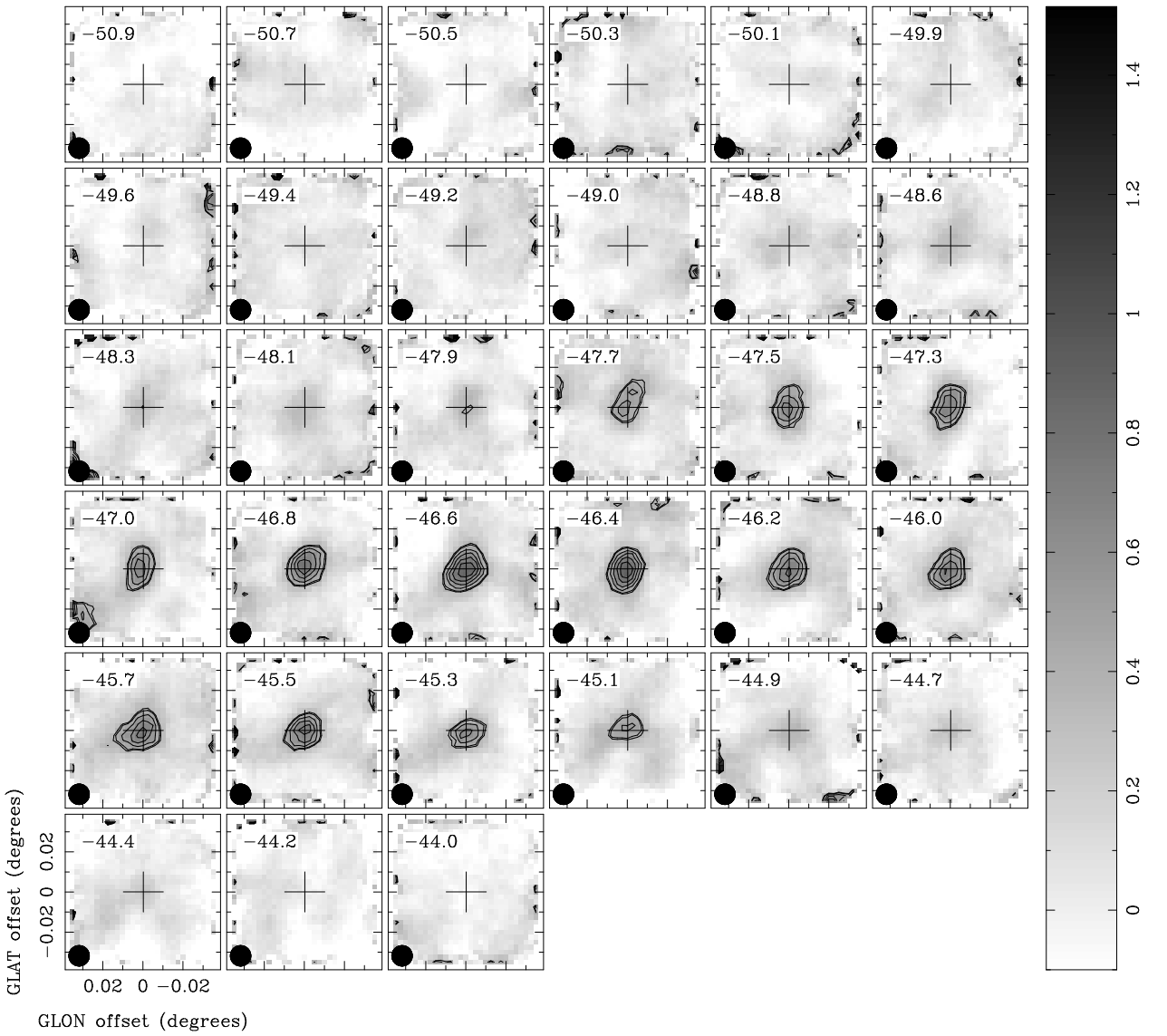

FIGURE E.12: Channel maps of N_2H^+(1-0) at region covering clumps D1.

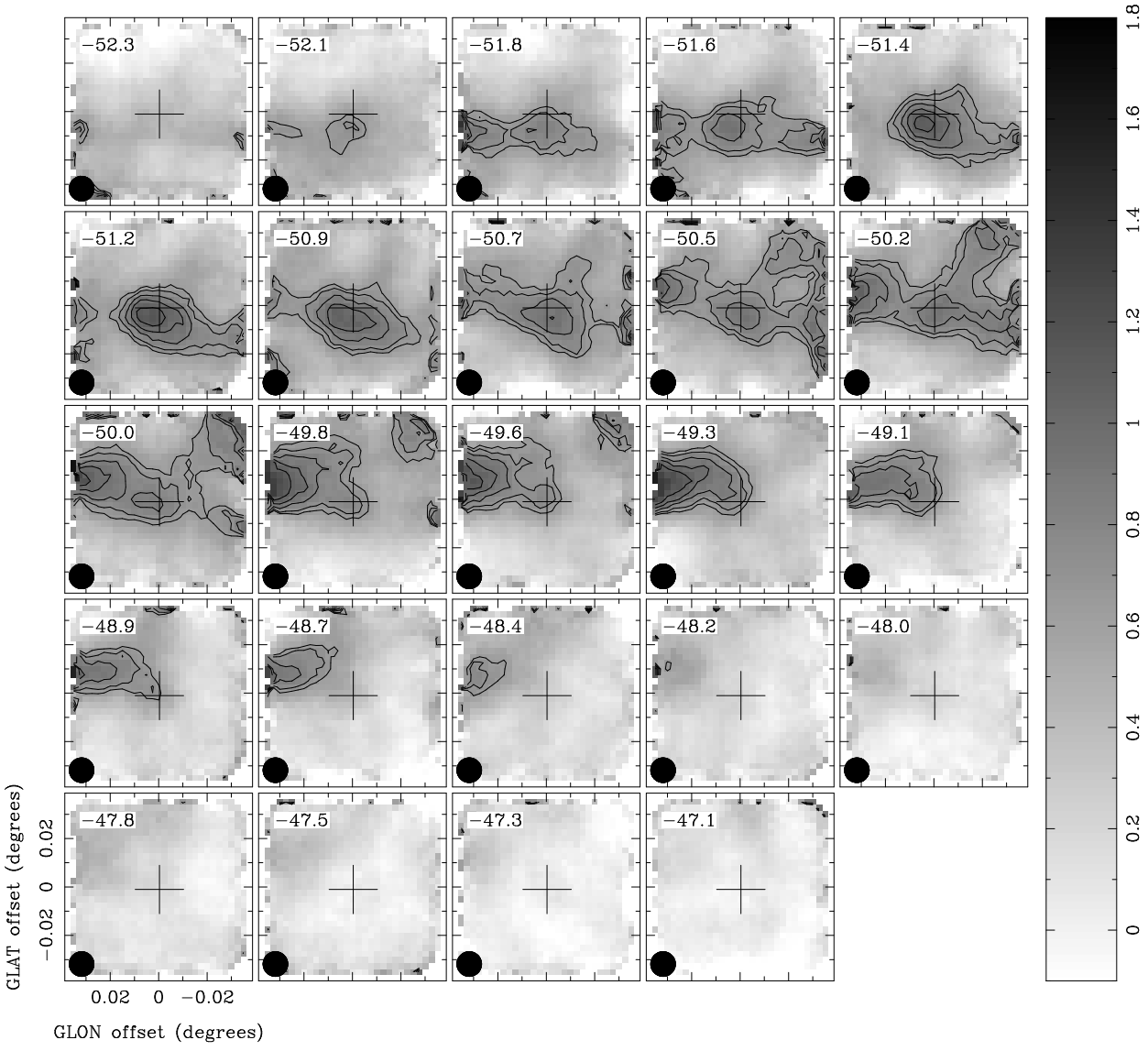

FIGURE E.13: Channel maps of HCO^+ at region covering clumps D5.

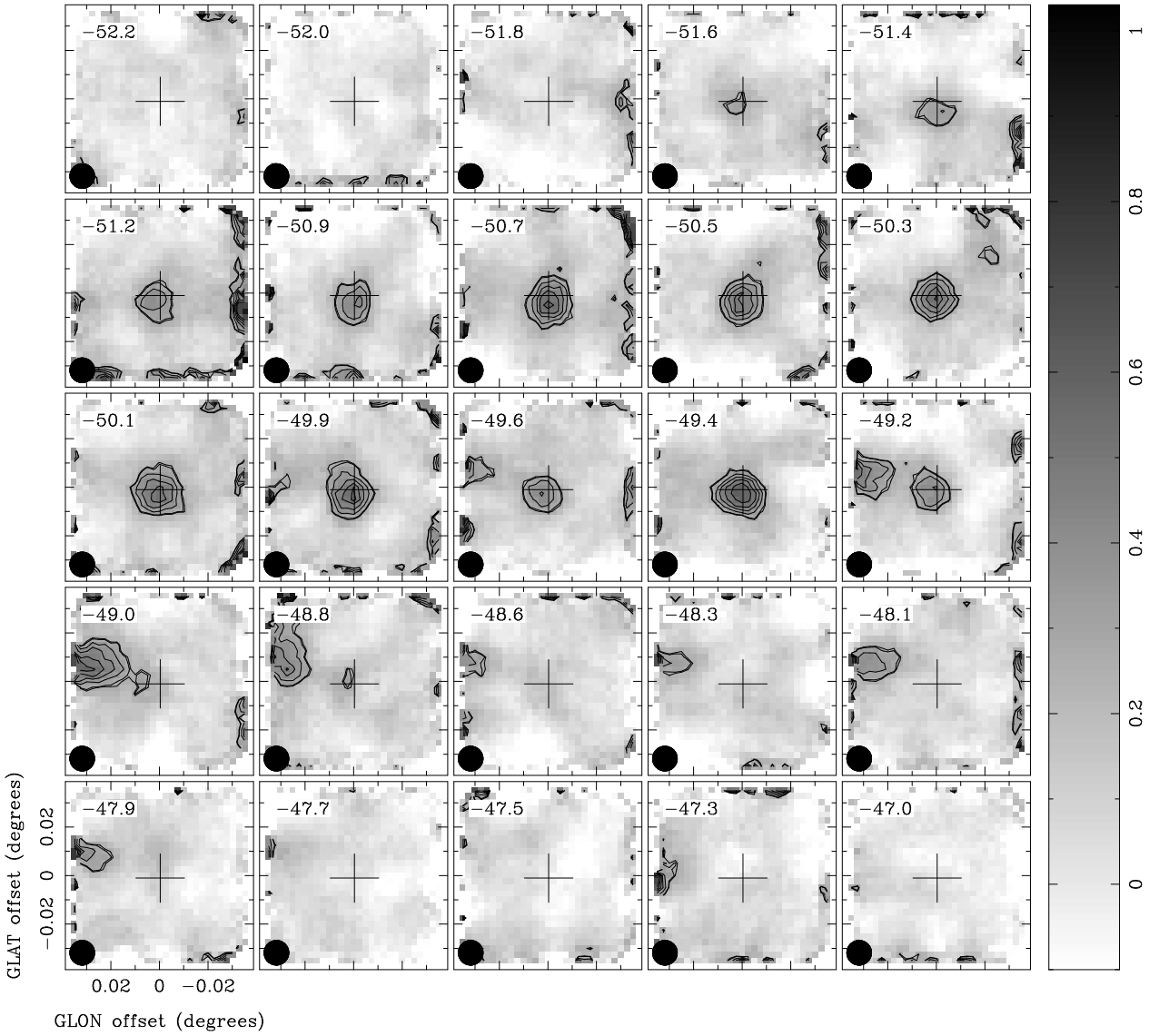

FIGURE E.14: Channel maps of N_2H^+(1-0) at region covering clumps D5.

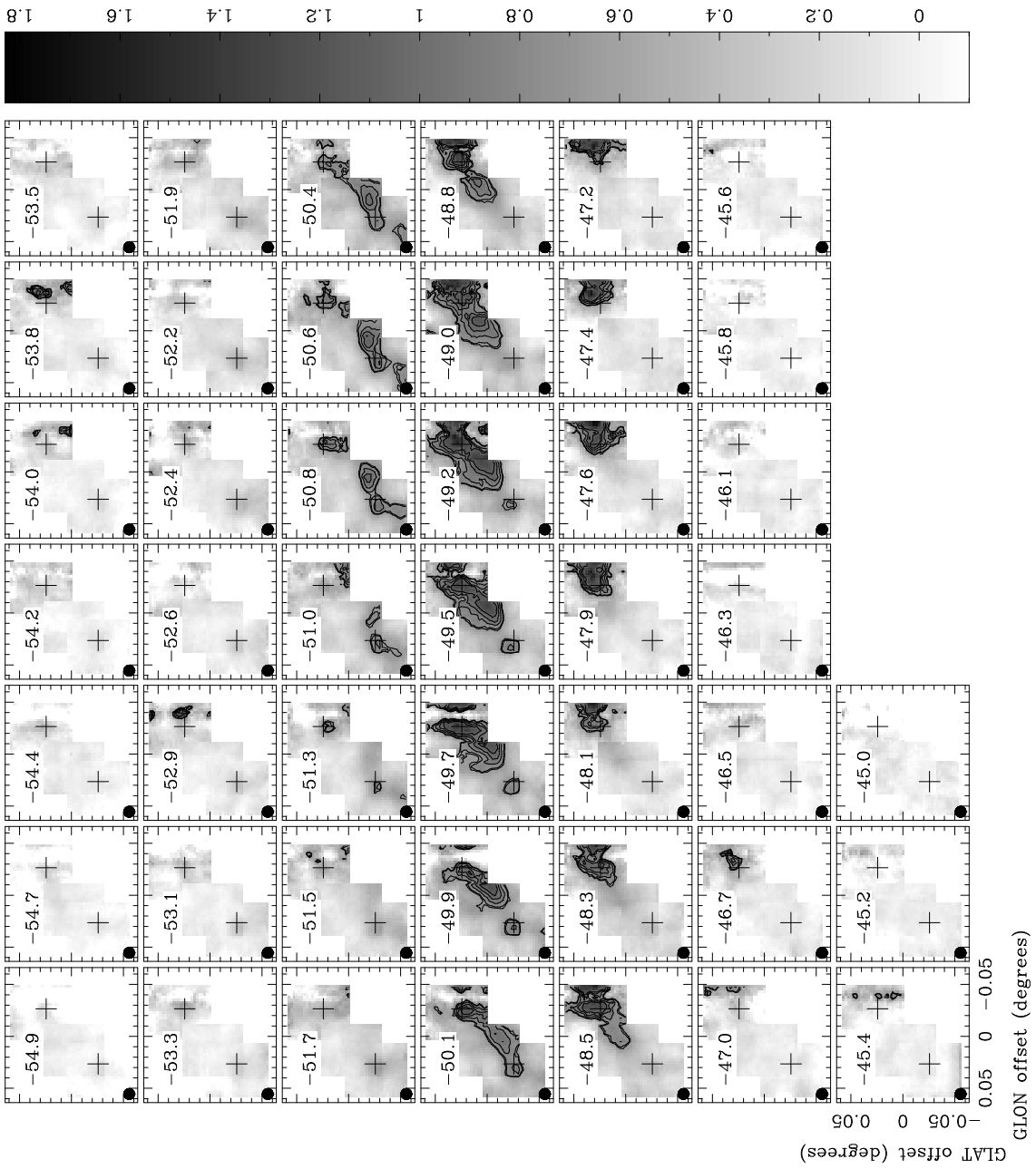

FIGURE E.15: Channel maps of HCO^+ at region covering clumps D7,D8 and D9.

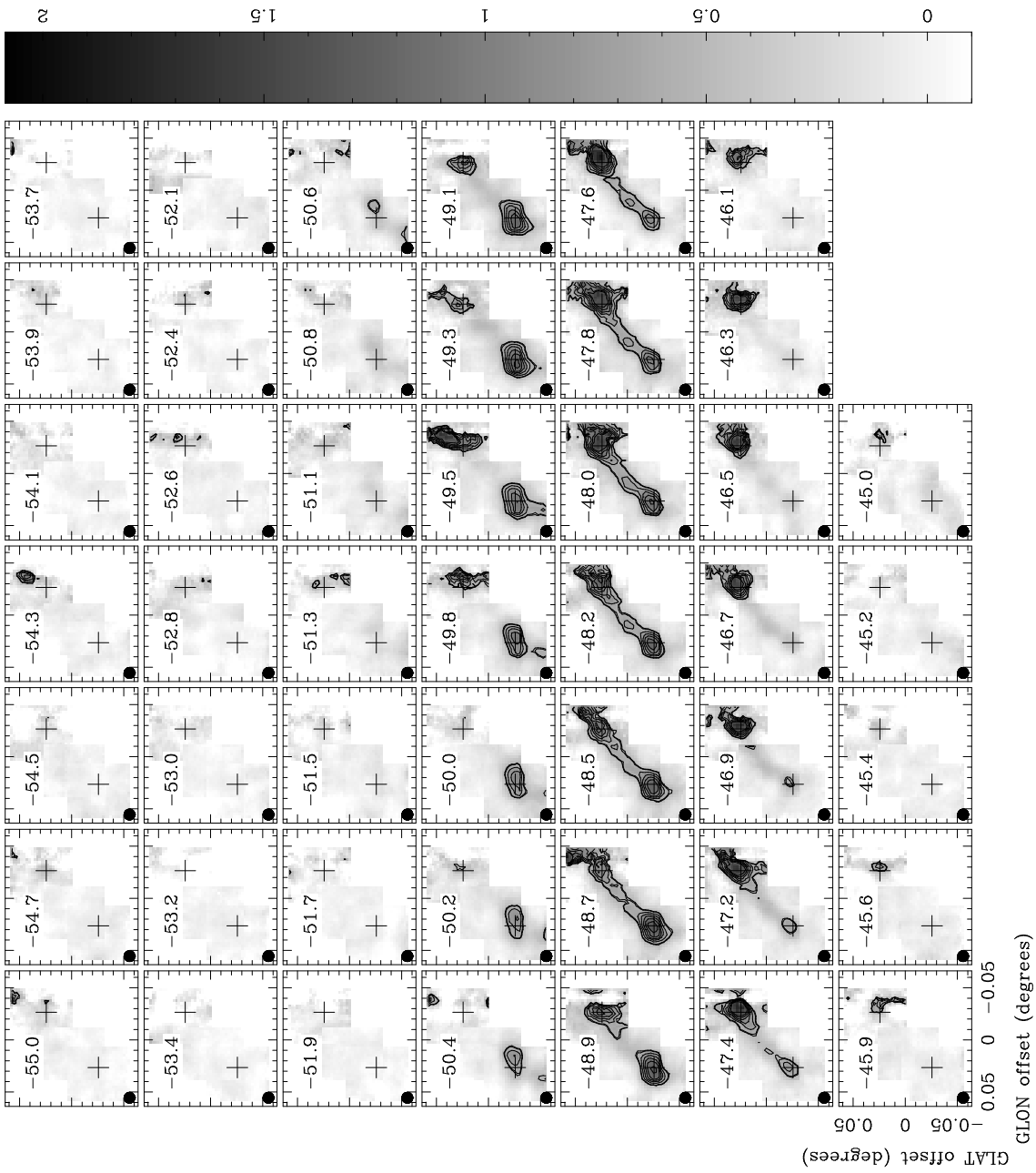

FIGURE E.16: Channel maps of N_2H^+(1-0) at region covering clumps D7, D8 and D9.

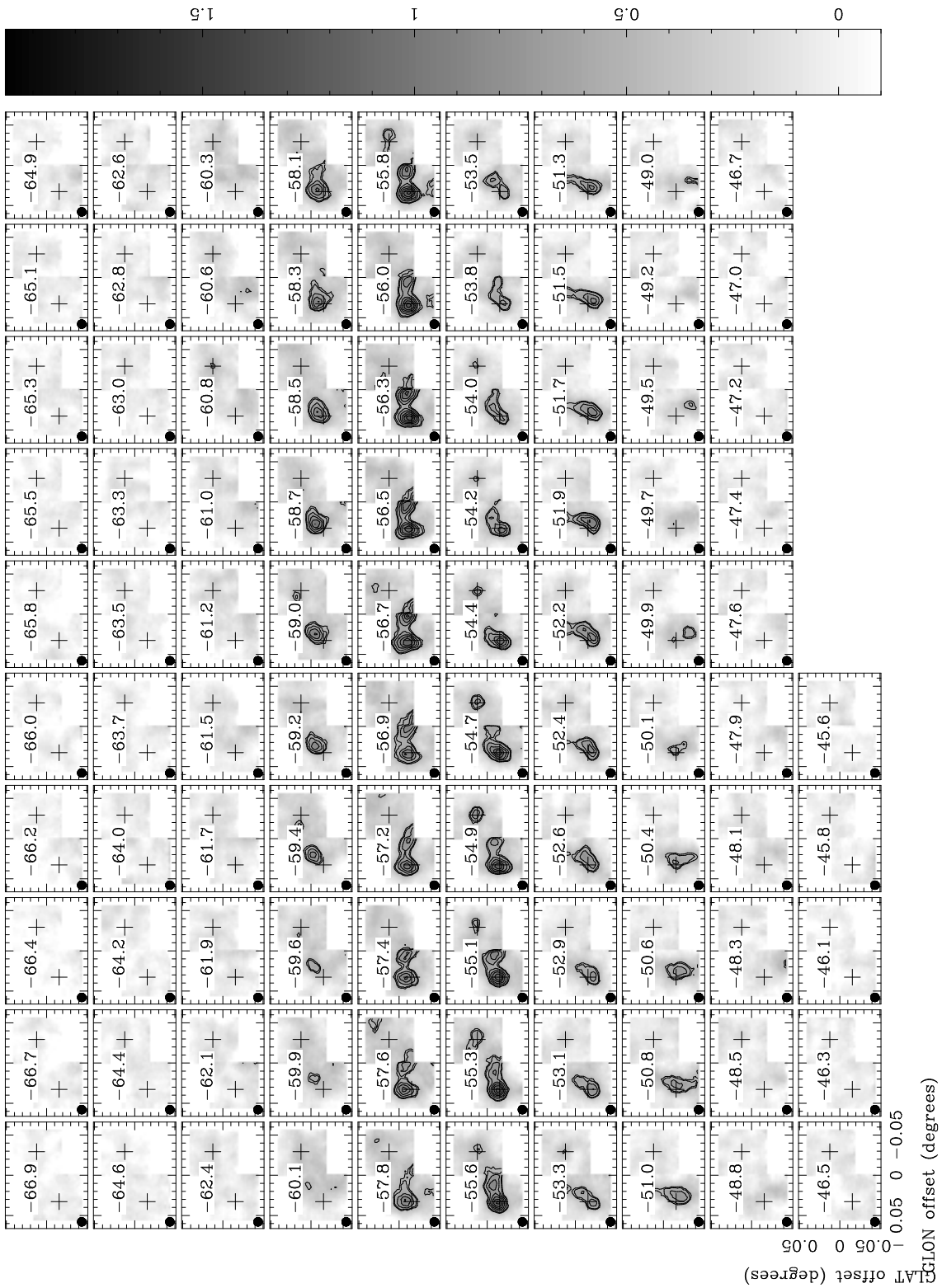

FIGURE E.17: Channel maps of HCO^+ at region covering clumps E1 and E2.

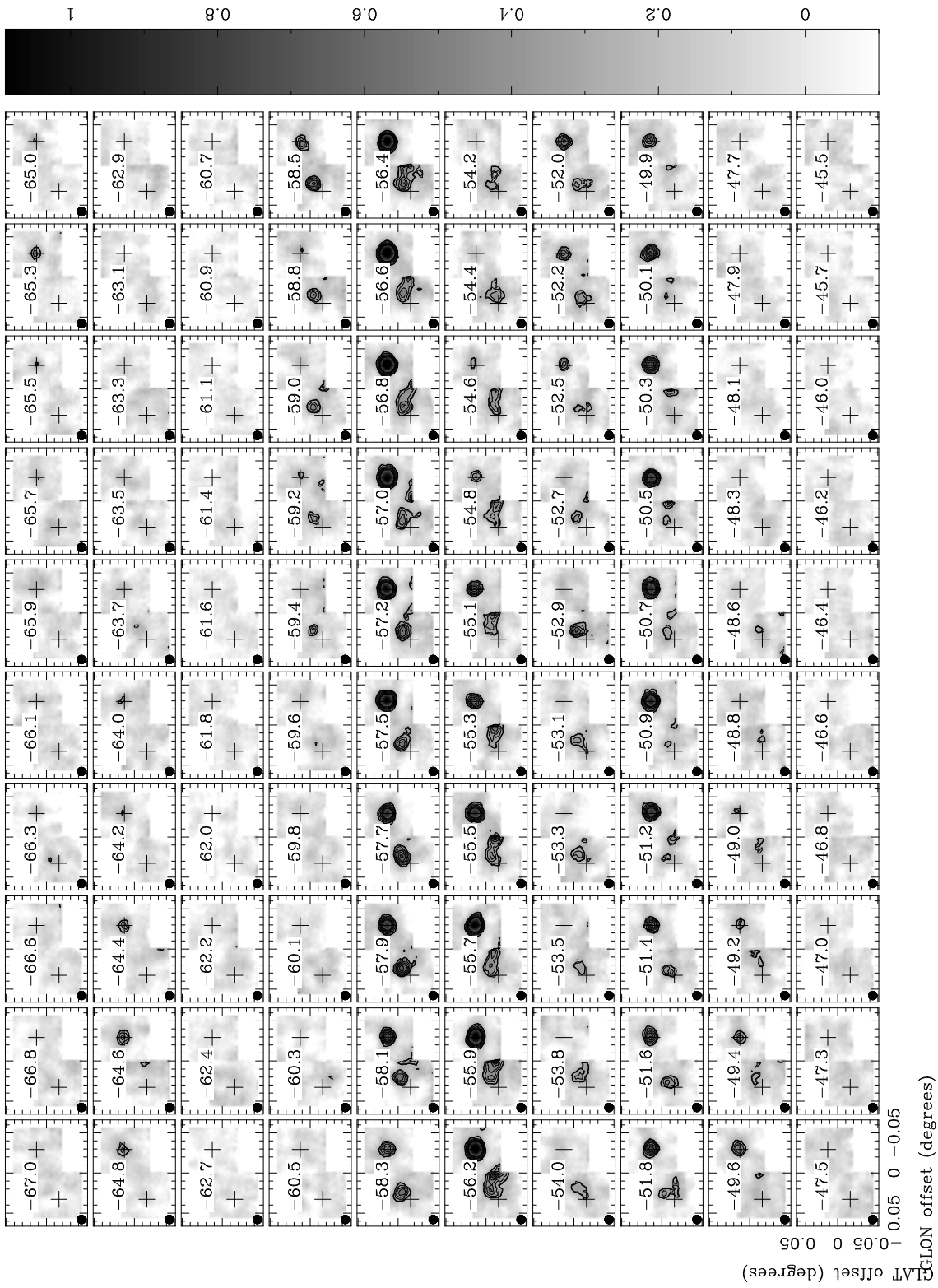

FIGURE E.18: Channel maps of N_2H^+(1-0) at region covering clumps E1 and E2.

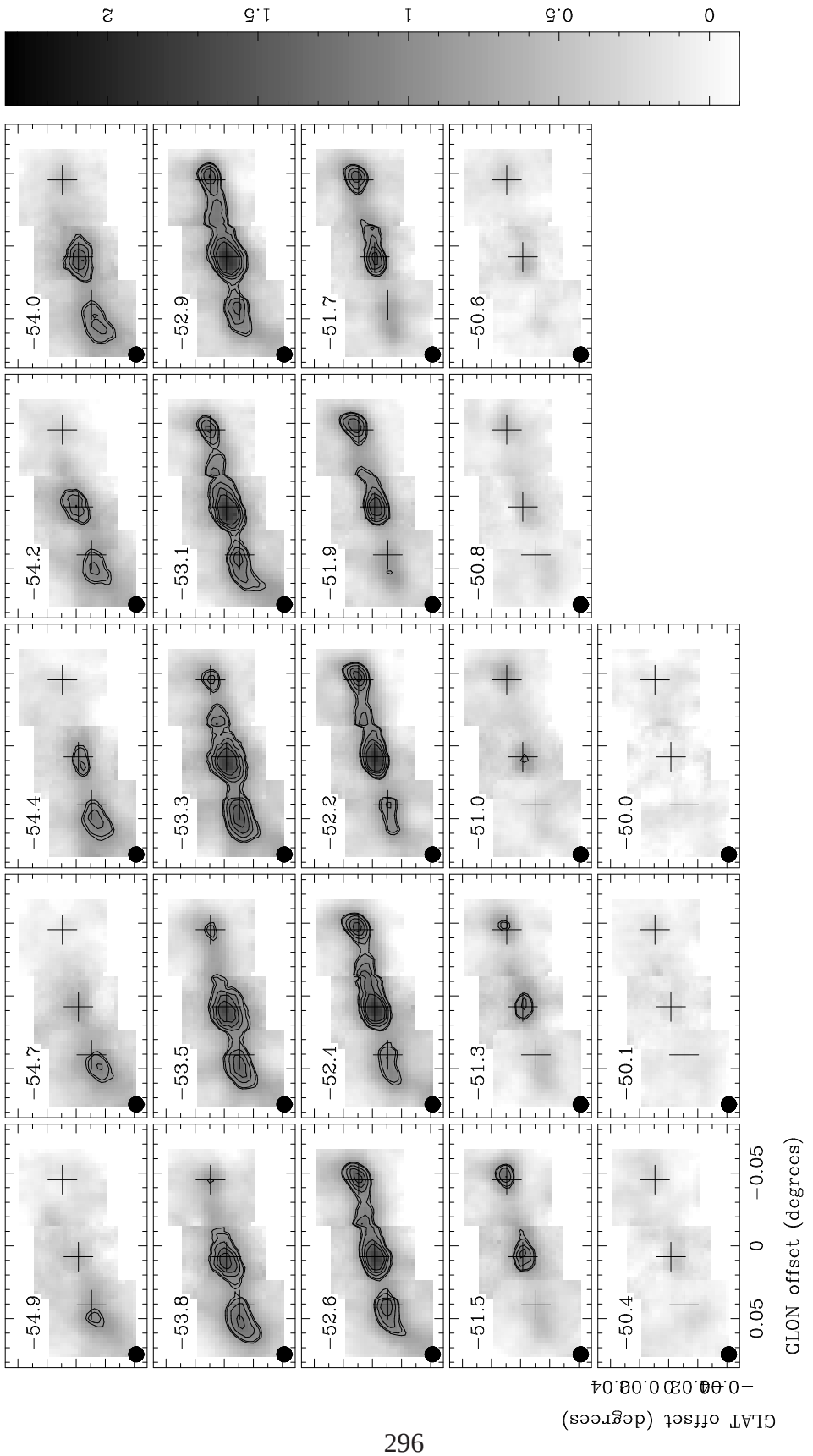

FIGURE E.19: Channel maps of HCO^+at region covering clumps E3, E4 and E5.

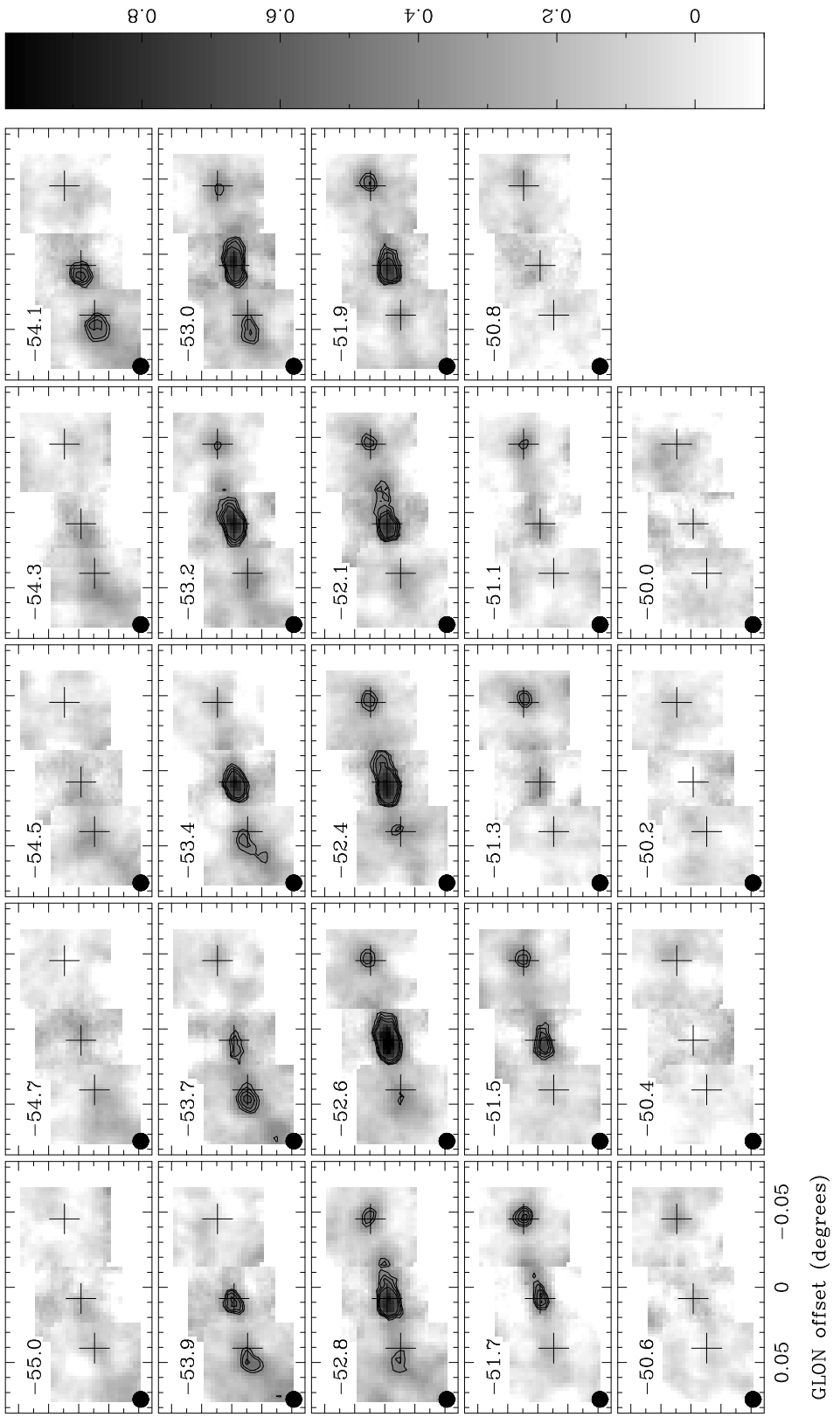

FIGURE E.20: Channel maps of N_2H^+(1-0) at region covering clumps E3, E4 and E5.

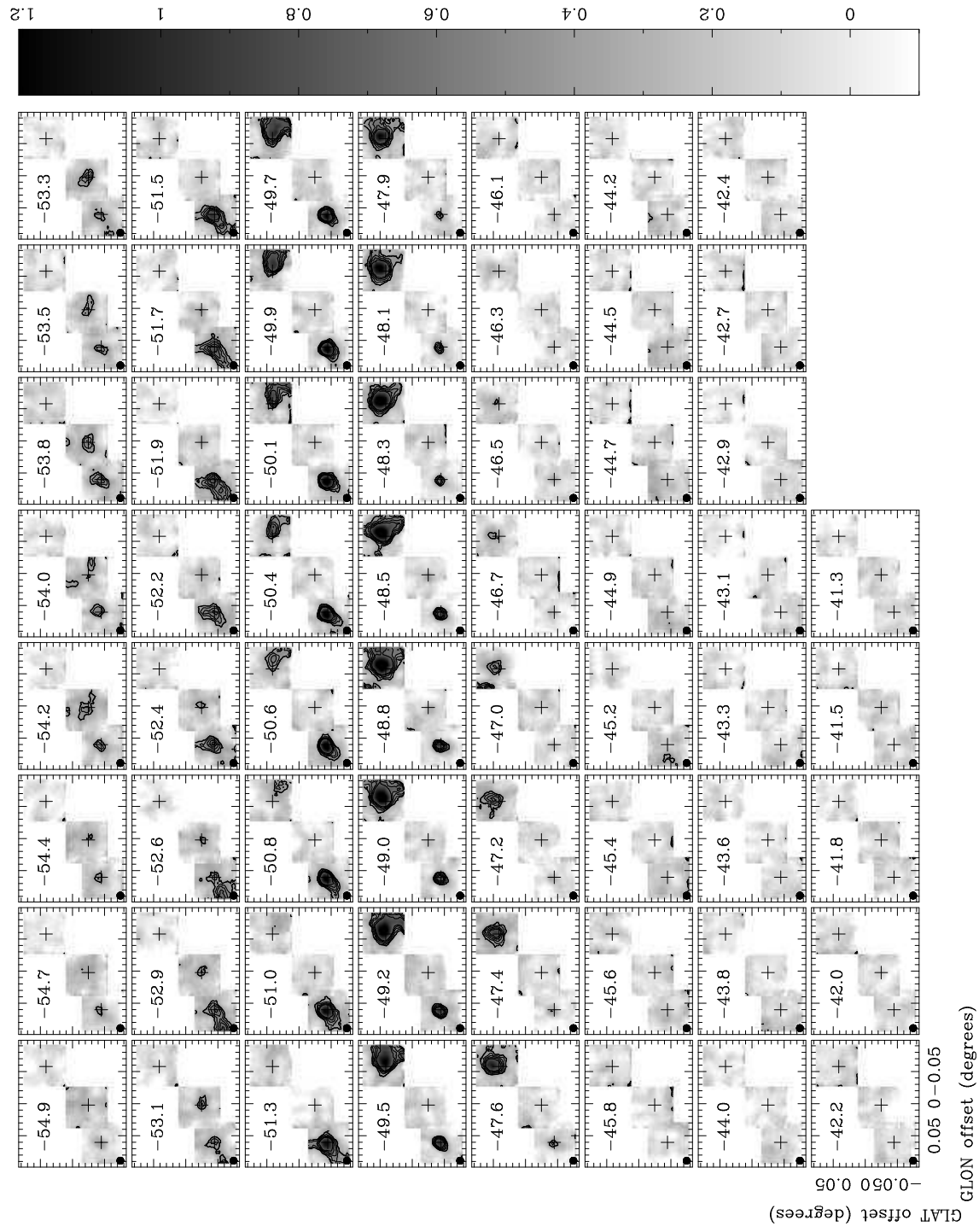

FIGURE E.21: Channel maps of HCO^+ at region covering clumps E6, E7 and E8.

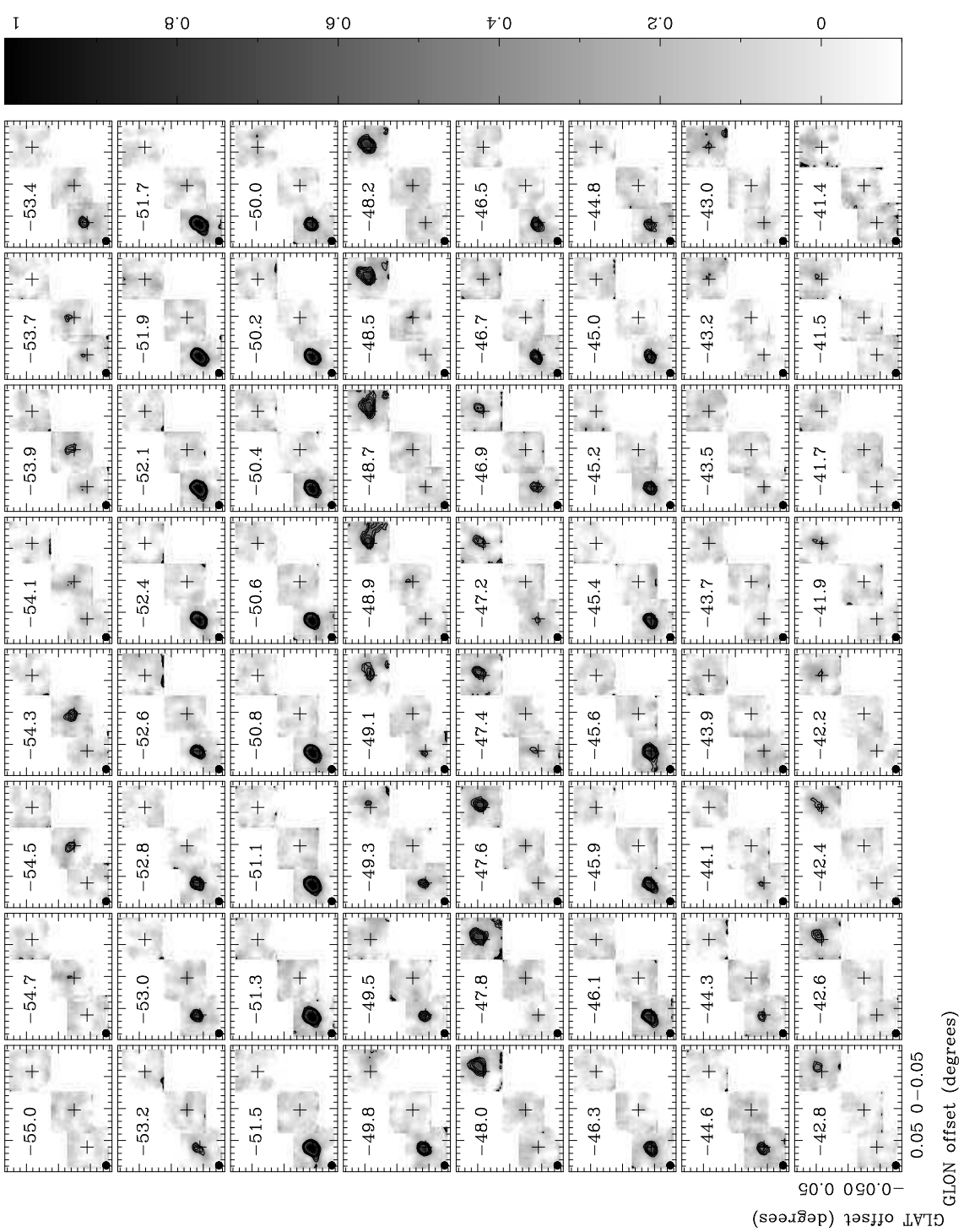

FIGURE E.22: Channel maps of N_2H^+(1-0) at region covering clumps E6, E7 and E8.

Bibliography

Aguirre, J. E., Ginsburg, A. G., Dunham, M. K., Drosback, M. M., Bally, J., Battersby, C., Bradley, E. T., Cyganowski, C., Dowell, D., Evans, II, N. J., Glenn, J., Harvey, P., Rosolowsky, E., Stringfellow, G. S., Walawender, J., and Williams, J. P.: 2011, *ApJS* **192**, 4

Alves, F. O., Franco, G. A. P., and Girart, J. M.: 2008, *A&A* **486**, L13

Alves, J., Lada, C. J., Lada, E. A., Kenyon, S. J., and Phelps, R.: 1998, *ApJ* **506**, 292

André, P., Men'shchikov, A., Bontemps, S., Könyves, V., Motte, F., Schneider, N., Didelon, P., Minier, V., Saraceno, P., Ward-Thompson, D., di Francesco, J., White, G., Molinari, S., Testi, L., Abergel, A., Griffin, M., Henning, T., Royer, P., Merín, B., Vavrek, R., Attard, M., Arzoumanian, D., Wilson, C. D., Ade, P., Aussel, H., Baluteau, J.-P., Benedettini, M., Bernard, J.-P., Blommaert, J. A. D. L., Cambrésy, L., Cox, P., di Giorgio, A., Hargrave, P., Hennemann, M., Huang, M., Kirk, J., Krause, O., Launhardt, R., Leeks, S., Le Pennec, J., Li, J. Z., Martin, P. G., Maury, A., Olofsson, G., Omont, A., Peretto, N., Pezzuto, S., Prusti, T., Roussel, H., Russeil, D., Sauvage, M., Sibthorpe, B., Sicilia-Aguilar, A., Spinoglio, L., Waelkens, C., Woodcraft, A., and Zavagno, A.: 2010, *A&A* **518**, L102

Andre, P., Ward-Thompson, D., and Motte, F.: 1996, *A&A* **314**, 625

Araya, E., Hofner, P., Churchwell, E., and Kurtz, S.: 2001, in *American Astronomical Society Meeting Abstracts*, Vol. 33 of *Bulletin of the American Astronomical Society*, p. 124.02

Arzoumanian, D., André, P., Didelon, P., Könyves, V., Schneider, N., Men'shchikov, A., Sousbie, T., Zavagno, A., Bontemps, S., di Francesco, J., Griffin, M., Hennemann, M., Hill, T., Kirk, J., Martin, P., Minier, V., Molinari, S., Motte, F., Peretto, N., Pezzuto, S., Spinoglio, L., Ward-Thompson, D., White, G., and Wilson, C. D.: 2011, *A&A* **529**, L6+

Bally, J., Lanber, W. D., Stark, A. A., and Wilson, R. W.: 1987, *ApJ* **312**, L45

Banerjee, R. and Pudritz, R. E.: 2008, in H. Beuther, H. Linz, & T. Henning (ed.), *Massive Star Formation: Observations Confront Theory*, Vol. 387 of *Astronomical Society of the Pacific Conference Series*, p. 216

Barnard, E. E.: 1919, *ApJ* **49**, 1

Benjamin, R. A., Churchwell, E., Babler, B. L., Bania, T. M., Clemens, D. P., Cohen, M., Dickey, J. M., Indebetouw, R., Jackson, J. M., Kobulnicky, H. A., Lazarian, A., Marston, A. P., Mathis, J. S., Meade, M. R., Seager, S., Stolovy, S. R., Watson, C., Whitney, B. A., Wolff, M. J., and Wolfire, M. G.: 2003, *PASP* **115**, 953

Benson, P. J., Caselli, P., and Myers, P. C.: 1998, *ApJ* **506**, 743

Bergin, E. A. and Tafalla, M.: 2007, *ARAA* **45**, 339

Bertin, E. and Arnouts, S.: 1996, *A&AS* **117**, 393

Beuther, H., Churchwell, E. B., McKee, C. F., and Tan, J. C.: 2007, *Protostars and Planets V* pp 165–180

Beuther, H., Tackenberg, J., Linz, H., Henning, T., Schuller, F., Wyrowski, F., Schilke, P., Menten, K., Robitaille, T. P., Walmsley, C. M., Bronfman, L., Motte, F., Nguyen-Luong, Q., and Bontemps, S.: 2012, *ApJ* **747**, 43

Beuther, H., Walsh, A., Schilke, P., Sridharan, T. K., Menten, K. M., and Wyrowski, F.: 2002, *A&A* **390**, 289

Bhattacharya, B. N. and Gordy, W.: 1960, *Physical Review* **119**, 144

Blake, G. A., Sutton, E. C., Masson, C. R., and Phillips, T. G.: 1987, *ApJ* **315**, 621

Blitz, L.: 1993, in E. H. Levy and J. I. Lunine (eds.), *Protostars and Planets III*, pp 125–161

Blitz, L. and Williams, J. P.: 1999, *ArXiv Astrophysics e-prints*

Bodenheimer, P. and Sweigart, A.: 1968, *ApJ* **152**, 515

Bohlin, R. C., Savage, B. D., and Drake, J. F.: 1978, *ApJ* **224**, 132

Bonnell, I. A.: 2002, in P. Crowther (ed.), *Hot Star Workshop III: The Earliest Phases of Massive Star Birth*, Vol. 267 of *Astronomical Society of the Pacific Conference Series*, p. 193

Bonnell, I. A., Bate, M. R., and Zinnecker, H.: 1998, *MNRAS* **298**, 93

Bonnell, I. A., Vine, S. G., and Bate, M. R.: 2004, *MNRAS* **349**, 735

Boulares, A. and Cox, D. P.: 1990, *ApJ* **365**, 544

Brand, J., Blitz, L., and Wouterloot, J.: 1985, *Mitteilungen der Astronomischen Gesellschaft Hamburg* **63**, 207

Bronfman, L., Nyman, L.-A., and May, J.: 1996, *A&AS* **115**, 81

Burton, W. B., Liszt, H. S., and Baker, P. L.: 1978, *ApJ* **219**, L67

Carey, S., Noriega-Crespo, A., Price, S., Padgett, D., Ali, B., Berriman, B., Boulanger, F., Cutri, R., Indebetouw, R., Ingalls, J., Kuchar, T., Kraemer, K., Latter, B., Marleau, F., Mizuno, D., Miville-Deschenes, M., Molinari, S., Rebull, L., and Testi, L.: 2005, in *Spitzer Proposal ID #20597*, pp 20597–+

Carey, S. J., Noriega-Crespo, A., Mizuno, D. R., Shenoy, S., Paladini, R., Kraemer, K. E., Price, S. D., Flagey, N., Ryan, E., Ingalls, J. G., Kuchar, T. A., Pinheiro Gonçalves, D., Indebetouw, R., Billot, N., Marleau, F. R., Padgett, D. L., Rebull, L. M., Bressert, E., Ali, B., Molinari, S., Martin, P. G., Berriman, G. B., Boulanger, F., Latter, W. B., Miville-Deschenes, M. A., Shipman, R., and Testi, L.: 2009, *PASP* **121**, 76

Caselli, P., Benson, P. J., Myers, P. C., and Tafalla, M.: 2002, *ApJ* **572**, 238

Caswell, J. L. and Haynes, R. F.: 1987, *Australian Journal of Physics* **40**, 215

Chandrasekhar, S.: 1961, *Hydrodynamic and hydromagnetic stability*

Chandrasekhar, S. and Fermi, E.: 1953, *ApJ* **118**, 116

Chapman, N. L., Goldsmith, P. F., Pineda, J. L., Clemens, D. P., Li, D., and Krčo, M.: 2011, *ApJ* **741**, 21

Cowie, L. L.: 1980, *ApJ* **236**, 868

Daniel, F., Cernicharo, J., and Dubernet, M.-L.: 2006, *ApJ* **648**, 461

de Geus, E. J., Bronfman, L., and Thaddeus, P.: 1990, *A&A* **231**, 137

Downes, D., Wilson, T. L., Bieging, J., and Wink, J.: 1980, *A&AS* **40**, 379

Draine, B. T.: 2003, *ARAA* **41**, 241

Edgar, R. and Clarke, C.: 2004, *MNRAS* **349**, 678

Egan, M. P., Price, S. D., Kraemer, K. E., Mizuno, D. R., Carey, S. J., Wright, C. O., Engelke, C. W., Cohen, M., and Gugliotti, M. G.: 2003, *VizieR Online Data Catalog* **5114**, 0

Egan, M. P., Shipman, R. F., Price, S. D., Carey, S. J., Clark, F. O., and Cohen, M.: 1998, *ApJ* **494**, L199

Ellingsen, S. P.: 2006, *ApJ* **638**, 241

Elmegreen, B. G.: 1982, *ApJ* **253**, 655

Faúndez, S., Bronfman, L., Garay, G., Chini, R., Nyman, L.-Å., and May, J.: 2004, *A&A* **426**, 97

Fiege, J. D., Johnstone, D., Redman, R. O., and Feldman, P. A.: 2004, *ApJ* **616**, 925

Fiege, J. D. and Pudritz, R. E.: 1999, *ArXiv Astrophysics e-prints*

Fiege, J. D. and Pudritz, R. E.: 2000, *MNRAS* **311**, 85

Field, G. B.: 1970, in H. J. Habing (ed.), *Interstellar Gas Dynamics*, Vol. 39 of *IAU Symposium*, p. 51

Foster, J. B., Jackson, J. M., Barris, E., Brooks, K., Cunningham, M., Finn, S. C., Fuller, G. A., Longmore, S. N., Mascoop, J. L., Peretto, N., Rathborne, J., Sanhueza, P., Schuller, F., and Wyrowski, F.: 2011, *ArXiv e-prints*

Fuller, G. A. and Myers, P. C.: 1992, *ApJ* **384**, 523

Gahm, G. F., Johansson, L. E. B., and Liseau, R.: 1993, *A&A* **274**, 415

Garay, G. and Lizano, S.: 1999, *PASP* **111**, 1049

Goldsmith, P. F., Heyer, M., Narayanan, G., Snell, R., Li, D., and Brunt, C.: 2008, *ApJ* **680**, 428

Green, J. A., Caswell, J. L., Fuller, G. A., Avison, A., Breen, S. L., Brooks, K., Burton, M. G., Chrysostomou, A., Cox, J., Diamond, P. J., Ellingsen, S. P., Gray, M. D., Hoare, M. G., Masheder, M. R. W., McClure-Griffiths, N. M., Pestalozzi, M., Phillips, C., Quinn, L., Thompson, M. A., Voronkov, M. A., Walsh, A., Ward-Thompson, D., Wong-McSweeney, D., Yates, J. A., and Cohen, R. J.: 2009, *MNRAS* **392**, 783

Grenier, I. A., Casandjian, J.-M., and Terrier, R.: 2005, *Science* **307**, 1292

Güsten, R., Booth, R. S., Cesarsky, C., Menten, K. M., Agurto, C., Anciaux, M., Azagra, F., Belitsky, V., Belloche, A., Bergman, P., De Breuck, C., Comito, C., Dumke, M., Duran, C., Esch, W., Fluxa, J., Greve, A., Hafok, H., Häupl, W., Helldner, L., Henseler, A., Heyminck, S., Johansson, L. E., Kasemann, C., Klein, B., Korn, A., Kreysa, E., Kurz, R., Lapkin, I., Leurini, S., Lis, D., Lundgren, A., Mac-Auliffe, F., Martinez, M., Melnick, J., Morris, D., Muders, D., Nyman, L. A., Olberg, M., Olivares, R., Pantaleev, M., Patel, N., Pausch, K., Philipp, S. D.,

Philipps, S., Sridharan, T. K., Polehampton, E., Reveret, V., Risacher, C., Roa, M., Sauer, P., Schilke, P., Santana, J., Schneider, G., Sepulveda, J., Siringo, G., Spyromilio, J., Stenvers, K.-H., van der Tak, F., Torres, D., Vanzi, L., Vassilev, V., Weiss, A., Willmeroth, K., Wunsch, A., and Wyrowski, F.: 2006, in *Ground-based and Airborne Telescopes. Edited by Stepp, Larry M.. Proceedings of the SPIE, Volume 6267, pp. 626714 (2006).*, Vol. 6267 of *Presented at the Society of Photo-Optical Instrumentation Engineers (SPIE) Conference*

Gutermuth, R. A., Myers, P. C., Megeath, S. T., Allen, L. E., Pipher, J. L., Muzerolle, J., Porras, A., Winston, E., and Fazio, G.: 2008, *ApJ* **674**, 336

Hennebelle, P., Pérault, M., Teyssier, D., and Ganesh, S.: 2001, *A&A* **365**, 598

Henning, T., Michel, B., and Stognienko, R.: 1995, *Planet. Space Sci.* **43**, 1333

Herbst, W. and Assousa, G. E.: 1977, *ApJ* **217**, 473

Hernandez, A. K. and Tan, J. C.: 2011, *ApJ* **730**, 44

Herschel, W.: 1785, *Royal Society of London Philosophical Transactions Series I* **75**, 213

Hildebrand, R. H.: 1983, *QJRAS* **24**, 267

Inutsuka, S.-I. and Miyama, S. M.: 1992, *ApJ* **388**, 392

Jackson, J. M., Finn, S. C., Chambers, E. T., Rathborne, J. M., and Simon, R.: 2010, *ApJ* **719**, L185

Jappsen, A., Klessen, R. S., Larson, R. B., Li, Y., and Mac Low, M.: 2005, *A&A* **435**, 611

Johnstone, D. and Bally, J.: 1999, in V. Ossenkopf, J. Stutzki, & G. Winnewisser (ed.), *The Physics and Chemistry of the Interstellar Medium*, pp 180–+

Joint Iras Science, W. G.: 1994, *VizieR Online Data Catalog* **2125**, 0

Klessen, R. S., Ballesteros-Paredes, J., Li, Y., and Mac Low, M.: 2004, in H. J. G. L. M. Lamers, L. J. Smith, & A. Nota (ed.), *The Formation and Evolution of Massive Young Star Clusters*, Vol. 322 of *Astronomical Society of the Pacific Conference Series*, pp 299–+

Kramer, C., Richer, J., Mookerjea, B., Alves, J., and Lada, C.: 2003, *A&A* **399**, 1073

Kroupa, P.: 2007, *ArXiv Astrophysics e-prints*

Kurtz, S., Cesaroni, R., Churchwell, E., Hofner, P., and Walmsley, C. M.: 2000, *Protostars and Planets IV* pp 299–326

Kwan, J.: 1979, *ApJ* **229**, 567

Kwan, J. and Valdes, F.: 1983, *ApJ* **271**, 604

Kylafis, N. D. and Pavlakis, K. G.: 1999, in C. J. Lada & N. D. Kylafis (ed.), *NATO ASIC Proc. 540: The Origin of Stars and Planetary Systems*, p. 553

Lada, C. J., Alves, J., and Lada, E. A.: 1999, *ApJ* **512**, 250

Lada, E. A.: 1998, in C. E. Woodward, J. M. Shull, & H. A. Thronson Jr. (ed.), *Origins*, Vol. 148 of *Astronomical Society of the Pacific Conference Series*, p. 198

Larson, R. B.: 1969, *MNRAS* **145**, 271

Lawrence, A., Warren, S. J., Almaini, O., Edge, A. C., Hambly, N. C., Jameson, R. F., Lucas, P., Casali, M., Adamson, A., Dye, S., Emerson, J. P., Foucaud, S., Hewett, P., Hirst, P., Hodgkin, S. T., Irwin, M. J., Lodieu, N., McMahon, R. G., Simpson, C., Smail, I., Mortlock, D., and Folger, M.: 2007, *MNRAS* **379**, 1599

Lee, J.-E., Bergin, E. A., and Evans, II, N. J.: 2004, *ApJ* **617**, 360

Li, Z. and Nakamura, F.: 2006, *ApJ* **640**, L187

Liszt, H. S., Burton, W. B., and Bania, T. M.: 1981, *ApJ* **246**, 74

Lo, N., Cunningham, M. R., Jones, P. A., Bains, I., Burton, M. G., Wong, T., Muller, E., Kramer, C., Ossenkopf, V., Henkel, C., Deragopian, G., Donnelly, S., and Ladd, E. F.: 2009, *MNRAS* **395**, 1021

McKee, C. F. and Ostriker, E. C.: 2007, *ARAA* **45**, 565

McKee, C. F. and Tan, J. C.: 2003, *ApJ* **585**, 850

Mitchell, G. F., Johnstone, D., Moriarty-Schieven, G., Fich, M., and Tothill, N. F. H.: 2001, *ApJ* **556**, 215

Molinari, S., Swinyard, B., Bally, J., Barlow, M., Bernard, J.-P., Martin, P., Moore, T., Noriega-Crespo, A., Plume, R., Testi, L., Zavagno, A., Abergel, A., Ali, B., André, P., Baluteau, J.-P., Benedettini, M., Berné, O., Billot, N. P., Blommaert, J., Bontemps, S., Boulanger, F., Brand, J., Brunt, C., Burton, M., Campeggio, L., Carey, S., Caselli, P., Cesaroni, R., Cernicharo, J., Chakrabarti, S., Chrysostomou, A., Codella, C., Cohen, M., Compiegne, M., Davis, C. J., de Bernardis, P., de Gasperis, G., Di Francesco, J., di Giorgio, A. M., Elia, D., Faustini, F., Fischera, J. F., Fukui, Y., Fuller, G. A., Ganga, K., Garcia-Lario, P., Giard, M., Giardino, G., Glenn, J. ., Goldsmith, P., Griffin, M., Hoare, M., Huang, M., Jiang, B., Joblin, C., Joncas, G., Juvela,

M., Kirk, J., Lagache, G., Li, J. Z., Lim, T. L., Lord, S. D., Lucas, P. W., Maiolo, B., Marengo, M., Marshall, D., Masi, S., Massi, F., Matsuura, M., Meny, C., Minier, V., Miville-Deschênes, M.-A., Montier, L., Motte, F., Müller, T. G., Natoli, P., Neves, J., Olmi, L., Paladini, R., Paradis, D., Pestalozzi, M., Pezzuto, S., Piacentini, F., Pomarès, M., Popescu, C. C., Reach, W. T., Richer, J., Ristorcelli, I., Roy, A., Royer, P., Russeil, D., Saraceno, P., Sauvage, M., Schilke, P., Schneider-Bontemps, N., Schuller, F., Schultz, B., Shepherd, D. S., Sibthorpe, B., Smith, H. A., Smith, M. D., Spinoglio, L., Stamatellos, D., Strafella, F., Stringfellow, G., Sturm, E., Taylor, R., Thompson, M. A., Tuffs, R. J., Umana, G., Valenziano, L., Vavrek, R., Viti, S., Waelkens, C., Ward-Thompson, D., White, G., Wyrowski, F., Yorke, H. W., and Zhang, Q.: 2010a, *PASP* **122**, 314

Molinari, S., Swinyard, B., Bally, J., Barlow, M., Bernard, J.-P., Martin, P., Moore, T., Noriega-Crespo, A., Plume, R., Testi, L., Zavagno, A., Abergel, A., Ali, B., André, P., Baluteau, J.-P., Benedettini, M., Berné, O., Billot, N. P., Blommaert, J., Bontemps, S., Boulanger, F., Brand, J., Brunt, C., Burton, M., Campeggio, L., Carey, S., Caselli, P., Cesaroni, R., Cernicharo, J., Chakrabarti, S., Chrysostomou, A., Codella, C., Cohen, M., Compiegne, M., Davis, C. J., de Bernardis, P., de Gasperis, G., Di Francesco, J., di Giorgio, A. M., Elia, D., Faustini, F., Fischera, J. F., Fukui, Y., Fuller, G. A., Ganga, K., Garcia-Lario, P., Giard, M., Giardino, G., Glenn, J. ., Goldsmith, P., Griffin, M., Hoare, M., Huang, M., Jiang, B., Joblin, C., Joncas, G., Juvela, M., Kirk, J., Lagache, G., Li, J. Z., Lim, T. L., Lord, S. D., Lucas, P. W., Maiolo, B., Marengo, M., Marshall, D., Masi, S., Massi, F., Matsuura, M., Meny, C., Minier, V., Miville-Deschênes, M.-A., Montier, L., Motte, F., Müller, T. G., Natoli, P., Neves, J., Olmi, L., Paladini, R., Paradis, D., Pestalozzi, M., Pezzuto, S., Piacentini, F., Pomarès, M., Popescu, C. C., Reach, W. T., Richer, J., Ristorcelli, I., Roy, A., Royer, P., Russeil, D., Saraceno, P., Sauvage, M., Schilke, P., Schneider-Bontemps, N., Schuller, F., Schultz, B., Shepherd, D. S., Sibthorpe, B., Smith, H. A., Smith, M. D., Spinoglio, L., Stamatellos, D., Strafella, F., Stringfellow, G., Sturm, E., Taylor, R., Thompson, M. A., Tuffs, R. J., Umana, G., Valenziano, L., Vavrek, R., Viti, S., Waelkens, C., Ward-Thompson, D., White, G., Wyrowski, F., Yorke, H. W., and Zhang, Q.: 2010b, *PASP* **122**, 314

Mouschovias, T. C., Shu, F. H., and Woodward, P. R.: 1974, *A&A* **33**, 73

Myers, P. C.: 2009, *ApJ* **700**, 1609

Nagasawa, M.: 1987, *Progress of Theoretical Physics* **77**, 635

Nakamura, F., Hanawa, T., and Nakano, T.: 1993, *PASJ* **45**, 551

Nordhaus, M. K., Evans, N. J., Aguirre, J., Bally, J., Burnett, C., Drosback, M., Glenn, J., Laurent, G., Chamberlin, R., Rosolowsky, E., Vaillancourt, J., Walawender, J., and Williams, J.: 2008, in

A. Frebel, J. R. Maund, J. Shen, & M. H. Siegel (ed.), *New Horizons in Astronomy*, Vol. 393 of *Astronomical Society of the Pacific Conference Series*, pp 243–+

Opik, E. J.: 1953, *Irish Astronomical Journal* **2**, 219

Ostriker, J.: 1964, *ApJ* **140**, 1056

Padovani, M., Walmsley, C. M., Tafalla, M., Galli, D., and Müller, H. S. P.: 2009, *A&A* **505**, 1199

Paladini, R., Davies, R. D., and De Zotti, G.: 2004, *MNRAS* **347**, 237

Paradis, D., Bernard, J.-P., and Mény, C.: 2009, *A&A* **506**, 745

Parker, E. N.: 1966, *ApJ* **145**, 811

Perault, M., Omont, A., Simon, G., Seguin, P., Ojha, D., Blommaert, J., Felli, M., Gilmore, G., Guglielmo, F., Habing, H., Price, S., Robin, A., de Batz, B., Cesarsky, C., Elbaz, D., Epchtein, N., Fouque, P., Guest, S., Levine, D., Pollock, A., Prusti, T., Siebenmorgen, R., Testi, L., and Tiphene, D.: 1996, *A&A* **315**, L165

Peretto, N., Fuller, G. A., Plume, R., Anderson, L. D., Bally, J., Battersby, C., Beltran, M. T., Bernard, J.-P., Calzoletti, L., Digiorgio, A. M., Faustini, F., Kirk, J. M., Lenfestey, C., Marshall, D., Martin, P., Molinari, S., Montier, L., Motte, F., Ristorcelli, I., Rodón, J. A., Smith, H. A., Traficante, A., Veneziani, M., Ward-Thompson, D., and Wilcock, L.: 2010, *A&A* **518**, L98

Planck Collaboration, Ade, P. A. R., Aghanim, N., Arnaud, M., Ashdown, M., Aumont, J., Baccigalupi, C., Balbi, A., Banday, A. J., Barreiro, R. B., and et al.: 2011, *A&A* **536**, A7

Poidevin, F., Bastien, P., and Matthews, B. C.: 2010, *ApJ* **716**, 893

Preibisch, T., Ossenkopf, V., Yorke, H. W., and Henning, T.: 1993, *A&A* **279**, 577

Rathborne, J. M., Jackson, J. M., Chambers, E. T., Stojimirovic, I., Simon, R., Shipman, R., and Frieswijk, W.: 2010, *ApJ* **715**, 310

Rathborne, J. M., Jackson, J. M., and Simon, R.: 2006, *ApJ* **641**, 389

Rosolowsky, E., Dunham, M. K., Ginsburg, A., Bradley, E. T., Aguirre, J., Bally, J., Battersby, C., Cyganowski, C., Dowell, D., Drosback, M., Evans, II, N. J., Glenn, J., Harvey, P., Stringfellow, G. S., Walawender, J., and Williams, J. P.: 2010, *ApJS* **188**, 123

Saito, R. K., Hempel, M., Minniti, D., Lucas, P. W., Rejkuba, M., Toledo, I., Gonzalez, O. A., Alonso-García, J., Irwin, M. J., Gonzalez-Solares, E., Hodgkin, S. T., Lewis, J. R., Cross, N., Ivanov, V. D., Kerins, E., Emerson, J. P., Soto, M., Amôres, E. B., Gurovich, S., Dékány, I.,

Angeloni, R., Beamin, J. C., Catelan, M., Padilla, N., Zoccali, M., Pietrukowicz, P., Moni Bidin, C., Mauro, F., Geisler, D., Folkes, S. L., Sale, S. E., Borissova, J., Kurtev, R., Ahumada, A. V., Alonso, M. V., Adamson, A., Arias, J. I., Bandyopadhyay, R. M., Barbá, R. H., Barbuy, B., Baume, G. L., Bedin, L. R., Bellini, A., Benjamin, R., Bica, E., Bonatto, C., Bronfman, L., Carraro, G., Chenè, A. N., Clariá, J. J., Clarke, J. R. A., Contreras, C., Corvillón, A., de Grijs, R., Dias, B., Drew, J. E., Fariña, C., Feinstein, C., Fernández-Lajús, E., Gamen, R. C., Gieren, W., Goldman, B., González-Fernández, C., Grand, R. J. J., Gunthardt, G., Hambly, N. C., Hanson, M. M., Hełminiak, K. G., Hoare, M. G., Huckvale, L., Jordán, A., Kinemuchi, K., Longmore, A., López-Corredoira, M., Maccarone, T., Majaess, D., Martín, E. L., Masetti, N., Mennickent, R. E., Mirabel, I. F., Monaco, L., Morelli, L., Motta, V., Palma, T., Parisi, M. C., Parker, Q., Peñaloza, F., Pietrzyński, G., Pignata, G., Popescu, B., Read, M. A., Rojas, A., Roman-Lopes, A., Ruiz, M. T., Saviane, I., Schreiber, M. R., Schröder, A. C., Sharma, S., Smith, M. D., Sodré, L., Stead, J., Stephens, A. W., Tamura, M., Tappert, C., Thompson, M. A., Valenti, E., Vanzi, L., Walton, N. A., Weidmann, W., and Zijlstra, A.: 2012, *A&A* **537**, A107

Sakai, T., Sakai, N., Hirota, T., and Yamamoto, S.: 2010, *ApJ* **714**, 1658

Schilke, P., Benford, D. J., Hunter, T. R., Lis, D. C., and Phillips, T. G.: 2001, *ApJS* **132**, 281

Schnee, S., Enoch, M., Noriega-Crespo, A., Sayers, J., Terebey, S., Caselli, P., Foster, J., Goodman, A., Kauffmann, J., Padgett, D., Rebull, L., Sargent, A., and Shetty, R.: 2010, *ApJ* **708**, 127

Schnee, S. and Goodman, A.: 2005, *ApJ* **624**, 254

Schneider, S. and Elmegreen, B. G.: 1979, *ApJS* **41**, 87

Schuller, F., Menten, K. M., Contreras, Y., Wyrowski, F., Schilke, P., Bronfman, L., Henning, T., Walmsley, C. M., Beuther, H., Bontemps, S., Cesaroni, R., Deharveng, L., Garay, G., Herpin, F., Lefloch, B., Linz, H., Mardones, D., Minier, V., Molinari, S., Motte, F., Nyman, L.-Å., Reveret, V., Risacher, C., Russeil, D., Schneider, N., Testi, L., Troost, T., Vasyunina, T., Wienen, M., Zavagno, A., Kovacs, A., Kreysa, E., Siringo, G., and Weiß, A.: 2009, *A&A* **504**, 415

Scoville, N. Z. and Hersh, K.: 1979, *ApJ* **229**, 578

Shu, F. H.: 1974, *A&A* **33**, 55

Shu, F. H., Lizano, S., and Adams, F. C.: 1987, in M. Peimbert & J. Jugaku (ed.), *Star Forming Regions*, Vol. 115 of *IAU Symposium*, pp 417–433

Simon, R., Rathborne, J. M., Shah, R. Y., Jackson, J. M., and Chambers, E. T.: 2006, *ApJ* **653**, 1325

Siringo, G., Kreysa, E., De Breuck, C., Kovacs, A., Lundgren, A., Schuller, F., Stanke, T., Weiss, A., Guesten, R., Jethava, N., May, T., Menten, K. M., Meyer, H.-G., Starkloff, M., and Zakosarenko, V.: 2010, *The Messenger* **139**, 20

Siringo, G., Kreysa, E., Kovács, A., Schuller, F., Weiß, A., Esch, W., Gemünd, H., Jethava, N., Lundershausen, G., Colin, A., Güsten, R., Menten, K. M., Beelen, A., Bertoldi, F., Beeman, J. W., and Haller, E. E.: 2009, *A&A* **497**, 945

Snell, R. L., Goldsmith, P. F., Erickson, N. R., Mundy, L. G., and Evans, II, N. J.: 1984, *ApJ* **276**, 625

Snow, T. P. and McCall, B. J.: 2006, *ARAA* **44**, 367

Spitzer, Jr., L.: 1942, *ApJ* **95**, 329

Stark, A. A.: 1979, *Ph.D. thesis*, Princeton Univ., NJ.

Suzuki, H., Yamamoto, S., Ohishi, M., Kaifu, N., Ishikawa, S.-I., Hirahara, Y., and Takano, S.: 1992, *ApJ* **392**, 551

Tackenberg, J., Beuther, H., Henning, T., Schuller, F., Wienen, M., Motte, F., Wyrowski, F., Bontemps, S., Bronfman, L., Menten, K., Testi, L., and Lefloch, B.: 2012, *A&A* **540**, A113

Thompson, M. A., Hatchell, J., Walsh, A. J., MacDonald, G. H., and Millar, T. J.: 2006, *A&A* **453**, 1003

Tilley, D. A. and Pudritz, R. E.: 2003, *ApJ* **593**, 426

Tomisaka, K.: 1995, *ApJ* **438**, 226

Urquhart, J. S., Hoare, M. G., Lumsden, S. L., Oudmaijer, R. D., and Moore, T. J. T.: 2008, in H. Beuther, H. Linz, and T. Henning (eds.), *Massive Star Formation: Observations Confront Theory*, Vol. 387 of *Astronomical Society of the Pacific Conference Series*, pp 381–+

Walsh, A. J., Burton, M. G., Hyland, A. R., and Robinson, G.: 1998, *MNRAS* **301**, 640

Williams, S. J., Fuller, G. A., and Sridharan, T. K.: 2004, *A&A* **417**, 115

Woodward, P. R.: 1976, *ApJ* **207**, 484

Wyrowski, F.: 2008, in H. Beuther, H. Linz, & T. Henning (ed.), *Massive Star Formation: Observations Confront Theory*, Vol. 387 of *Astronomical Society of the Pacific Conference Series*, pp 3–+

Zinnecker, H. and Yorke, H. W.: 2007, *ARAA* **45**, 481